NASA Contractor Report 4278

Heat Transfer Measurements From a NACA 0012 Airfoil in Flight and in the NASA Lewis Icing Research Tunnel

Philip E. Poinsatte
The University of Toledo
Toledo, Ohio

Prepared for
Lewis Research Center
under Grant NAG3-72

National Aeronautics and
Space Administration
Office of Management
Scientific and Technical
Information Division

1990

An Abstract of

"Heat Transfer Measurements from a NACA 0012 Airfoil in Flight and in the NASA Lewis Icing Research Tunnel"

Philip E. Poinsatte

Submitted in partial fulfillment of the requirements of
the Master of Science Degree in
Chemical Engineering
The University of Toledo
June 1989

Local heat transfer coefficients from a smooth and roughened NACA 0012 airfoil were measured using a steady state heat flux method. Heat transfer measurements on the specially constructed 0.533 meter chord airfoil were made both in flight on the NASA Lewis Twin Otter Research Aircraft and in the NASA Lewis Icing Research Tunnel (IRT). Roughness was obtained by the attachment of small, 2 mm diameter, hemispheres of uniform size to the airfoil surface in four distinct patterns. The flight data was taken for the smooth and roughened airfoil at various Reynolds Numbers based on chord in the range 1.24×10^6 to 2.50×10^6 and at various angles of attack up to 4 degrees. During these flight tests the free stream velocity turbulence intensity was found to be very low (<0.1%). The wind tunnel data was taken in the Reynolds Number range 1.20×10^6 to 4.52×10^6 and at angles of attack from -4 degrees to +8 degrees. The turbulence intensity in the IRT was 0.5 to 0.7% with the cloud making sprays off.

Results for both the flight and tunnel tests are presented as Frossling Number based on chord versus position on the airfoil surface for various roughnesses and angle of attack. A table of power law curve fits of Nusselt Number as a function of Reynolds Number is also provided. The higher level of turbulence in the IRT versus flight had little effect on heat transfer for the lower Reynolds Numbers but caused a moderate increase in heat transfer at the higher Reynolds Numbers. Turning on the cloud making spray air in the IRT did not alter the heat transfer. Roughness generally increased the heat transfer by locally disturbing the boundary layer flow. Finally, the present data was not only compared with previous airfoil data where applicable, but also with leading edge cylinder and flat plate heat transfer values which are often used to estimate airfoil heat transfer in computer codes.

ACKNOWLEDGEMENTS

I wish to thank my advisors, Drs. Kenneth J. DeWitt of the University of Toledo, Toledo, Ohio, and G. James Van Fossen of the NASA Lewis Research Center, Cleveland, Ohio, for their invaluable experience, guidance and especially patience throughout this project. I would like to acknowledge the support of the NASA Lewis Icing Research Group and specifically the late Mr. James Newton who initiated this work. Special thanks goes out to the NASA Lewis personnel of the Icing Research Tunnel, Flight Operations and Model Shop for their very capable work and assistance. Finally, the review of this work by Drs. T. G. Keith and A. A. Afjeh of the University of Toledo is greatly appreciated.

TABLE OF CONTENTS

	Page
ABSTRACT	iii
ACKNOWLEDGEMENTS	iv
NOMENCLATURE	vii
I. INTRODUCTION	1
A. Relationship of Study to Icing of Airfoils	1
B. Ice Accretion Thermal Physics	2
C. Need for Airfoil Data	5
D. Survey of Previous Data	6
E. Scope of Present Work	8
II. EXPERIMENT EQUIPMENT AND PROCEDURE	10
A. Apparatus	10
1. NACA 0012 Test Airfoil	10
2. Twin Otter Aircraft	14
3. Icing Research Tunnel	15
B. Test Procedure	17
1. Turbulence Measurements	17
2. Heat Transfer Measurements	20
a. Flight Measurements	20
b. Icing Research Tunnel Measurements	21
C. Data Reduction	22
III. RESULTS AND DISCUSSION OF FLIGHT DATA	26
A. Smooth Airfoil	26
B. Airfoil with Leading Edge Roughness	29
C. Airfoil with Sparse Roughness	29
D. Airfoil with Dense 1 Roughness	31
IV. RESULTS AND DISCUSSION OF ICING RESEARCH TUNNEL DATA	33
A. Smooth Airfoil	33
B. Airfoil with Leading Edge Roughness	38
C. Airfoil with Sparse Roughness	39
D. Airfoil with Dense 1 Roughness	41
E. Airfoil with Dense 2 Roughness	43
V. COMPARISON OF DATA	45
A. Flight Data Versus Icing Research Tunnel Data	45
B. Comparison with Previous Experimental Studies	50
C. Experimental Data Versus Cylinder and Flat Plate Correlations	51

D. Relationship to LEWICE Ice Accretion Code 53
E. Characterization of Roughness 56

VI. CONCLUSIONS 59

BIBLIOGRAPHY 62

TABLES 65

FIGURES 77

APPENDICES 180
A. Heat Loss Analysis 180
B. Error Analysis 183

NOMENCLATURE

A	surface area of gage
c	chord length
c_p	unit heat capacity of air
c_w	unit heat capacity of water
E	heater voltage
E_t	mean bridge voltage for turbulence measurements
E_{trms}	rms bridge voltage for turbulence measurements
E_{to}	mean bridge voltage corresponding to zero velocity for turbulence measurements
d	equivalent leading edge diameter
Fr_c	Frossling number based on chord
Fr_d	Frossling number based on equivalent diameter
g	gravitational constant
h_c	local heat transfer coefficient
I	heater current
J	mechanical equivalent of heat
k	thermal conductivity of air
k_{ep}	thermal conductivity of gap epoxy
k_s	sand grain roughness height
L	length of heat transfer gage
L_e	latent heat of vaporization of water
L_f	latent heat of fusion of water
m	evaporation fraction

Ma	Mach number
n	freezing fraction
Nu_c	Nusselt number based on chord
Nu_d	Nusselt number based on equivalent diameter
P_a	ambient absolute pressure
p_{va}	vapor pressure of atmospheric moisture
p_{vs}	vapor pressure of water at T_{sur}
Q_{con}	corrected heat flow from each gage
Q_{EI}	electric power input to heater
Q_{end}	heat loss from unguarded end of heater
Q_{gap}	heat loss through gap
Q_{rad}	heat loss due to radiation
Q_c	heat flow due to convection
Q_e	heat flow due to evaporation
Q_f	heat flow due to latent heat of fusion
Q_k	heat flow due to kinetic energy of liquid particles
Q_v	heat flow due to viscous heating
Q_w	heat flow due to absorption by impinging liquid
R_w	unit rate of water catch
r	recovery factor
Re_c	Reynolds number based on chord
Re_d	Reynolds number based on equivalent diameter
S	icing surface area
T_a	ambient free stream temperature
T_f	film temperature

T_s measured static temperature

T_{sur} icing surface temperature

T_t total temperature

T_w measured gage temperature

Tu turbulence level

V free stream velocity

W width of heat transfer gage

z depth of heat transfer gage

Greek symbols

α_n roots of gap and end solution

ε surface emissivity of polished aluminum

μ viscosity of air

ρ density of air

σ Stefan-Boltzman constant

I. INTRODUCTION

The reasons for the present work to obtain heat transfer data from an airfoil were to add to the relatively small amount of experimental data available for airfoils and to provide heat transfer values to be used in numerical codes that simulate ice accretion. Because of this second reason, a short description of the icing problem and the energy balance needed to describe ice accretion will be given.

A. Relationship of Study to Icing of Airfoils

The problem of ice accretion on aircraft historically has drawn considerable attention. The hazards associated with ice formation on wings and engine inlets are well studied and quite apparent. Glaze or rime ice formations on an airfoil add weight, reduce lift, increase drag and may cause flight control problems [1-4]. A further danger arises when pieces of ice shed off a wing or engine inlet and, flying into the engine intake or smashing into the aircraft further aft, cause damage to parts of the aircraft such as the compressor blades, tail, rotors, etc. Also, ice formation on rotary aircraft has drawn much study because of the difficulty of preventing or removing it [5]. These problems have once again come into focus for civilian and military aircraft, especially in the application of low

flying missiles and helicopters in regions of cooler climate.

The two general methods used to alleviate the problems of ice accretion are anti-icing and de-icing. Anti-icing methods prevent ice from forming, most often by heating the affected area above the water freezing temperature. De-icing methods, on the other hand, remove ice after it begins to grow but before it causes much adverse effect. This is accomplished generally by melting or mechanically cracking the ice and allowing centrifugal or aerodynamic forces to shed it. In order to most efficiently apply either of these methods, it is first necessary to attain a good understanding of the icing phenomenon and to be able to predict whether or not ice will grow under specific environmental conditions and for specific locations. Further, ice growth prediction is especially vital in applications in which no ice protection equipment is used.

B. Ice Accretion Thermal Physics

The following description of the heat balance of the ice accretion process is adapted directly from Hardy [6], Messinger [7], and Cansdale and McNaughtan [8]. If an aircraft, or more specifically for this work, an airfoil, passes through sufficiently cool air containing sufficient liquid moisture content (often supercooled liquid water droplets) such that the latent heat of fusion of the water droplets can be removed during impact with the airfoil, then ice may form on that surface. For such an icing situation,

the six significant modes of heat transfer involved are outlined below. Figure 1 is an illustration of a typical control volume used. An energy balance on the control volume yields:

$$Q_c + Q_e + Q_w = Q_f + Q_v + Q_k$$

where the individual terms represent

(1) the heat lost from the surface due to convection:

$$Q_c = h_c \, S \, (T_{sur} - T_a)$$

(2) the heat lost by evaporation of the water:

$$Q_e = m \, R_w \, L_e \, S = 2.90 \, L_e \, S \, h_c \, ((P_{vs}-P_{va})/P_a)$$

(3) the heat lost from the surface due to absorption by the impinging liquid:

$$Q_w = R_w \, S \, c_w \, (T_{sur} - T_a)$$

4) the heat gained due to the latent heat of fusion as the liquid impinges and changes to the solid state at 32°F:

$$Q_f = n \, L_f \, R_w \, S$$

(5) the heat gained due to the viscous or frictional heating in the boundary layer:

$$Q_v = h_c \, S \, (r \, V^2 \, / \, 2 \, g \, J \, c_p), \quad \text{and}$$

(6) the heat gained due to the kinetic energy of the liquid particles as they strike the icing surface:

$$Q_k = R_w \, S \, (V^2 \, / \, 2 \, g \, J)$$

In the above equations,

h_c is the local heat transfer coefficient;

S is the surface area;

T_{sur} is the surface temperature;

T_a is the ambient free stream temperature;

L_e is the latent heat of vaporization of water;

m is the evaporation fraction;

R_w is the unit rate of water catch;

P_{vs} is the vapor pressure of water at T_{sur};

P_{va} is the vapor pressure of the atmospheric moisture;

P_a is the ambient absolute pressure;

c_w is the unit heat capacity of water;

L_f is the latent heat of fusion of water;

n is the freezing fraction;

r is the recovery factor;

V is the free stream velocity;

g is the gravitational constant;

J is the mechanical equivalent of heat; and

c_p is the unit heat capacity of air.

Other energy transfer modes such as radiation and conduction through the air are relatively insignificant and hence are neglected. It should also be noted that in the case in which a significant portion of the liquid water does not freeze on impact, the heat balance must include a term to account for the heat content of the runback water.

Inspection of the above terms describing the ice accretion process shows that if the convective and evaporative cooling, as well as the warming of the impinging droplets, can sufficiently overcome the kinetic and viscous heating and thus remove the latent heat of fusion from the impinging droplets, then ice will form on the surface. The dominant heat loss terms in this thermal analysis are

convective and evaporative cooling; hence the importance of the local heat transfer coefficient, h_c.

C. Need for Airfoil Data

Icing facilities and ice accretion modeling codes must accurately reproduce and simulate heat transfer in natural icing conditions. Wind tunnels typically have higher free stream turbulence levels than are found in flight, and since heat transfer is dependent on the turbulence level, this may present a problem. In this study turbulence intensity has been measured up to 210 miles per hour to be equal to or less than 0.7% in the NASA Lewis Icing Research Tunnel (IRT) with cloud making sprays off. Turbulence intensities with the cloud making nozzle atomizing air sprays turned on were found to be difficult to measure with hot wire equipment because the ambient tunnel air temperature generally averaged 20°F while the spray air temperature had to be maintained near 180°F to prevent spray nozzle freeze-up. Since hot wire equipment is a heat transfer sensing device, it was thought that readings would be affected by this temperature difference and would not measure true turbulent velocity fluctuations. Previous studies measured the IRT turbulence levels to be around 0.5% with the cloud making air sprays off and around 2% with spray equipment operating [9]; however, this latter result is somewhat suspect because of the aforementioned reasons. Again employing hot wire equipment, turbulence intensity for flight conditions measured during

this study have been found to be too low to make a meaningful measurement (<0.1%) for smooth air. Previous measurements in rough air below a layer of cumulus clouds have given somewhat higher levels (0.2-0.4%) [9]. This difference between free stream and wind tunnel turbulence has raised questions as to the validity of results obtained in icing wind tunnels.

One objective of the present tests was to determine the differences in local heat transfer from a smooth and roughened airfoil between flight and tunnel conditions in which different turbulence intensities were measured. A second objective of this work was to obtain much needed airfoil heat transfer data to better describe the thermal physics occurring during the icing process and, specifically, to provide accurate airfoil heat transfer data ice growth prediction computer codes. One such code, NASA's LEWICE [10], currently incorporates an integral boundary layer subroutine to calculate heat transfer coefficients. The present data will be used to verify these results. Often heat transfer from an airfoil is estimated with cylinder-in-crossflow heat transfer data for the stagnation region and flat plate heat transfer coefficients for the rest of the airfoil surface. The present tests provide actual data for a NACA 0012 airfoil for a smooth surface as well as for quantifiable roughness patterns.

D. Survey of Previous Data

Little data presently exists for heat transfer from an

airfoil. A NACA study (1946-1951) [11,12] compared in-flight heat transfer from an airfoil, in clear air and during icing conditions, with results from the IRT. For the flight data two separate airfoils, a NACA 0012 and a NACA 65,2-016, were tested at a 0 degree angle of attack, while only the 65,2-016 was subsequently used in the IRT. In the "flat plate" region (i.e., the region away from the stagnation area), the data showed a substantial difference between flight and IRT heat transfer on the forward portion of the airfoil where the boundary layer was laminar. The IRT data was over 30% higher than the flight data. This difference has been attributed to the higher turbulence intensities present in the IRT. This conclusion is also supported by the fact that the flight and IRT data agreed fairly well on the downstream portion of the airfoil where the boundary layer was assumed fully turbulent.

Besides being restricted to a 0 degree angle of attack, two other factors limit the usefulness of the previous data for computer code predictions. First, the data is incomplete and somewhat inconsistent in the stagnation region, the area where ice growth initiates. Secondly, this data was not taken for a rough surface, which can significantly alter boundary layer characteristics and thus the local heat transfer. Roughness, the result of early ice growth, may force a laminar boundary layer into transition in the ice formation zone. This behavior was observed in recent experiments performed on a cylinder in crossflow under different turbulence and roughness conditions [13]. Hence

the background turbulence of the IRT may not hinder the simulation of airfoil ice accretion in nature.

A 1985 study at the University of Kentucky [14] included the determination of heat transfer coefficients from a smooth NACA 0012 airfoil in a subsonic wind tunnel, as well as from a five minute ice accretion shape. The smooth airfoil measurements were taken at various angles of attack (-8 through +8 degrees) and for a chord-based Reynolds Number range of 7.6×10^5 to 2.0×10^6. While the 0 degree angle of attack data generally agreed with the NACA study, the data showed a much larger angle dependence on the suction side as compared to the pressure side. The data also demonstrated a Nusselt Number dependence on the square root of the Reynolds Number. Concerning the five minute ice shape, a correlation with the smooth airfoil data for Nusselt Number based on distance from stagnation was suggested. Again, however, more complete roughness data is lacking.

E. Scope of Present Work

The present study focused on heat transfer measurements on a NACA 0012 airfoil. The NACA 0012 was chosen because it is a symmetric profile that is commonly used in helicopter main rotor and tail rotor applications where ice growth may not be controlled by electric heating or pneumatic boots. Local heat transfer coefficients were calculated from measurements taken on a smooth and roughened NACA 0012 airfoil with a 0.533 meter (21 inch) chord length. Roughness

was obtained by the attachment of small hemispheres of uniform size (2 millimeter diameter) onto the airfoil in a set and reproducible pattern. Several distinct position patterns, similar to those employed by Schlicting [15] in his boundary layer work, were used. These patterns were chosen to facilitate numerical modeling of the roughness in various computer codes. Heat transfer measurements were recorded in flight on the NASA Lewis Twin Otter icing research aircraft and in the NASA Lewis Icing Research Tunnel. Flight data was collected for smooth and roughened surfaces at various aircraft speeds and various angles of attack up to 4 degrees. Data was acquired in the IRT for smooth and roughened airfoil surfaces at various tunnel airspeeds, with and without spray nozzle atomizing air, and for various angles of attack from negative 4 degrees (heat flux gages on the pressure side) to positive 8 degrees (heat flux gages on the suction side). Results from both sets of tests are presented separately as Frossling Number versus position on the airfoil for various roughness patterns and angles of attack. Stagnation region data is compared with Frossling's cylinder-in-crossflow solution [16] and data further aft on the airfoil is compared with flat plate correlations [17]. IRT tunnel data and Twin Otter flight data are compared with each other as well as with previously published results.

II. EXPERIMENT EQUIPMENT AND PROCEDURE

A. Apparatus

1. NACA 0012 Test Airfoil

Heat transfer measurements were made on a NACA 0012 airfoil that was designed specifically for that purpose. The airfoil had a chord length of 0.533 meters (21 inches) and a span length of 1.8 meters (6 feet). The airfoil, constructed in the NASA Lewis wood model shop, was made of mahogany and had two spars of square hollow steel tubing embedded in it. The airfoil is shown in Figure 2.

An array of heat transfer gages was located in a removable section at the center of the span. The gages were constructed of aluminum and were 6.60 centimeters (2.60 inches) long in the spanwise direction, 0.476 centimeters (0.1875 inch) wide in the flow direction, and 0.318 centimeters (0.125 inch) deep, as shown in Figure 3. Each gage had a groove machined into it which contained a type E (chromel-constantan) thermocouple which was held in place by peening the sides of a hole drilled at the base of the groove to pinch the thermocouple ball. Thermocouple extension leads were held in the groove with a room temperature vulcanizing silicone based adhesive. A commercially available thin foil heater was fastened to the back of each gage with a pressure sensitive adhesive. The heat transfer gages were held in place with an epoxy that was filled with hollow glass

microspheres and colloidal silica which made final contouring to the airfoil profile easier. Guard heaters were located beneath the heat flux gages to prevent heat from leaking out the back side of the airfoil. The airfoil and epoxy around the gages were sprayed with a thin layer of epoxy to seal them from moisture. The surface of the gages was not coated but was polished to a high luster with a polish made for aluminum.

Each heat flux gage was connected to an individual circuit that allowed the gages to be operated in a constant temperature mode. The temperature of each gage was controlled by a circuit (see Figure 4) that sensed thermocouple voltage, amplified it, compared that voltage to a reference voltage and adjusted the heater current to maintain the desired temperature. The gain of each amplifier could be manually altered to adjust the temperature of the individual gages. The reference voltage was common to all circuits and could be changed to increase or decrease the temperature of all of the gages simultaneously.

Figure 5 shows a cross-section of the airfoil and the location of the heat transfer gages. Table 1 lists the surface distance from the geometric stagnation point to the center of each gage and its heat transfer surface area.

The airfoil actually contained twenty-eight heat flux gages but only twelve of them in the forward region were used in these tests due to the time needed to stabilize each gage using the automatic control and data acquisition system. It

was felt that the gages in the forward region were of the most interest because this is where ice growth initiates. Of these twelve gages only ten were used to report data; gages 1 and 12 were employed as guard heaters to limit the amount of heat leaked from the measuring gages.

The airfoil was also instrumented with two static pressure taps. These taps were located on opposite sides of the airfoil at the 12% chord position. They were used to obtain a measure of angle of attack but were not calibrated for that purpose. Also, for the IRT tests, two thermocouples were added to the geometric stagnation point of the airfoil, on opposite sides and several inches away from the stagnation point gage (gage 4). These thermocouples protruded out from the surface less than 1 millimeter. They were used to measure the total temperature.

Surface roughness was added to the airfoil by fastening hemispheres of silver alloy to the surface with cyanoacrylic adhesive. The hemispheres were 2 millimeters in diameter and were attached to the airfoil in different patterns. Three patterns were employed in the flight tests while four were used in the tunnel tests. Photographs of the patterns are shown in Figure 6. Figure 7 shows planar sketches of the location of the roughness elements relative to the heat flux gages for each of the patterns. The thermal resistance of the gage surface was not altered significantly because of the sparse spacing of the elements and the high conductivity of the silver alloy. A numerical heat conduction computer model

predicted that the temperature at the tip of each roughness element was less than 0.28°C (0.5°F) lower than the temperature of the smooth aluminum gage surface. Also, each roughness element generally increased the heat transfer surface area by only one percent. No attempt was made to account for the presence of the roughness elements in the data reduction.

Data collection and recording was controlled by a microcomputer. For the flight tests all parameters necessary to calculate aircraft true airspeed, total temperature, pressure altitude, angle of attack and yaw were scanned by a commercially available unit which contained a multiplexer, signal conditioning amplifiers, and a 12-bit analog to digital converter. For the IRT tests, parameters to calculate tunnel temperature, pressures and speed were scanned with the same apparatus. Voltages and currents from the heat flux gages were also digitized with this unit. Digitized signals from this unit were passed to the microcomputer which scanned and recorded each channel ten times for each data point. This equipment is shown in Figure 8.

Thermocouple extensions were terminated at a constant temperature reference block whose temperature was read with a calibrated platinum resistance thermometer. Individual thermocouple channels were switched, using a relay type multiplexer, to a digital multimeter that was capable of reading down to 1 microvolt. The output from this multimeter

was then recorded by the microcomputer. Each thermocouple channel was also scanned and recorded ten times.

2. Twin Otter Aircraft

The NACA 0012 airfoil was flown atop the NASA Lewis Twin Otter Icing Research Aircraft. The aircraft with the airfoil mounted is shown during an aerodynamic check flight in Figure 9. The Twin Otter is a typical twin engine commuter type aircraft powered by two 550 shaft horsepower turboprop engines. The maximum sustainable speed with the NACA 0012 research airfoil mounted was around 154 miles per hour (135 knots) at 1585-2250 meters (5200-7400 feet) pressure altitude and a temperature range of 10-21°C (60-70°F). The airfoil was mounted on the aircraft by attaching the lower end of it to a column that extended through the research hatch to the floor of the fuselage. The upper end of the airfoil was secured by flying wires that were attached to the sides of the fuselage. Airspeed was measured using the pitot-static probe built into the boom attached to the nose of the aircraft, as shown in Figure 9.

Angle of attack and yaw were measured using four pressure sensing ports in the hemispherical tip of the boom. The pressure difference from the two vertically opposed pressure taps was calibrated to measure aircraft angle of attack by comparing it to the deck angle measured with an inclinometer. The zero yaw Δp obtained from the horizontally opposed pressure taps was calibrated by aligning a string attached to the nose of the aircraft which followed the

airstream with the aircraft centerline. The slope of the yaw Δp versus yaw angle was assumed to be the same as that for the angle of attack.

Free stream static temperature was measured with a commercially available temperature probe which contained a platinum resistance thermometer in a specially designed scoop housing. The manufacturer supplied calibration data to obtain static temperature from the recovery temperature measured by the probe and the true airspeed [18]. The total temperature was calculated using the one-dimensional energy equation for a perfect gas under isentropic conditions.

A previous calibration of airspeed measured at the boom versus airspeed measured at the location of the airfoil was used to obtain free stream velocity, total temperature and static pressure at the test airfoil.

Flight tests were performed in darkness to avoid any effect that solar heating may have had on the heat flux gage temperatures.

3. Icing Research Tunnel

The NACA 0012 heat transfer airfoil was also tested in the NASA-Lewis Icing Research Tunnel (IRT). The IRT is a closed-loop subsonic refrigerated air tunnel used primarily for icing studies. A plan view of the IRT is shown in Figure 10. Air flow is induced by a 5000 horsepower, 7.31 meter (24 foot) diameter fan, and airspeed in the 1.83 by 2.74 meter (6 by 9 foot) test section can be varied from about 20 to 280 miles per hour. The air is cooled by passage through a heat

exchanger unit which is integrated to an external refrigeration unit. The system maintained total air temperature around -6.7°C (20°F), plus or minus 0.55°C (1°F). The tunnel air temperature was measured by a collection of eleven thermocouples strategically positioned on the first turning vane upstream of the test section. Spray bars, located approximately 14.6 meters (48 feet) upstream of the test section, are used to produce the icing cloud. The spray bars contain a collection of properly spaced and calibrated spray nozzles. The cleverly designed nozzles shoot a combination of pressurized air and water to yield a continuous and uniform cloud of very small unfrozen water droplets. The spray bars are also heated with a separate closed steam loop to prevent nozzle freeze-up. The liquid water content of the tunnel icing cloud can generally range from about 0.2 to 3.0 grams per cubic meter, and the drop size diameter can range from about 5 to 40 microns [19]. Typical cloud conditions require the nozzle atomizing spray air to be set at 60 psi at roughly 82.2°C (180°F). In the present heat transfer test, ice growth on the airfoil was to be avoided; therefore, when the spray bars were employed, only the 60 psi air was used. No water was passed through the nozzles.

Airspeed was measured using a pitot-static probe attached to the wall in the tunnel test section. It was positioned roughly 3.05 meters (10 feet) in front of the test airfoil, about 63 cm (25 inches) from the ceiling and 51 cm

(20 inches) from the wall. The velocity determined at this point is assumed to be the free stream velocity at the center of the tunnel and this assumption is generally thought to be correct within 2-3 miles per hour.

The airfoil was mounted vertically on the turntable in the floor of the test section as shown in Figure 11. The lower end was fastened securely to the floor turntable in such a position that the chord of the airfoil was parallel to the tunnel walls when the turntable angle was set at zero degrees. The top of the airfoil was fitted with a metal collar and attached to the tunnel ceiling at a single point such that the airfoil could rotate with the turntable.

The tunnel parameters: airspeed, spray bar settings, and turntable angle were monitored and controlled by the tunnel operators through a Westinghouse computer system. Control of the temperature was primarily the responsibility of the refrigeration unit personnel. The airfoil heat transfer data collection and recording apparatus was located beneath the floor of the tunnel, just below the turntable.

B. Test Procedure

1. Turbulence Measurements

Turbulence measurements were made with a standard constant temperature hot wire anemometer operating in an uncalibrated mode [20]. The probe positioned in the airflow was constructed of a single tungsten wire. The mean component of the turbulent velocity signal was read from an

integrating digital voltmeter. The fluctuating component of the turbulent velocity signal was measured with a true RMS meter which could integrate the signal over an adjustable time period. The turbulence intensity was calculated as:

$$Tu = [(4\ E_t\ E_{trms})/(E_t^2 - E_{to}^2)] \times 100\% \qquad (1)$$

where E_t is the mean bridge voltage, E_{trms} is the RMS bridge voltage and E_{to} is the mean bridge voltage corresponding to zero velocity. The value of E_{to} is determined by covering the hot wire probe with a plastic cylinder and allowing it to come to an equilibrium temperature with the air stream.

At very low turbulence intensities (less than about 0.2%), hot wire measurements are subject to several sources of error that are not important at higher intensities. Vibrations of the prongs that the wire is mounted on and vibrations of the wire itself are among the causes of high frequency fluctuating signals that can be interpreted as turbulence if one only measures the bridge RMS voltage. To eliminate some of the effects of these false signals, the bridge voltage was run through a low pass filter that was set to cut the signal at frequencies above 5 kHz.

In this test, turbulence was measured during heat transfer test flights which took place in darkness through smooth air. The turbulence probe was mounted above the fuselage about 2.8 meters (9.2 feet) forward of the airfoil and slightly offset from the aircraft centerline. Measurements of turbulence intensity were also taken in

previous tests [9] without the heat transfer airfoil in place and were used to determine if turbulence from any part of the aircraft would interfere with the heat transfer measurements. The probe was mounted about 0.9 meter (3 feet) above the fuselage in the same position as the test airfoil heat flux gages. The aircraft was flown in daylight both in smooth air and under a layer of cumulus clouds.

For both flights, the level of turbulence intensity in smooth air was measured to be around 0.1%. Based on previous work done with hot wire equipment in low turbulence wind tunnels and examination of the bridge signal on an oscilloscope, it was felt that the turbulence intensity for these flights was as close to zero as one can get, even though the numbers from the hot wire equipment indicated otherwise. For the flight under the layer of cumulus clouds, the intensity was measured to be between 0.2 and 0.4%. This increased intensity was probably due to large scale fluctuations that the aircraft flew through. It was determined from the hot wire measurements that turbulence generated by the aircraft structure was not a problem and that there was no change in intensity at any of the different flight conditions.

Turbulence measurements were made in the IRT with the same constant temperature hot wire equipment. The probe was positioned in the center of the tunnel about a foot in front of the gages on the test airfoil. Turbulence intensity level, measured with the spray air off, was found to be 0.6,

0.52 and 0.7% at tunnel air speeds of 70, 140 and 210 miles per hour, respectively. Previous NASA tests [9] have measured the IRT turbulence levels at 0.5% without spray and 2% with the spray air on. However, these latter results are somewhat suspect due to the previously discussed concerns over the temperature difference between the spray air and the tunnel air temperatures.

2. Heat Transfer Measurements

a. Flight Measurements

All heat transfer data acquisition flights were made in darkness to avoid solar radiation on the gages and the airfoil. Flights were conducted at an arbitrary altitude that provided smooth atmospheric conditions. At low speeds, flaps were deployed to minimize the aircraft deck angle. At 80.5 miles per hour (70 knots), the measured angle of attack was about 1.5 degrees. This small angle of attack resulted in a slightly swept back test airfoil; this effect was ignored in analysis of the data.

When steady state air flow conditions were established, the heated aluminum strips were all adjusted to a constant temperature which was typically in the range of 32-41°C (90-105°F). The heat flux gages were operated in the constant temperature mode. When steady state conditions were reached, data recording was initiated. About two minutes was required to obtain and record the required ten scans of all data channels.

To obtain data for various angles of attack on the

research airfoil, the pilot yawed the aircraft (aircraft yaw = research airfoil angle of attack) using a combination of rudder and aileron. The difference in pressure between the two static pressure taps on the airfoil gave a measure of the angle of attack; this quantity was recorded with the other data. Figure 12 is a plot of aircraft yaw angle measured from the boom Δp versus the pressure difference between the two static taps on the airfoil, made dimensionless by dividing by the dynamic pressure. The scatter in this plot represents the accuracy with which the pilot could set and hold the aircraft yaw (and airfoil angle of attack).

b. Icing Research Tunnel Measurements

The heat transfer tests done in the IRT were performed in much the same way as the flight tests. After the initial (roughly 45 minutes) tunnel cooldown, the heat transfer experiments were begun. The airfoil angle of attack was set by rotating the floor turntable to the desired position and the tunnel air velocity was varied by adjusting the fan speed. When steady state tunnel conditions were achieved, the airfoil heaters were all adjusted to a constant temperature, typically in the range of 32 to 38°C (90 to 100°F). Again, data recording was initiated after steady state conditions were obtained. Roughly two minutes were required to obtain and record ten scans of all data channels. Runs were made with and without the spray air turned on.

C. Data Reduction

The average heat transfer coefficient from each gage was obtained from the applied voltage and current and the calculated temperature difference between the gage and the free stream total temperature. In the Twin Otter tests the total temperature was calculated, while in the IRT tests the total temperature was measured. Since only the convective heat transfer was desired, the radiation heat loss had to be subtracted from the total electric power input to each heater. Further, the heater gages embedded in the airfoil were secured in place and separated from each other by an epoxy resin. Some heat was conducted from the edges of each heater gage through the epoxy and convected from the surface of the airfoil in the gaps between the gages and from the unguarded ends of the gages. These losses were also subtracted from the electric power. Therefore, the local heat transfer coefficient, h_c, for each aluminum heater gage was calculated from:

$$h_c = (Q_{EI} - Q_{rad} - Q_{gap} - Q_{end}) / (A\ (T_w - T_t)) \qquad (2)$$

where Q_{EI} (voltage x current) is the total electric power input to each heater. The quantity Q_{rad} is the radiation heat loss, which is estimated by:

$$Q_{rad} = \sigma\ A\ \varepsilon\ (T_w^4 - T_t^4) \qquad (3)$$

A value of 0.045 was used for ε, the emissivity of polished aluminum, and σ is the Stefan-Boltzman constant. The

quantities Q_{gap} and Q_{end} are the heat lost through the epoxy gaps separating the aluminum gages and the unguarded ends of the heaters, respectively. These quantities were obtained from an exact solution for heat conduction in a rectangle with appropriate boundary conditions, which is detailed in Appendix A. The remaining quantities are: A, the surface area of each aluminum strip; T_w, the wall temperature measured by the thermocouple embedded into each strip; and T_t, the total temperature. For the flight data, T_t was calculated from the measured static temperature, T_s, and the true airspeed, i.e.,

$$T_t = T_s(1 + Ma/5) \tag{4}$$

where Ma is the Mach Number. For the IRT data, T_t was measured with two thermocouples positioned on the leading edge of the airfoil.

Two Frossling Numbers were employed in this analysis, one based on chord length and the other based on an equivalent leading edge diameter. This equivalent diameter is defined as the diameter of a cylinder inscribed in the leading edge of the airfoil. The Frossling Number based on chord was calculated as:

$$Fr_c = Nu_c \,/\, Re_c^{0.5} = [(h_c c/k) \,/\, (\rho V c/\mu)^{0.5}] \tag{5}$$

where c is the 0.533 meter (21 inch) chord length. The Frossling Number based on equivalent diameter was calculated as:

$$Fr_d = Nu_d / Re_d^{0.5} = [(h_c d/k) / (\rho V d/\mu)^{0.5}] \quad (6)$$

where the equivalent diameter, d, for a NACA 0012 airfoil is 3.16% of the chord or 0.0169 meters (0.664 inch) for the airfoil tested [21]. The density, ρ, was calculated from the ideal gas relation for air using the static temperature and pressure at the test airfoil location. The velocity, V, for flight data was measured with Twin Otter instrumentation and converted to the true test section velocity with the aid of calibrations obtained on previous Twin Otter flights, while the velocity for tunnel data was measured with the IRT pitot static probe. The thermal conductivity, k, and viscosity, μ, were obtained as functions of temperature from air data in Reference 22. These thermal properties were evaluated at the film temperature given by:

$$T_f = (T_w + T_t)/2 \quad (7)$$

An error analysis according to the method of Kline and McClintock [23] was performed on the calculated local heat transfer coefficient and the Frossling Number. This analysis is presented in Appendix B. The errors for each gage were similar and averaged around 4.5% for h_c and 5% for Fr_c. A substantial part of this error was found to be due to uncertainty in the gap heat loss term because the thermal conductivity of the epoxy gap material, k_{ep}, was not known exactly and was assumed to be 0.11 (with a $\pm$50% uncertainty), a typical value for epoxy of this nature. This would not be a random error but would tend to bias the data either high or

low. However, good general agreement with flat plate data seemed to confirm that the k_{ep} value used was correct.

III. RESULTS AND DISCUSSION OF FLIGHT DATA

In this section flight heat transfer data for smooth and roughened airfoil surfaces will be presented as Frossling Number based on chord length versus dimensionless surface distance from the stagnation point, s/c. The quantity c is the airfoil chord length, 21 inches. These results will be presented for nominal 0, 2, and 4 degree angles of attack, and for various Reynolds Numbers in the range 1.24×10^6 to 2.50×10^6. Table 2 contains the Frossling Numbers for all gages, Reynolds Numbers, and angles of attack for the data taken.

A. Smooth Airfoil

Figure 13 shows Frossling Number based on chord as a function of s/c for the smooth airfoil at a 0 degree angle of attack for several Reynolds Numbers. The data plotted in this manner collapses onto a single curve which shows that the Nusselt Number is proportional to the square root of the Reynolds Number. Table 3 shows the results of a least squares curve fit of the equation $Nu_c = A\ (Re_c)^B$ for the present flight data. Inspection of Table 3 shows that the Nusselt Number for the smooth airfoil more correctly correlates with Reynolds Number raised to a power of around 0.43. However, given the error involved, it is felt that the

Nusselt Number data of Figure 13 (and subsequent figures) correlates sufficiently well with the square root of the Reynolds Number. The curve fit information in Table 3 is discussed more fully in Chapter V. The solid line in Figure 13 represents the interpolated, smooth-surface, 1.93×10^6 Reynolds Number data and will be plotted on subsequent flight data figures for reference. As expected, the Frossling Number is greatest at the stagnation point (gage 4), an average value of 4.3 being observed, and then trails off smoothly to an average value of 0.93 at an s/c value of 0.083. The "bump" at s/c = 0.048 (gage 8) cannot be explained; there are no obvious roughness or steps on the surface of the airfoil at this or any other point. Possibly there is a subtle anomaly in the surface profile at this point that has not been detected.

Defining Frossling Number in terms of an airfoil leading edge equivalent diameter allows comparison of Frossling's analytical solution for heat transfer in the stagnation region of a circular cylinder [16] with the present data. The experimental average Frossling Number based on leading edge equivalent diameter for the smooth airfoil was found to be 0.76, roughly 20% lower than the 0.945 value predicted by Frossling's cylinder solution. Frossling's analytical results are often used with an equivalent leading edge diameter to compute heat transfer in the stagnation region for airfoils and turbine blades. However, it is uncertain as to whether the validity of this method has been proven

experimentally.

Figure 14 is a plot of Frossling Number based on chord against s/c for the smooth airfoil at a 2 degree angle of attack. Data for the suction side of the airfoil are represented by the positive s/c values. This convention will be maintained throughout this section. The data again collapses onto a single curve and, given the aforementioned Reynolds Number discussion, illustrates relatively good agreement with the Nusselt Number dependence on the square root of the Reynolds Number. Comparison with the 0 degree smooth airfoil data shows no notable difference.

Figure 15 shows Frossling Number for a smooth airfoil at a 4 degree angle of attack. Again the data for all Reynolds Numbers can be represented quite well by a single curve for most of the gages. A slightly different Reynolds Number variation is seen for the leading edge and the first gage on the pressure side (gage 3). Comparison with the 0 and 2 degree data shows very little angle dependence except for these same two positions: a slight increase (11%) on the leading edge and a slight decrease (6%) on the first gage of the pressure side of the airfoil. This behavior can be explained by the movement of the aerodynamic stagnation point; the stagnation region sees an effectively larger equivalent diameter as it moves toward gage 3 and this results in a lower heat transfer coefficient. The flow is then accelerated around the leading edge, thus increasing the heat transfer at the geometric stagnation point.

B. Airfoil with Leading Edge Roughness

Figures 16, 17 and 18 show Frossling Number based on chord versus s/c for an airfoil with roughness elements attached to the leading edge, as shown in Figure 7, for angles of attack equal to 0, 2, and 4 degrees, respectively. The roughness elements row positions are denoted by the arrows below the abscissa. The data of these graphs also appear to collapse onto single respective curves, and Table 3 confirms more nearly the dependence of the Nusselt number on the square root of Reynolds Number. Compared with data from the smooth airfoil, the leading edge roughness increases the heat transfer an average of 8% at the stagnation region. This increase can be partially explained by the 4% increase in surface area due to the presence of the hemispherical roughness elements. It could also be attributed to a disturbance of the boundary layer by the relatively huge roughness elements followed by a return to laminar flow sufficiently past the leading edge trip point. Note also that this data set for an angle of attack equal to 4 degrees exhibits the same behavior for the first pressure side and leading edge gages as the smooth airfoil. In addition, the first gage on the suction side measures slightly higher (8%) heat transfer for the 4 degree angle of attack than for the 0 or 2 degree angles.

C. Airfoil with Sparse Roughness

Frossling Numbers based on chord as a function of s/c

for the sparse roughness pattern are shown in Figures 19, 20 and 21 at 0, 2 and 4 degree angles of attack, respectively. The sparse roughness pattern is shown in Figure 7. Compared with the smooth airfoil, this data set contains somewhat more scatter but still can be represented by a single curve which is generally consistent with the $Re_c^{0.5}$ dependence of the Nusselt Number. For the 0 degree angle of attack case, the heat transfer increase at stagnation (gage 4) is 11%, which is comparable to the leading edge roughness case. Past the stagnation region the heat transfer exhibits a pattern of increasing at and immediately downstream of the roughness row position, and then falling off slightly. At gage 7 (s/c = 0.038), the heat transfer increases by 55% over the smooth airfoil case, increases to 59% at gage 8, and then falls to a 52% increase at gage 9. At gage 10 the next row of roughness elements is encountered. The heat transfer at gages 10 and 11 increases by about 170% over the smooth case. The sensitivity of the boundary layer to the roughness seems to increase with downstream location.

The angle of attack dependence is also more pronounced for the sparse roughness pattern than for the smooth and leading edge roughened cases. For the sparsely roughened airfoil, the Frossling Numbers for a 2 degree angle of attack for gages 7 through 11 increase gradually with s/c from 8 to 15% over the 0 degree case, and from 14 to 26% going from 0 to 4 degrees. Increasing angle of attack causes heat

transfer to increase with s/c over the 0 degree case. Note that for 4 degrees, the characteristic increase at stagnation and slight decrease on the first gage of the pressure side of the airfoil are also observed.

D. Airfoil with Dense 1 Roughness

Frossling Number based on chord versus s/c for the dense 1 roughness pattern (Figure 7) at 0, 2 and 4 degree angles of attack are presented in Figures 22, 23 and 24, respectively. For the 0 degree angle of attack case, the data points still tend to fall reasonably well on one curve, indicating a $Re_c^{0.5}$ dependence of the Nusselt Number. Increasing the density of the roughness elements from the sparse to the dense 1 pattern has a dramatic effect on the heat transfer downstream. For the 0 degree angle of attack, gage 6 increased 32% and gages 7 and 8 increased an average of 54% over the sparse roughness case. Further downstream past gage 7, the density of roughness elements decreases, and at gages 10 and 11, the effect of the increased density of the roughness elements upstream seems to have nearly damped out. This trend indicates that if there is roughness of sufficient magnitude present, the boundary layer is perturbed locally and immediately downstream. However, as the density of roughness is reduced in the downstream direction, the heat transfer recovers to a level that is consistent with the sparse roughness pattern.

For the 2 and 4 degree angles of attack there is considerably more scatter in the data than was present in the smooth airfoil cases. At high values of s/c, the Frossling Numbers increase monotonically with Reynolds Number; this indicates a trend away from the $Re_c^{0.5}$ dependence with increasing roughness and angle of attack. Table 3 shows that the Nusselt Number from gages greater than gage number 8 increases with Reynolds Number raised to the 0.6-0.7th power. The magnitude of the heat transfer on these gages is consistent with a transitional boundary layer on a flat plate.

The angle of attack dependence is much more prominent in the dense roughness case as compared to the previous cases discussed. An increase from 0 to 2 degrees caused roughly a 20% increase in Frossling Number for the gages between s/c of .02 and .05, while a 4 degree change yielded an increase of roughly 39%. For gages at s/c locations greater than .05, increasing angle of attack from 0 to 2 degrees caused a 15% increase and from 0 to 4 degrees a 27% increase in Frossling Number. Finally, the 4 degree data shows the characteristic increase at stagnation and slight decrease on the first gage of the pressure side as was observed for the previous cases.

IV. RESULTS AND DISCUSSION OF ICING RESEARCH TUNNEL DATA

In this section results of the heat transfer tests performed in the Icing Research Tunnel will be presented and discussed. This heat transfer data will again be presented as Frossling Number based on chord length versus dimensionless surface distance from the stagnation point (s/c). The heat transfer data for smooth and roughened airfoil surfaces will be presented for 0, 2, 4, 6, 8, and -4 degree angles of attack, with and without the tunnel spray air, and for various Reynolds Numbers in the range from 1.20×10^6 to 4.52×10^6. Tables 4 and 5 contain the Frossling Numbers for all conditions of this test.

A. Smooth Airfoil

Figure 25 shows Frossling Number based on chord as a function of s/c for the smooth airfoil at a 0 degree angle of attack with no spray air for several Reynolds Numbers. As with the flight data plotted in this manner, the tunnel data also collapses onto a single curve which shows that the Nusselt Number is proportional to the square root of the Reynolds Number. This tunnel data was also correlated as $Nu_C = A\ (Re_C)^B$ with the constants presented in Table 6, and this data does indeed show a consistent Reynolds number raised to the 0.5 power heat transfer dependence. The solid line represents the interpolated data for a Reynolds

Number of 2.43×10^6, and this curve will be plotted on subsequent tunnel data figures for reference. The Frossling Number is again greatest at the stagnation point, with an average value of 4.56, and then trails off smoothly to an average value of 1.06 at an s/c value of 0.083. The stagnation point average value of 4.56 is only 6% higher than the average stagnation value of 4.3 for the flight data. The "bump" at s/c = 0.048 is still present in the tunnel data as it was in the flight data. Calculating the Frossling Number in terms of an airfoil leading edge equivalent diameter for comparison with Frossling's analytical cylinder heat transfer solution [16] gives an average value of 0.806, roughly 15% lower than the 0.945 value predicted by Frossling's laminar flow solution.

Figure 26 is a plot of Frossling Number based on chord versus s/c for the smooth airfoil at a 0 degree angle of attack with the spray bar air on. As previously stated, the solid line represents the smooth airfoil, 0 degree, no spray air data. The stagnation point average value for the spray air run was found to be 4.69, less than a 3% increase from the no spray air case. The rest of the gages on the airfoil show virtually no change at all (less than 1%) relative to the no spray air case.

Figure 27 is a plot of Frossling Number based on chord versus s/c for the smooth airfoil at a 2 degree angle of attack without spray air. Data for the suction side of the airfoil are represented by the positive s/c values. This

convention will again be maintained throughout this section. This data also collapses onto a single curve and illustrates good agreement with the $Re_c^{0.5}$ dependence of the Nusselt Number, though it should be noted that the lowest Reynolds Number displays a slightly higher Frossling Number on the stagnation gage than the other Reynolds Numbers. Comparison with the 0 degree, without spray air, smooth airfoil data shows no change on the pressure side, a 3% increase to an average value of 4.68 at the stagnation gage, and a growing decrease on the suction side from 3% on gage 5 to 10% on gage 11. Turning on the spray air had minimal effect on the smooth airfoil at a 2 degree angle of attack, as illustrated in Figure 28. Only the stagnation heat transfer changed, experiencing a 6% increase over the 2 degree without spray air case.

Figure 29 shows Frossling Number for a smooth airfoil without spray air at a 4 degree angle of attack. Again the data for all Reynolds Numbers can be represented by a single curve which is again confirmed by Table 6. Comparison with the zero degree data shows a 9% decrease on the first pressure side gage of the airfoil and a 9% increase on the stagnation gage. This is very similar to the behavior in the 4 degree angle of attack flight data. However, on the suction side the heat transfer gradually decreases, up to 13% on gages 8 through 11. As Figure 30 shows, the addition of spray air had very little effect, average values differing by less than 2% from the runs

without spray air.

Data for a 6 degree angle of attack, smooth airfoil, without and with spray air are illustrated in Figures 31 and 32, respectively. Both figures show data generally falling onto single curves, except in the stagnation region for the spray on case where the heat transfer increases slightly with decreasing Reynolds Number. Also, in the range of s/c greater or equal to 0.06, the Nusselt Number increases greatly with increasing Reynolds Number. The drastic effect on the heat transfer at this point is most likely the result of boundary layer transition to turbulent flow. Compared with the 0 degree case, the Frossling Number on gage 4 is 8% higher for the 6 degree case without air and 15% with spray air. Both figures show a Frossling Number decrease on the suction side of the airfoil up to s/c = 0.05. Relative to the 0 degree case, the heat transfer from gage 5 is 10% lower, gage 6 is 17% lower, gage 7 is 22% lower, and gage 8 is 25% lower. The data beyond gage 8 is somewhat scattered, but generally increases with Reynolds Number and is well above the 0 degree heat transfer values, the greatest being nearly 300% increase at gage 11. It should be noted that Figures 31 and 32 show one of the few notable discrepancies between the IRT data with and without spray air. The 1.2×10^6 Reynolds Number with spray air case (Figure 32) begins to exhibit this transitional departure from laminar flow while the same Reynolds Number without air (Figure 31) does not.

The addition of spray air and the possible resulting slight increase in turbulence may initiate transition at a lower Reynolds Number as is often observed. It is also possible, however, that this phenomenon was caused by the angle of attack; Tables 4 and 5 show that the spray air case was at an angle of attack equal to 6.0 degrees, but the case without spray air had an actual angle of attack equal to 5.9 degrees.

Figure 33 shows Frossling Number for a smooth airfoil without spray air at an 8 degree angle of attack. This data was taken at essentially a single Reynolds Number. Comparison with the zero degree case shows that the Frossling Number increases 4% at gage 3 and 11% at gage 4. The Frossling Number on the suction side decreases to a minimum average value of 1.2 on gage 8, 42% lower than the 0 degree value. Further downstream, boundary layer transition is again seen; at gage 9, the heat transfer increases to 135% over the zero degree case, to 259% at gage 10, and then falls to a 233% increase at gage 11.

Figures 34 and 35 show Frossling Number versus s/c for a smooth airfoil at a -4 degree angle of attack without and with spray air, respectively. Again the data for various Reynolds Numbers fall onto a single curve. No noticeable effect of spray air on heat transfer is present. The heat transfer on the stagnation gage is 15% higher than the 0 degree case. Most of the remaining pressure side gages show heat transfer less than 5% higher than the respective

0 degree values.

B. Airfoil with Leading Edge Roughness

Figures 36 and 37 show Frossling Number based on chord versus s/c for an airfoil with roughness elements attached to the leading edge, as shown in Figure 7, for a 0 degree angle of attack, without and with spray air, respectively. The Nusselt Number dependence on the 0.5 power of the Reynolds Number is clearly shown by the resulting single curves. The roughness elements row positions are denoted by the arrows below the abscissa. The data, though slightly higher, exhibits the same behavior as the leading edge roughness flight data. The figures show evidence of boundary layer disturbance in the stagnation region by a 10% increase in heat transfer on gage 4 as compared with the smooth 0 degree tunnel data, but the downstream gages show this disturbance being damped out.

Figures 38 and 39, respectively, show Frossling Number versus s/c for leading edge roughness for an angle of attack of 4 degrees, without and with spray air. No dependence on spray air is apparent. While this tunnel data is somewhat higher than the flight data in the stagnation region, it also displays the same general 4 degree angle dependence, i.e., an increase on gage 4 and a decrease on gage 3 as compared with the 0 degree data. However, at s/c greater than 0.02, the Nusselt Number dependence on the Reynolds Number is no longer the square root relationship.

Both cases with and without spray air show boundary layer transition. The $1.3x10^6$ Reynolds Number data are comparable to the smooth airfoil data, but the higher Reynolds Numbers show steadily increasing Frossling Number with increasing Reynolds Number.

C. Airfoil with Sparse Roughness

Frossling Number as a function of s/c for the sparse roughness pattern, at a 0 degree angle of attack, without and with spray air are presented in Figures 40 and 41, respectively. Again the spray air does not seem to affect the heat transfer. In the stagnation region, the data is very close to the flight data (within 3%). Compared with the 0 degree case, the tunnel data shows an 8% increase on the stagnation gage but only little changes on gages 2, 3, 5 and 6, which is similar behavior to the leading edge roughness case. As with the flight data past the stagnation region, the Frossling Number again exhibits a pattern of increasing immediately downstream of the roughness row position, followed by a slight falling off. At s/c greater than 0.02, the Nusselt Number moves away from the $Re^{0.5}$ dependence and the Frossling Number increases with Reynolds Number. For a Reynolds Number equal to $1.2x10^6$, the average Frossling Number at gage 7 is 35% higher than the smooth airfoil value, 39% at gage 8, and 29% at gage 9. After encountering another roughness row at gage 10, the heat transfer rises to 118% and 128%

over the smooth airfoil values on gages 10 and 11, respectively. The heat transfer for 2.4×10^6 Reynolds Number exhibits similar behavior but of greater magnitude, increasing 52% at gage 7, 56% at gage 8, and 45, 171 and 190% at gages 9, 10, and 11, respectively. Finally, for a Reynolds Number of 3.55×10^6, the heat transfer on gage 7 increases 63%, 70% on gage 8, 61% on gage 9, 209% on gage 10 and 239% on gage 11, respectively. While little change is experienced around the stagnation region, the slightly higher turbulence level in the tunnel seems to have greatly affected the heat transfer away from the stagnation region.

Frossling data for the sparsely roughened airfoil with and without spray air, at angles of attack of 2, 4, 6 and 8 degrees are presented in Figures 42 through 49. The first point to be made is that the addition of spray air has virtually no effect on the heat transfer. Secondly, in the front region of the airfoil (gages 2, 3, 4, 5, 6) the data fall onto respective curves, illustrating the $Re^{0.5}$ dependence of the Nusselt Number, and for the 2 and 4 degree cases agrees fairly well with the flight data. On gage 3, the Frossling Number doesn't change going from 0 to 2 degrees, characteristically decreases at 4 degrees, increases slightly going to 6 degrees, and finally at 8 degrees increases to a level above the 0 degree smooth airfoil value. The Frossling Number on the stagnation gage (gage 4) does not change going from 0 to 2 degrees but increases 11% at 4 degrees and 20% at 6 and 8 degrees

relative to the 0 degree sparse data. Further aft of the airfoil at s/c greater than 0.03, the Frossling Number generally increases with increasing angle of attack as well as with increasing Reynolds Number. The 2 and 4 degree cases generally follow the same pattern as the 0 degree case, i.e., Frossling Number increasing at roughness rows and falling off thereafter. However, the 6 and 8 degree cases show slightly different behavior of increasing at gage 7, increasing again at gage 8 and then falling off to an almost constant level at gages 9, 10 and 11, a level consistent with a turbulent boundary layer on a flat plate.

Finally, Figures 50 and 51 show Frossling data for the pressure side (-4 degree angle of attack). This data also generally falls on one curve and follows the usual pattern of increasing at roughness rows and then eventually falling off behind them. Comparing this with the suction side data at a 4 degree angle of attack (Figures 44 and 45), shows consistency in the stagnation region of the airfoil, but the downstream Frossling Number on the pressure side is certainly lower than on the suction side. For example, at a Reynolds Number around 2.4×10^6, the Frossling Number on the pressure side (s/c<-0.03 on Figures 50 and 51) is from 31 to 41% lower than on the suction side (s/c>0.03 on Figures 44 and 45).

D. Airfoil with Dense 1 Roughness

Figures 52 through 63 show Frossling Number data

versus s/c for the Dense 1 roughness pattern (Figure 7) at conditions without and with spray air, and angles of attack of 0, 2, 4, 6, 8 and -4 degrees. Again no noticeable effect on heat transfer can be attributed to the spray air. For the 0 degree case, the data illustrates $Re^{0.5}$ dependence only on the stagnation gage; the remainder of the airfoil exhibits Reynolds Number dependence similar to that seen with the sparse roughness pattern, i.e., a gradual increase in the Frossling Number with increasing Reynolds Number. As expected, the heat transfer in the stagnation region averages 16% higher than the 0 degree smooth airfoil case. Further downstream, definite Reynolds Number dependence is observed. It should be noted here that the 1.2×10^6 Reynolds Number data match the flight data fairly well, while the higher Reynolds Numbers show much greater heat transfer, with gage 7 having the maximum for all of the Reynolds Numbers tested. The Frossling Number values on gages 10 and 11, where the roughness density decreases to the sparse pattern, are comparable to the sparsely roughened 0 degree airfoil data.

The angle dependence for the Dense 1 pattern airfoil is consistent with the angle dependence for the other roughness patterns. The downstream gages show increasing Frossling Number with angle as well as with Reynolds Number, with gage 7 still showing the maximum. Changing the angle of attack from 0 to 2 degrees caused most downstream gages to increase by 10-20%; 4 degrees resulted

in 20-30% increases, while 6 and 8 degrees resulted in 30-40 and 40-50% higher Frossling Number on most downstream gages. The stagnation region also exhibits typical angle dependence; the heat transfer from gage 4 increases monotonically with angle, while gage 3 decreases to a minimum value at 4 degrees and then increases again at 6 and 8 degrees. It should also be mentioned that as the aerodynamic stagnation point moves closer to the pressure side gages (i.e., gages 2 and 3), the $Re^{0.5}$ dependence is seen to exist at those gages. I.e., the Nusselt Number at the aerodynamic stagnation point always has a $Re^{0.5}$ dependence.

The -4 degree dense 1 data also follows the established pattern. It is consistent with the 4 degree suction side data in the stagnation region and also shows lower heat transfer on the pressure side versus the suction side.

E. Airfoil with Dense 2 Roughness

Finally, Frossling data versus s/c for the dense 2 roughness pattern, Figure 7, are presented for cases without and with spray air for 0, 2, 4, 6, 8 and -4 degree angles of attack in Figures 64 through 75, respectively. Examination of previous figures shows that the dense 2 roughness pattern is very similar to the dense 1 roughness pattern, except that the roughness element density is constant throughout and does not decrease at s/c greater

than 0.04 as the dense 1 pattern does. As expected, the results shown in these dense 2 graphs are very similar to the results of the dense 1 cases. The data show the strong $Re^{0.5}$ dependence of the Nusselt Number at the aerodynamic stagnation region as well as following the common trend of the downstream gages of increasing Frossling Number with Reynolds Number and angle of attack from 0 to 8 degrees. Maximum heat transfer is still encountered on gage 7. The 4 degree angle of attack case also demonstrates characteristic behavior. The only notable difference between the dense 2 and the dense 1 cases occurs in the region for s/c greater than 0.04, where the roughness density is greater in the dense 2 cases relative to the dense 1 cases. The Frossling Number in all dense 2 cases in this region, while still falling off from the gage 7 maximum and then leveling off, is somewhat higher than the dense 1 data. I.e., the dense 2 roughness data exhibit the same heat transfer behavior as the dense 1 cases, except that the dense 2 data yield a higher Frossling Number in the region of higher roughness density (s/c >0.04). These values are comparable with turbulent boundary layer flat plate heat transfer. There is no upstream heat transfer effect due to the increase of downstream roughness density.

V. COMPARISON OF DATA

A. Flight Data Versus Icing Research Tunnel Data

In this section the results of the heat transfer tests conducted in the Icing Research Tunnel (IRT) and the data obtained during the Twin Otter aircraft flights will be compared with special emphasis on the effect of the different free stream turbulence levels. The turbulence intensity measured with hot wire equipment during the flight runs was found to be very low (<0.1%). However, in the IRT with the cloud making sprays off, hot wire measurements yielded turbulence values generally around 0.5%, with a maximum of 0.7% at 210 mph. As previously mentioned, due to required tunnel conditions when the spray air is turned on, turbulence measurements made with hot wire equipment do not yield meaningful values. In the following discussion, representative cases of tunnel and flight data under similar conditions (i.e., same angle of attack and comparable Reynolds Number) will be compared.

Figure 76 shows the heat transfer data plotted as Frossling Number based on chord versus dimensionless surface distance, s/c, for the flight test as well as for both spray conditions of the IRT tests. This data is for the smooth airfoil at a 0 degree angle of attack and a nominal Reynolds Number equal to 1.2×10^6. Compared with the flight data, gages 2-6 show a Frossling Number only 2-3% higher for the tunnel cases without spray air, and 3-5% higher with spray

air. Further aft on the airfoil (gage no.>6), the Frossling Number averages 6% higher for both with and without spray air cases. All of these values are within the limits of the calculated experimental error. Figure 77 shows similar Frossling Number behavior for a nominal Reynolds Number of $2.4x10^6$. The two tunnel cases, with and without spray air, again agree quite well (within 2%). However, comparing both cases with the flight data shows that the Frossling Number tunnel data is roughly 7% higher on gages 2-6 and 10% higher on gages greater than 6.

Figures 78 and 79 show the flight and tunnel heat transfer data for the smooth airfoil at 2 degrees for Reynolds Numbers of $1.2x10^6$ and $2.4x10^6$, respectively. For the lower Reynolds Number, all three cases agree within the calculated error range except at gage 4 where some scatter is present. At the higher Reynolds Number, a much greater turbulence effect is illustrated. While the tunnel data with and without spray air agree very well (except at gage 4), both cases are roughly 7% higher than the flight data on gages 2-6 and 10-12% higher for gages greater than No. 6. The 4 degree smooth airfoil data also exhibited this behavior, showing good general agreement between tunnel and flight data at the lower Reynolds Number, while at the higher Reynolds Number the Frossling Number for the tunnel cases was somewhat higher (3-10%) than the flight data. It seems evident that, at least in this range, the small increase in turbulence level does slightly affect the heat transfer and

this effect is magnified with increasing Reynolds Number. A consequence of this behavior is seen in the Nusselt versus Reynolds Number power law constants of Tables 3 and 6. Generally the B constants on the downstream gages of the IRT data are slightly higher than the corresponding flight data. Further, and perhaps more importantly, the addition of spray air (recall that in these experiments only spray air and not any spray water was turned on) to the tunnel stream does not seem to affect the turbulence level and certainly does not affect the heat transfer. It should be mentioned, however, that it is possible that the spray air does increase the tunnel turbulence but the leading edge heat transfer is not sensitive to this change.

The leading edge roughness, 0 degree angle of attack case generally exhibited the same behavior. Essentially no change was detected in the tunnel data with the addition of spray air. The tunnel data agreed fairly well with the flight data for the low Reynolds Number case (Re = 1.2×10^6), but are generally higher than the flight data for the 2.4×10^6 Reynolds Number case, being up to 9-10% higher on some gages. The 4 degree, leading edge roughness case shows a more pronounced effect attributed to the higher free stream turbulence in the tunnel as compared with flight. Figure 80 shows comparable heat transfer for flight and tunnel experiments for a nominal Reynolds Number of 1.2×10^6. However, as Figure 81 illustrates, the tunnel data for a Reynolds Number of 2.4×10^6 show boundary layer transition

beginning around gage 9, whereas the flight data certainly does not show transition at gage 9. In fact, the flight data does not definitely show transition at all, unless the slight increase from gage 10 to gage 11 is interpreted as the beginning of transition. Regardless, the slightly higher turbulence level in the tunnel appears to have moved the transition point forward on the airfoil, as has often been reported. This behavior is probably also encountered on the smooth airfoil. Unfortunately, for this range of Reynolds Numbers, at a 0 degree angle of attack, the usual transition point is several inches beyond the last heat transfer gage employed on this test apparatus. Thus, this suspected behavior could not be observed.

The flight and tunnel data for the sparsely roughened airfoil at a 0 degree angle of attack and Reynolds Numbers 1.2×10^6 and 2.4×10^6 are presented in Figures 82 and 83, respectively. With few exceptions the Frossling Number values on most gages agreed within the error limits for the low Reynolds Number case. At the higher Reynolds Number, as with the smooth case, the two tunnel conditions agreed quite well, but most gages for both cases show values 4-10% higher than corresponding flight values. Similar trends were also observed on the 2 and 4 degree data, though the 4 degree case exhibited somewhat higher magnitude; some gages for the 2.4×10^6 Reynolds Number show tunnel heat transfer data up to 16% higher than the flight data.

The data for the 0 degree, dense 1 roughened airfoil are

illustrated in Figures 84 and 85. For the lower Reynolds Number of $1.2x10^6$, both tunnel data sets again agree; however, they show values 2-8% higher than the flight data. The $2.4x10^6$ Reynolds Number case illustrates similar behavior, with the tunnel data being 18-25% higher than the flight data. This result is somewhat surprising because it would seem that as the boundary layer is more and more disturbed by the roughness, the free stream turbulence would have less and less effect on the Frossling Number. However, in this dense 1 case the free stream turbulence appears to have a greater effect on the heat transfer than in the sparse roughness cases. Moving to a higher angle of attack did not alter this trend. Figures 86 and 87 present 4 degree, dense 1 Frossling Number data for the IRT and flight at nominal Reynolds Numbers of $1.2x10^6$ and $2.4x10^6$, respectively. For the lower Reynolds Number case, the tunnel data with and without spray air for the most part agree, although some scatter is present in the s/c range of 0.0 to 0.05. All of the tunnel data are from 3-18% higher than the flight data except at gage 5, where the flight data is higher. The higher Reynolds Number shows the same behavior; both sets of tunnel data agree very well with each other and are from 3-16% greater than the flight data, except at gage 5 where the flight data results are higher.

Generally, it would seem that the IRT is a relatively clean wind tunnel, at least with respect to heat transfer in the forward portion of an airfoil. The slightly higher

turbulence level in the tunnel had minimal effect on the heat transfer from the smooth airfoil at the lower Reynolds Number; the higher Reynolds Number did illustrate a greater turbulence induced heat transfer increase. The addition of surface roughness, however, seemed to magnify the effect of turbulence on heat transfer and, in at least one case, was observed to move the boundary layer transition point forward on the airfoil. The addition of spray atomizing air had virtually no effect on the heat transfer, and it is therefore believed that the spray air did not alter the free stream turbulence level in the tunnel.

B. Comparison with Previous Experimental Studies

Figures 88, 89 and 90 compare the present smooth airfoil results with previously published experimental data. Figure 88 shows a comparison of the present Twin Otter flight data with the 1946 NACA flight test data for both a NACA 0012 and a NACA 65,2-016 airfoil [11]. Aside from a few exceptional points, good general agreement is observed, most values agreeing within 10%. Note that the heat transfer at the stagnation point of the NACA 0012 airfoil was found to be substantially higher in the 1946 study than in the present work. It is possible that this discrepancy is due to problems with the 1946 equipment, perhaps the thermocouple at the stagnation point, because the temperature that was recorded in the 1946 study for the stagnation region was around 30^{o}F lower than the rest of the airfoil surface.

Figures 89 and 90 illustrate the comparison of the present smooth airfoil, 0 and 4 degree angle of attack IRT data, with the NACA 0012 wind tunnel data obtained at the University of Kentucky [14]. Relatively good agreement exists up to s/c about 0.05; however, further down the airfoil the Frossling Numbers differ by 300%. This could be due to roughness of the Reference 14 model surface. In a personal communication with the author of Reference 14, it was indicated that the surface of their airfoil was "rough". Data for various other angles of attack compared similarly.

C. Experimental Data Versus Cylinder and Flat Plate Correlations

In computer codes, heat transfer from airfoils is often estimated by using cylinder heat transfer values in the leading edge region and flat plate heat transfer values further aft. Figures 91 and 92 show Frossling Number values corresponding to Frossling's cylinder solution [16], together with laminar and turbulent flat plate values [17] on the same graphs as the present 0 degree smooth airfoil flight and tunnel data (without spray), respectively. Both graphs show good agreement with the laminar flat plate correlation at s/c greater than 0.06, the flight data being around 8% lower and the tunnel data around 3% higher. However, in the stagnation region the experimental heat transfer is somewhat lower than that predicted by Frossling. Gages 2-5 show a 19-21% lower Frossling Number for the flight data and 14-17% lower for the

tunnel data. In addition, both the flight and the IRT data fall between the laminar and turbulent flat plate values for $0.01 < s/c < 0.06$. It seems, therefore, that the inscribed cylinder method for estimating the heat transfer from the forward portion of an airfoil does not accurately work; in this case the method substantially overpredicts the measured heat transfer. However, it should be noted that the equivalent leading edge diameter of the NACA 0012 airfoil is only about 26.5% (0.664 inches/2.5 inches) of the maximum airfoil thickness and it is possible that an airfoil with a larger leading edge diameter relative to the airfoil maximum thickness (i.e., a shape more closely approaching that of a streamlined cylinder) would more closely agree with Frossling's cylinder solution.

Figure 93 shows the IRT data for the dense 2, 0 degree, without spray condition compared with the cylinder and flat plate heat transfer values. The heat transfer in the stagnation region for the dense 2 roughened airfoil agrees fairly well with Frossling's smooth cylinder laminar flow solution. Moving downstream on the airfoil, the heat transfer drastically increases, reaching a maximum level at s/c of roughly 0.035, and then decreases to a level fairly consistent with turbulent flow flat plate heat transfer values. The measured heat transfer at specific Reynolds Numbers are somewhat higher than their respective flat plate turbulent values. However the higher measured heat transfer may be due to the increase in surface area due to the

roughness elements (3-7% increase on each gage for the dense roughness patterns) that was not taken into account in the data analysis. It may be mentioned here that the maximum heat transfer is in the same general region, if slightly aft, of ice horn growth observed during glaze ice accretion [2].

D. Relationship to LEWICE Ice Accretion Code

As previously mentioned, the present data finds special application in the area of aircraft icing. Due to the importance of convective and evaporative cooling in the icing process, the local heat transfer coefficient is an extremely important parameter in the determination of ice growth rates and resulting shapes. Some ice accretion modeling codes, such as NASA's LEWICE, use an integral boundary layer routine to calculate the local heat transfer coefficient. Important inputs to the boundary layer calculations are the boundary layer edge velocity distribution and a sand grain roughness height, k_s. An inherent difficulty resides in the fact that sand grain roughness does not suitably resemble the changing surface roughness of ice shapes, especially glaze ice shapes. The value of k_s which is input into the model has a dramatic effect on the calculated heat transfer coefficient and thus on the overall predicted ice shape. Because obtaining accurate predictions of experimental ice shapes is the goal of LEWICE, the input value of k_s has been correlated with freestream velocity, static temperature, and liquid water

content to yield accurate ice shapes. Unfortunately, however, obtaining proper ice shapes does not necessarily ensure correct heat transfer predictions.

Figure 94 shows the smooth airfoil, 0 degree, IRT without spray air Frossling Number data versus dimensionless surface distance. Also plotted on this graph is the dimensionless laminar flow heat transfer curve (solid line) from a boundary layer integral solution similar to that employed in LEWICE. Note that the sand grain roughness parameter, k_s, is not used for the smooth airfoil heat transfer prediction. While the prediction generally follows the same trend as the experimental data, its magnitude is somewhat higher: roughly 25% at the stagnation point and from 15-60% further aft.

Figure 95 shows the dense 2, 0 degree, IRT data together with the integral boundary layer solution for a rough surface. A value of 0.00152 ft for k_s was determined from the LEWICE correlations [10] for velocity (105 ft/sec), static temperature (20°F) and liquid water content (assumed the baseline value of 0.5 grams/m^3). The boundary layer model predicts laminar flow up to s/c of about 0.01, where the flow becomes turbulent. Compared with the experimental data the model drastically overpredicts the heat transfer. It predicts a maximum Frossling Number of 7.1 at s/c of 0.02 while the experimental data shows a maximum of 5.4 between s/c of 0.036 and 0.048.

Schlicting [15,24] developed the concept of an equivalent sand grain roughness to characterize other types of roughness

elements and patterns. Since the dense 2 roughness pattern employed here is similar to the roughness elements and patterns used by Schlicting, an estimate of k_s for the dense 2 roughness can be made based on Schlicting's data. An equivalent sand grain roughness value for the dense 2 roughness has been estimated at 0.001 ft. It must be noted, however, that the dense 2 pattern is not exactly the same as any one roughness pattern employed by Schlicting and thus the k_s value of 0.001 must be treated only as a very general estimate. Figure 96 shows that using this k_s value in the integral boundary layer solution yields heat transfer values that overall are lower than the k_s=0.00152 case and show a later transition point. This heat transfer distribution is somewhat closer in magnitude to the experimental values but still does not completely reproduce the experimental data, especially further downstream on the airfoil. A "best fit" of the experimental data was obtained using a k_s value of 0.00083.

The boundary layer solution does even worse at higher velocities as Figures 97 and 98 illustrate. The LEWICE correlations yield k_s values of 0.00188 and 0.00225 ft for the 205 and 310 ft/sec cases, respectively. In both of these cases the heat transfer is greatly overpredicted by the boundary layer model, and employing a k_s value of 0.001 still overpredicts the experimental data. The k_s inputs that best

fit the experimental data are 0.000425 and 0.00027 ft for 205 and 310 ft/sec, respectively.

The integral boundary layer solution generally gives adequate results for the smooth airfoil. However, the boundary layer solution with the sand roughness parameter does not appear to predict the dense 2 roughened airfoil heat transfer very well. The LEWICE correlation for k_s, based on velocity, static temperature and liquid water content, while capable predicting proper ice shapes, may unfortunately overpredict the heat transfer. This is certainly true for the heat transfer from a dense 2 roughened airfoil. Since the dense 2 roughness pattern does not accurately represent ice roughness any more completely than sand roughness does, it probably could not be expected that the LEWICE correlation for ice shape would accurately predict the dense 2 heat transfer. However, it was hoped that somewhat closer results could have been achieved.

The present data is somewhat limited in its usefulness to validating an integral boundary layer solution based on a sand roughened surface. It would be more useful to a complete Navier-Stokes solution which contained a more microscopic treatment of the rough surface, i.e., roughness elements and patterns of discrete dimensions.

E. Characterization of Roughness

The present heat transfer data in terms of Nusselt Number for the smooth airfoil seem to exhibit fairly good agreement

with a $Re^{0.5}$ dependence. The addition of roughness to the airfoil, however, causes a deviation from this $Re^{0.5}$ dependence of the Nusselt Number, with a much greater Reynolds Number dependence being observed. The experimental heat transfer at each gage for various conditions can be correlated as:

$$Nu_c = A\ (Re_c)^B$$

where the constants A and B are determined by a least squares fit of the data. Tables 3 and 6 show the constants A and B for certain gages for various roughness and flight/tunnel conditions. Inspection of the smooth airfoil data in these tables show that the constant B for tunnel data is indeed quite close to 0.5; however as previously mentioned, the flight data value of B for most gages is closer to 0.43 or 0.44. The rest of the data show that although the flight data value of B is generally slightly lower than the tunnel data, the trends with roughness are quite similar. It should also be noted that the flight data did not correlate quite as nicely as the tunnel data, as evidenced by the R^2 values. For these reasons and especially because the tunnel data are a more complete set with regard to roughness patterns and angle of attack, the tunnel data will be used to discuss the heat transfer dependence on roughness.

Figures 99-103 present 0 degree, chord based Nusselt Number data versus chord based Reynolds number for the smooth and roughened airfoil. Figure 99 shows decreasing Nusselt Number with increasing gage number, and, for each of the

gages shown, the Nusselt Number varies with the square root of the Reynolds Number as evidenced by the constant slopes of roughly 0.5. This is consistent with a laminar boundary layer. Figure 100 illustrates that the Nusselt Number from gage 4 (stagnation) still varies as $Re^{0.5}$ even with the addition of leading edge roughness. Data for the sparsely roughened airfoil (Figure 101) show gages 4 and 6 behaving as the smooth airfoil with respect to Nusselt Number dependence on Reynolds number; however, gages 8 and 10 deviate from this $Re^{0.5}$ dependence with the slopes being closer to 0.7 and 0.8, respectively. This is more indicative of a transitional or even turbulent boundary layer rather than a laminar one. Figures 102 and 103 illustrate that the $Re^{0.5}$ dependence is still valid on gage 4 for the dense 1 and dense 2 roughened airfoil, but not for the rest of the airfoil. Data from the other gages display a Reynolds Number dependence ranging from a 0.7 to a 0.8th power, again normally associated with a transitional or turbulent boundary layer.

It is clear then that surface roughness does affect the boundary layer and thus the heat transfer. Roughness on the leading edge seems to have little effect on the heat transfer, and further downstream the flow appears to return to laminar. If the roughness covers more than the leading edge and especially if it is fairly dense, then the flow apparently goes into transition and the heat transfer is greatly increased.

VI. CONCLUSIONS

Local heat transfer measurements from a smooth and roughened NACA 0012 airfoil were successfully obtained in flight and in the NASA Lewis Icing Research Tunnel using the method and apparatus described in this work.

Aside from the intrinsic value of the collected data, several other purposes specific to aircraft icing studies are also served. This data is meant to supplement heat transfer data currently employed in icing codes that presently use heat transfer from cylinder and flat plate correlations or an integral boundary layer solution. This data also has the advantage of well-defined roughness elements and patterns. Comparison of the flight and IRT data allows the determination of the effect that a slight increase in the free stream turbulence intensity has on heat transfer from an airfoil. This information may aid in the assessment of any discrepancies found in results of studies performed in natural versus simulated icing conditions.

The heat transfer results of both the flight and IRT tests are presented as Frossling Number distributions along the surface of a smooth and roughened airfoil for a range of flow conditions. Where applicable, the flight and tunnel data obtained in this study exhibited adequate general agreement with previously published airfoil heat transfer results. In addition, power law curve fits of Nusselt Number

as a function of Reynolds Number are presented in tabular form.

Major conclusions resulting from this study are:

1. For both the flight and IRT data, small angles of attack (2°) generally had small but common effects on the heat transfer. However, at the higher angles of attack (6,8°) tested, the heat transfer indicated that some flow transition had occurred. The Nusselt Number at the aerodynamic stagnation point always seemed to correlate with $Re^{0.5}$. The influence of angle of attack on heat transfer was magnified with the addition of surface roughness.

2. In general, for the 4 degree angle of attack cases (the only angle for which pressure side data was taken), the heat transfer was lower on the pressure side versus the suction side of the airfoil.

3. The flight and tunnel smooth airfoil data show relatively good agreement with the laminar flat plate heat transfer values for s/c equal or greater than 0.06. In the leading edge region, the measured heat transfer is somewhat lower than that predicted by Frossling's laminar flow cylinder solution: 15% lower in the IRT and 20% lower in flight. Therefore, it would appear that the method of using an inscribed cylinder for approximating the leading edge heat transfer does not work for the NACA 0012 airfoil.

4. The addition of roughness to the airfoil surface drastically increased the heat transfer downstream of stagnation. It is believed that the roughness elements

disturbed the laminar boundary layer flow and in some cases caused a transition to turbulent flow.

5. The smooth airfoil Frossling Number data for flight with a measured turbulence intensity of <0.1% and for the IRT with a 0.5-0.7% turbulence intensity showed fairly good agreement at the lower Reynolds Number ($Re=1.2x10^6$). At the higher Reynolds Numbers ($Re=2.4x10^6$), the IRT data was somewhat higher than the flight data.

6. Comparison of the flight and tunnel rough surface data showed that the effect of turbulence, i.e., the slight increase in heat transfer, was enhanced by the addition of roughness.

7. The higher turbulence level in the IRT caused the flow transition point to move slightly forward on the airfoil surface.

8. Finally, it would seem that the IRT is a fairly clean wind tunnel, with a measured intensity of turbulence level around 0.5-0.7%. The addition of spray air to the tunnel flow did not change the heat transfer and thus it is thought that the turbulence level was not significantly altered by the spray air.

BIBLIOGRAPHY

1. Cebeci, T., "Effects of Environmentally Imposed Roughness on Airfoil Performance", NASA CR-179639, June, 1987.

2. Olsen, W. A., Shaw, R. J. and J. E. Newton, "Ice Shapes and the Resulting Drag Increase for a NACA-0012 Airfoil", NASA TN-83556, January, 1984.

3. Bragg, M. B., Gregorek, G. M. and R. J. Shaw, "Wind Tunnel Investigation of Airfoil Performance Degradation Due to Icing", AIAA-82-0582, 1982.

4. Young, A. D.and J. H. Paterson, "Aircraft Excrescence Drag", AGARDograph No. 264, July, 1981.

5. Korkan, K. D., "Performance Degradation of Propeller/Rotor Systems Due to Rime Ice Accretion", report delivered at NASA Lewis Research Center Icing Analysis Workshop, February, 1983.

6. Hardy, J. K., "Protection of Aircraft Against Ice", Royal Aeronautical Society Journal 51, 435, 1947.

7. Messinger, B. L., "Equilibrium Temperature of Unheated Icing Surface as a Function of Airspeed", Journal of Aeronautical Sciences 20, 29, 1953.

8. Cansdale, J. T. and I. I. McNaughtan, "Calculation of Surface Temperature and Ice Accretion Rate in a Mixed Water/Ice Crystal Cloud", RAE Technical Report 77090, June, 1977.

9. Van Fossen, G. J., unpublished studies performed at NASA Lewis Research Center, Cleveland, Ohio, 1980-86.

10. Ruff, G. A., "Users Manual for the NASA Lewis Ice Accretion Prediction Code (LEWICE)", to be published as a NASA-CR.

11. Neel, C. B., Bergrun, N. R., Jukoff, D. and B. A. Schlaff, "The Calculation of Heat Required for Wind Thermal Ice Prevention in Specified Icing Conditions", NACA TN-1472, 1947.

12. Gelder, T. F. and J. P. Lewis, "Comparison of Heat Transfer from Airfoil in Natural and Simulated Icing Conditions", NACA-2480, September, 1951.

13. Van Fossen, G. J., Simoneau, R. J., Olsen, W. A. and R. J. Shaw, "Heat Transfer Distributions Around Nominal Ice Accretion Shapes Formed on a Cylinder in the NASA Lewis Icing Research Tunnel", AIAA paper 84-0017 presented at the AIAA 22nd Aerospace Sciences Meeting, Reno, Nevada, January, 1984. NASA TM-83557.

14. Pais, M. R.,Singh, S. N. and L. Zou, "Determination of the Local Heat Transfer Characteristics on Glaze Ice Accretions on a NACA-0012 Airfoil", AIAA paper 88-0292, presented at AIAA 26th Aerospace Sciences Meeting, Reno, Nevada, January, 1988.

15. Schlicting, H., "Experimental Investigation of the Problem of Surface Roughness", NACA TM-823, April, 1937.

16. Frossling, N., "Evaporation, Heat Transfer, and Velocity in Two Dimensional and Rotationally Symmetrical Laminar Boundary Layer Flow", NACA TM-1432, 1958.

17. Welty, J. R., Wicks, C. E., and R. E. Wilson, Fundamentals of Momentum, Heat, and Mass Transfer, Wiley & Sons, 370, 1984.

18. Anon., "Series 154 Total Temperature Sensors for Aircraft Gas Turbine Engine Inlets", Product Data Sheet 2186, Rosemont, Inc., Minneapolis, Minnesota, 1973.

19. Anon., "Icing Research Tunnel", brochure from ASME International Historic Landmark ceremony, NASA B-87-0011, May 20, 1987.

20. Anon., "Hot Wire and Hot Film Measurements and Applications", Thermal Systems, Inc., Technical Bulletin No. 4, 35.

21. Abbott, I. H., von Doenhoff, A. E. and L. S. Stivers, "Summary of Airfoil Data, NACA Report No. 824, 71, 1945.

22. Hillsenrath, J., Beckett, C. W., Benedict, W. S., Fano, L. and H. J. Hobe, "Tables of Thermal Properties of Gases", NBS Circular 564, November, 1955.

23. Kline, S. J. and F. A. McClintock, "Describing Uncertainties in Single Sample Experiments", Mechanical Engineering, 75, 3, January, 1953.

24. Coleman, H. W., Hodge, B. K. and R. P. Taylor "A Re-Evaluation of Schlicting's Surface Roughness Experiment", Journal of Fluids Engineering 106, 60, March 1984.

25. Carslaw, H. S., and J. C. Jeager, Conduction of Heat in Solids, 2nd edition, Clarendon Press, Oxford, 167, 1959.

Table 1. Location and surface area of heat transfer gages.

Gage #	s/c	Surface Area (sq. cm.)
1	-0.036	3.145
2	-0.024	3.145
3	-0.012	3.145
4	0.0	3.187
5	0.012	3.145
6	0.024	3.145
7	0.036	3.145
8	0.048	3.145
9	0.060	3.145
10	0.072	3.145
11	0.083	3.145
12	0.095	3.145

Table 2. Frossling Numbers for each gage for all conditions of the flight tests. Prandlt No. = 0.71

Roughness Pattern	Angle of Attack	Re_c	T_w (°F)	T_t (°F)	Frossling Number for Gage Number: 2	3	4	5	6	7	8	9	10	11
none	-0.03	1291850	94	58	3.140	3.959	4.495	3.960	2.899	2.312	2.003	1.167	1.034	0.988
none	0.44	1924300	101	61	3.027	3.803	4.261	3.787	2.780	2.207	1.915	1.133	1.004	0.954
none	0.44	1935420	101	60	3.077	3.858	4.332	3.867	2.806	2.208	1.929	1.145	1.003	0.954
none	0.13	1935620	100	60	2.935	3.691	4.174	3.703	2.716	2.169	1.866	1.122	0.971	0.919
none	0.31	2482730	96	61	3.016	3.752	4.190	3.798	2.804	2.225	1.938	1.154	0.999	0.925
none	2.60	1285880	93	58	3.151	3.949	4.646	3.906	2.825	2.239	1.892	1.151	0.993	0.958
none	2.33	1937560	99	60	3.079	3.845	4.410	3.907	2.694	2.140	1.861	1.111	0.956	0.886
none	2.46	2482670	96	62	3.061	3.794	4.289	3.761	2.815	2.150	1.816	1.046	0.930	0.873
none	4.41	1273580	93	59	3.210	3.747	4.916	3.943	2.765	2.157	1.826	1.097	0.948	0.899
none	4.49	1283910	93	57	3.189	3.734	4.898	3.912	2.721	2.107	1.784	1.075	0.915	0.866
none	4.35	1934040	99	61	3.106	3.504	4.749	3.727	2.620	2.071	1.736	1.031	0.903	0.824
none	4.32	2465000	95	61	2.966	3.315	4.505	3.719	2.622	2.064	1.733	1.056	0.898	0.846
lead edge	0.57	1258000	93	52	3.165	4.069	4.857	4.065	2.938	2.341	2.002	1.181	1.045	0.996
lead edge	0.27	1886310	100	52	3.104	3.921	4.662	3.866	2.817	2.251	1.921	1.168	1.004	0.927
lead edge	0.42	2424730	95	55	3.156	3.973	4.730	4.014	2.907	2.313	1.898	1.167	1.015	0.949
lead edge	2.32	1265320	93	53	3.177	4.018	4.872	3.973	2.850	2.246	1.933	1.153	1.009	0.952
lead edge	2.34	1878440	98	53	3.005	3.771	4.577	3.725	2.692	2.194	1.848	1.078	0.966	0.866
lead edge	2.42	1884740	99	53	3.031	3.833	4.571	3.766	2.700	2.124	1.830	1.072	0.963	0.878
lead edge	2.32	2392890	94	54	3.028	3.825	4.519	3.881	2.771	2.443	1.814	1.090	0.975	1.142
lead edge	2.31	2396510	95	54	3.039	3.817	4.520	3.850	2.867	2.321	1.864	1.039	0.946	0.836
lead edge	4.78	1244970	92	52	3.155	3.649	5.158	4.064	2.819	2.181	1.863	1.128	1.008	1.003
lead edge	4.33	1879440	96	53	2.998	3.442	4.933	4.208	2.655	2.016	1.478	1.207	0.953	0.898
lead edge	4.37	2422480	94	56	3.066	3.506	5.089	4.131	2.860	2.203	1.859	1.166	1.115	1.216
sparse	0.27	1257300	95	53	3.254	4.160	5.044	4.205	2.989	3.487	3.071	1.728	2.577	2.502
sparse	0.14	1884970	99	54	3.084	3.973	4.736	3.904	2.817	3.406	3.057	1.727	2.690	2.663
sparse	0.33	1886120	98	54	3.028	3.911	4.626	3.904	2.714	3.384	3.016	1.715	2.658	2.626
sparse	0.30	2415640	95	56	3.085	3.920	4.662	3.936	2.807	3.487	3.142	1.774	2.837	2.816
sparse	1.94	1260160	94	53	3.299	4.181	5.052	4.129	2.882	3.602	3.173	1.819	2.796	2.765
sparse	2.32	1896200	92	53	3.147	3.897	4.701	3.911	2.745	3.631	3.276	1.871	2.978	2.946
sparse	2.28	2420490	92	55	3.110	3.905	4.685	3.970	2.798	3.771	3.444	1.991	3.237	3.232
sparse	2.33	2461170	92	57	3.156	3.956	4.738	4.041	2.883	3.901	3.565	2.057	3.315	3.325
sparse	4.24	1244580	93	52	3.417	3.971	5.586	4.433	3.001	4.002	3.591	2.142	3.342	3.177
sparse	4.46	1263380	93	53	3.342	3.914	5.499	4.322	2.935	3.865	3.473	2.049	3.218	3.062
sparse	4.44	1890090	92	54	3.122	3.594	5.133	4.099	2.749	3.866	3.579	2.140	3.503	3.294
sparse	4.38	2434720	92	56	3.001	3.431	4.987	4.103	2.745	4.000	3.783	2.333	3.526	3.466

Table 2 (continued)

Roughness Pattern	Angle of Attack	Re_c	T_w (°F)	T_t (°F)	Frossling Number for Gage Number: 2	3	4	5	6	7	8	9	10	11
dense 1	-0.10	1269450	103	67	3.732	4.339	5.072	4.737	3.562	5.424	4.668	2.456	2.590	2.439
dense 1	-0.89	1276420	104	67	3.771	4.328	5.066	4.708	3.576	5.497	4.679	2.484	2.614	2.427
dense 1	0.32	1887710	105	67	4.010	4.081	4.717	4.421	3.814	5.605	4.740	2.498	2.738	2.572
dense 1	0.63	1908240	106	67	3.963	3.985	4.696	4.361	3.819	5.564	4.717	2.514	2.710	2.532
dense 1	0.34	2446790	105	66	4.136	3.962	4.434	4.261	3.891	5.555	4.761	2.562	2.811	2.657
dense 1	2.80	1275150	102	63	3.430	4.158	5.026	4.840	4.354	6.295	5.204	2.764	2.891	2.684
dense 1	2.21	1929750	104	64	3.543	4.011	4.738	4.759	4.549	6.535	5.402	2.896	3.099	2.899
dense 1	2.34	2466420	103	66	3.660	3.952	4.661	4.809	4.821	6.748	5.721	3.124	3.276	3.064
dense 1	4.83	1275190	102	63	3.308	3.740	5.379	5.414	5.138	7.273	5.730	3.030	3.157	2.932
dense 1	4.24	1899520	101	64	3.209	3.566	5.215	5.452	5.473	7.356	5.958	3.230	3.383	3.125
dense 1	4.40	2439820	100	65	3.283	3.545	5.284	5.699	5.889	7.924	6.460	3.539	3.657	3.381

Table 3. Constants for curve fit of $Nu_c = A\ (Re_c)^B$ for flight data. R is the correlation coefficient.

Roughness Pattern	Nominal Angle of Attack	Gage No.	A	B	R^2
None	0	2	8.205	0.431	0.966
		3	13.452	0.413	0.969
		4	21.689	0.388	0.975
		5	10.793	0.428	0.967
		6	6.847	0.438	0.969
		7	6.180	0.429	0.972
		8	4.776	0.437	0.961
		9	1.702	0.472	0.984
		10	2.411	0.439	0.974
		11	4.236	0.396	0.973
	2	2	5.923	0.455	1.000
		4	25.810	0.378	1.000
		6	7.074	0.434	0.992
		8	4.408	0.440	0.999
		10	4.010	0.401	1.000
	4	2	14.509	0.393	0.995
		4	26.768	0.380	0.993
		6	8.075	0.423	0.994
		8	4.679	0.432	0.994
		10	2.158	0.440	0.989
Leading edge	0	2	3.542	0.492	0.996
		3	7.280	0.458	0.993
		4	9.211	0.454	0.991
		5	6.036	0.471	0.976
		6	4.063	0.476	0.984
		7	3.330	0.474	0.987
		8	6.425	0.417	0.999
		9	1.512	0.482	1.000
		10	2.094	0.450	0.993
		11	3.284	0.414	0.969
	2	2	8.364	0.430	0.987
		4	24.618	0.384	0.992
		6	3.247	0.489	0.950
		8	5.586	0.424	0.983
		10	2.895	0.425	0.986
	4	2	6.368	0.449	0.984
		4	7.633	0.471	0.983
		6	2.549	0.506	0.949
		8	3.893	0.443	0.562
		10	0.170	0.625	0.907

Table 3 (continued)

Roughness Pattern	Nominal Angle of Attack	Gage No.	A	B	R^2
Sparse	0	2	11.713	0.408	0.973
		3	16.235	0.403	0.989
		4	30.989	0.370	0.970
		5	20.316	0.387	0.968
		6	13.883	0.390	0.939
		7	3.963	0.490	0.987
		8	2.128	0.525	0.988
		9	1.089	0.532	0.993
		10	0.364	0.639	0.994
		11	0.215	0.674	0.996
	2	2	9.584	0.424	0.994
		4	21.216	0.397	0.985
		6	3.661	0.482	0.977
		8	0.365	0.653	0.991
		10	0.091	0.743	0.993
	4	2	43.282	0.318	0.993
		4	55.724	0.336	0.995
		6	18.481	0.369	0.983
		8	0.995	0.590	0.989
		10	0.630	0.618	0.991
Dense 1	0	2	0.456	0.650	0.999
		3	35.038	0.351	0.986
		4	84.253	0.300	0.998
		5	47.578	0.335	0.995
		6	0.487	0.642	0.998
		7	3.385	0.534	0.997
		8	3.136	0.528	1.000
		9	1.211	0.551	0.999
		10	0.503	0.617	0.999
		11	0.390	0.630	0.998
	2	2	0.881	0.597	0.999
		4	25.996	0.383	0.997
		6	0.532	0.649	0.997
		8	0.742	0.638	0.996
		10	0.207	0.688	0.999
	4	2	4.196	0.483	0.991
		4	8.385	0.468	0.994
		6	0.284	0.706	0.997
		8	0.423	0.685	1.000
		9	0.139	0.722	0.997

Table 4. Frossling Numbers for each gage for all conditions tested in the IRT with spray air off. Prandlt No. = 0.71

Roughness Pattern	Angle of Attack	Re_c	T_w (°F)	T_t (°F)	Frossling Number for Gage Number: 2	3	4	5	6	7	8	9	10	11
none	0.05	1218637	93	19	3.194	4.054	4.697	4.040	2.963	2.438	2.094	1.234	1.097	1.046
none	0.00	1234773	94	19	3.121	3.997	4.561	3.980	2.922	2.394	2.049	1.219	1.072	1.027
none	0.05	2425532	95	20	3.123	3.962	4.502	3.989	2.918	2.374	2.041	1.196	1.058	1.000
none	-0.10	3505816	95	19	3.144	4.010	4.523	4.009	2.949	2.406	2.406	1.197	1.054	0.996
none	-0.10	4519479	95	19	3.186	4.015	4.480	4.029	3.033	2.477	2.143	1.303	1.215	1.248
none	2.00	1200887	94	18	3.220	4.025	4.806	3.917	2.859	2.304	1.979	1.172	1.031	0.971
none	1.90	2398677	95	19	3.172	4.018	4.640	3.883	2.822	2.274	1.935	1.136	1.007	0.955
none	1.95	3540922	95	19	3.160	4.042	4.587	3.871	2.811	2.252	1.913	1.116	0.985	0.938
none	4.10	1199698	94	22	3.259	3.755	4.987	3.816	2.700	2.149	1.818	1.067	0.940	0.883
none	3.95	2391361	95	19	3.210	3.556	4.957	3.780	2.669	2.113	1.779	1.043	0.906	0.866
none	3.95	2406692	95	19	3.201	3.635	4.960	3.774	2.658	2.119	1.783	1.037	0.915	0.871
none	3.95	3519072	95	19	3.208	3.619	4.984	3.796	2.698	2.152	1.877	1.151	1.052	1.069
none	5.90	1233124	94	17	3.235	3.765	4.936	3.656	2.511	1.924	1.553	0.889	0.777	0.763
none	6.00	2375344	95	18	3.198	3.636	4.951	3.636	2.454	1.850	1.495	0.935	1.275	3.022
none	6.10	3529845	94	17	3.097	3.860	4.967	3.630	2.445	1.830	1.537	1.883	4.139	4.110
none	5.90	3556646	95	17	3.140	3.770	4.919	3.638	2.447	1.907	1.658	1.643	3.340	4.234
none	7.95	1200568	95	17	3.141	4.228	5.135	3.563	2.248	1.456	1.353	2.897	3.899	3.517
none	8.05	1242591	94	19	3.073	4.141	5.017	3.494	2.194	1.340	1.032	2.888	3.992	3.535
none	-4.00	1215810	92	18	2.917	3.888	5.318	3.700	3.049	2.541	2.178	1.269	1.160	1.099
none	-4.00	2401158	93	18	2.884	3.837	5.234	3.584	3.047	2.492	2.149	1.247	1.134	1.082
none	-4.00	3528412	95	18	2.903	3.890	5.243	3.515	3.050	2.490	2.156	1.247	1.141	1.079
lead edge	0.10	1270612	95	19	3.134	4.025	4.889	3.970	2.912	2.381	2.051	1.199	1.069	1.025
lead edge	0.00	2398765	91	19	3.149	4.116	5.107	4.046	2.953	2.415	2.066	1.177	1.070	1.011
lead edge	-0.05	3536747	89	18	3.174	4.141	5.061	4.074	3.001	2.446	2.157	1.207	1.091	1.044
lead edge	3.90	1331642	95	20	3.156	3.652	5.211	3.978	2.745	2.162	1.804	1.080	0.955	0.967
lead edge	4.00	2422148	90	18	3.202	3.670	5.585	4.204	2.893	2.321	2.124	1.402	1.555	1.907
lead edge	4.00	3558652	89	18	3.224	3.609	5.628	4.299	3.003	2.544	2.599	1.898	2.227	2.554
sparse	-0.10	1218170	95	18	3.083	4.018	4.951	4.038	2.855	3.131	2.806	1.549	2.325	2.329
sparse	-0.05	2396097	96	19	3.132	4.137	4.916	4.080	2.909	3.694	3.253	1.793	2.997	3.090
sparse	0.10	3617570	95	20	3.123	4.078	4.879	4.068	2.904	3.888	3.516	1.961	3.366	3.573
sparse	1.95	1211371	95	19	3.240	4.067	5.072	4.004	2.813	3.534	3.138	1.753	2.839	2.861
sparse	2.00	2421399	96	19	3.151	3.993	4.887	3.954	2.742	3.890	3.503	1.982	3.422	3.501
sparse	2.00	3530273	96	20	3.181	4.004	4.898	4.041	2.813	4.266	3.961	2.284	3.930	4.043
sparse	4.00	1217078	96	18	3.293	3.857	5.443	4.172	2.752	3.846	3.425	1.971	3.369	3.267
sparse	4.00	2416035	93	19	3.224	3.697	5.424	4.300	2.819	4.433	4.254	2.706	4.015	3.859
sparse	4.00	3563491	96	19	3.197	3.598	5.495	4.339	2.873	4.985	5.202	3.505	4.176	4.164
sparse	6.00	2438888	94	20	3.184	3.797	5.763	4.489	2.935	5.376	5.991	3.817	4.010	3.899
sparse	6.00	3513405	96	18	3.149	3.763	5.979	4.582	3.082	6.316	7.196	4.224	4.292	4.288
sparse	8.10	1217221	96	19	3.037	4.185	5.820	4.561	2.848	5.133	5.792	3.557	3.659	3.399
sparse	-4.10	2383168	94	20	3.044	4.324	5.495	3.642	3.042	3.039	2.699	1.421	2.204	2.140
sparse	-4.00	3501333	97	19	3.100	4.369	5.534	3.552	3.019	3.219	2.807	1.504	2.446	2.478

Table 4 (continued)

Roughness Pattern	Angle of Attack	Re_c	T_w (°F)	T_t (°F)	Frossling Number for Gage Number: 2	3	4	5	6	7	8	9	10	11
dense1	0.10	1203043	97	19	3.504	4.625	5.305	4.294	3.852	5.541	4.687	2.403	2.698	2.479
dense1	0.05	2404876	92	18	4.525	4.720	5.261	4.406	4.982	6.640	5.508	2.911	3.286	3.207
dense1	0.00	3488347	96	19	5.013	4.851	5.306	4.457	5.279	7.119	6.113	3.345	3.617	3.619
dense1	0.00	4446989	97	25	5.134	4.908	5.317	4.488	5.528	7.494	6.547	3.587	3.791	3.824
dense1	2.00	1207522	96	20	3.198	4.411	5.255	4.323	4.549	6.827	5.434	2.780	3.067	2.876
dense1	2.00	2386763	93	19	3.518	4.337	5.110	4.536	5.789	7.691	6.318	3.380	3.644	3.513
dense1	2.00	3487815	96	18	3.894	4.373	5.123	4.692	6.224	8.408	7.090	3.825	3.981	3.933
dense1	4.05	1218213	96	20	3.213	3.966	5.743	4.966	5.753	7.871	5.905	3.078	3.283	3.112
dense1	4.00	2398214	94	18	3.353	3.810	5.828	5.447	6.789	8.815	6.978	3.712	3.859	3.743
dense1	4.00	3458011	96	17	3.417	3.748	6.086	5.835	7.484	9.433	7.810	4.174	4.249	4.200
dense1	6.05	1206426	96	20	3.293	4.157	6.236	5.960	6.696	8.806	6.477	3.420	3.575	3.385
dense1	6.00	2378045	94	18	3.318	3.792	6.616	6.368	7.752	9.414	7.518	4.014	4.108	3.943
dense1	6.00	3481969	97	17	3.262	3.925	6.979	6.787	8.449	9.869	8.302	4.430	4.418	4.317
dense1	8.00	1213736	96	18	3.028	4.335	6.715	6.532	7.180	9.034	6.819	3.604	3.705	3.497
dense1	-3.95	1200441	96	18	5.371	5.392	5.745	3.670	3.319	3.570	3.114	1.668	2.028	1.854
dense1	-4.00	2387339	95	20	6.394	5.766	5.789	3.514	3.344	4.042	3.583	1.819	2.206	2.111
dense1	-4.00	3488097	97	19	7.162	6.053	6.115	3.461	3.446	4.420	3.816	1.976	2.405	2.421
dense2	0.00	1203664	91	18	3.530	4.533	5.289	4.285	3.738	5.418	5.453	3.449	3.635	3.315
dense2	0.00	2396356	95	18	4.527	4.677	5.253	4.391	4.826	6.509	6.335	3.930	4.144	3.876
dense2	0.00	3469558	96	20	5.023	4.817	5.303	4.497	5.223	7.123	6.919	4.355	4.519	4.336
dense2	2.00	1159063	91	20	3.276	4.321	5.454	4.389	4.349	6.738	6.272	3.815	3.926	3.602
dense2	2.05	2382992	95	20	3.549	4.337	5.176	4.629	5.659	7.668	7.093	4.326	4.423	4.137
dense2	2.00	3496185	96	19	3.895	4.374	5.137	4.804	6.148	8.335	7.780	4.776	4.806	4.580
dense2	4.00	1218212	93	18	3.351	3.998	5.754	5.049	5.730	7.858	6.874	4.097	4.183	3.800
dense2	4.00	2374660	96	19	3.346	3.764	5.752	5.392	6.608	8.666	7.698	4.658	4.677	4.348
dense2	4.00	3474083	96	18	3.435	3.740	6.027	5.783	7.413	9.356	8.548	5.207	5.095	4.804
dense2	6.00	2390764	96	17	3.285	3.903	6.471	6.300	7.631	9.309	8.255	4.964	4.860	4.485
dense2	6.00	3570199	97	17	3.227	3.891	6.759	6.546	8.292	9.686	8.869	5.344	5.139	4.811
dense2	8.05	1191984	94	19	3.112	4.424	6.824	6.674	7.236	9.155	7.675	4.513	4.499	4.057
dense2	-4.00	1204178	95	21	5.351	5.154	5.706	3.673	3.228	3.484	3.682	2.300	3.043	2.800
dense2	-4.00	2420831	96	17	6.429	5.713	5.749	3.512	3.295	3.950	4.395	2.958	3.403	3.175
dense2	-4.00	3520357	97	18	7.230	6.023	5.940	3.460	3.388	4.366	4.719	3.268	3.660	3.497

Table 5. Frossling Numbers for each gage for all conditions tested in the IRT with spray air on. Prandlt No. = 0.71

Roughness Pattern	Angle of Attack	Re_c	T_w (°F)	T_t (°F)	Frossling Number for Gage Number: 2	3	4	5	6	7	8	9	10	11
none	0.05	1208985	93	21	3.275	4.183	4.800	4.140	3.047	2.197	2.139	1.256	1.107	1.061
none	0.05	1288857	94	21	3.162	4.048	4.641	3.976	2.934	2.392	2.056	1.198	1.061	1.021
none	0.00	2408339	93	19	3.135	4.031	4.761	3.954	2.970	2.402	2.066	1.181	1.062	1.018
none	0.00	3517046	94	20	3.177	4.028	4.539	4.019	2.974	2.392	2.048	1.190	1.051	1.010
none	2.00	1247998	92	19	3.236	4.007	5.126	3.887	2.822	2.312	1.983	1.147	1.040	0.988
none	2.00	2389530	93	19	3.211	4.061	4.957	3.885	2.841	2.287	1.953	1.113	1.009	0.962
none	2.00	3534583	94	20	3.209	3.997	4.872	3.886	2.848	2.281	1.982	1.084	1.002	0.949
none	4.10	1209313	94	20	3.391	3.917	5.162	3.886	2.761	2.191	1.855	1.086	0.950	0.924
none	4.00	3532023	94	18	3.230	3.564	4.990	3.804	2.689	2.113	1.750	1.022	0.890	0.953
none	6.00	1200616	92	18	3.289	4.169	5.386	3.702	2.520	1.914	1.560	0.952	1.395	2.385
none	6.00	2381396	94	19	3.209	3.901	5.197	3.636	2.473	1.844	1.569	1.214	3.041	3.853
none	6.00	2402803	94	19	3.204	3.882	5.159	3.596	2.456	1.829	1.543	1.207	2.838	3.835
none	-4.00	1237652	92	18	2.925	3.903	5.329	3.719	3.047	2.581	2.235	1.269	1.198	1.124
none	-4.00	2411087	93	18	2.901	3.864	5.262	3.602	3.038	2.503	2.151	1.253	1.137	1.092
none	-4.00	3503155	94	20	2.897	3.859	5.231	3.513	3.020	2.511	2.177	1.226	1.145	1.069
lead edge	0.10	1215028	95	20	3.235	4.141	5.044	4.076	2.986	2.452	2.089	1.286	1.092	1.052
lead edge	0.00	2405826	91	19	3.172	4.104	5.087	4.017	2.944	2.399	2.086	1.152	1.077	1.010
lead edge	-0.05	3545135	89	19	3.183	4.137	5.051	4.067	3.018	2.439	2.082	1.196	1.081	1.035
lead edge	3.90	1295518	95	20	3.201	3.659	5.299	4.029	2.779	2.201	1.862	1.134	1.038	1.111
lead edge	4.00	2394880	90	19	3.250	3.711	5.632	4.227	2.900	2.361	2.159	1.441	1.675	2.095
lead edge	4.00	3571933	90	18	3.204	3.618	5.648	4.324	3.007	2.543	2.624	1.916	2.206	2.664
sparse	-0.10	1213822	95	20	3.202	4.155	5.040	4.127	2.916	3.359	2.944	1.621	2.466	2.492
sparse	-0.05	2391245	96	19	3.087	4.052	4.859	4.001	2.903	3.644	3.231	1.784	2.967	3.070
sparse	0.10	3516296	95	20	3.170	4.185	4.948	4.109	2.931	3.955	3.549	2.001	3.422	3.623
sparse	1.95	1298896	95	19	3.174	4.034	5.059	3.938	2.739	3.535	3.115	1.760	2.875	2.863
sparse	2.00	2411439	92	19	3.205	4.044	5.007	4.027	2.806	4.011	3.613	2.058	3.569	3.639
sparse	2.00	3541428	96	20	3.186	4.011	4.942	4.059	2.814	4.286	3.961	2.287	3.958	4.049
sparse	4.00	1216864	96	19	3.325	3.894	5.457	4.183	2.788	3.910	3.512	2.094	3.431	3.292
sparse	4.00	2395630	93	20	3.260	3.701	5.496	4.305	2.819	4.495	4.332	2.802	4.020	3.874
sparse	4.00	3545318	96	19	3.210	3.603	5.527	4.351	2.891	5.019	5.283	3.535	4.190	4.167
sparse	6.00	2393427	94	20	3.208	3.932	5.861	4.532	2.952	5.435	6.124	3.875	4.051	3.940
sparse	6.00	3522626	96	19	3.158	3.773	5.913	4.562	3.099	6.271	7.179	4.207	4.263	4.257
sparse	8.10	1256507	96	19	3.155	4.241	6.001	4.579	2.895	5.413	6.140	3.612	3.692	3.479
sparse	-4.10	2392934	95	20	3.051	4.355	5.501	3.643	3.077	3.095	2.742	1.455	2.217	2.157
sparse	-4.00	3482703	97	20	3.109	4.377	5.572	3.565	3.042	3.247	2.842	1.522	2.424	2.476

Table 5 (continued).

Roughness Pattern	Angle of Attack	Re_c	T_w (°F)	T_t (°F)	Frossling Number for Gage Number: 2	3	4	5	6	7	8	9	10	11
dense1	0.10	1211454	96	20	3.653	4.637	5.298	4.331	4.296	5.736	4.785	2.457	2.705	2.532
dense1	0.05	2413368	92	19	4.560	4.710	5.247	4.413	5.058	6.652	5.534	2.946	3.254	3.202
dense1	0.00	3486616	96	19	4.997	4.841	5.316	4.495	5.321	7.163	6.213	3.373	3.628	3.631
dense1	0.00	4401687	97	24	5.141	4.856	5.302	4.526	5.566	7.565	6.573	3.608	3.823	3.849
dense1	2.00	1203405	96	20	3.266	4.476	5.400	4.429	5.054	6.916	5.491	2.834	3.082	2.925
dense1	2.00	2395432	93	19	3.639	4.308	5.142	4.562	5.829	7.749	6.325	3.389	3.629	3.491
dense1	2.00	3481734	96	19	3.953	4.388	5.126	4.753	6.249	8.442	7.094	3.823	3.980	3.939
dense1	4.05	1205082	96	20	3.404	4.042	5.906	5.214	6.085	8.075	6.041	3.170	3.377	3.186
dense1	4.00	2414792	94	18	3.387	3.808	5.861	5.484	6.837	8.837	6.965	3.712	3.899	3.757
dense1	4.00	3492575	96	18	3.432	3.732	6.091	5.832	7.452	9.393	7.804	4.147	4.224	4.159
dense1	6.05	1240236	96	20	3.254	4.227	6.393	6.010	6.760	8.708	6.437	3.387	3.527	3.354
dense1	6.00	2406489	94	18	3.300	3.983	6.558	6.375	7.766	9.406	7.568	3.991	4.065	3.941
dense1	8.00	1221102	96	19	3.140	4.552	7.011	6.688	7.435	9.089	6.930	3.661	3.777	3.544
dense1	-3.95	1207915	96	19	5.333	5.444	5.785	3.708	3.378	3.666	3.280	1.711	2.039	1.899
dense1	-4.00	2398540	95	20	6.374	5.715	5.789	3.552	3.393	4.172	3.628	1.851	2.225	2.162
dense1	-4.00	3435586	97	20	7.201	6.109	6.055	3.487	3.492	4.488	3.909	2.002	2.417	2.454
dense2	0.00	1191041	91	21	3.727	4.564	5.386	4.354	4.163	5.658	5.606	3.445	3.664	3.333
dense2	0.00	2389651	95	18	4.566	4.684	5.263	4.392	4.891	6.523	6.337	3.946	4.183	3.905
dense2	0.00	3474259	96	20	4.998	4.793	5.303	4.508	5.250	7.119	6.954	4.357	4.511	4.333
dense2	2.00	1246161	92	20	3.225	4.163	5.284	4.394	4.853	6.674	6.228	3.722	3.892	3.533
dense2	2.05	2370689	95	20	3.701	4.321	5.271	4.657	5.719	7.745	7.111	4.363	4.487	4.159
dense2	2.00	3509328	96	19	3.954	4.340	5.140	4.807	6.157	8.313	7.745	4.778	4.800	4.587
dense2	4.00	1212621	93	19	3.416	3.993	5.836	5.174	5.866	7.947	6.748	4.048	4.120	3.744
dense2	4.00	2380654	96	19	3.366	3.738	5.747	5.374	6.633	8.715	7.680	4.650	4.563	4.332
dense2	4.00	3493395	96	18	3.447	3.682	6.004	5.763	7.412	9.309	8.493	5.169	5.059	4.790
dense2	6.00	1195580	94	19	3.316	4.235	6.416	6.004	6.639	8.696	7.289	4.333	4.356	3.917
dense2	6.00	2380788	96	18	3.264	3.986	6.561	6.325	7.664	9.332	8.256	4.933	4.850	4.490
dense2	6.00	3555147	97	17	3.247	3.925	6.807	6.598	8.341	9.700	8.861	5.358	5.130	4.814
dense2	8.05	1200082	94	20	3.208	4.512	7.011	6.704	7.348	9.097	7.811	4.533	4.479	4.035
dense2	-4.00	1201672	95	21	5.453	5.252	5.766	3.735	3.332	3.635	3.867	2.436	3.101	2.851
dense2	-4.00	2383034	96	18	6.582	5.772	5.905	3.594	3.396	4.171	4.486	2.996	3.437	3.200
dense2	-4.00	3496381	97	18	7.280	6.023	6.009	3.487	3.461	4.421	4.773	3.285	3.660	3.521

Table 6. Constants for curve fit of $Nu_c = A\ (Re_c)^B$ for IRT data with spray air off. R is the correlation coefficient.

Roughness Pattern	Nominal Angle of Attack	Gage No.	A	B	R^2
None	0	2	3.049	0.502	0.999
		3	4.209	0.497	0.999
		4	6.818	0.472	0.999
		5	3.895	0.502	1.000
		6	2.371	0.515	0.998
		7	2.090	0.510	0.997
		8	1.730	0.512	0.996
		9	0.879	0.523	0.989
		10	0.570	0.545	0.975
		11	0.346	0.576	0.947
	2	2	4.142	0.482	1.000
		4	8.905	0.456	1.000
		6	3.579	0.484	1.000
		8	3.089	0.468	1.000
		10	1.837	0.459	1.000
	4	2	4.100	0.483	1.000
		4	5.114	0.498	1.000
		6	2.850	0.496	0.999
		8	1.369	0.519	0.990
		10	0.303	0.578	0.951
	6	2	5.321	0.465	0.999
		4	4.870	0.501	1.000
		6	3.538	0.475	1.000
		8	1.021	0.529	0.976
		10	4.6E-10	2.005	0.939
	-4	2	3.152	0.494	1.000
		4	6.488	0.486	1.000
		6	3.043	0.500	1.000
		8	2.531	0.489	1.000
		10	1.479	0.482	0.999
Leading edge	0	2	2.636	0.512	1.000
		3	2.694	0.529	1.000
		4	2.919	0.537	0.998
		5	2.766	0.526	1.000
		6	1.947	0.529	1.000
		7	1.659	0.526	1.000
		8	1.067	0.546	0.998
		9	1.143	0.503	0.997
		10	0.831	0.518	0.999
		11	0.833	0.514	0.997
	4	2	2.323	0.522	1.000
		4	1.659	0.582	0.998
		6	0.761	0.591	1.000
		8	0.011	0.863	0.994
		10	5.3E-6	1.357	0.999

Table 6 (continued)

Roughness Pattern	Nominal Angle of Attack	Gage No.	A	B	R^2
Sparse	0	2	2.573	0.513	1.000
		3	3.208	0.516	0.998
		4	5.964	0.487	1.000
		5	3.625	0.508	1.000
		6	2.261	0.517	1.000
		7	0.183	0.704	0.998
		8	0.152	0.708	1.000
		9	0.074	0.717	1.000
		10	0.019	0.843	0.999
		11	0.009	0.896	1.000
	2	2	4.272	0.480	0.999
		4	8.306	0.465	0.999
		6	2.991	0.495	0.997
		8	0.163	0.710	0.996
		10	0.042	0.800	0.999
	4	2	4.869	0.472	1.000
		4	4.909	0.507	1.000
		6	1.583	0.539	1.000
		8	0.016	0.881	0.996
		10	0.188	0.706	0.997
	6	2	4.970	0.470	1.000
		4	1.303	0.601	1.000
		6	0.408	0.634	1.000
		8	0.004	1.002	1.000
		10	0.257	0.687	1.000
	-4	2	1.513	0.548	1.000
		4	4.199	0.518	1.000
		6	4.098	0.480	1.000
		8	0.602	0.602	1.000
		10	0.041	0.771	1.000
Dense 1	0	2	0.051	0.803	0.996
		3	2.423	0.546	1.000
		4	5.153	0.502	1.000
		5	2.670	0.534	1.000
		6	0.080	0.778	0.995
		7	0.220	0.731	0.999
		8	0.132	0.755	1.000
		9	0.031	0.809	0.999
		10	0.067	0.764	1.000
		11	0.022	0.837	0.999
	2	2	0.254	0.680	0.998
		4	7.549	0.474	0.999
		6	0.066	0.802	0.997
		8	0.170	0.747	0.999
		10	0.097	0.747	1.000
	4	2	1.396	0.560	1.000
		4	2.779	0.551	0.998
		6	0.170	0.751	1.000
		8	0.143	0.765	1.000
		10	0.104	0.746	1.000

Table 6 (continued)

Roughness Pattern	Nominal Angle of Attack	Gage No.	A	B	R^2
Dense 1	6	2	3.624	0.493	0.999
		4	1.448	0.604	0.999
		6	0.311	0.719	1.000
		8	0.249	0.732	1.000
		10	0.216	0.700	1.000
	-4	2	0.126	0.768	1.000
		4	3.331	0.539	0.998
		6	2.109	0.532	0.999
		8	0.212	0.692	1.000
		10	0.229	0.656	0.998
Dense 2	0	2	0.032	0.837	0.999
		3	2.066	0.556	1.000
		4	5.202	0.501	1.000
		5	2.301	0.544	1.000
		6	0.041	0.823	0.998
		7	0.144	0.759	1.000
		8	0.237	0.724	1.000
		9	0.165	0.717	0.999
		10	0.209	0.704	1.000
		11	0.099	0.750	0.999
	2	2	0.395	0.651	0.997
		4	12.000	0.443	0.999
		6	0.050	0.820	0.998
		8	0.428	0.692	0.999
		10	0.314	0.681	1.000
	4	2	2.494	0.521	0.999
		4	3.304	0.539	0.996
		6	0.192	0.742	0.999
		8	0.394	0.704	0.998
		10	0.309	0.686	1.000
	6	2	4.623	0.476	1.000
		4	3.454	0.544	0.998
		6	0.388	0.703	1.000
		8	0.591	0.679	1.000
		10	0.522	0.652	1.000
	-4	2	0.108	0.778	1.000
		4	3.523	0.534	0.999
		6	1.758	0.543	1.000
		8	0.139	0.734	1.000
		10	0.279	0.671	1.000

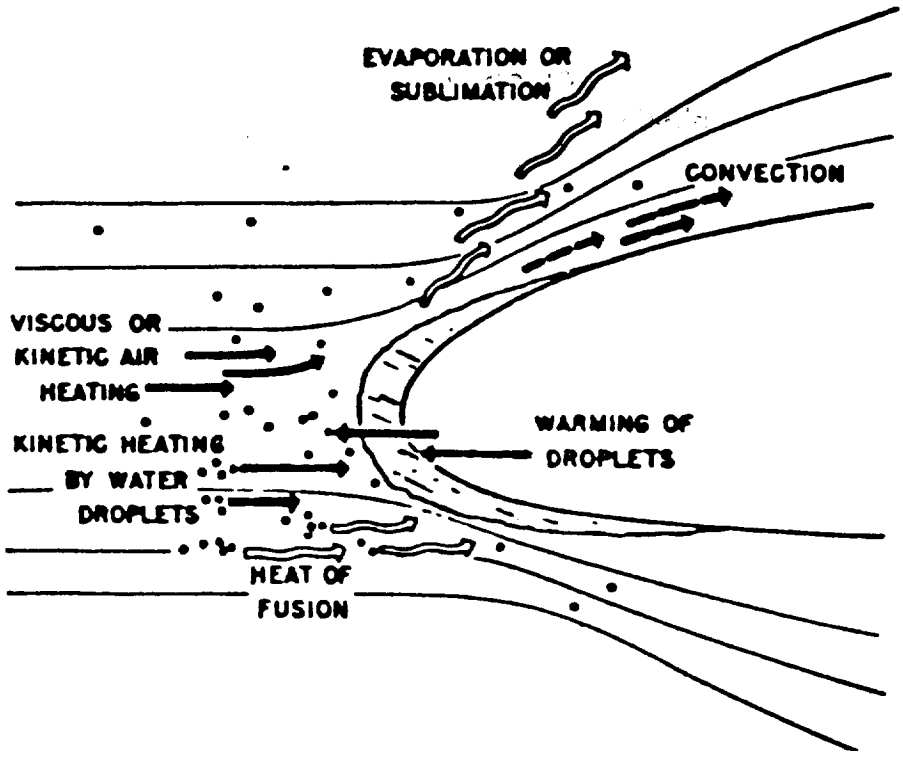

Modes of energy transfer for an unheated airfoil in icing conditions [7].

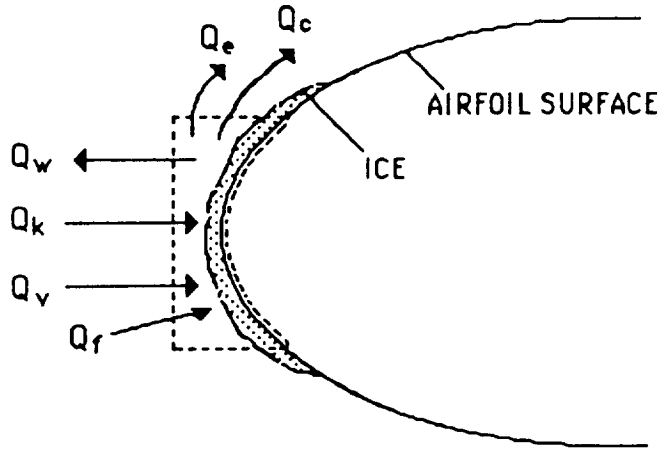

Figure 1. Typical energy balance control volume.

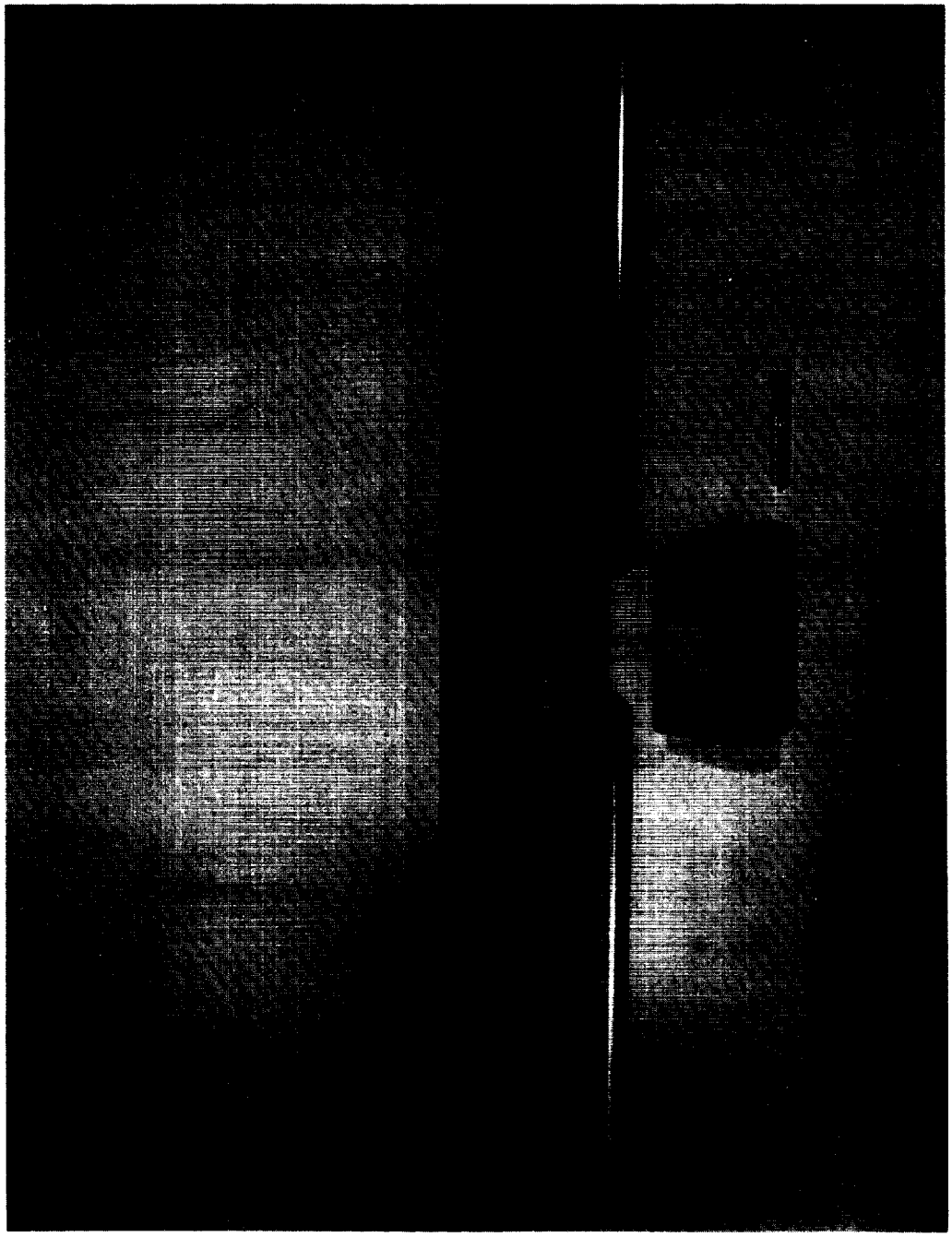

Figure 2. NACA 0012 test airfoil.

ORIGINAL PAGE
BLACK AND WHITE PHOTOGRAPH

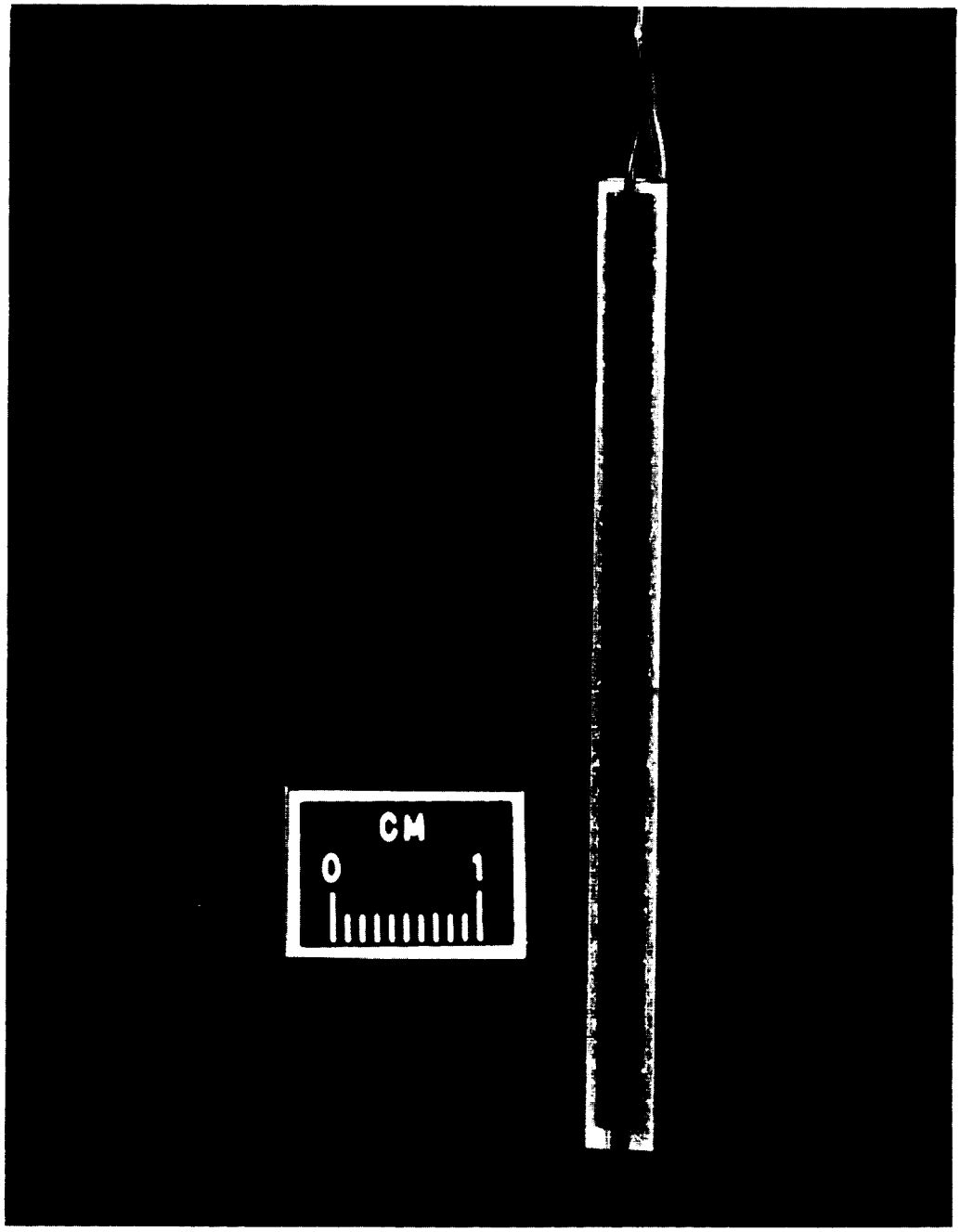

Figure 3. Heat transfer gage.

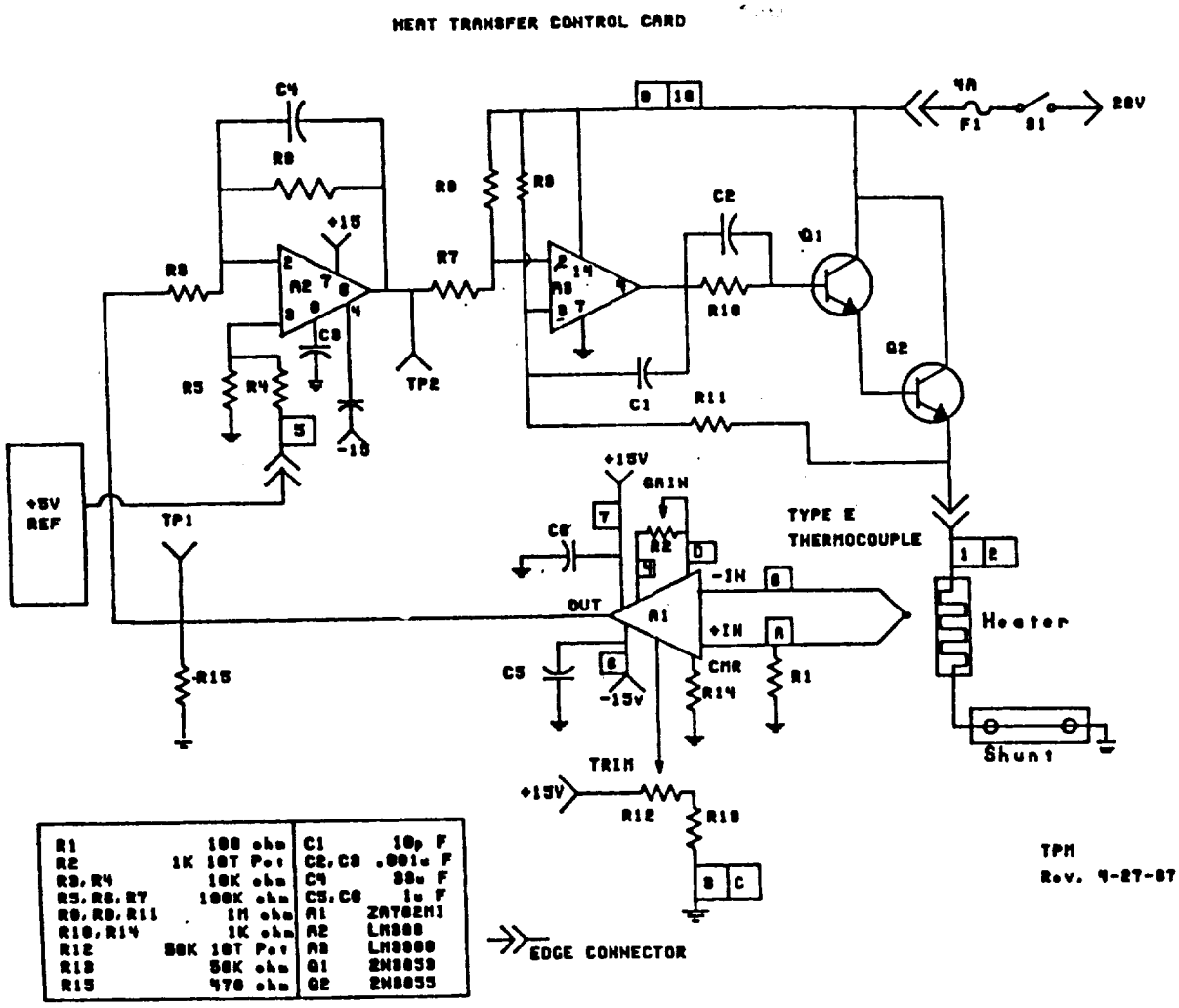

R1	100 ohm	C1	10p F
R2	1K 10T Pot	C2, C3	.001u F
R3, R4	10K ohm	C4	33u F
R5, R6, R7	100K ohm	C5, C6	1u F
R8, R9, R11	1M ohm	A1	ZAY02MI
R10, R14	1K ohm	A2	LM308
R12	50K 10T Pot	A3	LM3080
R13	56K ohm	Q1	2N3053
R15	470 ohm	Q2	2N3055

Figure 4. Heat transfer control circuit.

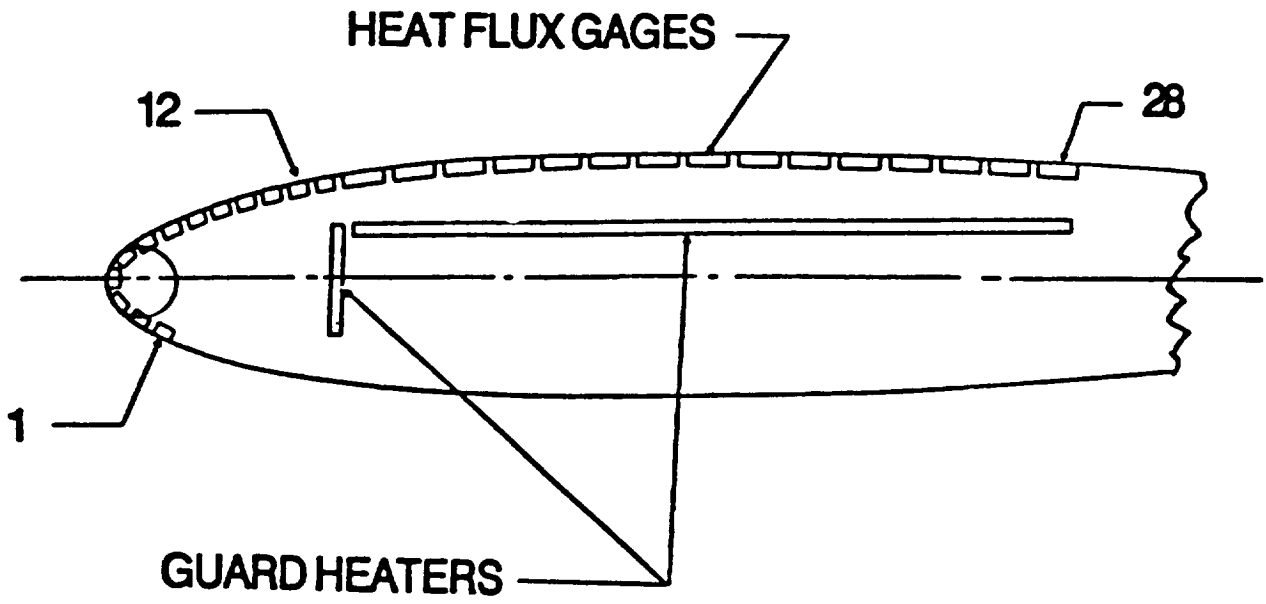

Figure 5. Cross-section of NACA 0012 airfoil with heat flux gages.

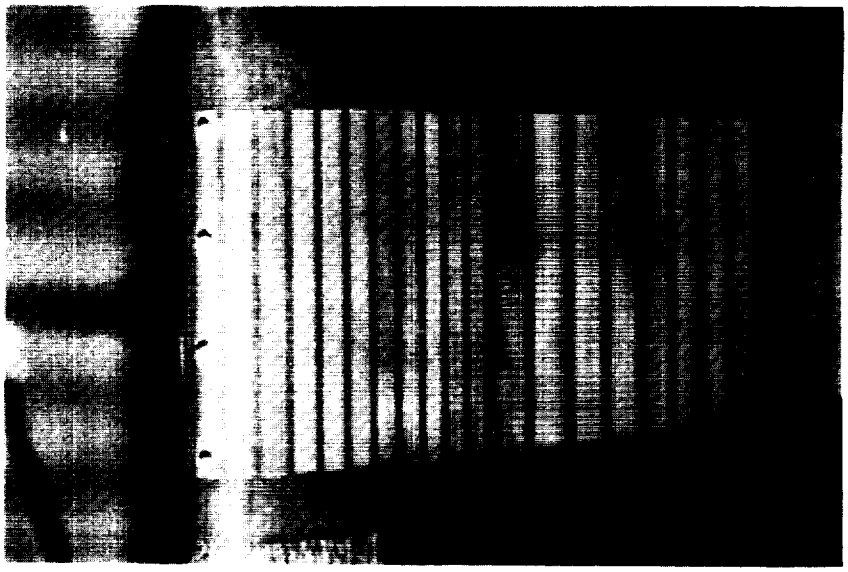

Leading edge roughness pattern

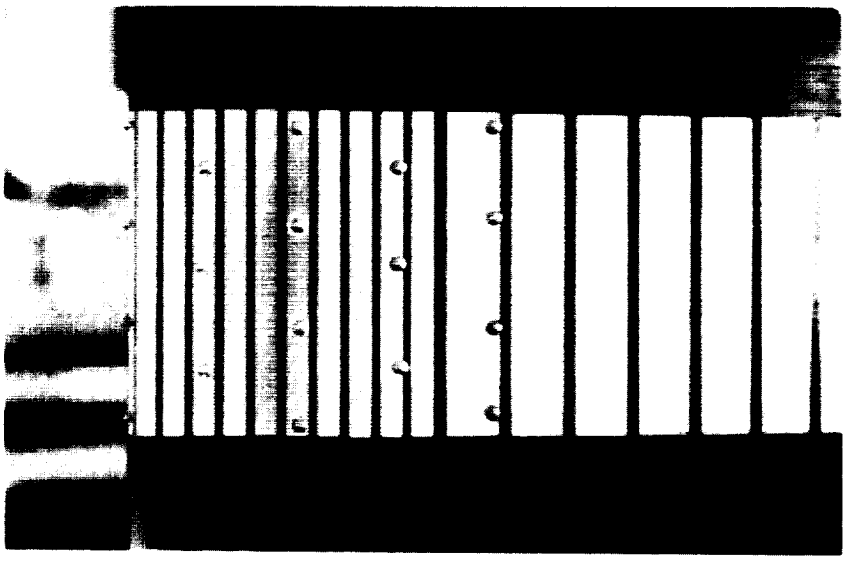

Sparse roughness pattern

Figure 6. Roughness patterns

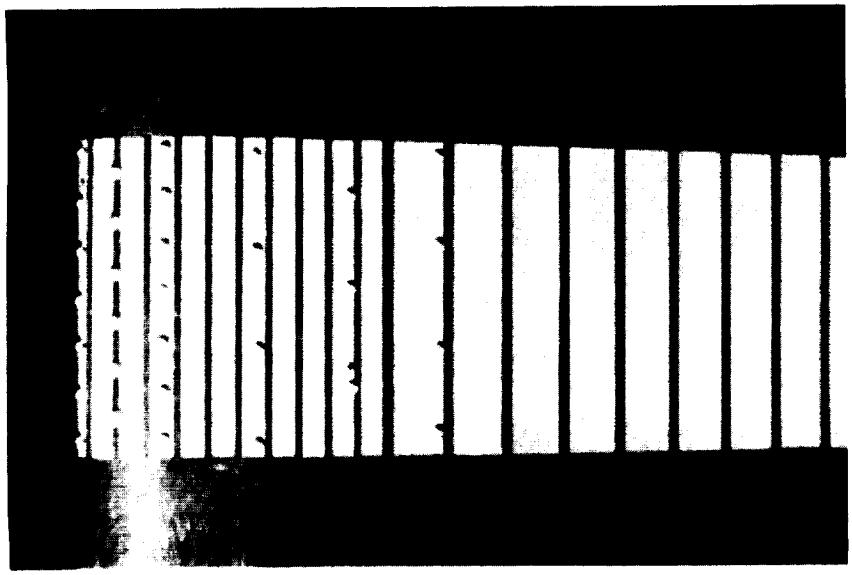

Dense 1 roughness pattern

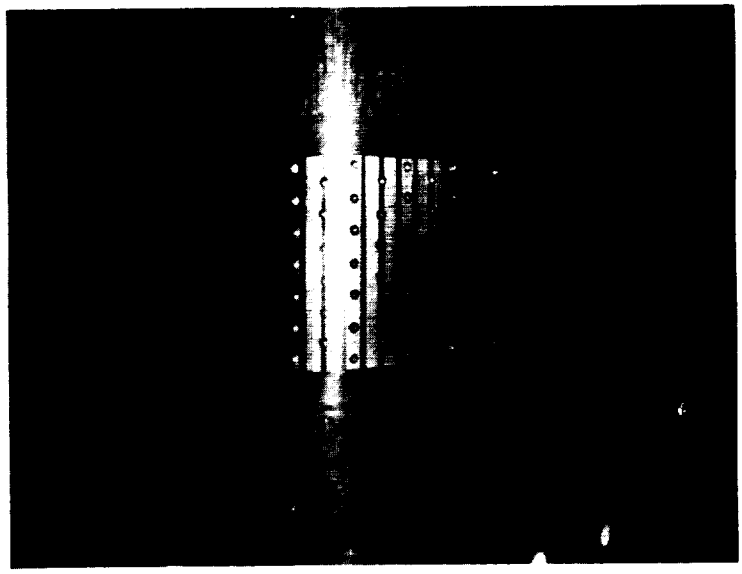

Dense 2 roughness pattern

Figure 6 (continued) Roughness patterns.

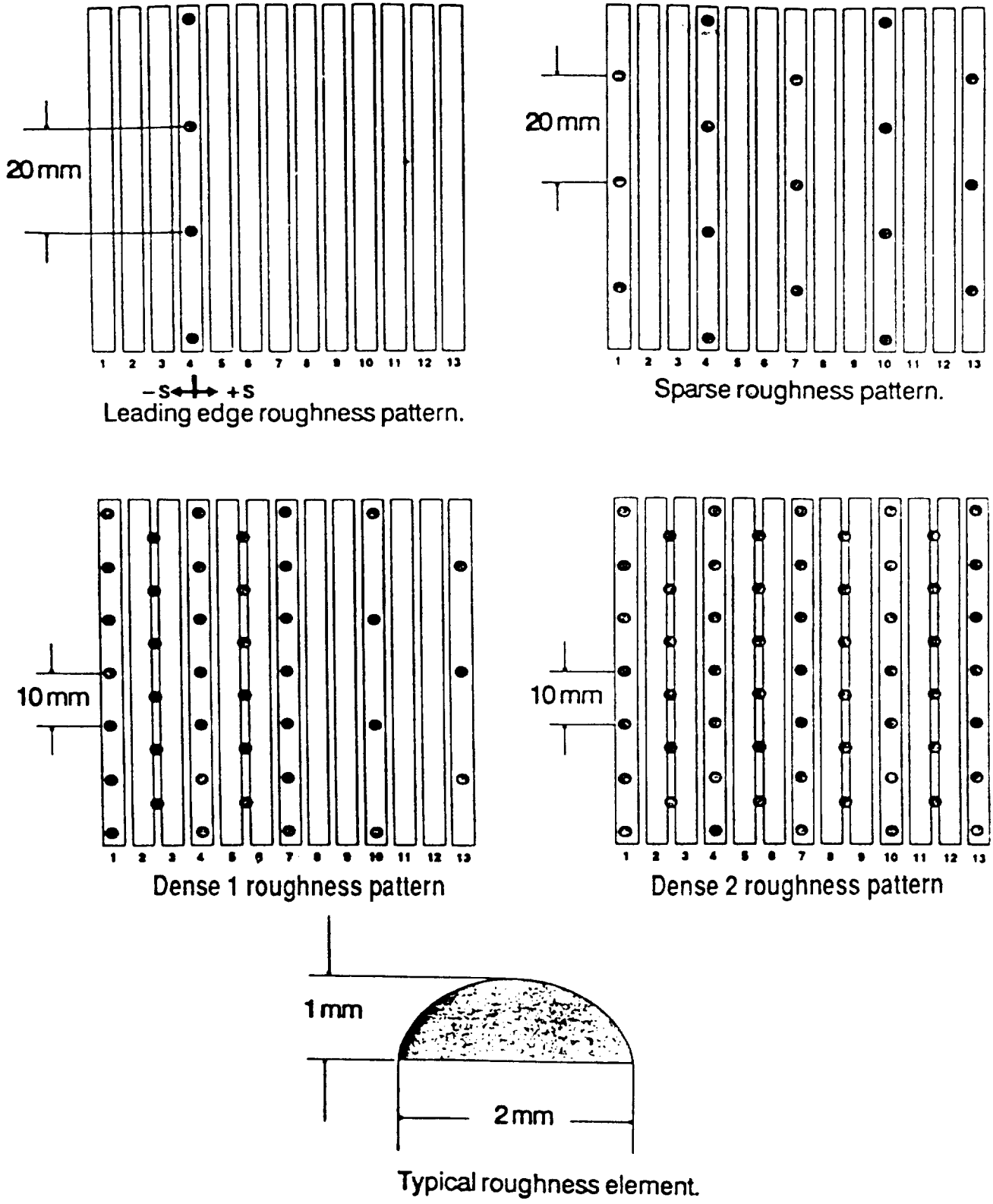

Figure 7. Location of roughness elements relative to heat flux gages.

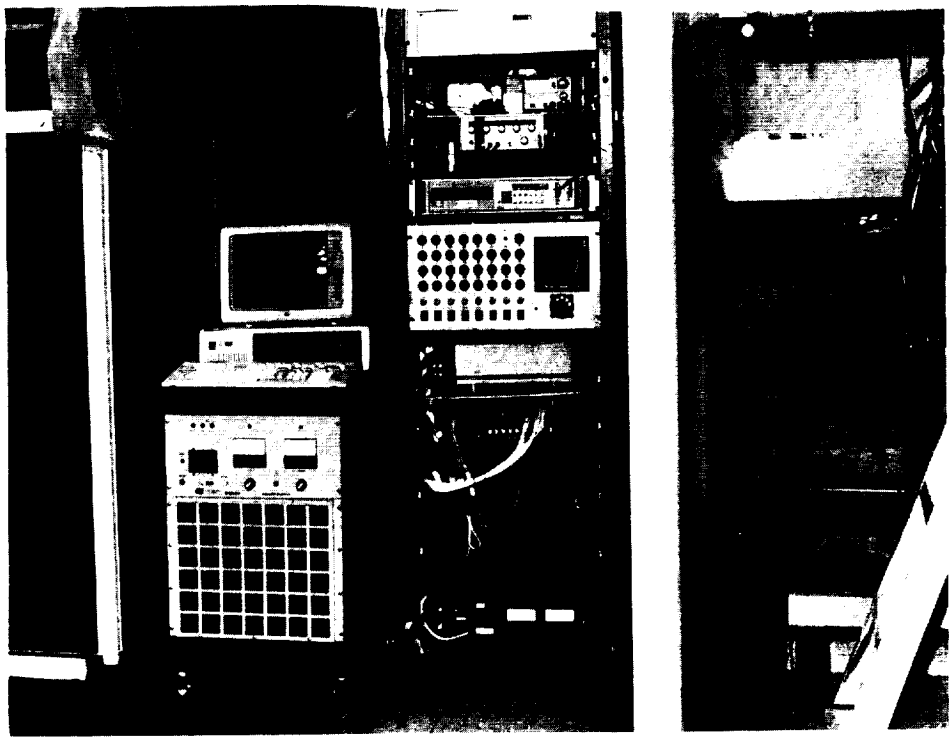

Figure 8. Data acquisition system.

ORIGINAL PAGE
BLACK AND WHITE PHOTOGRAPH

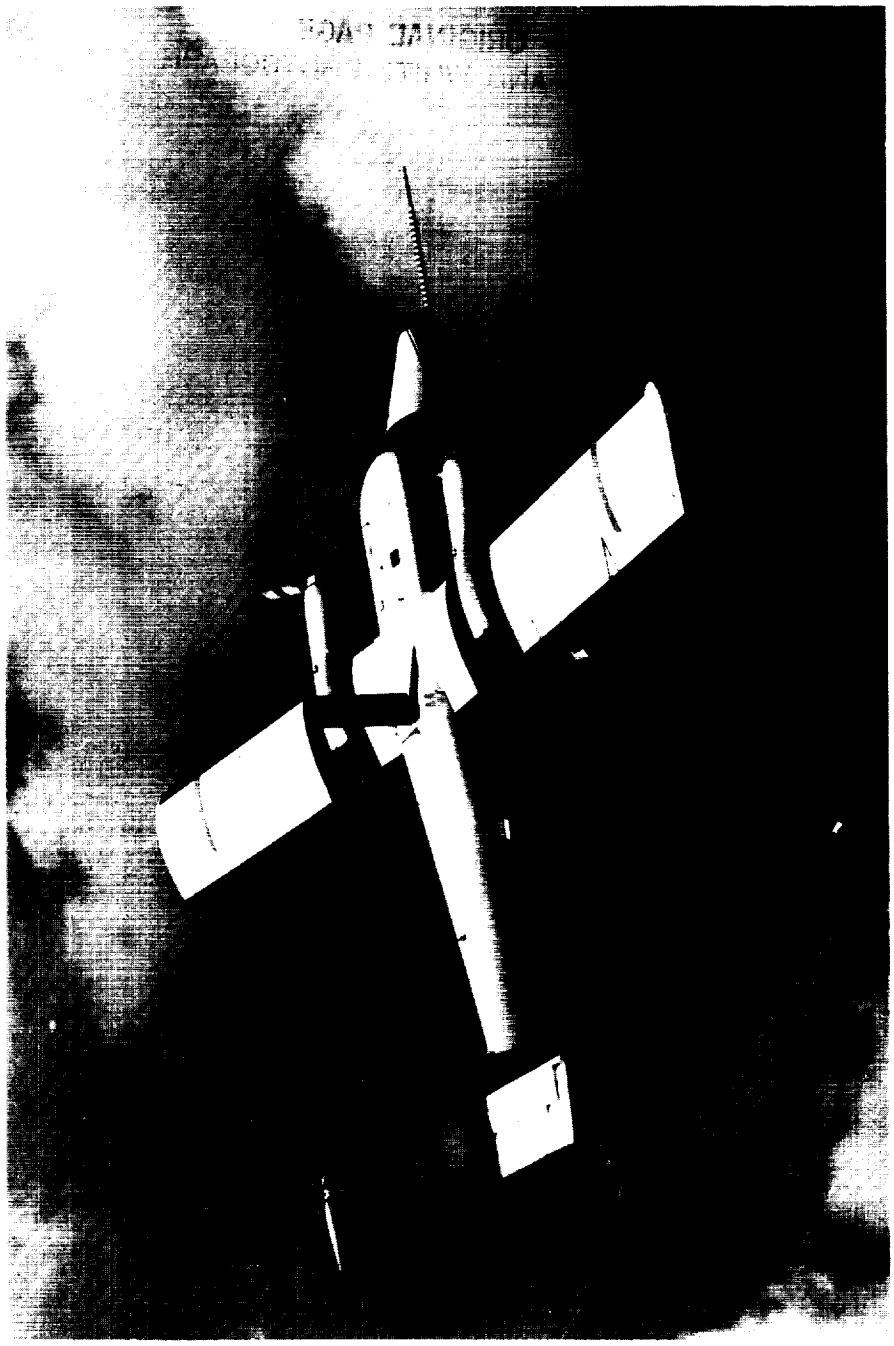

Figure 9. NASA Lewis Twin Otter Research Aircraft with mounted airfoil.

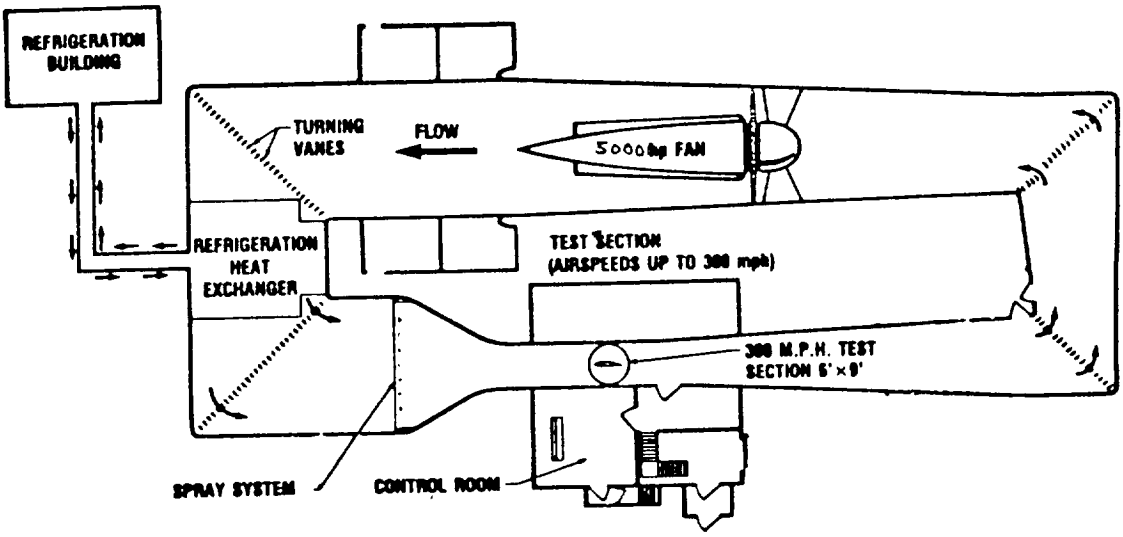

Figure 10. NASA Lewis Icing Research Tunnel [19].

ORIGINAL PAGE
BLACK AND WHITE PHOTOGRAPH

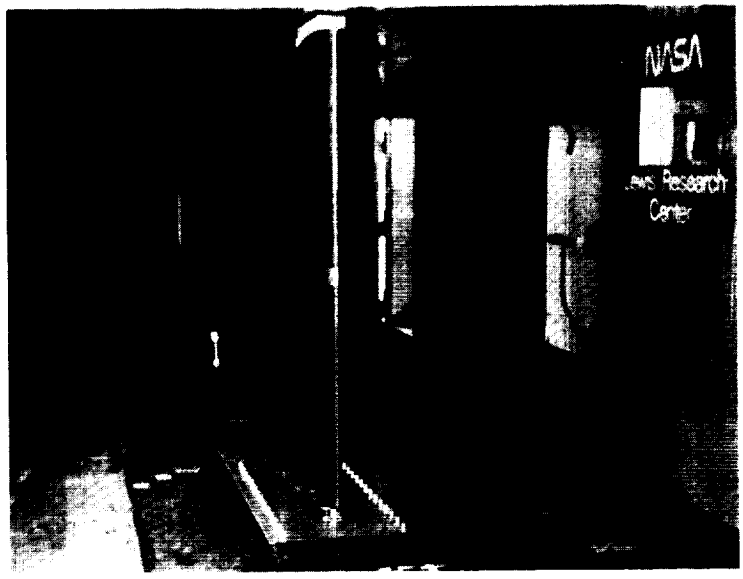

Figure 11. Test airfoil position in Icing Research Tunnel.

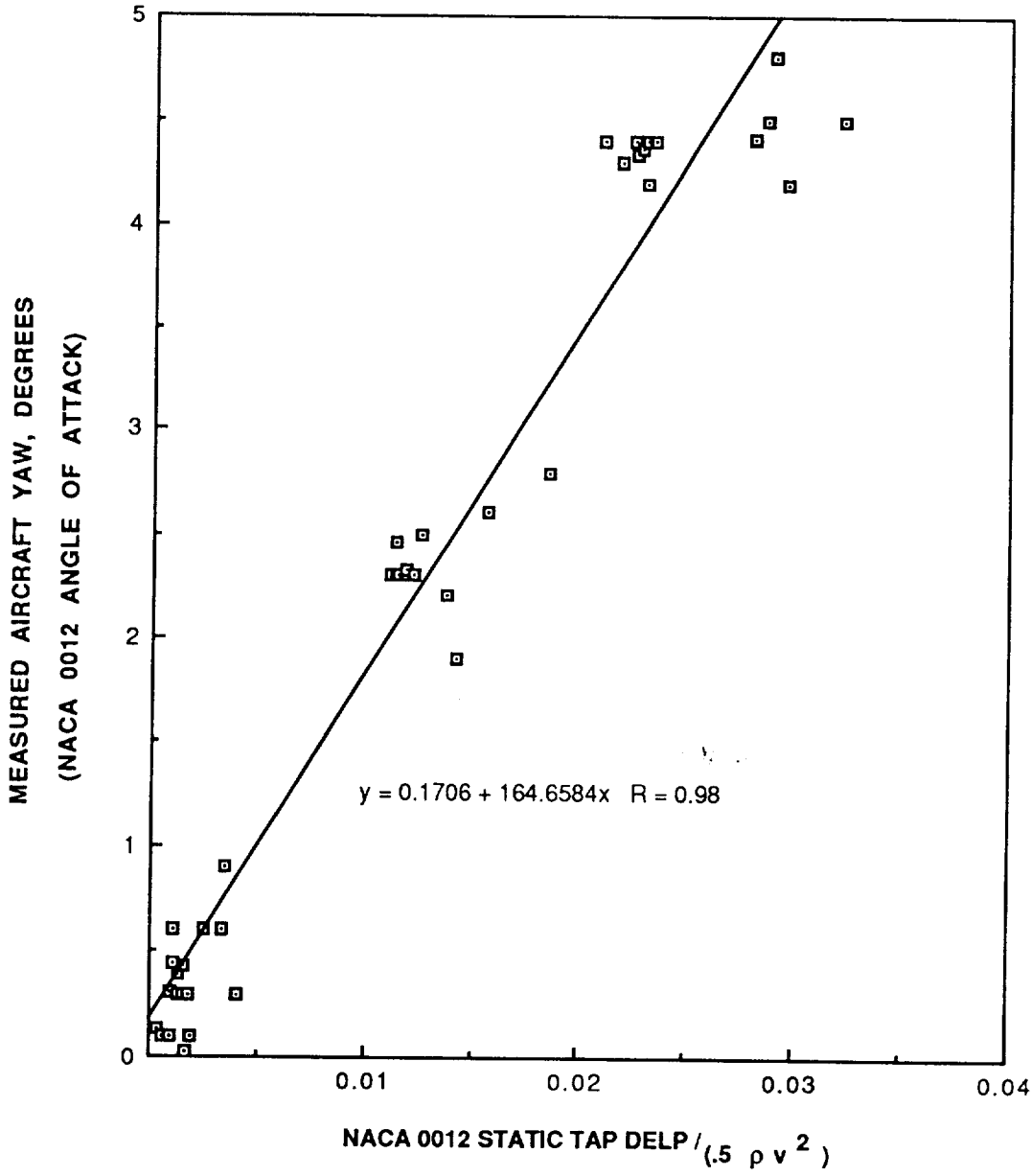

Figure 12. Aircraft yaw versus dimensionless pressure difference.

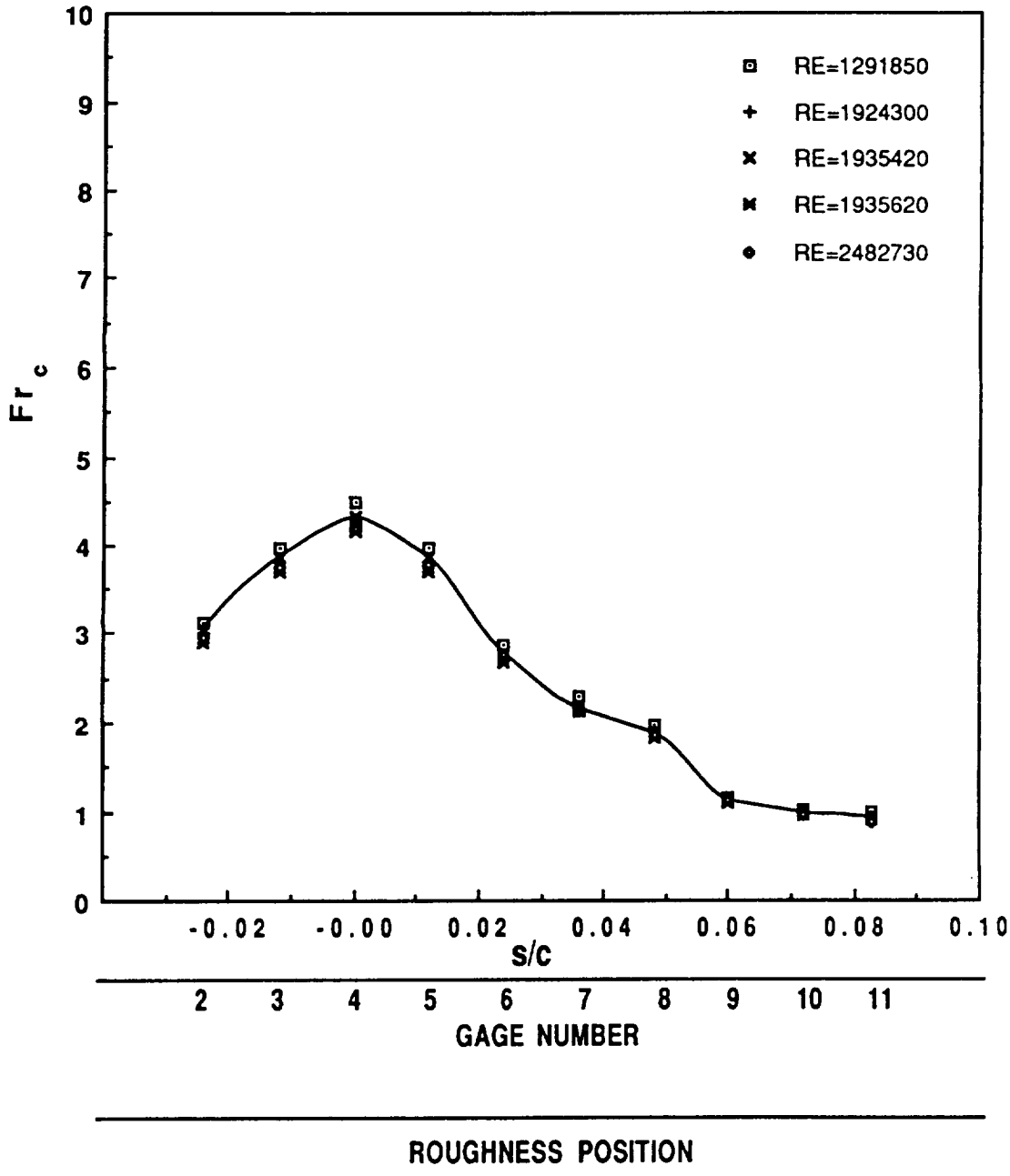

Figure 13. Frossling Number versus dimensionless surface distance: smooth airfoil, 0 degree angle of attack, flight data.

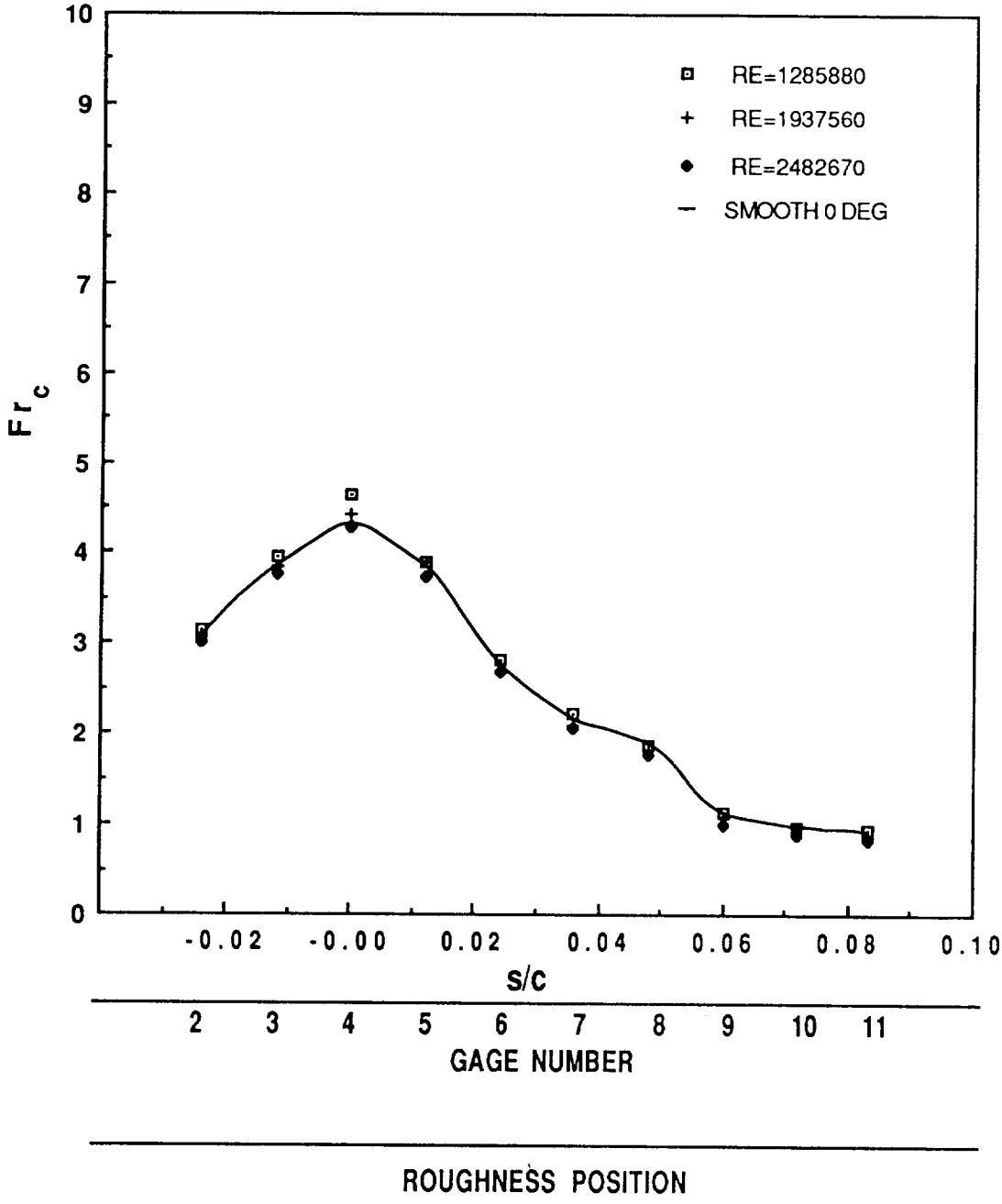

Figure 14. Frossling Number versus dimensionless surface distance: smooth airfoil, 2 degree angle of attack, flight data.

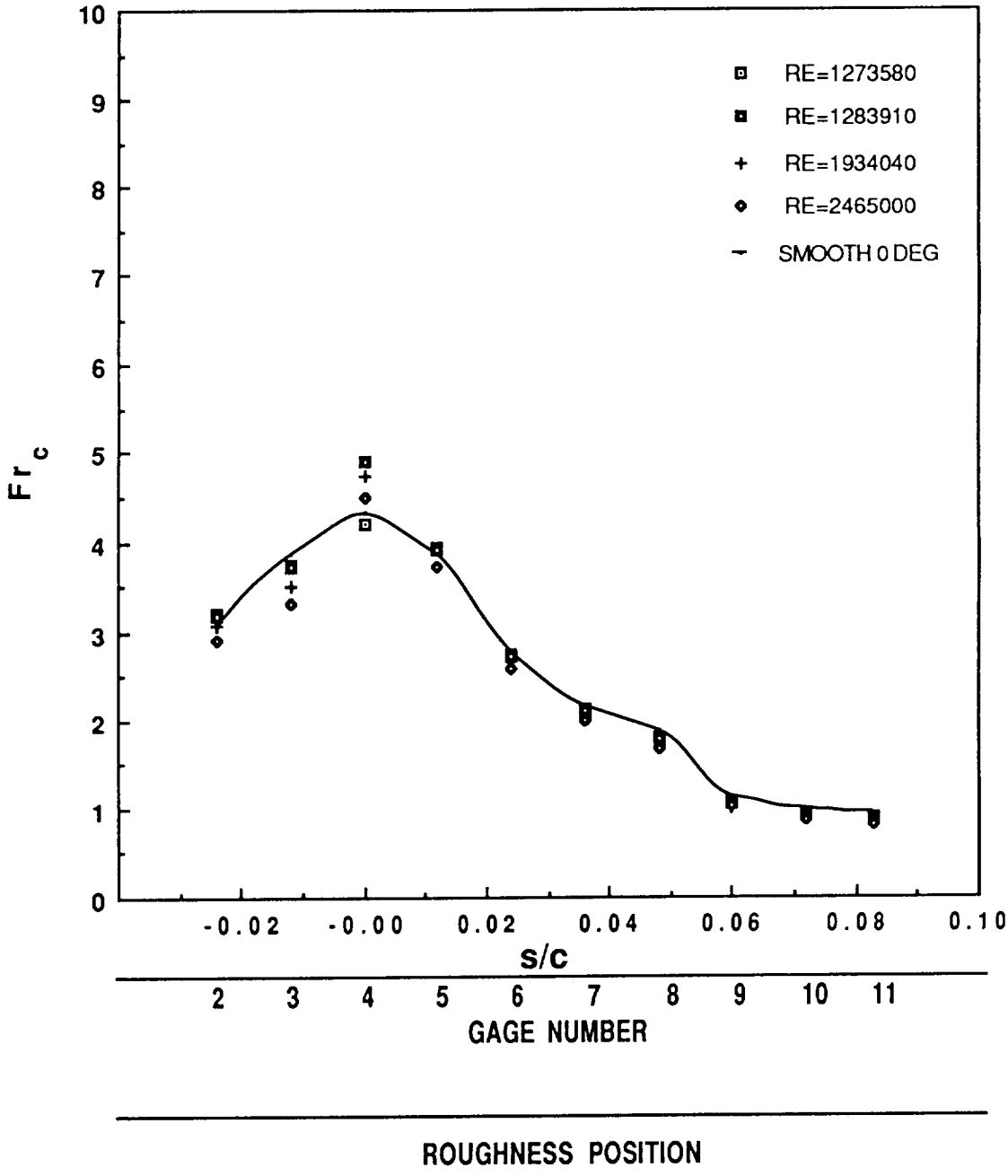

Figure 15. Frossling Number versus dimensionless surface distance: smooth airfoil, 4 degree angle of attack, flight data.

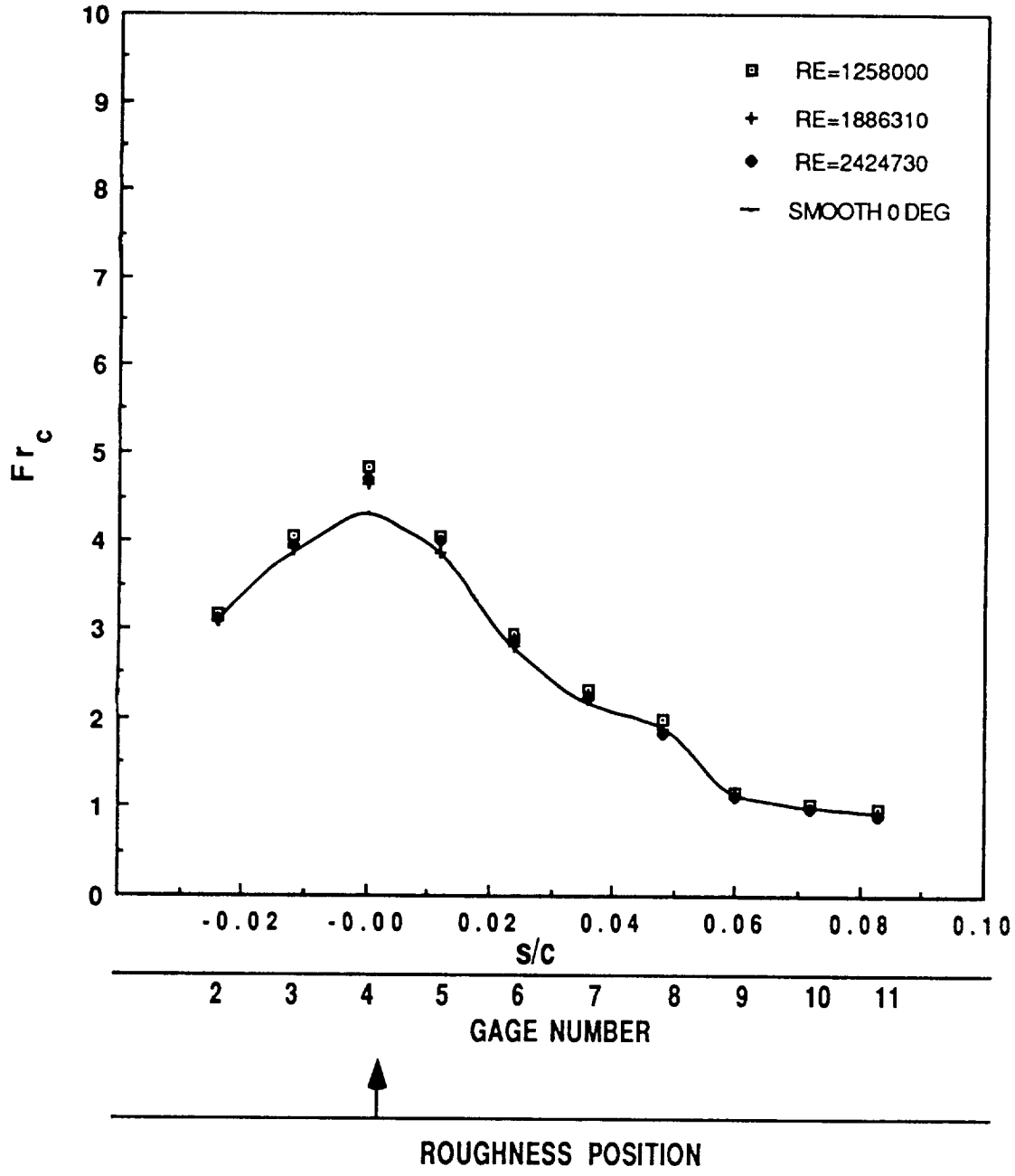

Figure 16. Frossling Number versus dimensionless surface distance: leading edge roughness, 0 degree angle of attack, flight data.

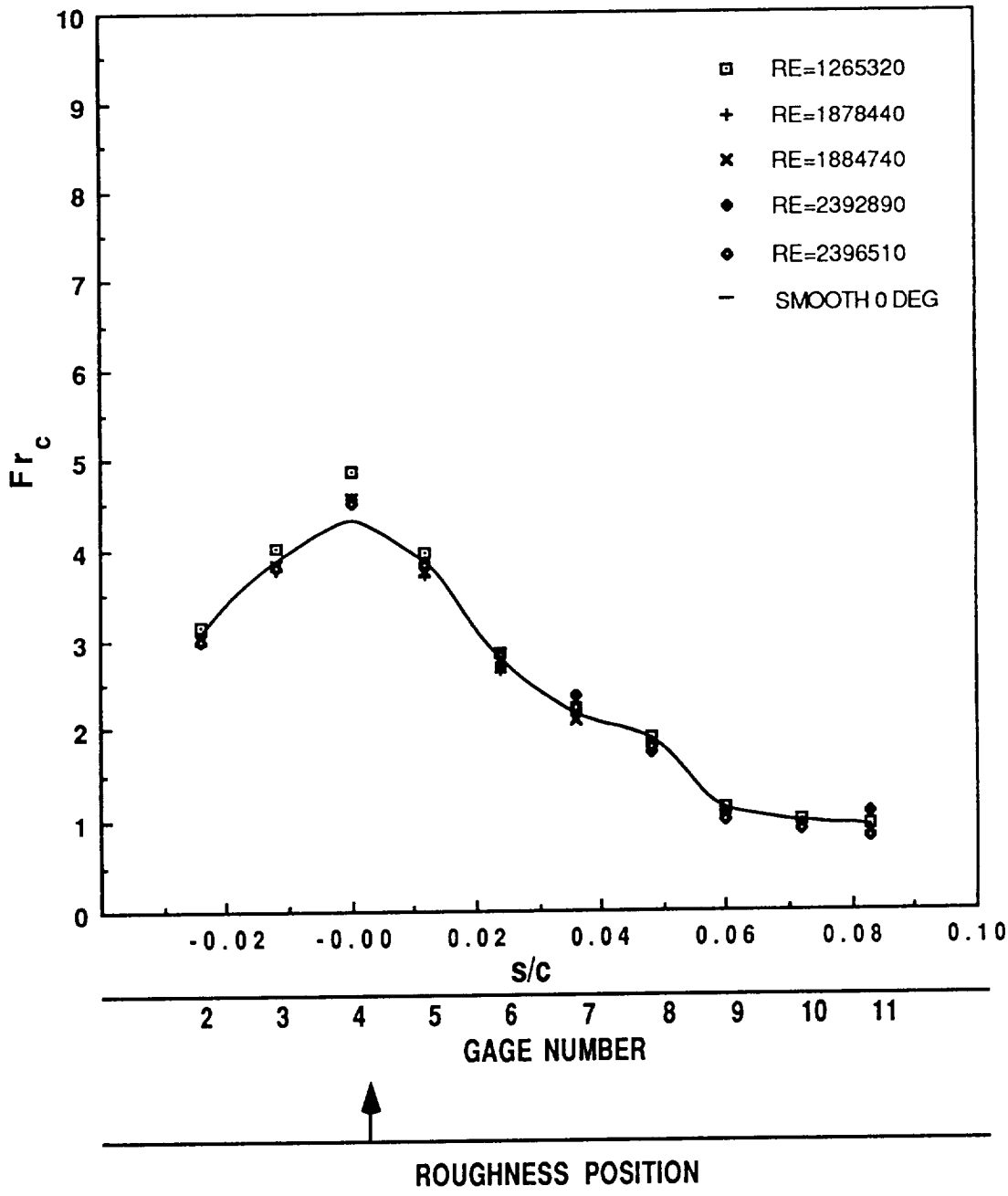

Figure 17. Frossling Number versus dimensionless surface distance: leading edge roughness, 2 degree angle of attack, flight data.

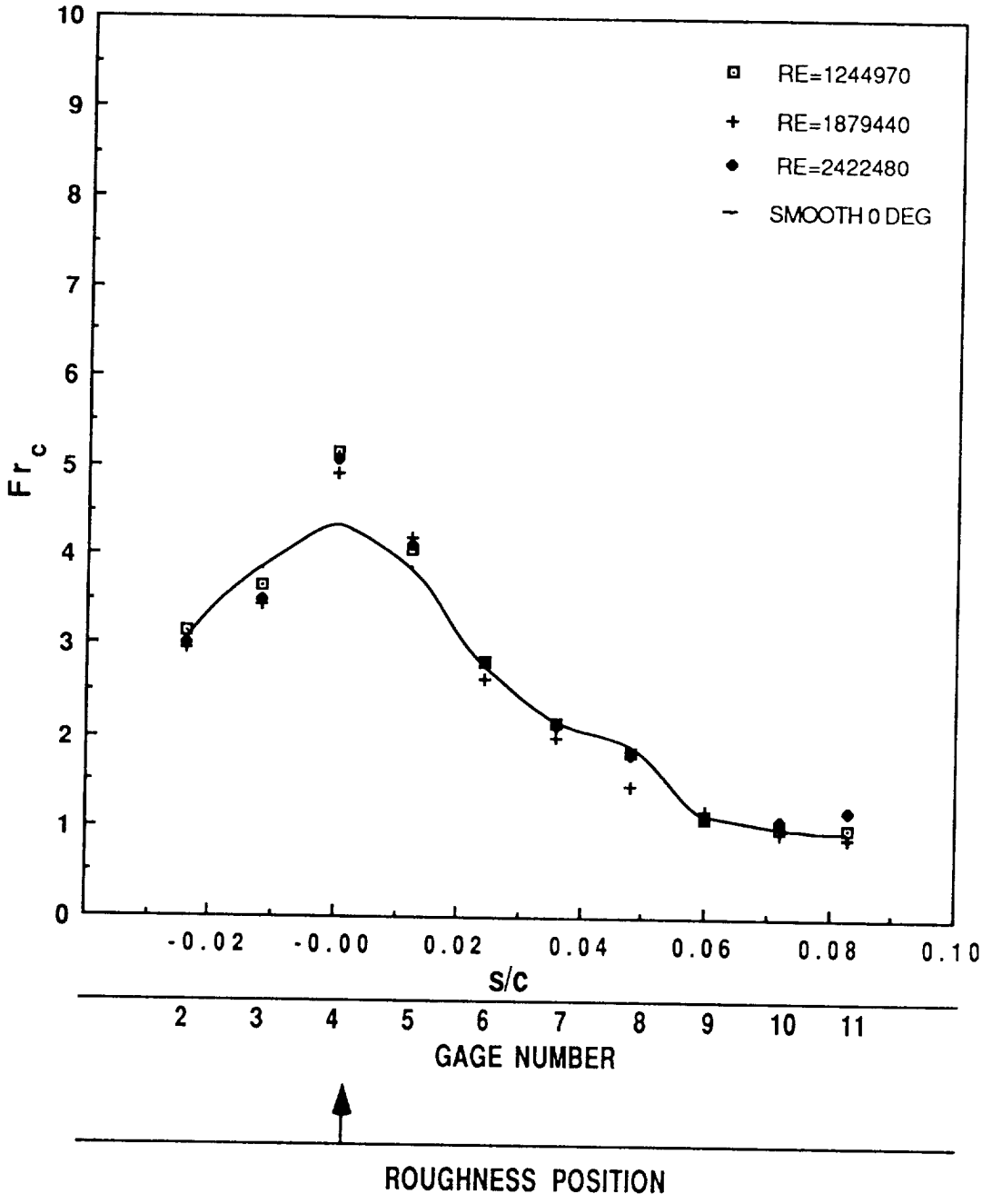

Figure 18. Frossling Number versus dimensionless surface distance: leading edge roughness, 4 degree angle of attack, flight data.

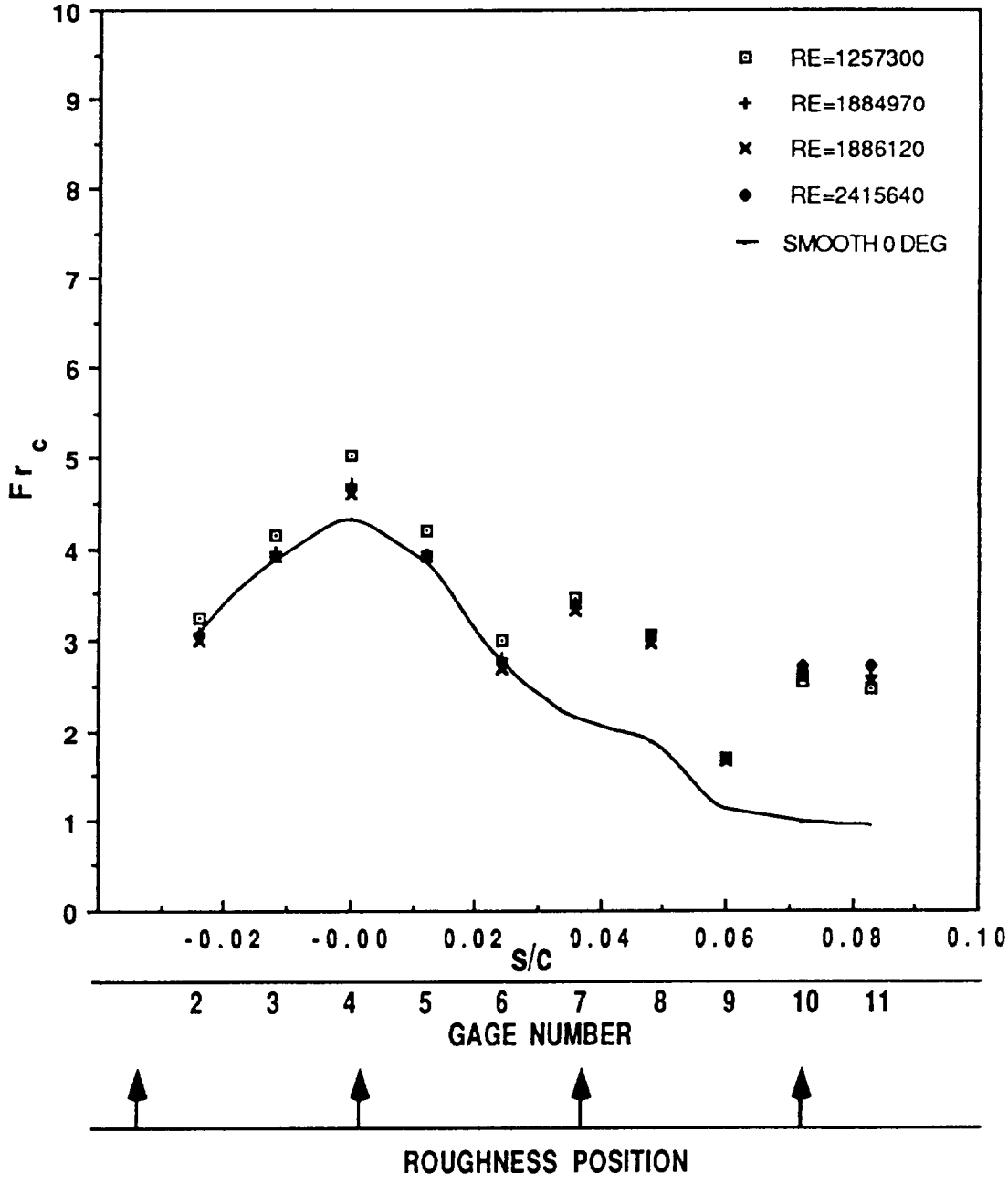

Figure 19. Frossling Number versus dimensionless surface distance: sparse roughness, 0 degree angle of attack, flight data.

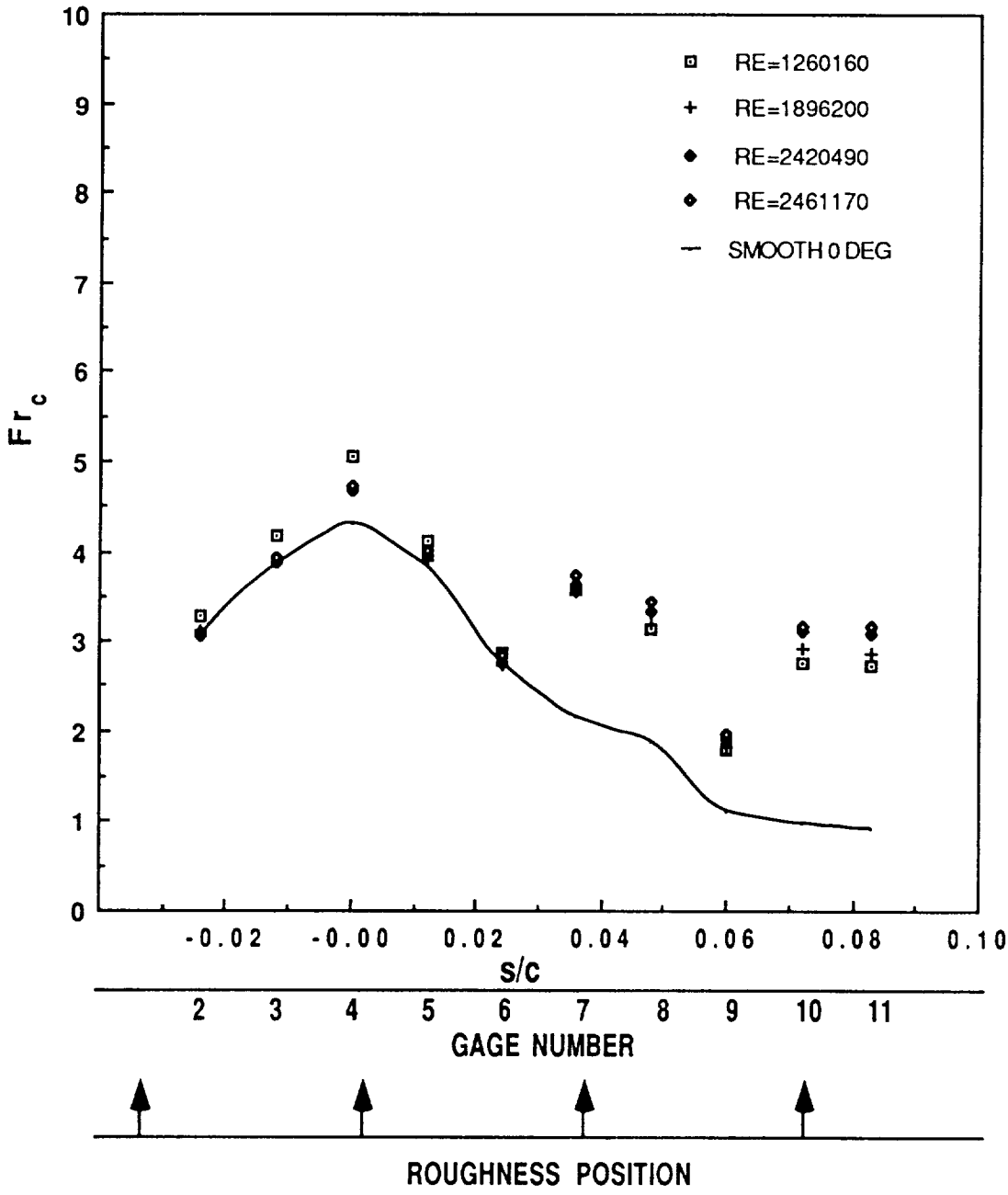

Figure 20. Frossling Number versus dimensionless surface distance: sparse roughness, 2 degree angle of attack, flight data.

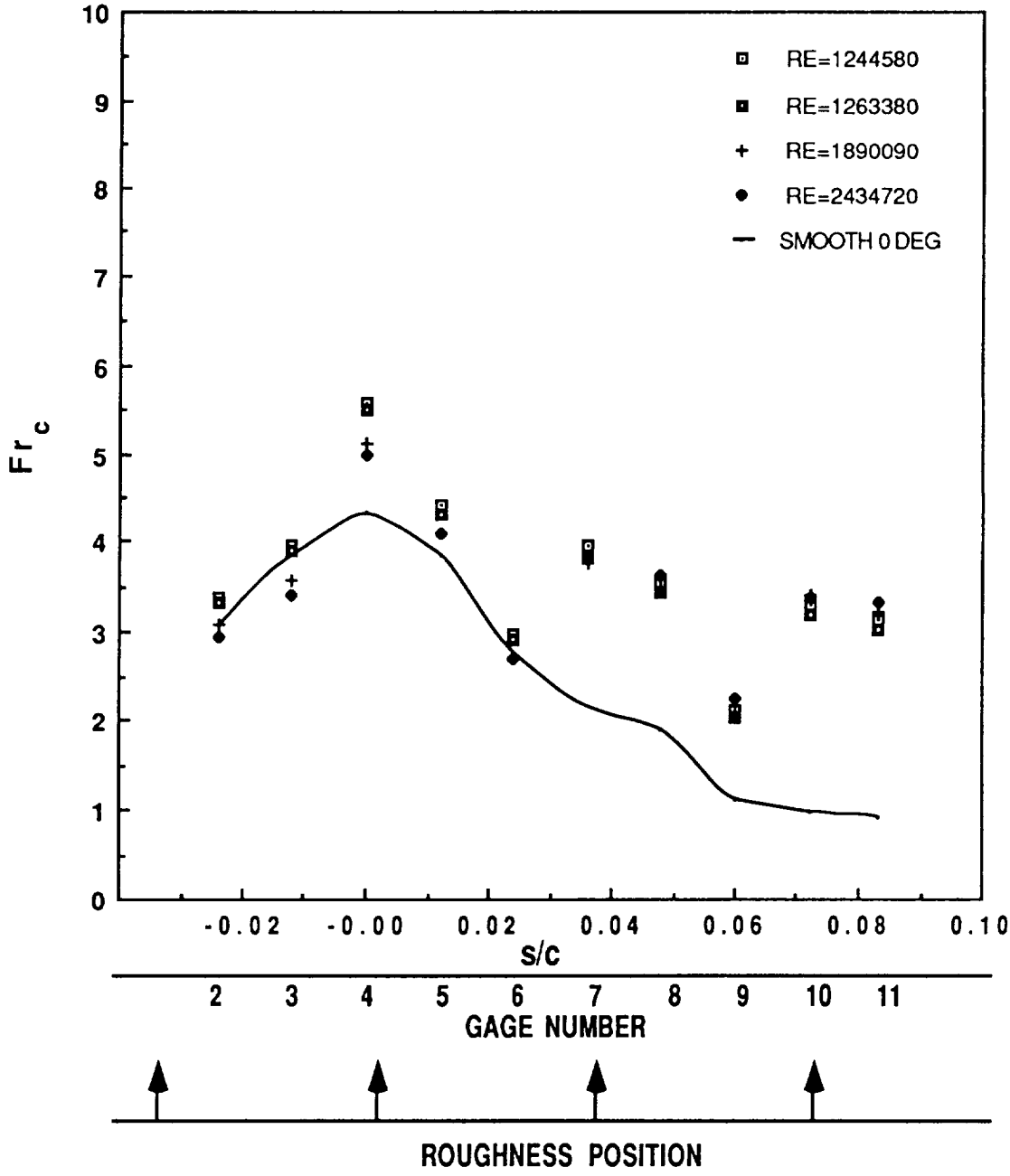

Figure 21. Frossling Number versus dimensionless surface distance: sparse roughness, 4 degree angle of attack, flight data.

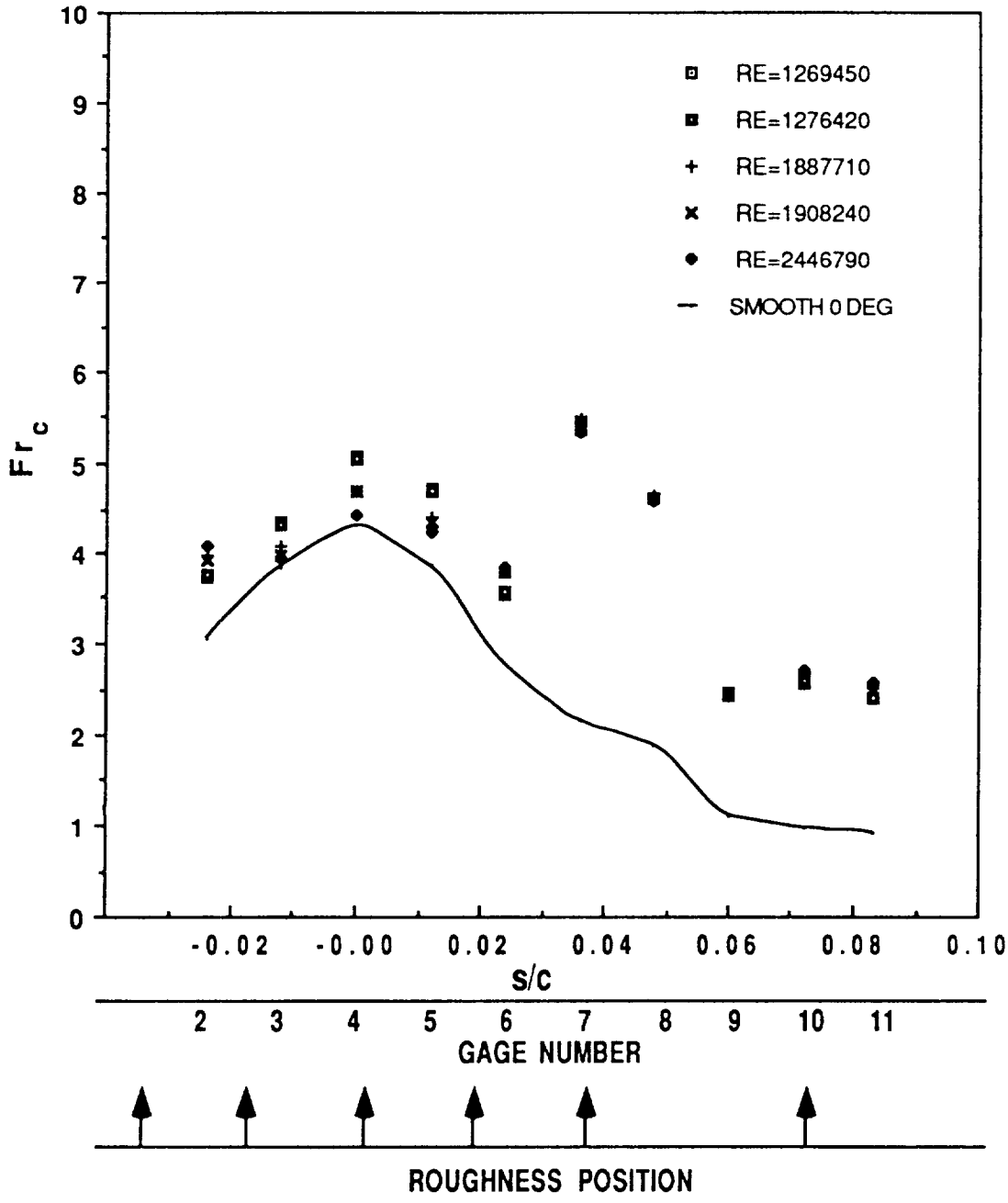

Figure 22. Frossling Number versus dimensionless surface distance: dense 1 roughness, 0 degree angle of attack, flight data.

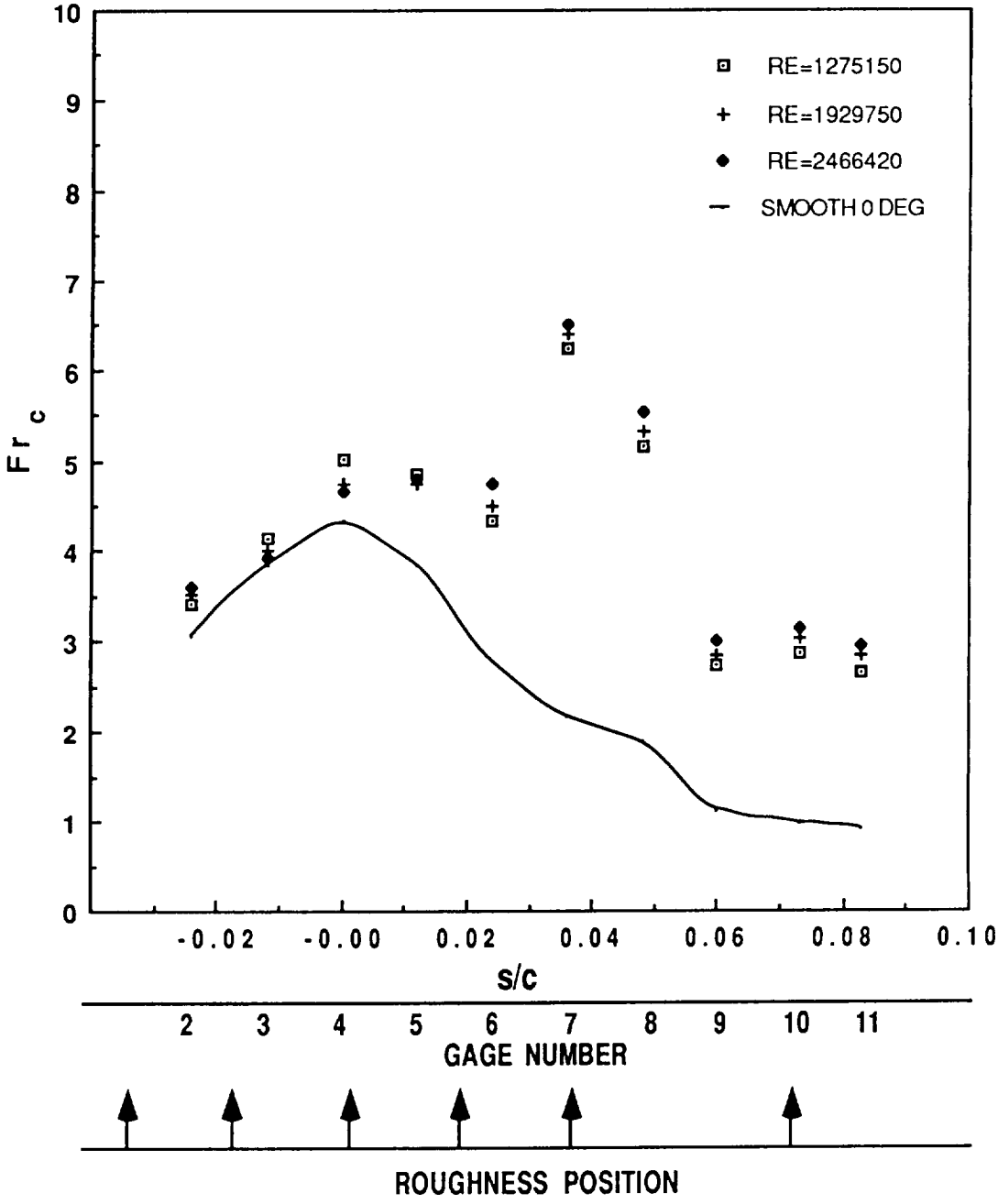

Figure 23. Frossling Number versus dimensionless surface distance: dense 1 roughness, 2 degree angle of attack, flight data.

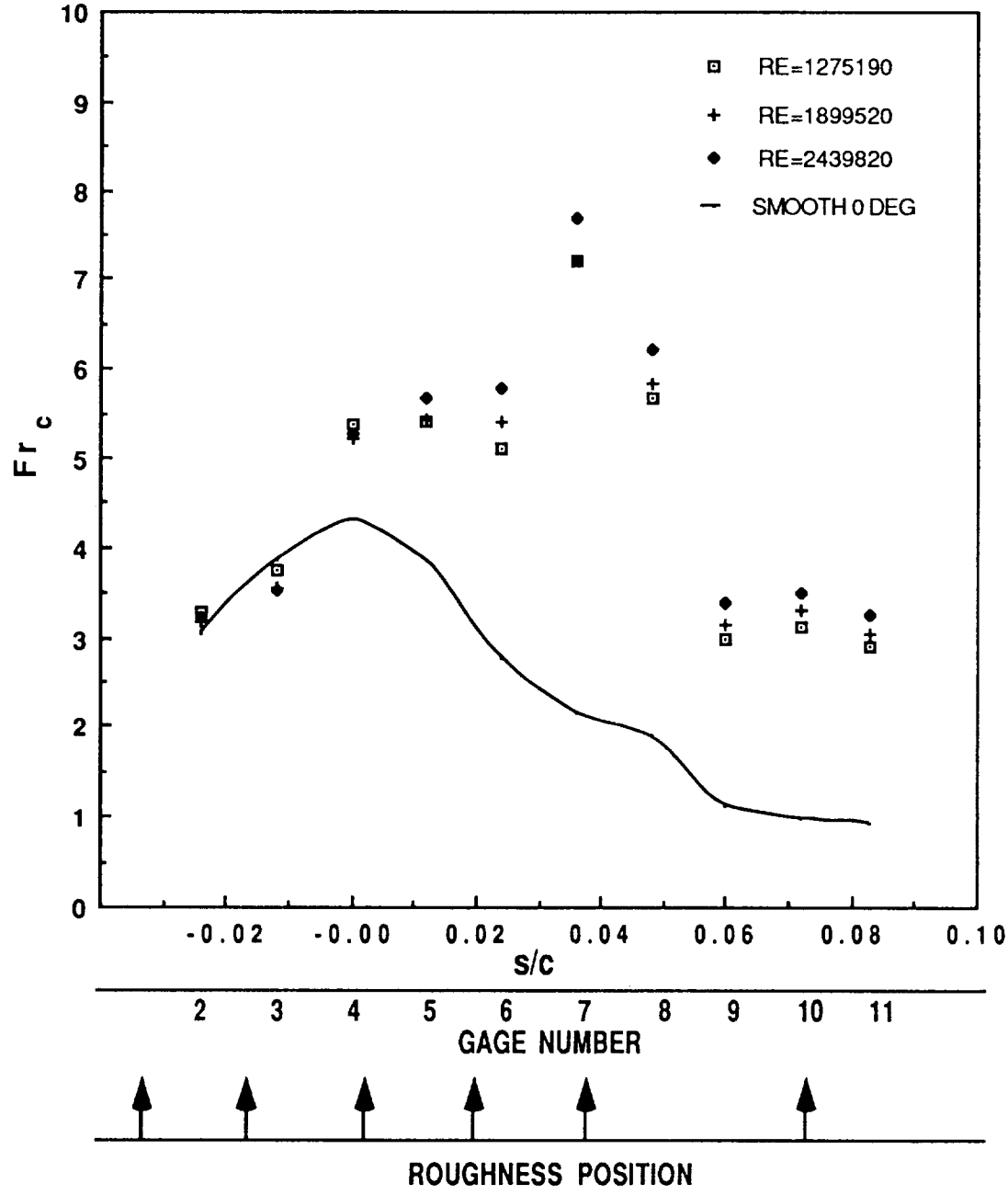

Figure 24. Frossling Number versus dimensionless surface distance: dense 1 roughness, 4 degree angle of attack, flight data.

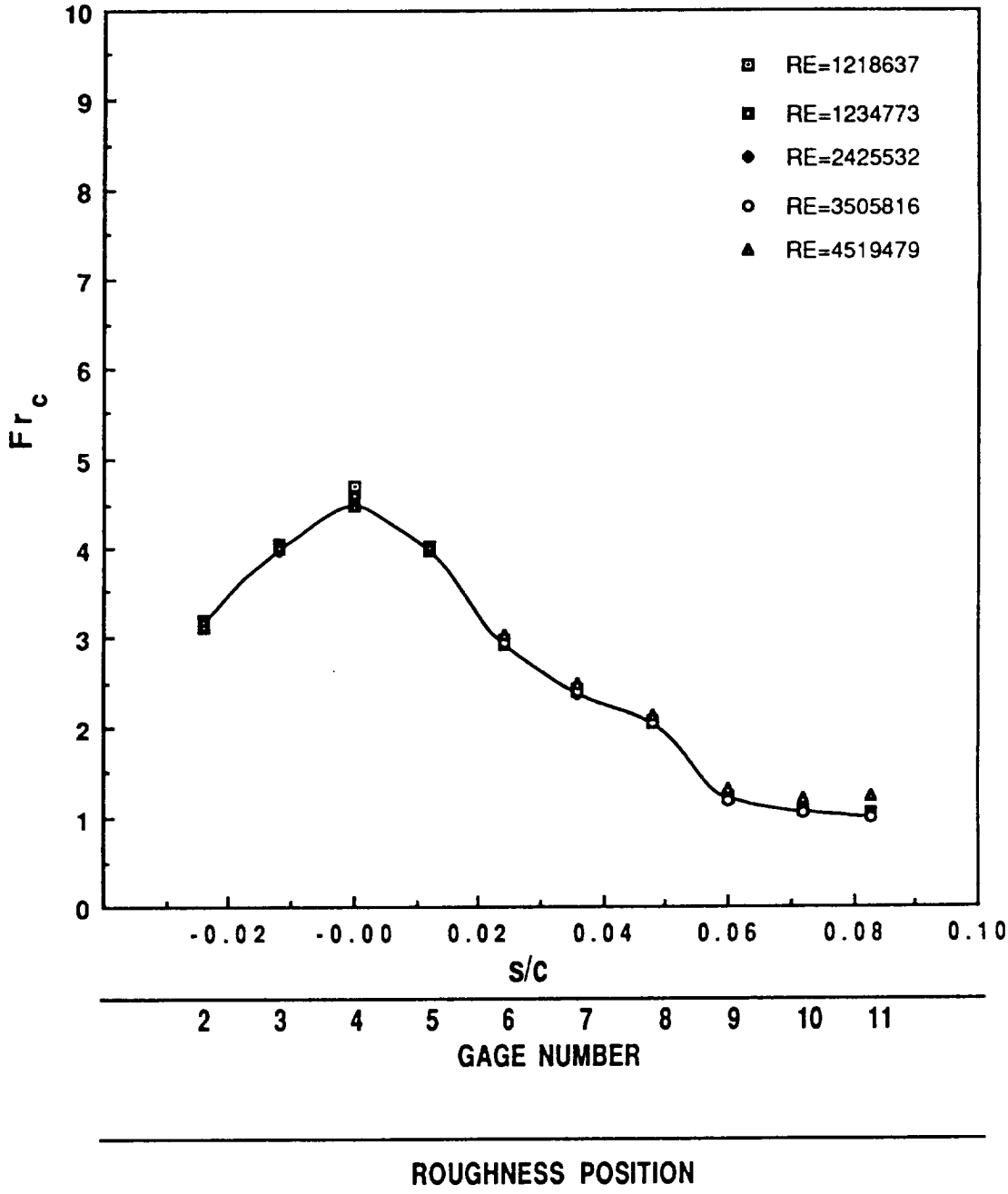

Figure 25. Frossling Number versus dimensionless surface distance: smooth airfoil, 0 degree angle of attack, no spray air, IRT data.

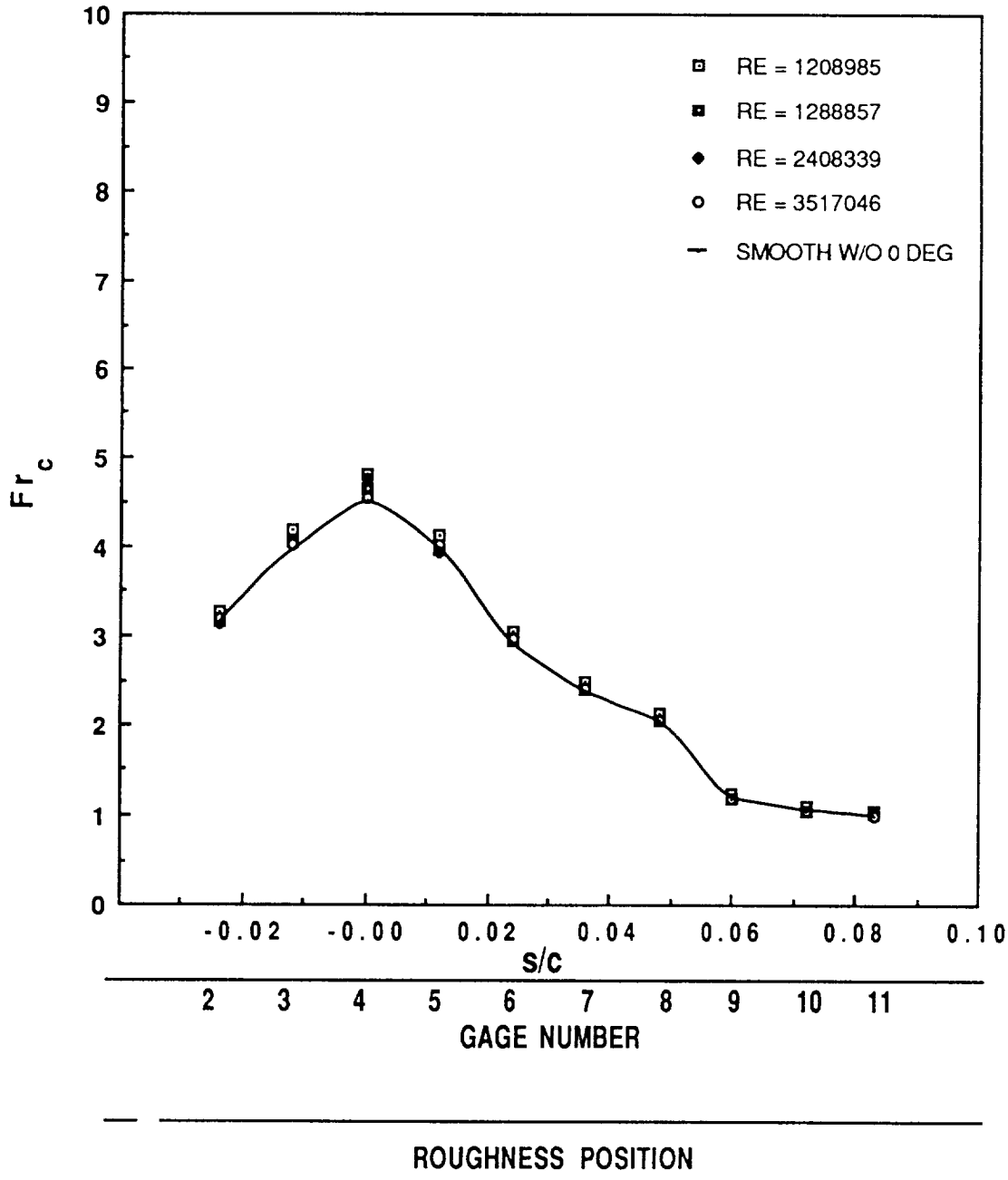

Figure 26. Frossling Number versus dimensionless surface distance: smooth airfoil, 0 degree angle of attack, with spray air, IRT data.

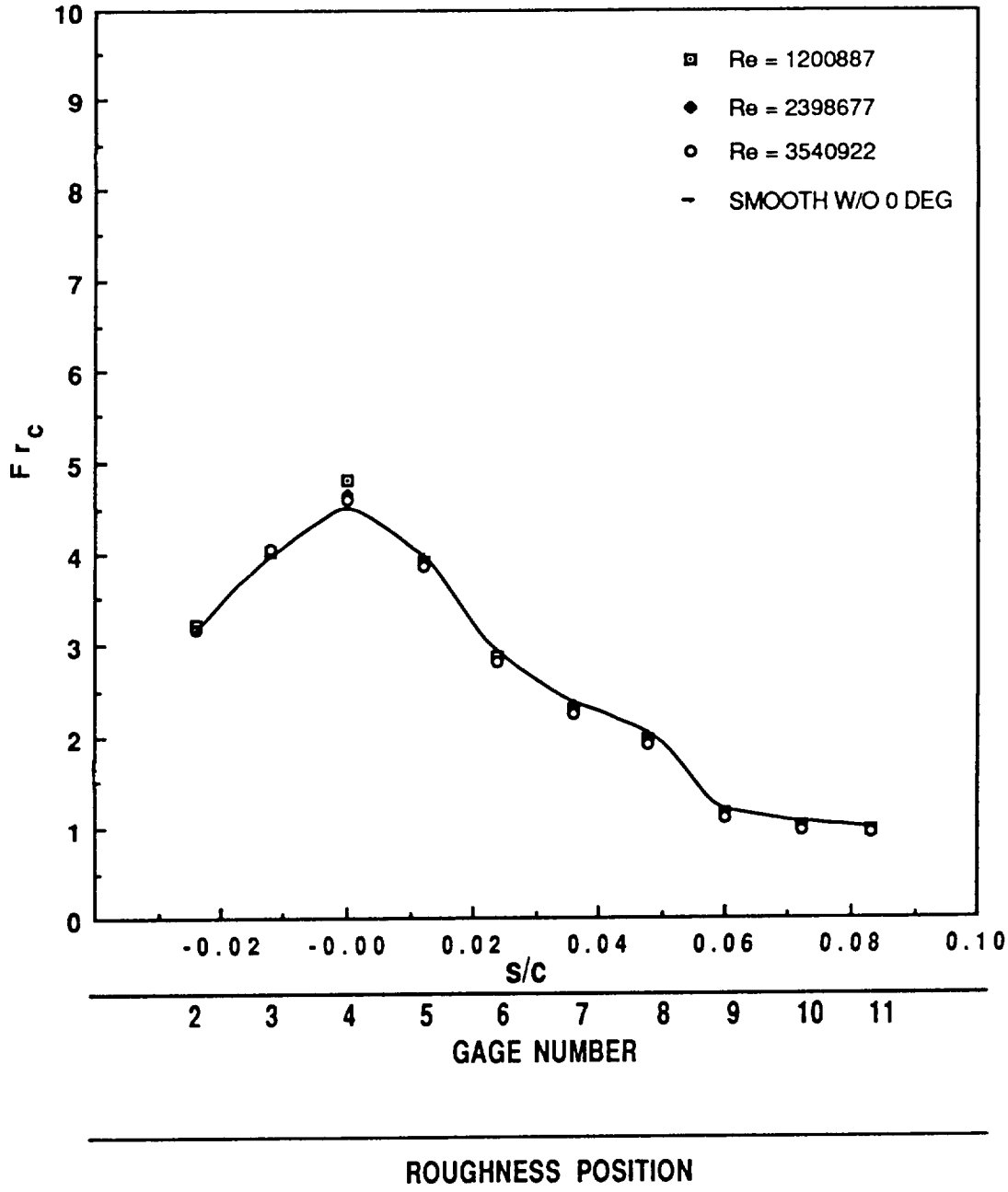

Figure 27. Frossling Number versus dimensionless surface distance: smooth airfoil, 2 degree angle of attack, no spray air, IRT data.

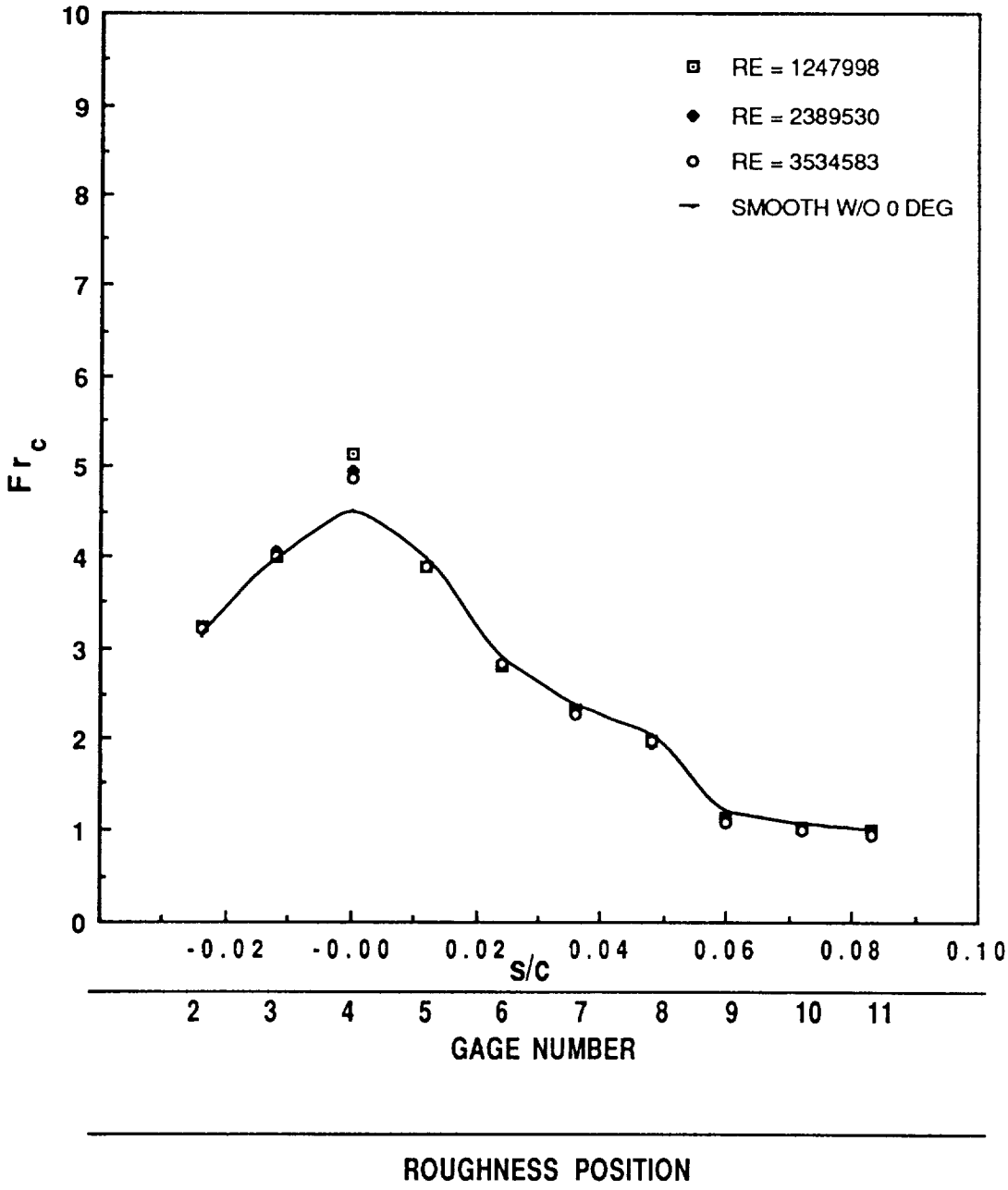

Figure 28. Frossling Number versus dimensionless sureace distance: smooth airfoil, 2 degree angle of attack, with spray air, IRT data.

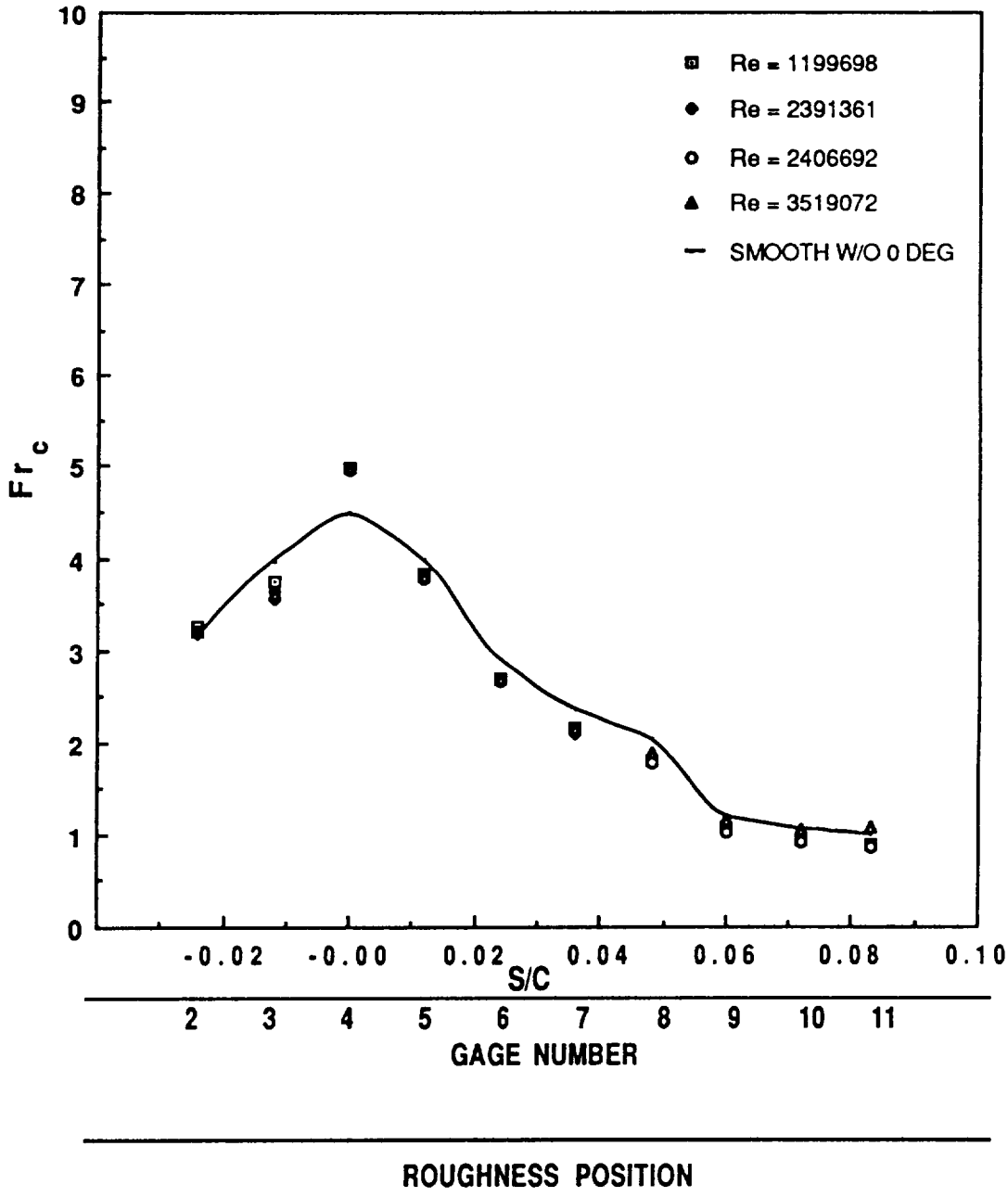

Figure 29. Frossling Number versus dimensionless surface distance: smooth airfoil, 4 degree angle of attack, no spray air, IRT data.

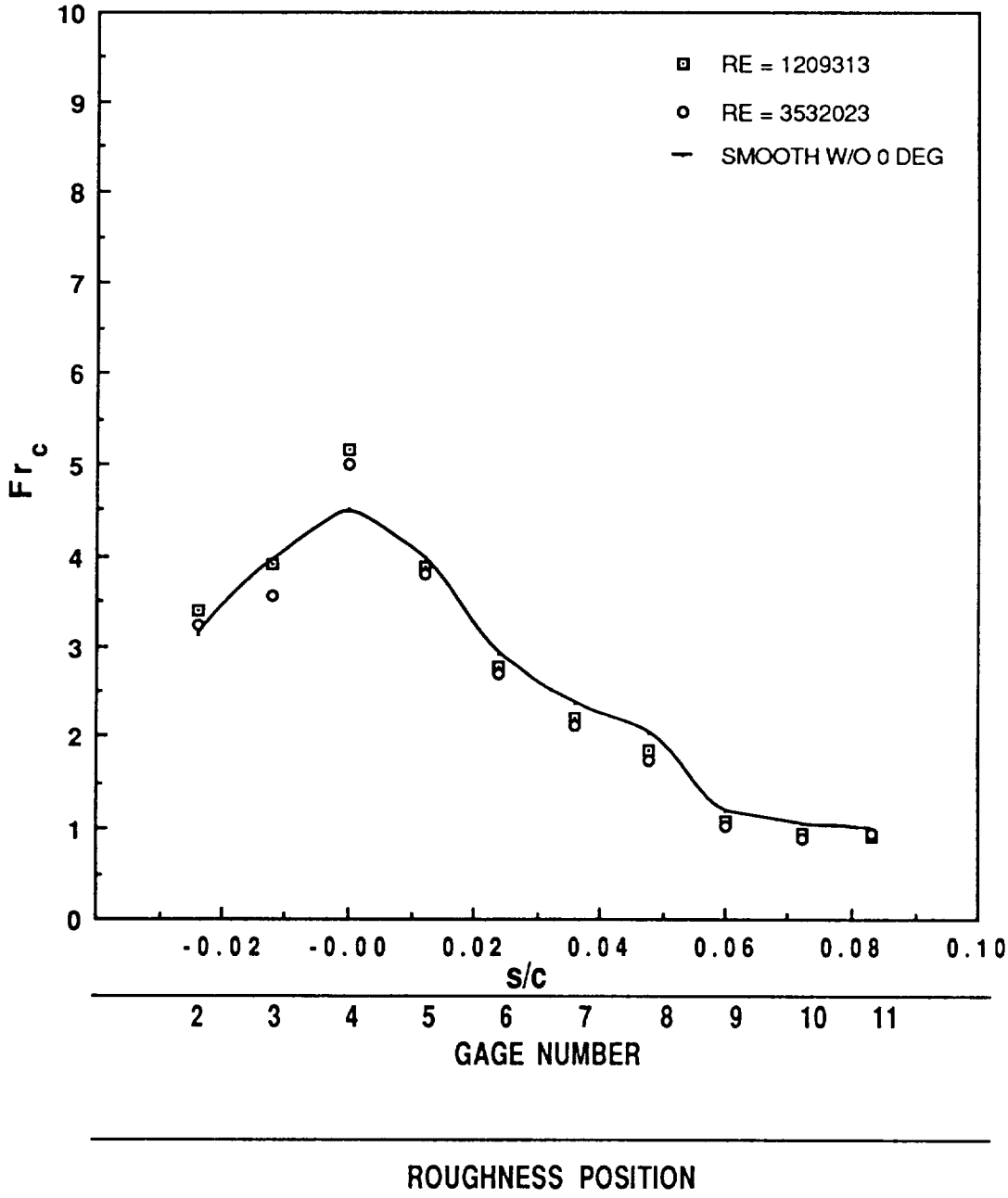

Figure 30. Frossling Number versus dimensionless surface distance: smooth airfoil, 4 degree angle of attack, with spray air, IRT data.

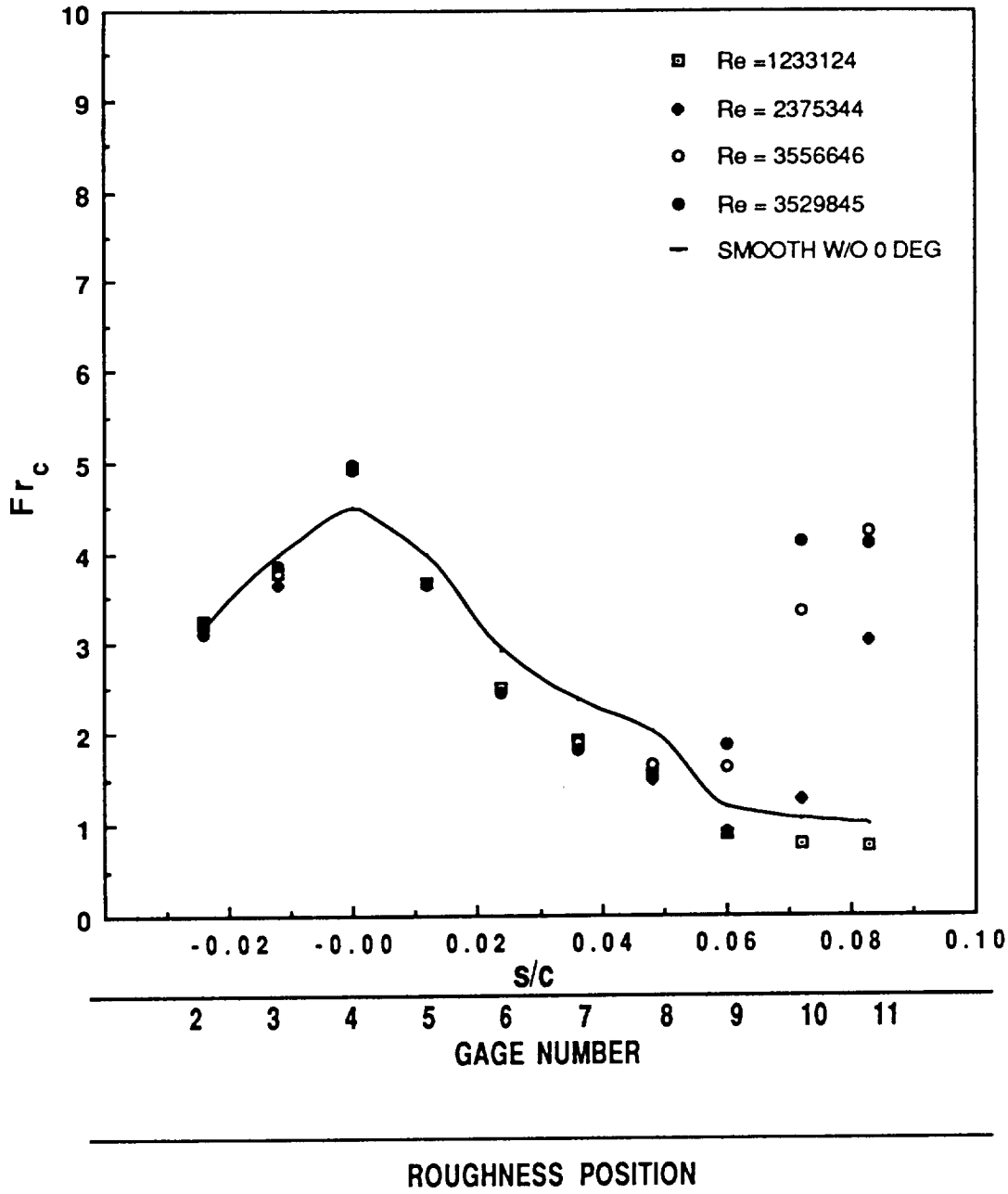

Figure 31. Frossling Number versus dimensionless surface distance: smooth airfoil, 6 degree angle of attack, no spray air, IRT data.

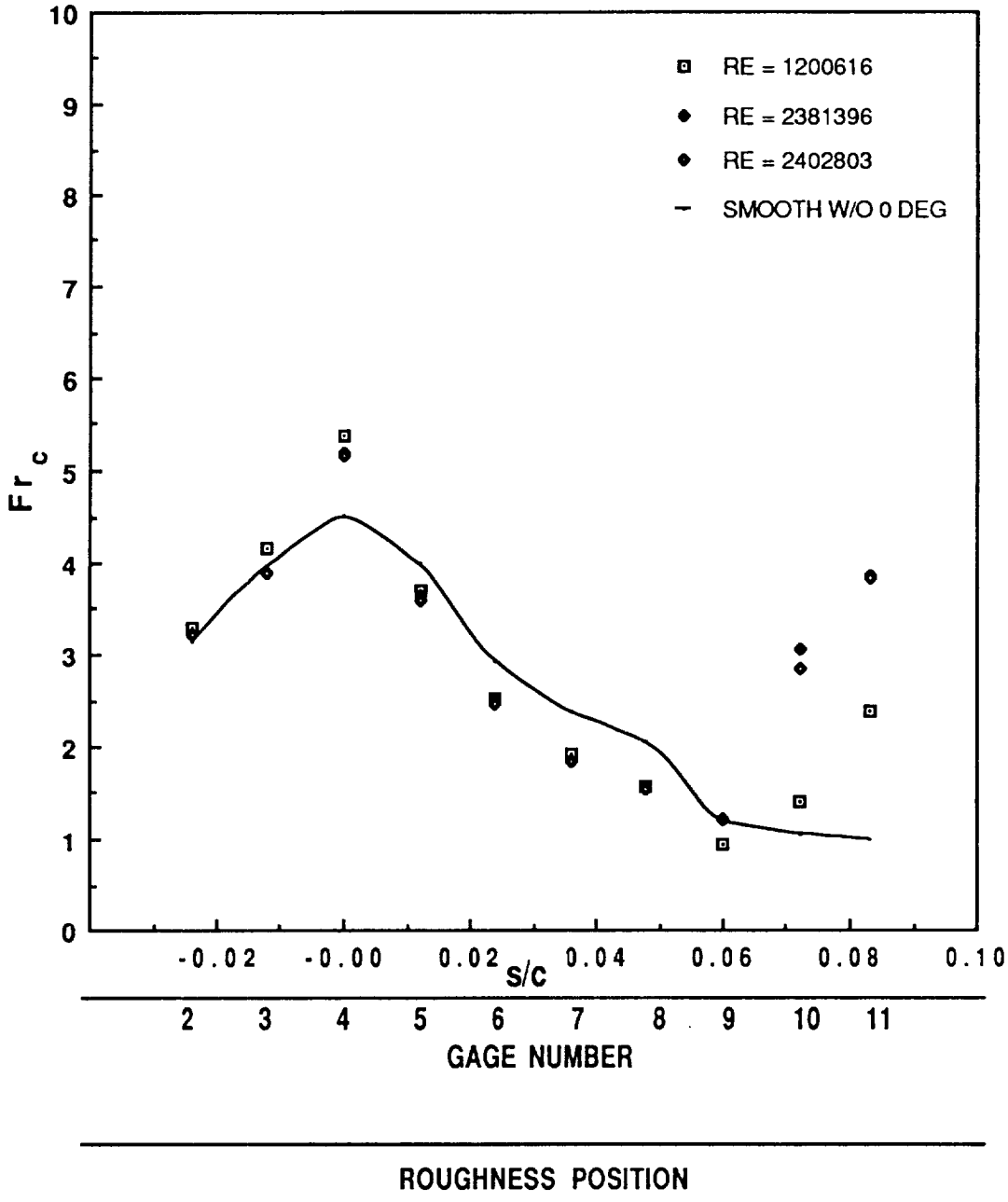

Figure 32. Frossling Number versus dimensionless surface distance: smooth airfoil, 6 degree angle of attack, with spray air, IRT data.

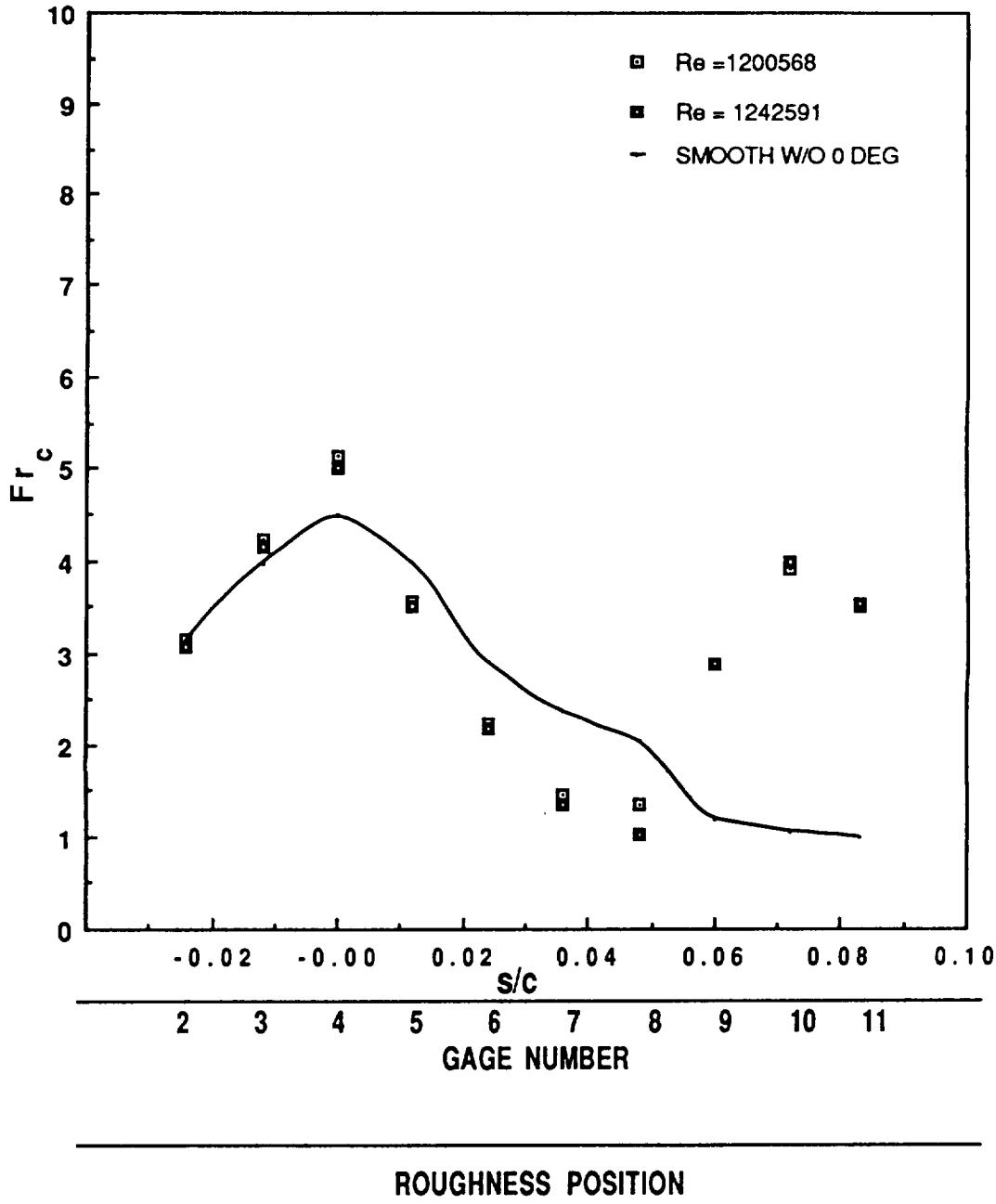

Figure 33. Frossling Number versus dimensionless surface distance: smooth airfoil, 8 degree angle of attack, no spray air, IRT data.

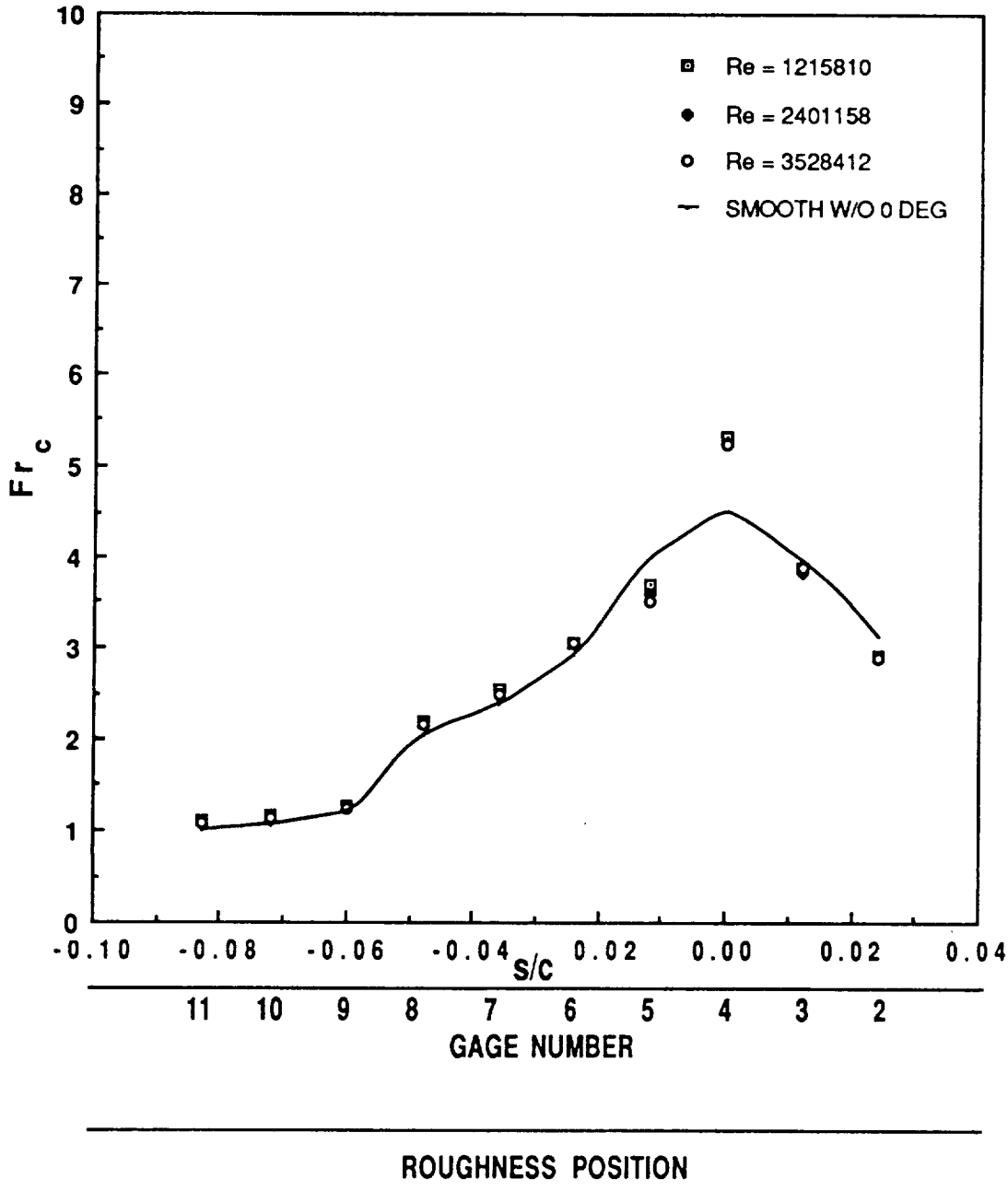

Figure 34. Frossling NUmber versus dimensionless surface distance: smooth airfoil, -4 degree angle of attack, no spray air, IRT data.

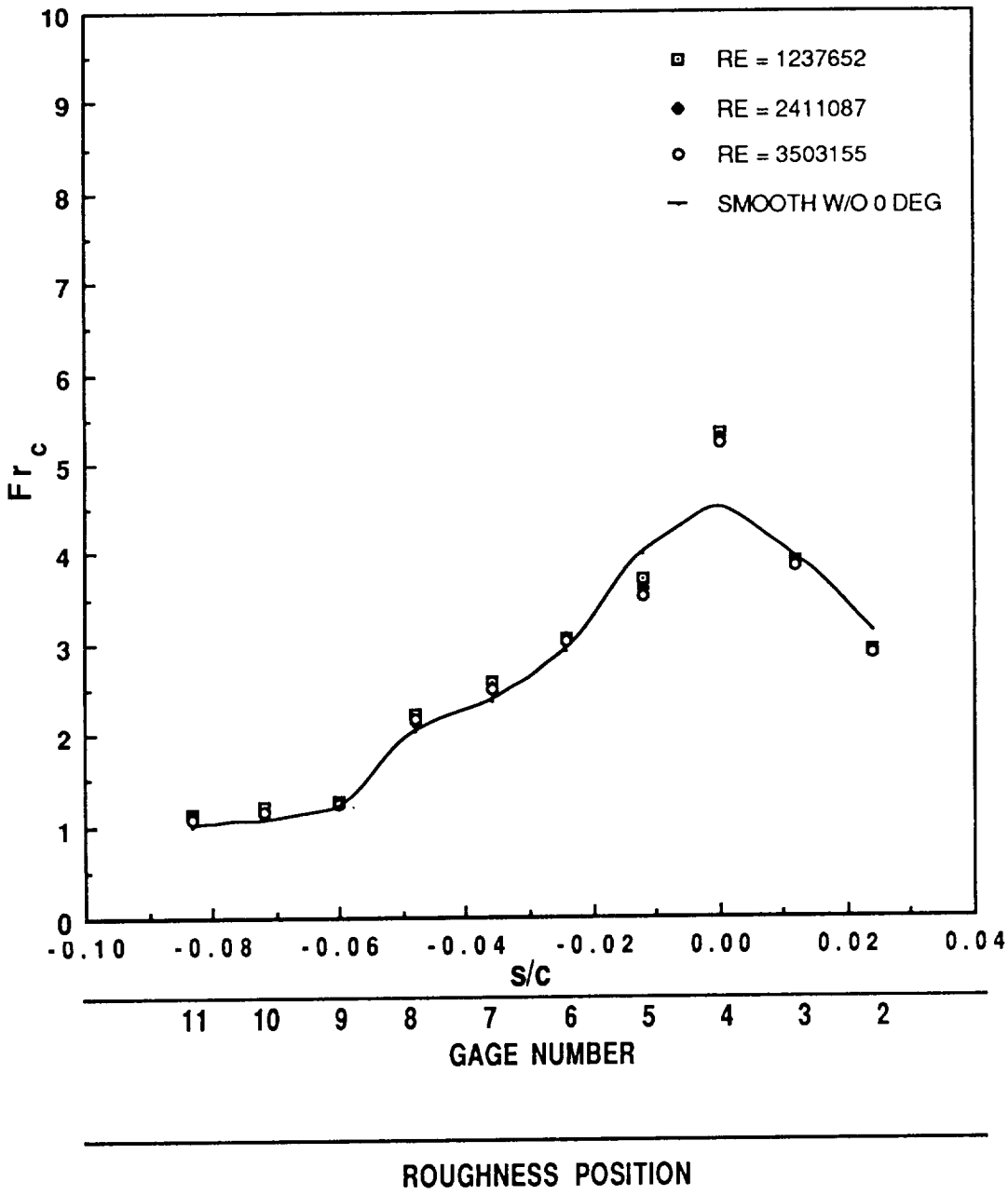

Figure 35. Frossling Number versus dimensionless surface distance: smooth airfoil, -4 degree angle of attack, with spray air, IRT data.

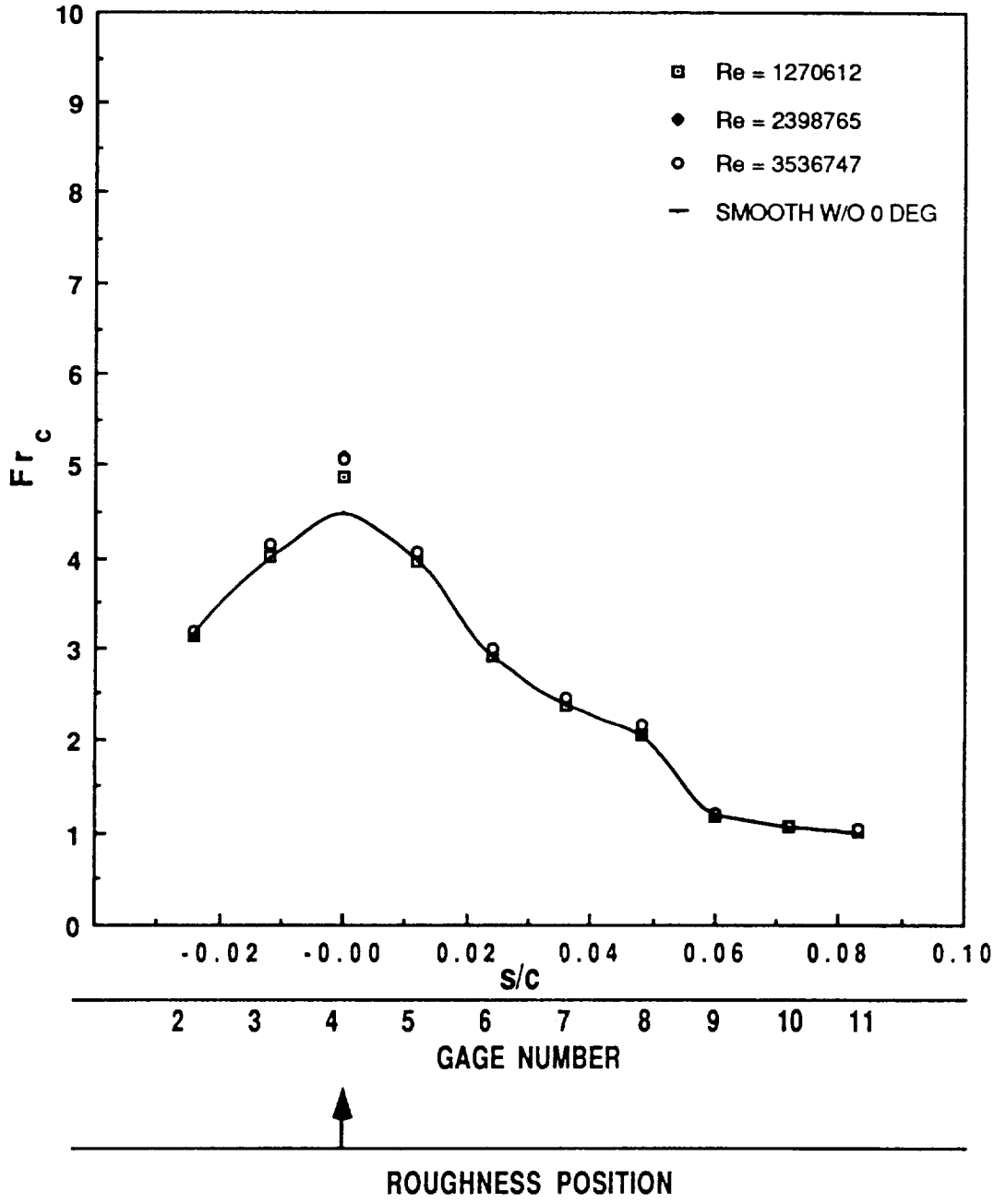

Figure 36. Frossling Number versus dimensionless surface distance: leading edge roughness, 0 degree angle of attack, no spray air, IRT data.

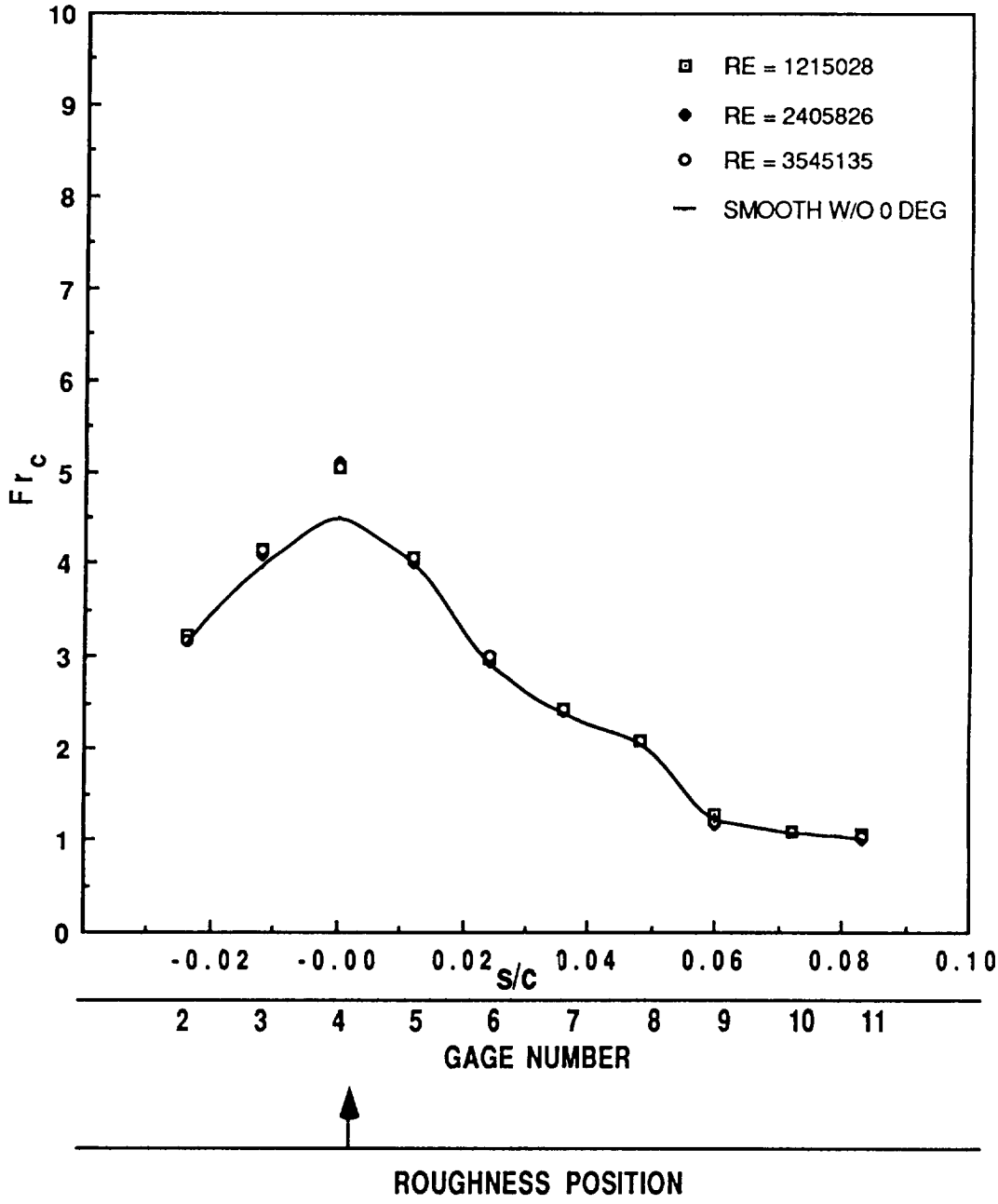

Figure 37. Frossling Number versus dimensionless surface distance: leading edge roughness, 0 degree angle of attack, with spray air, IRT data.

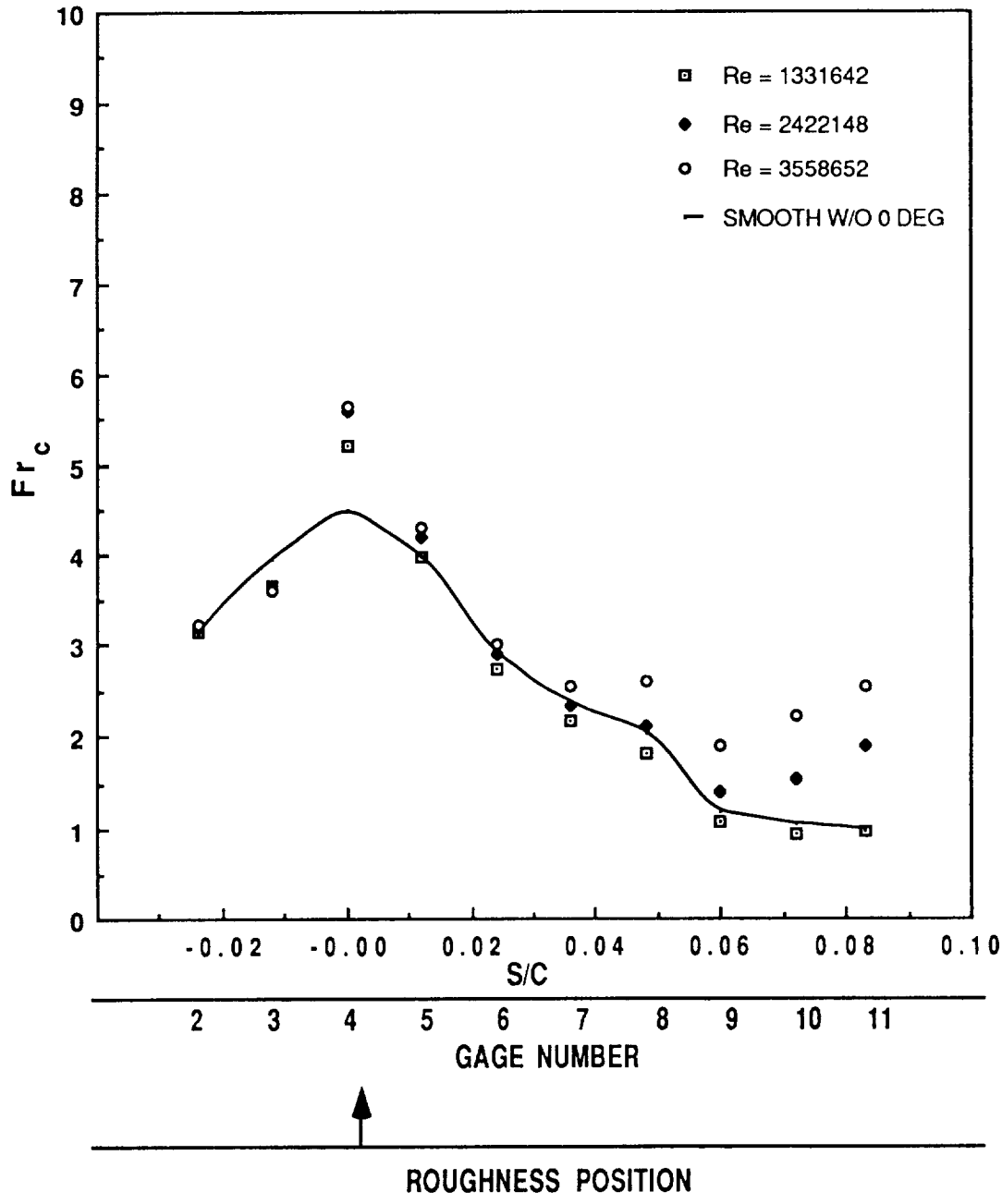

Figure 38. Frossling Number versus dimensionless surface distance: leading edge roughness, 4 degree angle of attack, no spray air, IRT data.

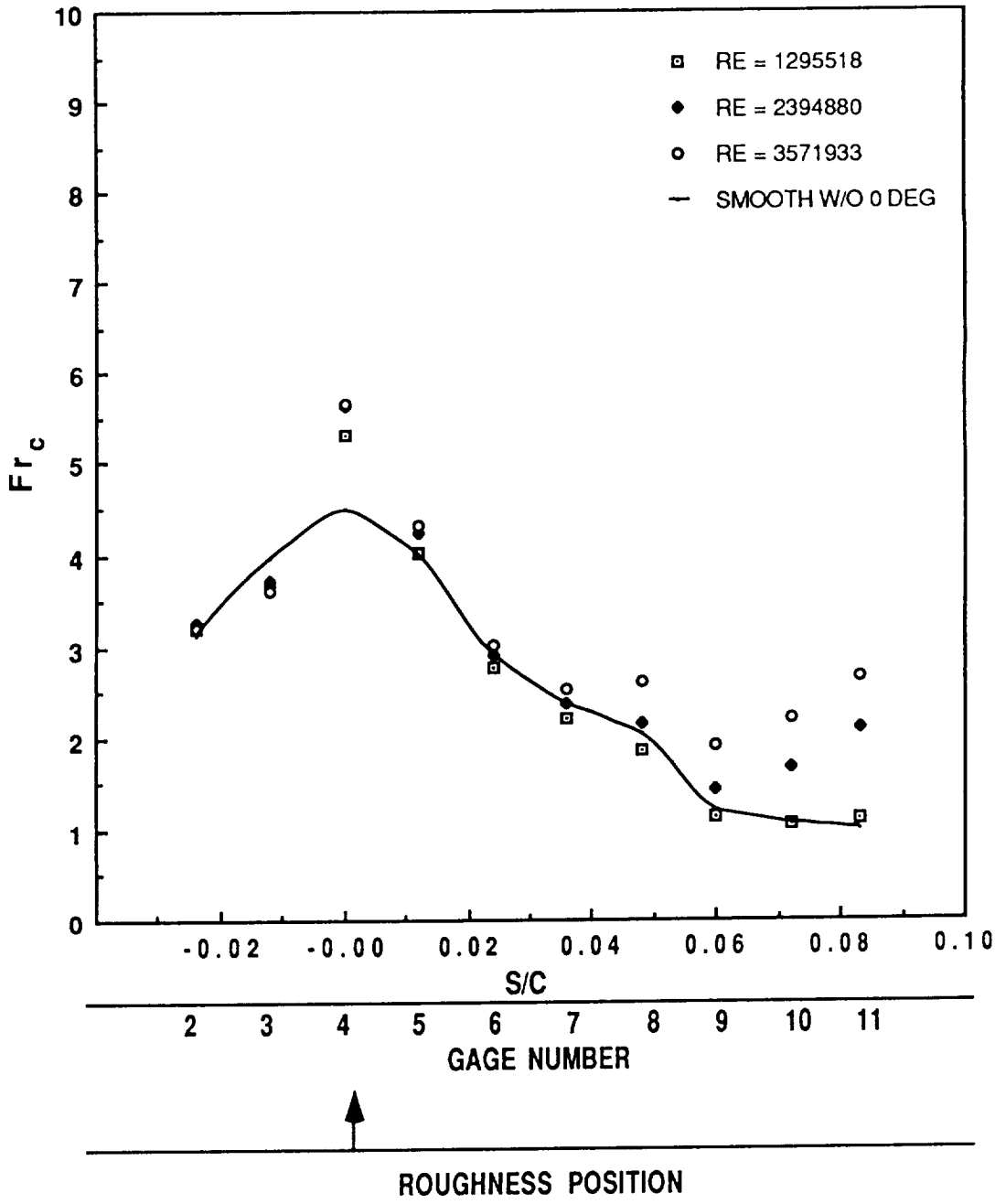

Figure 39. Frossling Number versus dimensionless surface distance: leading edge roughness, 4 degree angle of attack, with spray air, IRT data.

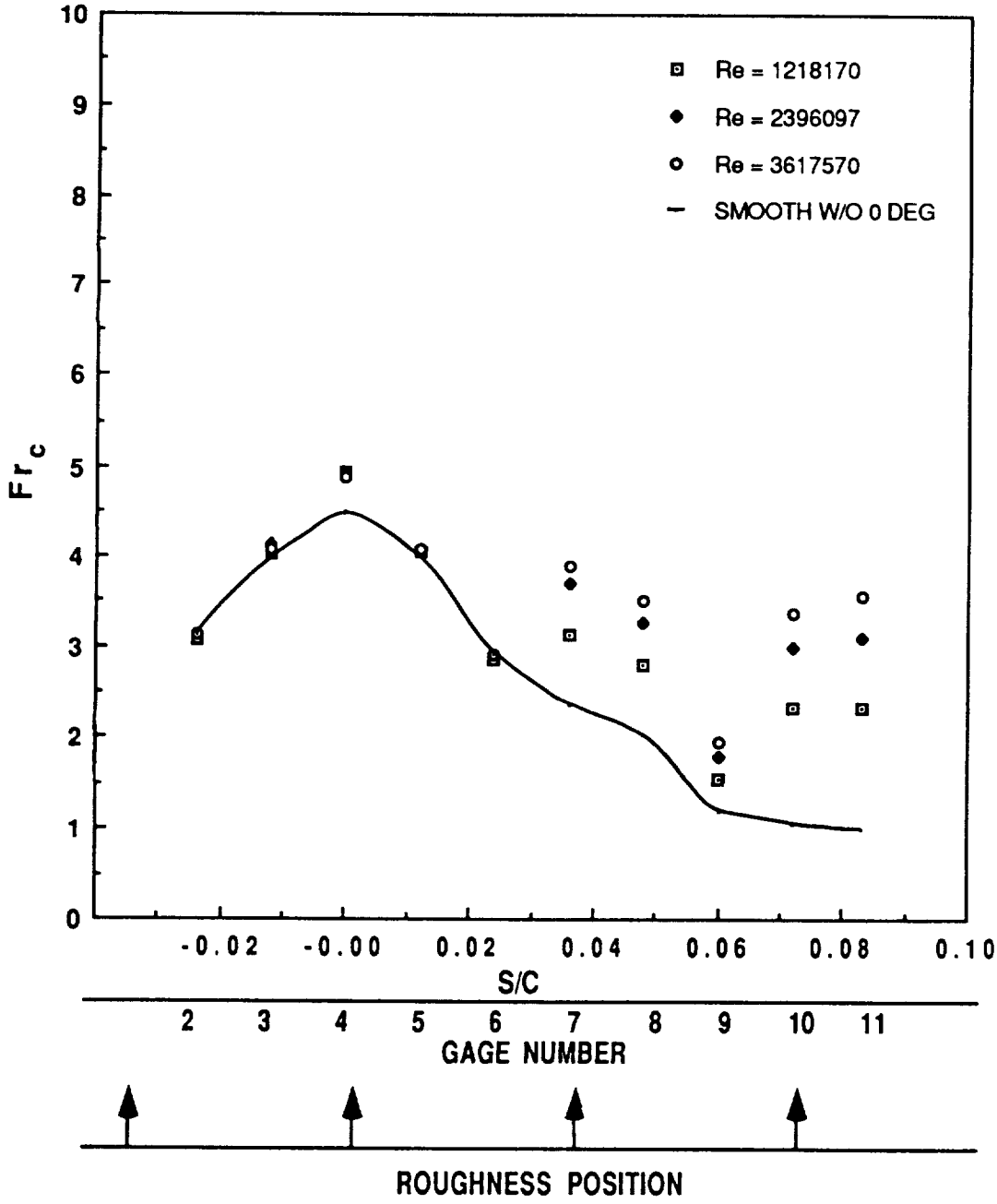

Figure 40. Frossling Number versus dimensionless surface distance: sparse roughness, 0 degree angle of attack, no spray air, IRT data.

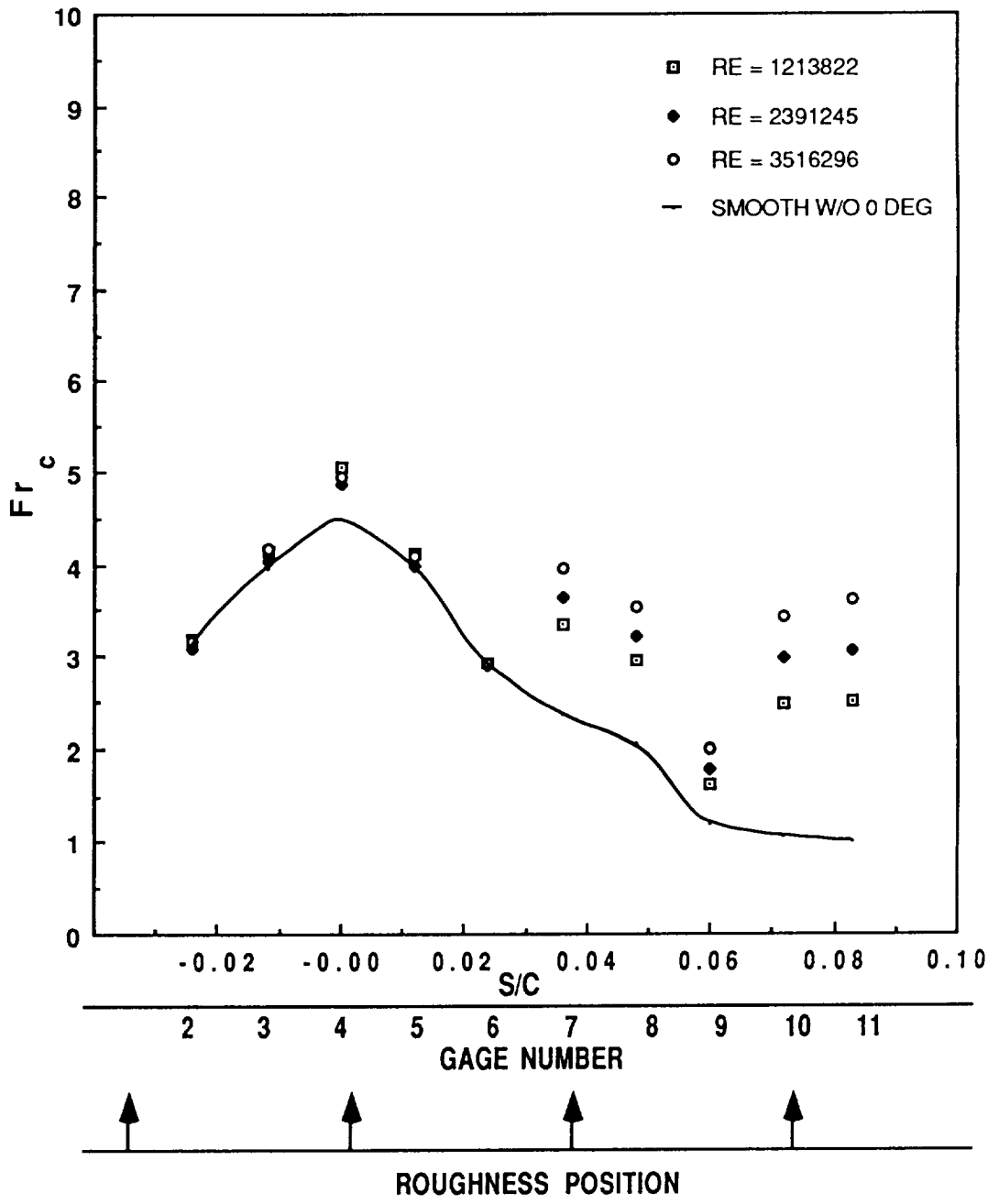

Figure 41. Frossling Number versus dimensionless surface distance: sparse roughness, 0 degree angle of attack, with spray air,IRT data.

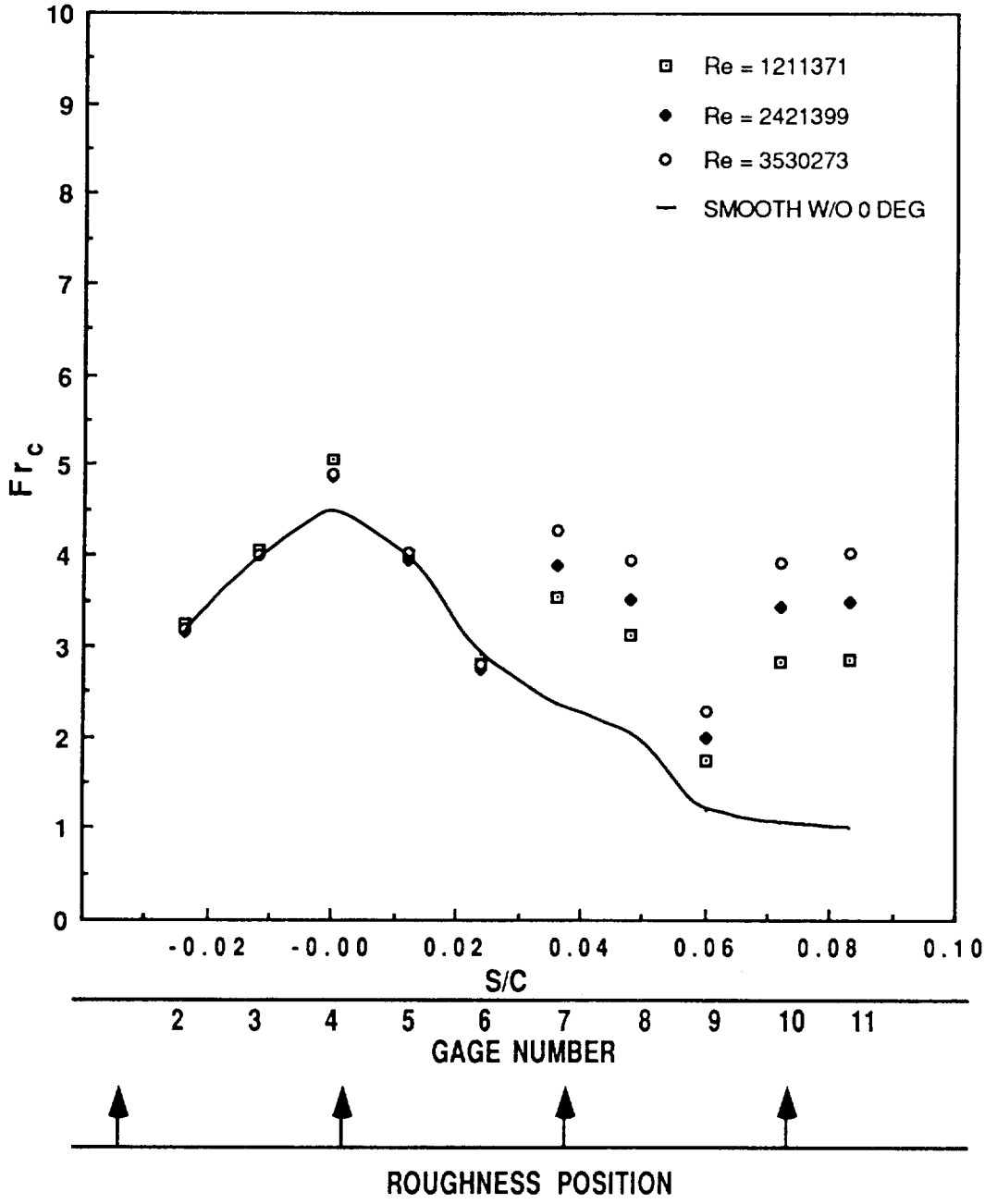

Figure 42. Frossling Number versus dimensionless surface distance: sparse roughness, 2 degree angle of attack, no spray air, IRT data.

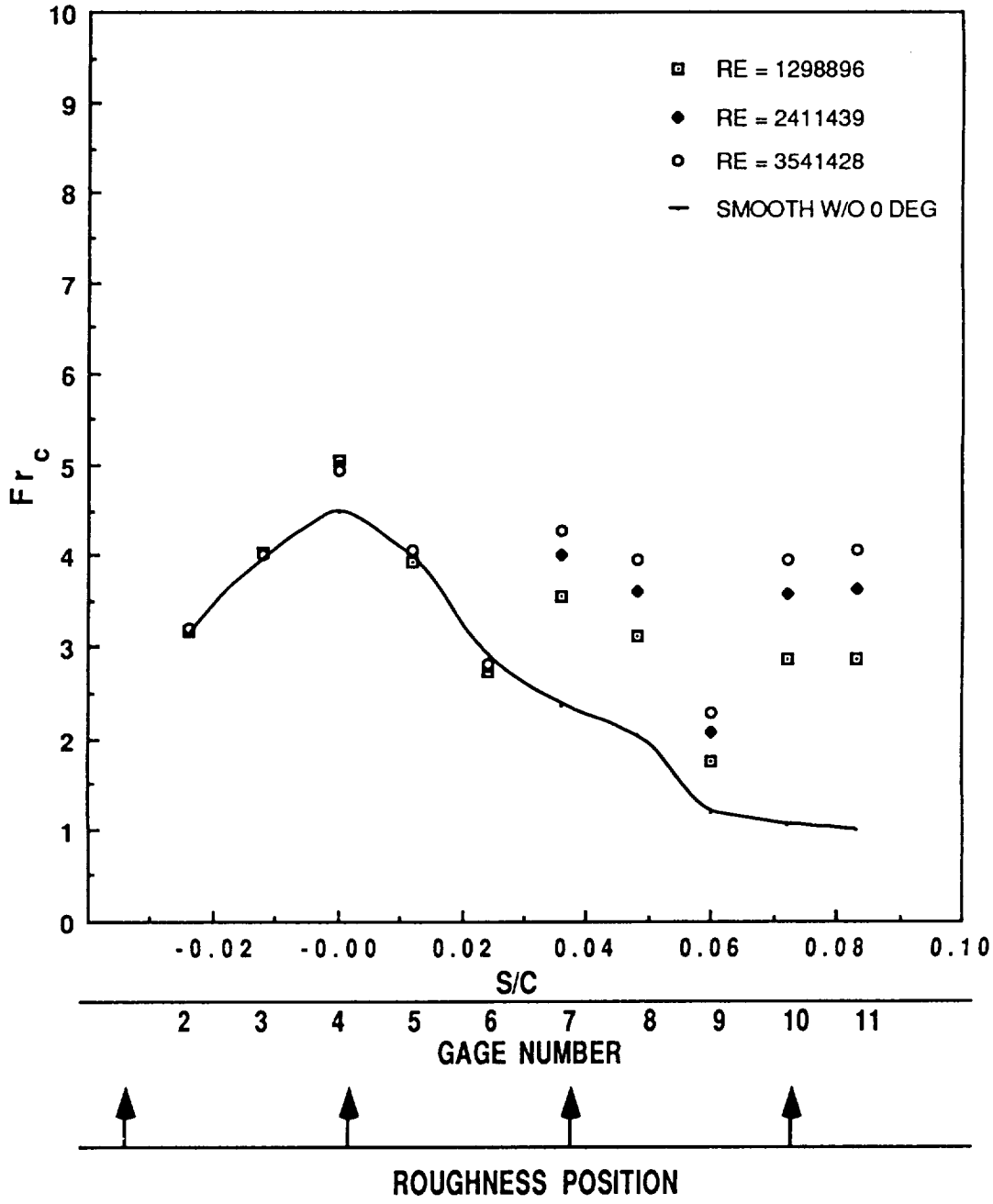

Figure 43. Frossling Number versus dimensionless surface distance: sparse roughness, 2 degree angle of attack, with spray air, IRT data.

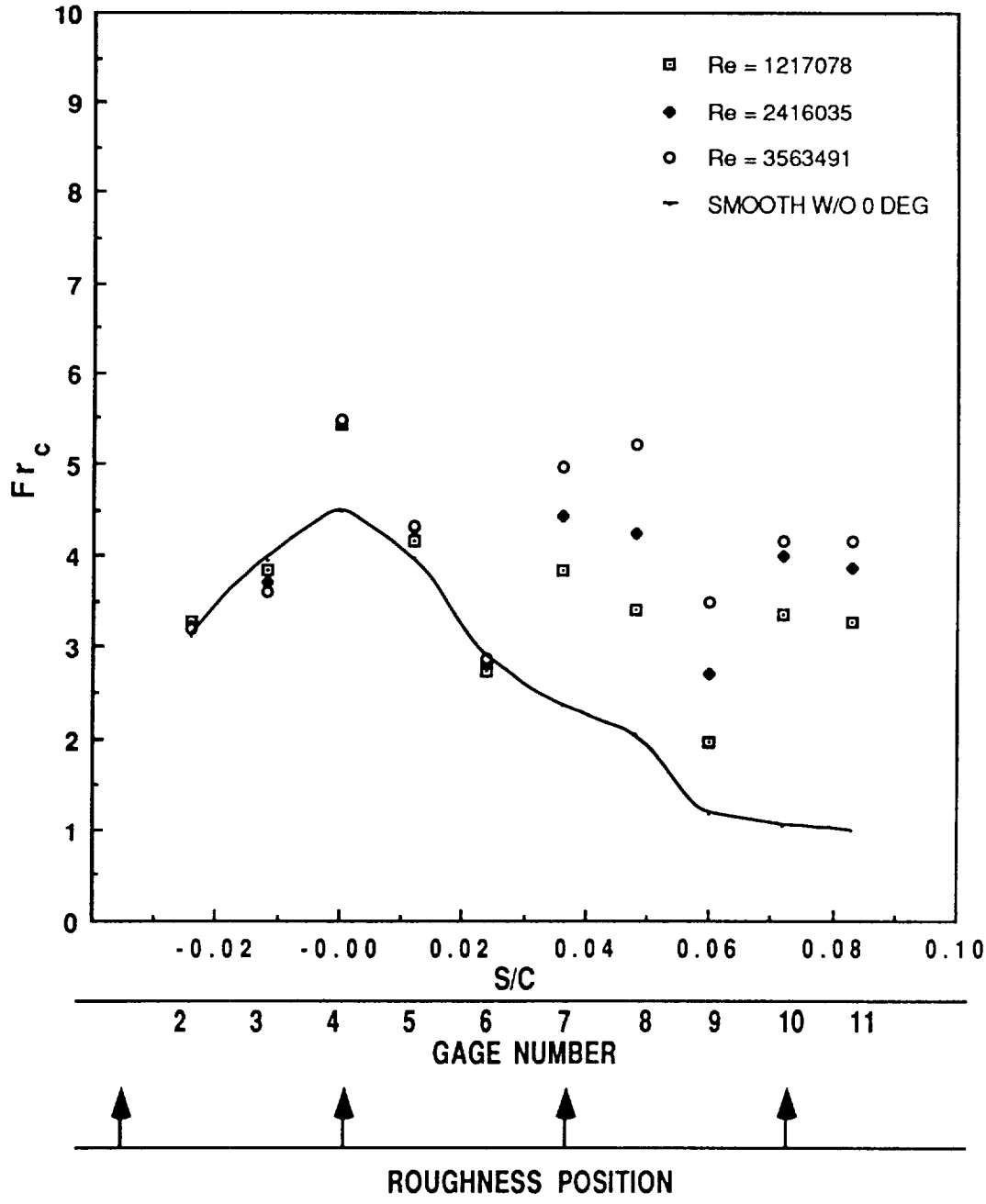

Figure 44. Frossling Number versus dimensionless surface distance: sparse roughness, 4 degree angle of attack, no spray air, IRT data.

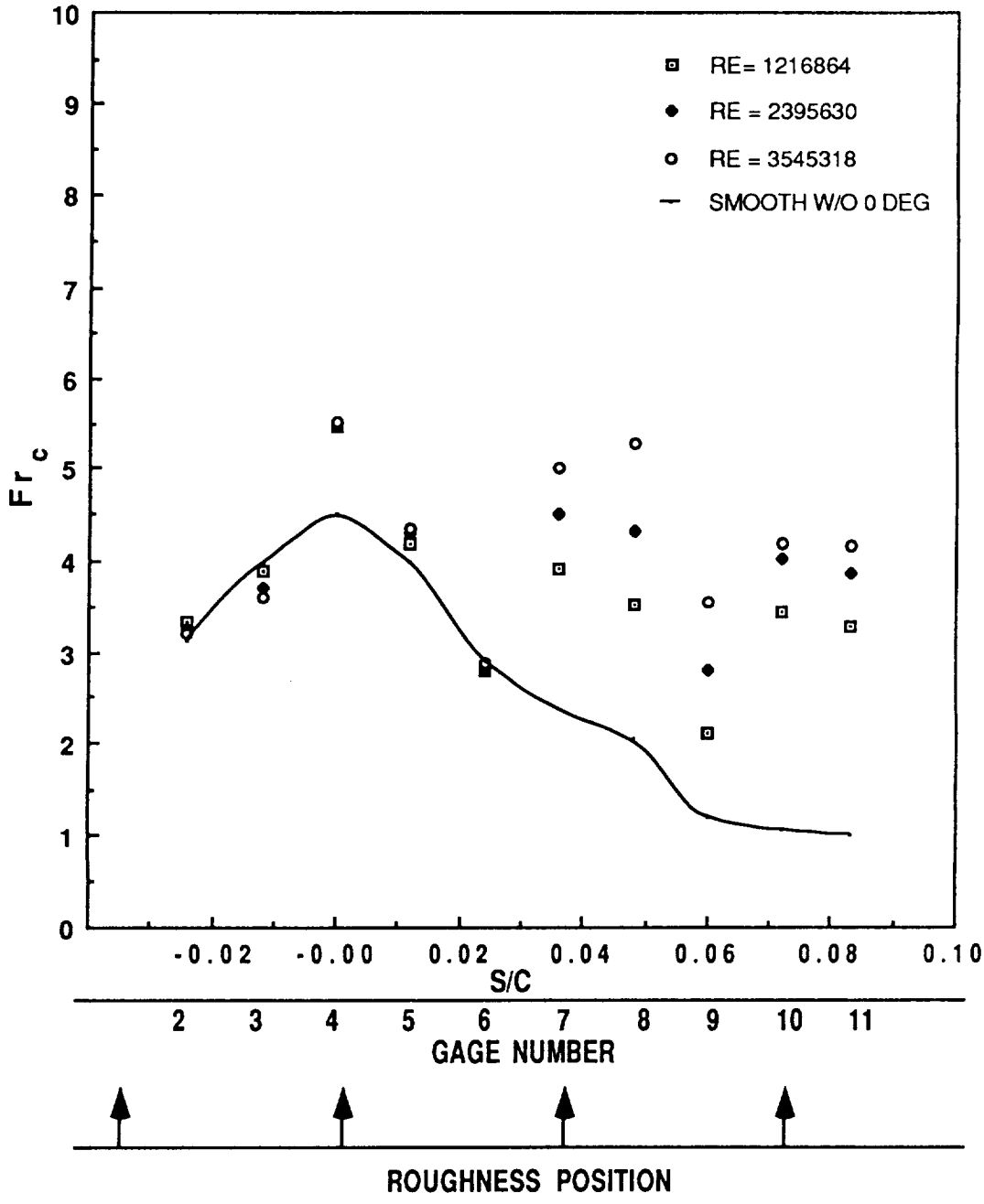

Figure 45. Frossling Number versus dimensionless surface distance: sparse roughness, 4 degree angle of attack, with spray air, IRT data.

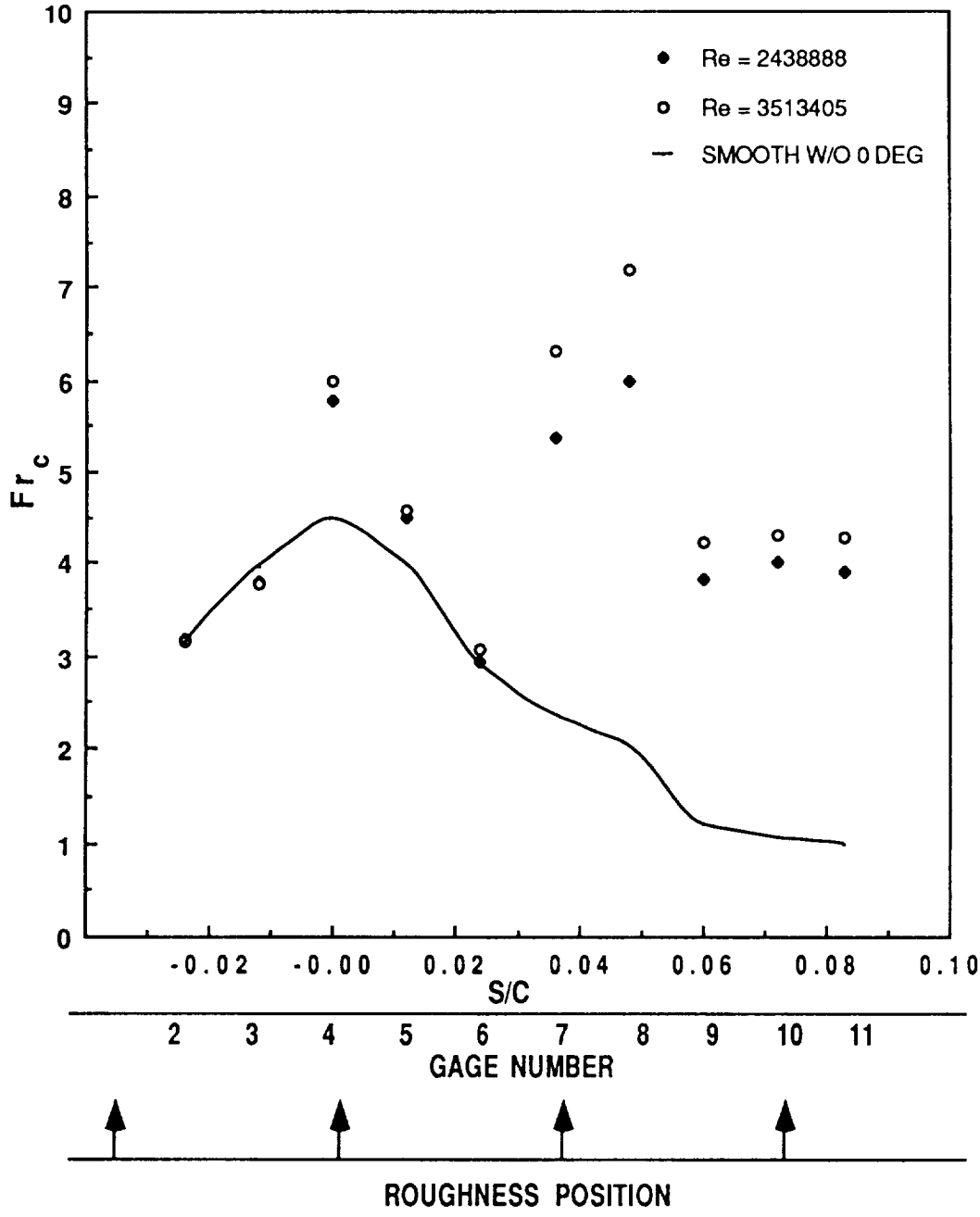

Figure 46. Frossling Number versus dimensionless surface distance: sparse roughness, 6 degree angle of attack, no spray air, IRT data.

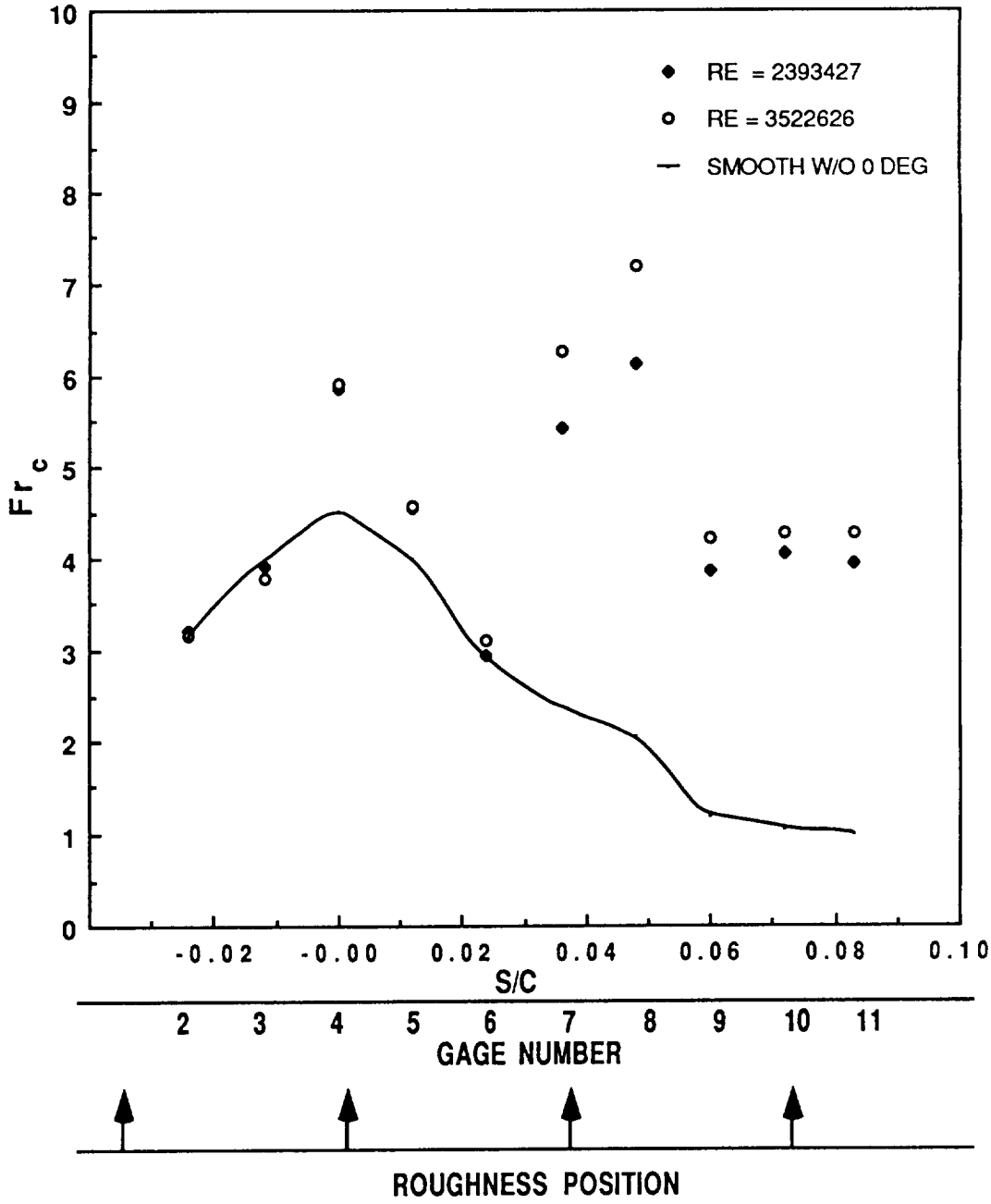

Figure 47. Frossling Number versus dimensionless surface distance: sparse roughness, 6 degree angle of attack, with spray air, IRT data.

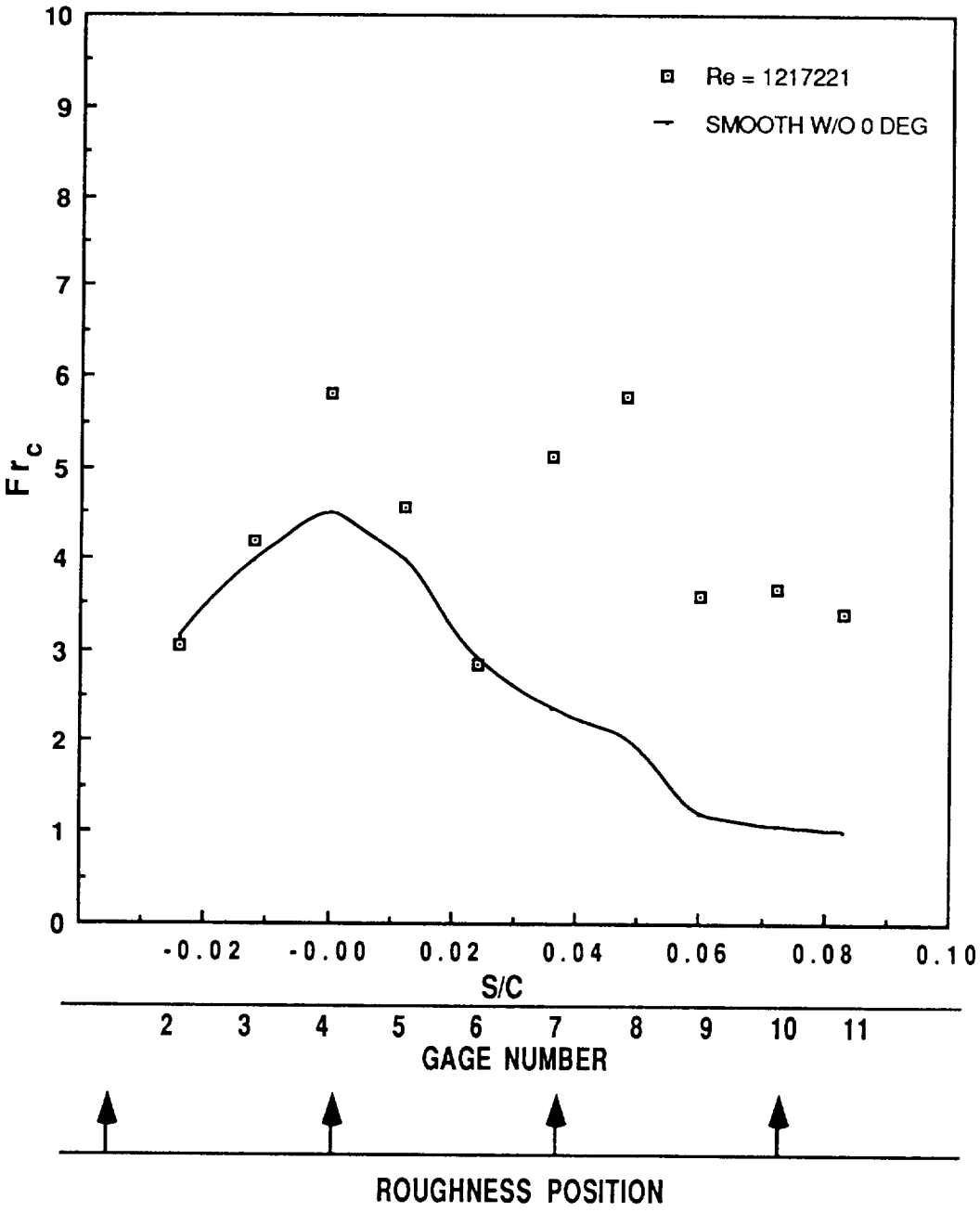

Figure 48. Frossling Number versus dimensionless surface distance: sparse roughness, 8 degree angle of attack, no spray air, IRT data.

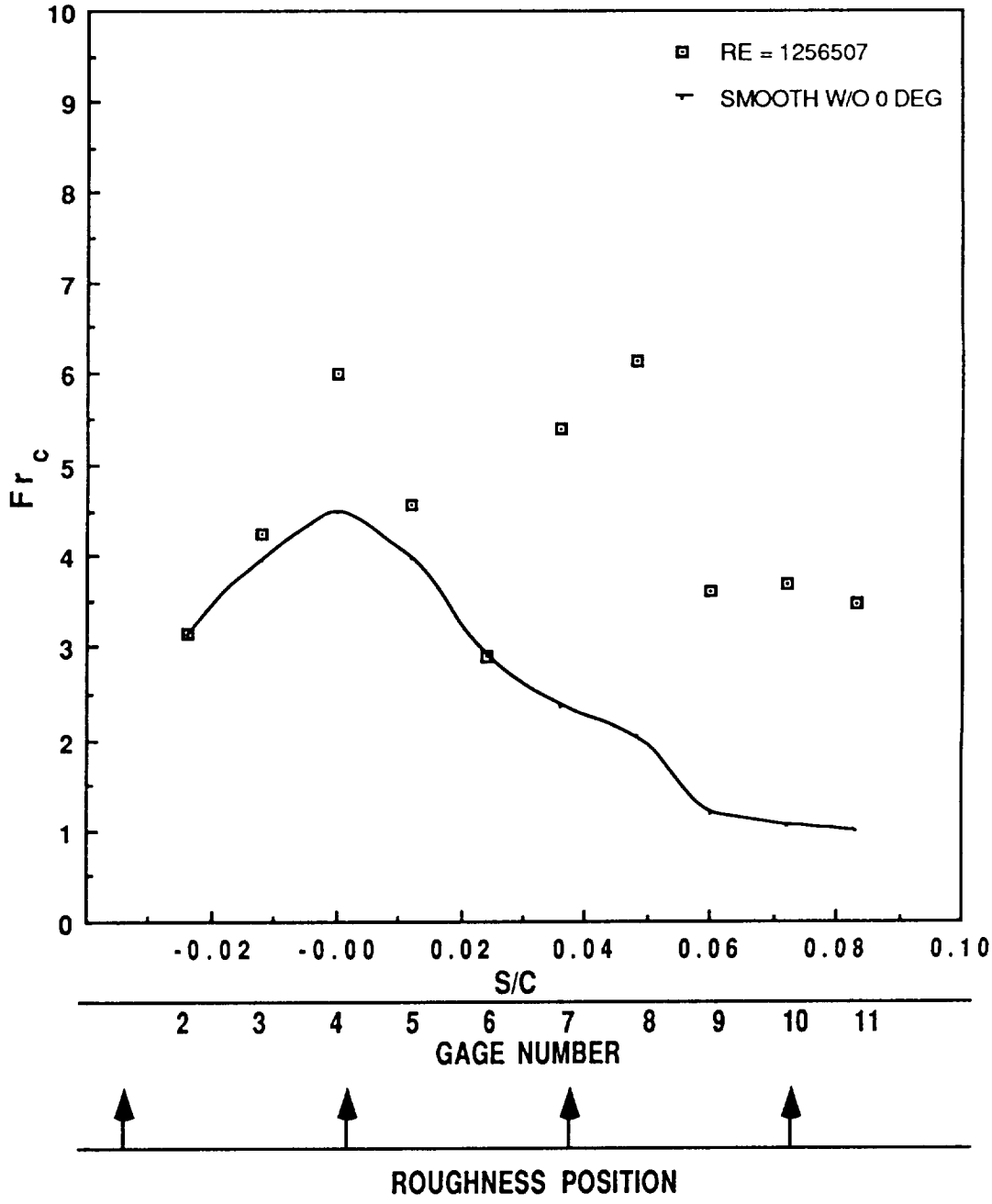

Figure 49. Frossling Number versus dimensionless surface distance: sparse roughness, 8 degree angle of attack, with spray air, IRT data.

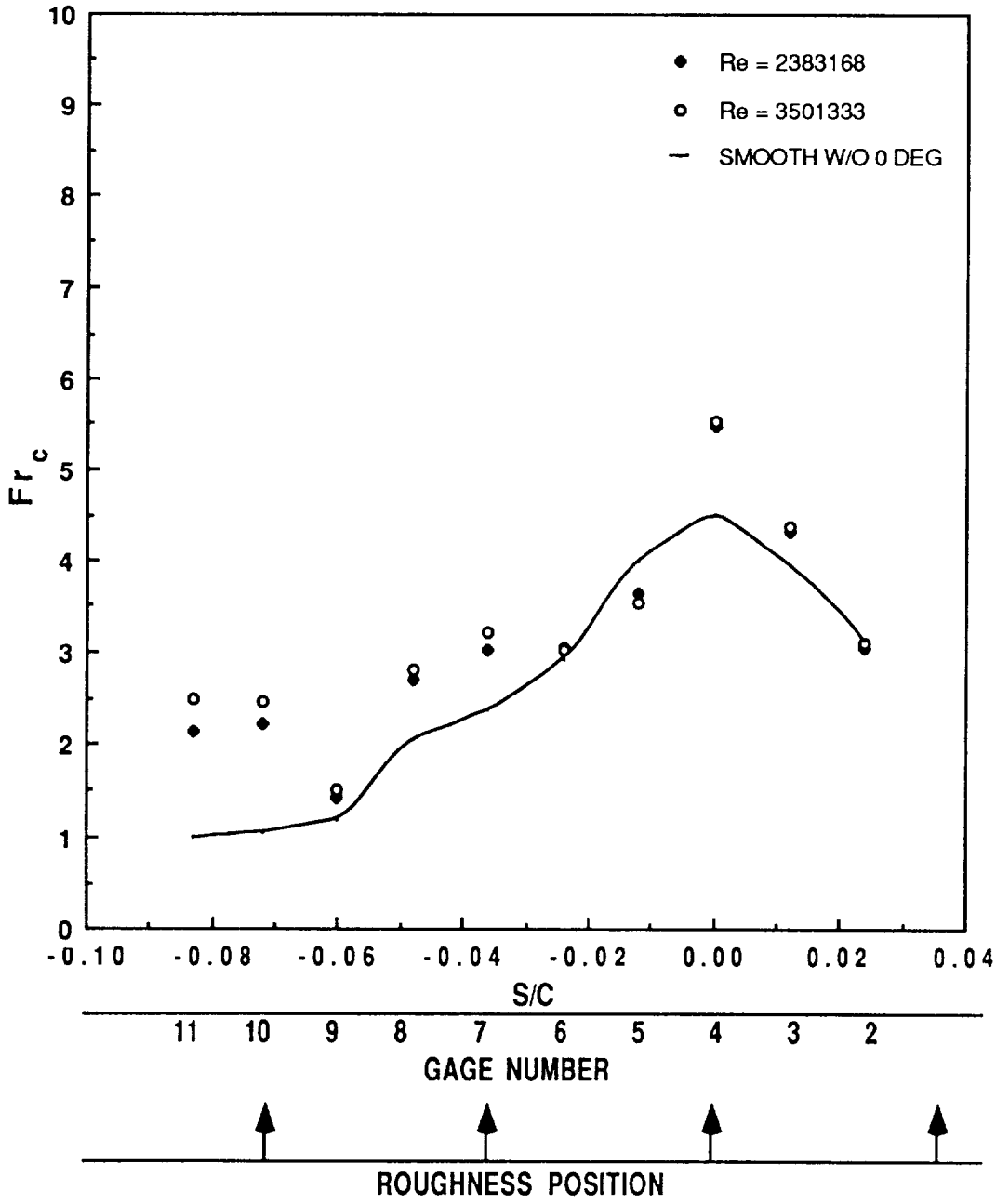

Figure 50. Frossling Number versus dimensionless surface distance: sparse roughness, -4 degree angle of attack, no spray air, IRT data.

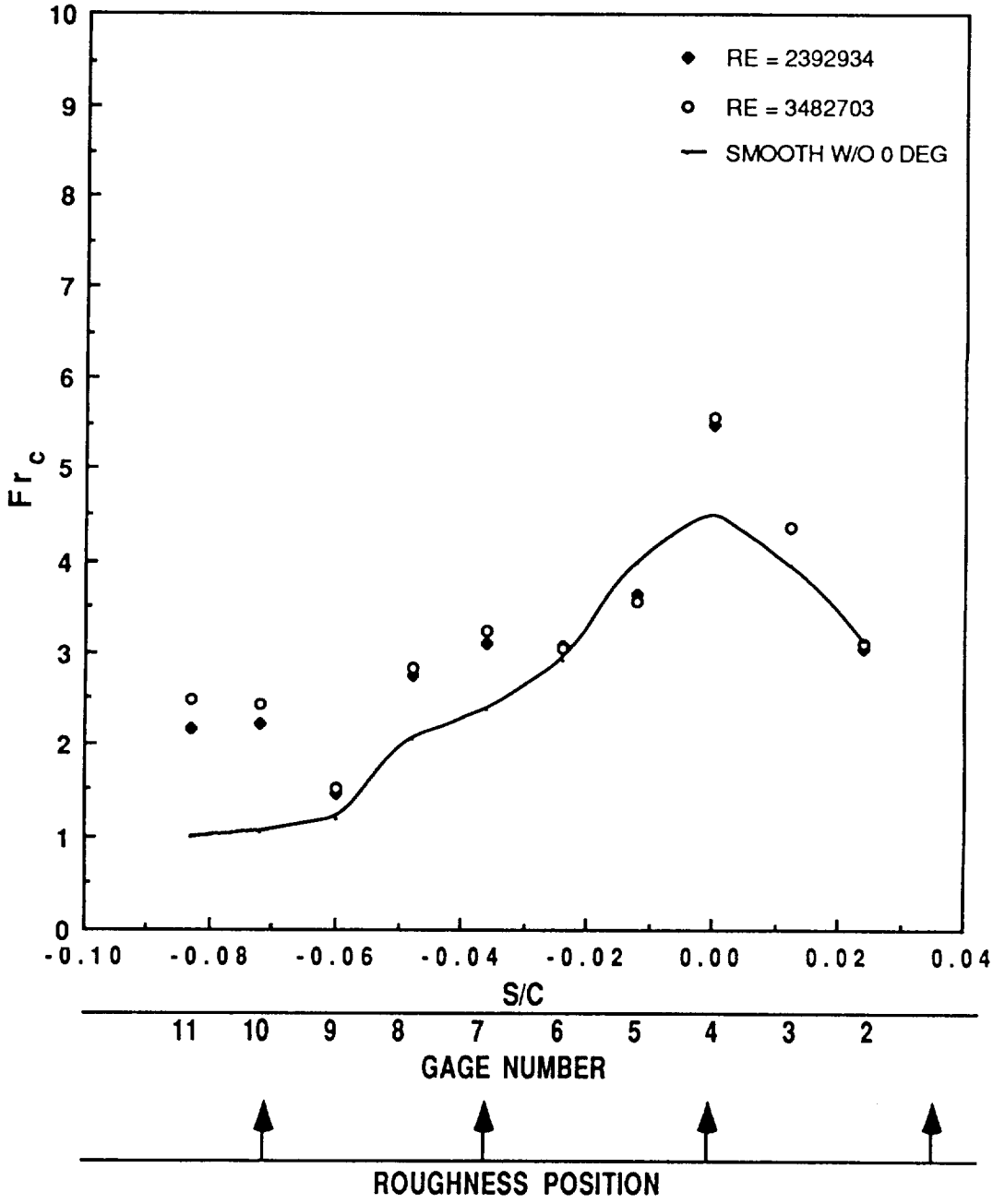

Figure 51. Frossling Number versus dimensionless surface distance: sparse roughness, -4 degree angle of attack, with spray air, IRT data.

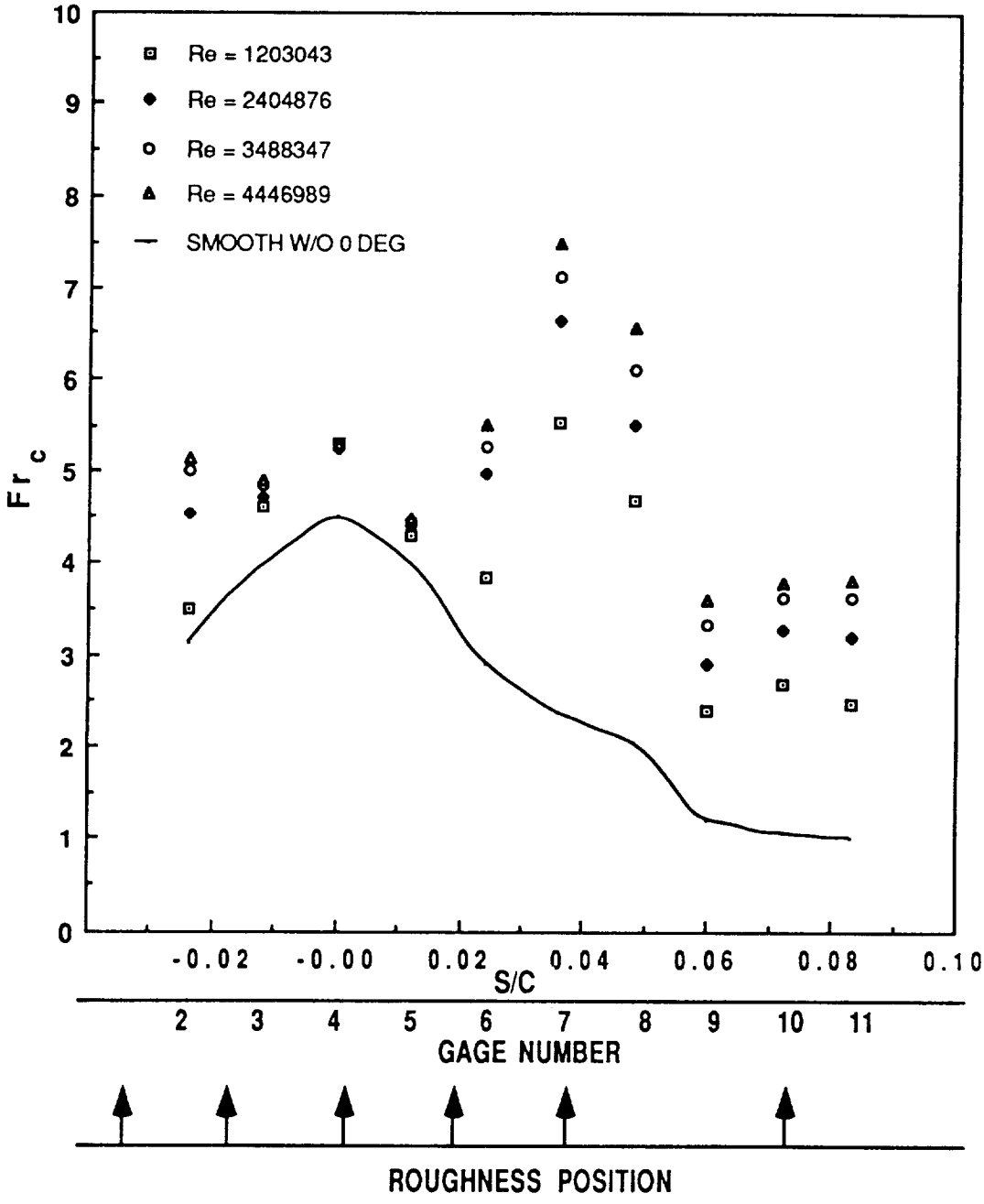

Figure 52. Frossling Number versus dimensionless surface distance: dense 1 roughness, 0 degree angle of attack, no spray air, IRT data.

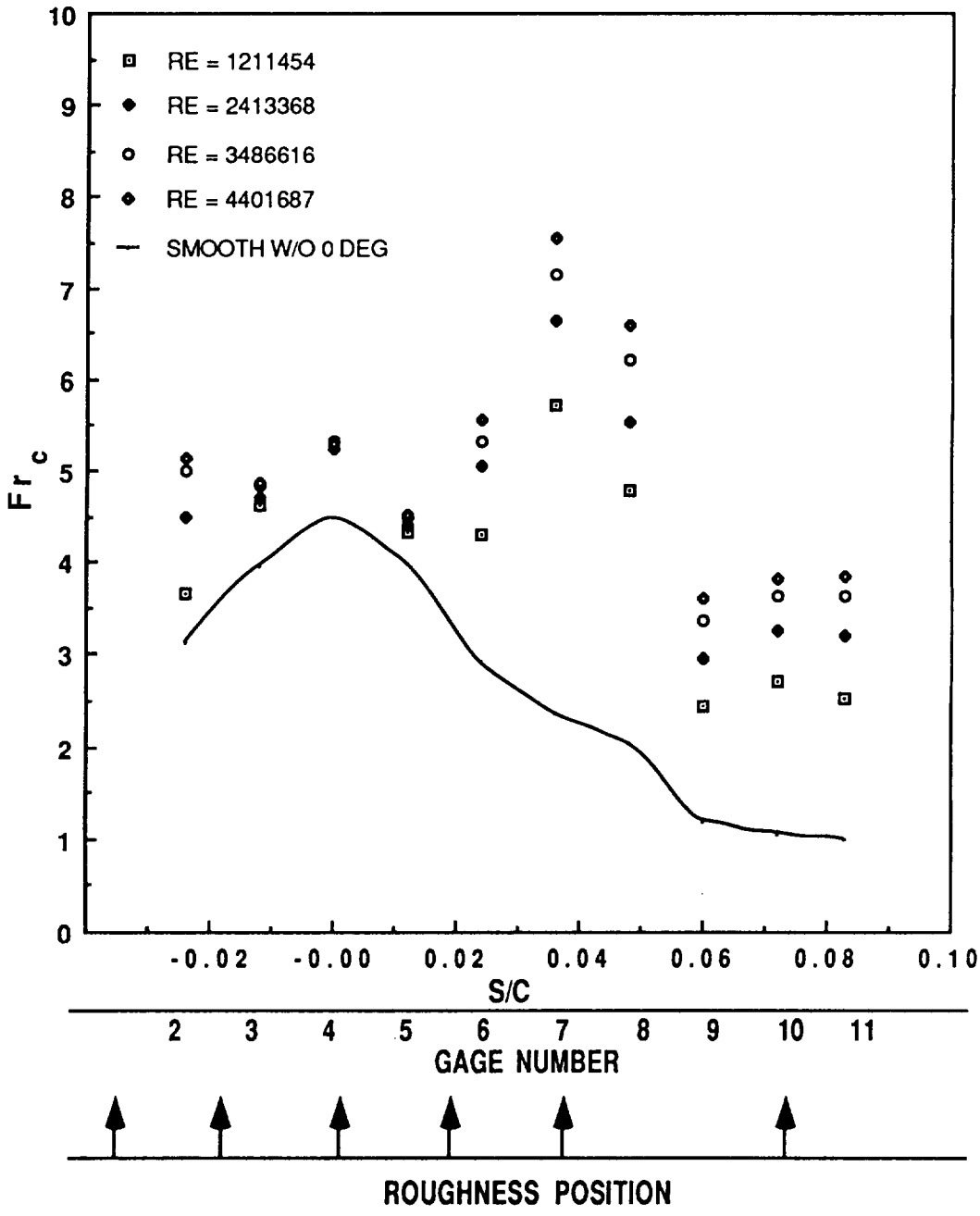

Figure 53. Frossling Number versus dimensionless surface distance: dense 1 roughness, 0 degree angle of attack, with spray air, IRT data.

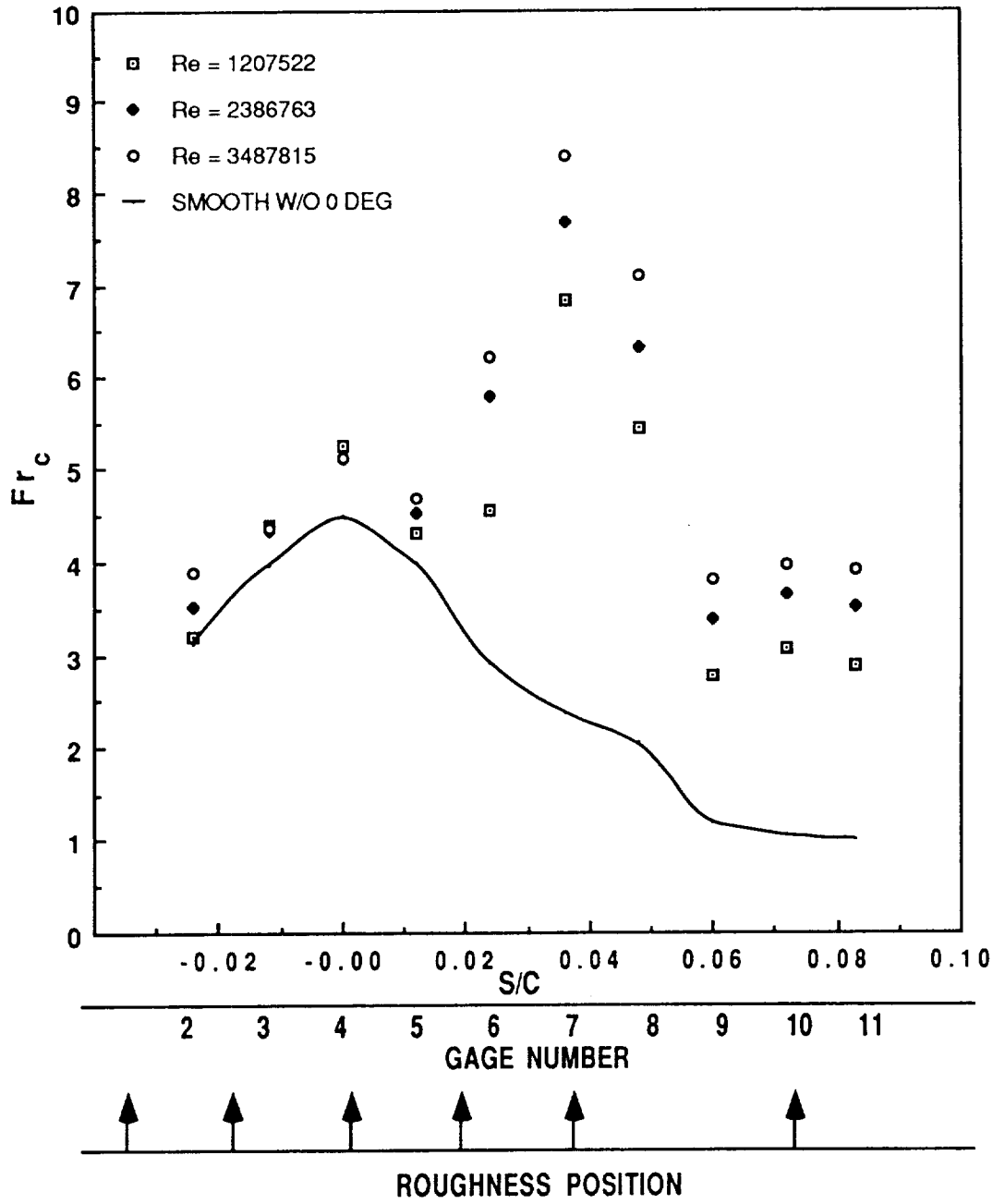

Figure 54. Frossling Number versus dimensionless surface distance: dense 1 roughness, 2 degree angle of attack, no spray air, IRT data.

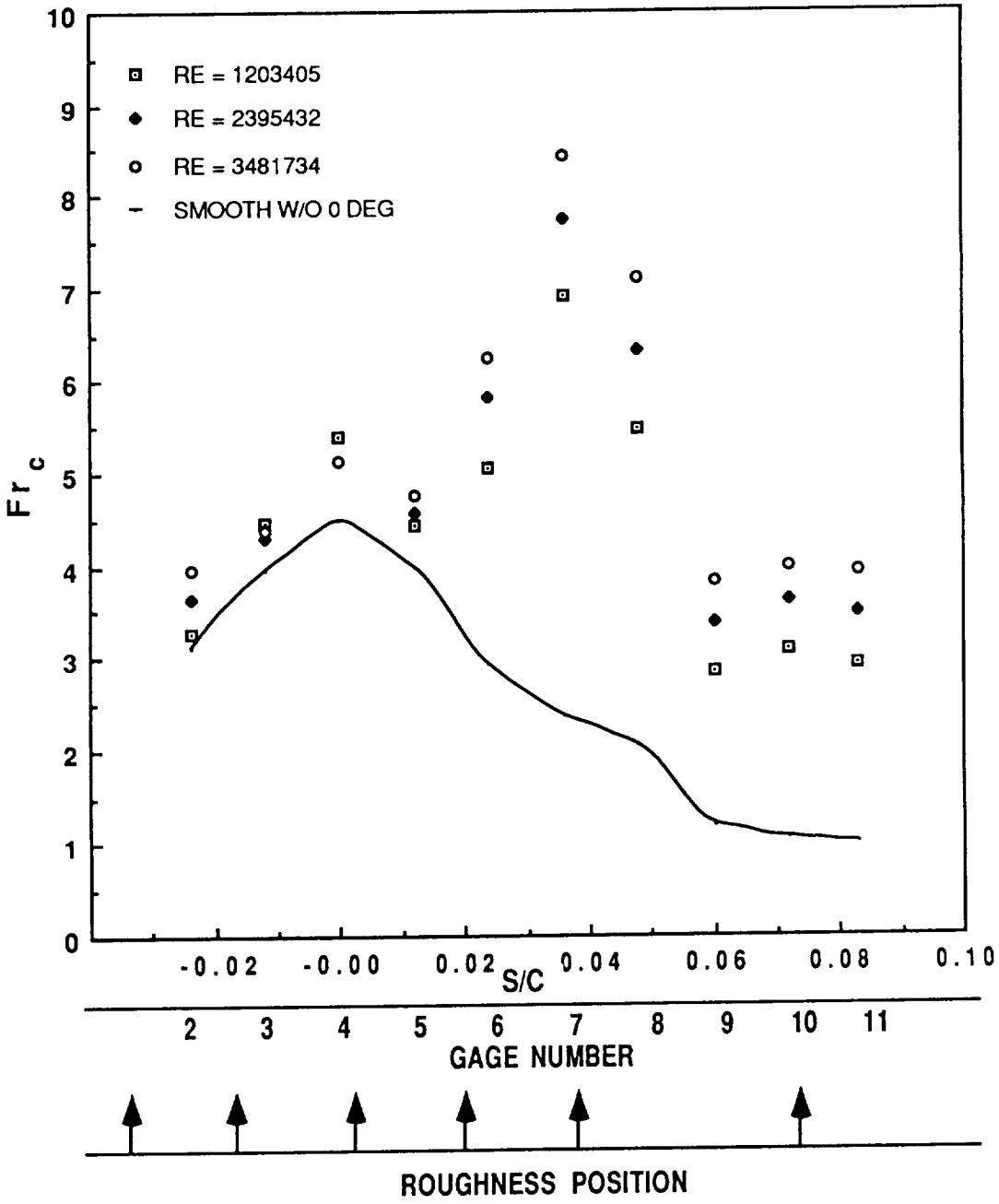

Figure 55. Frossling Number versus dimensionless surface distance: dense 1 roughness, 2 degree angle of attack, with spray air, IRT data.

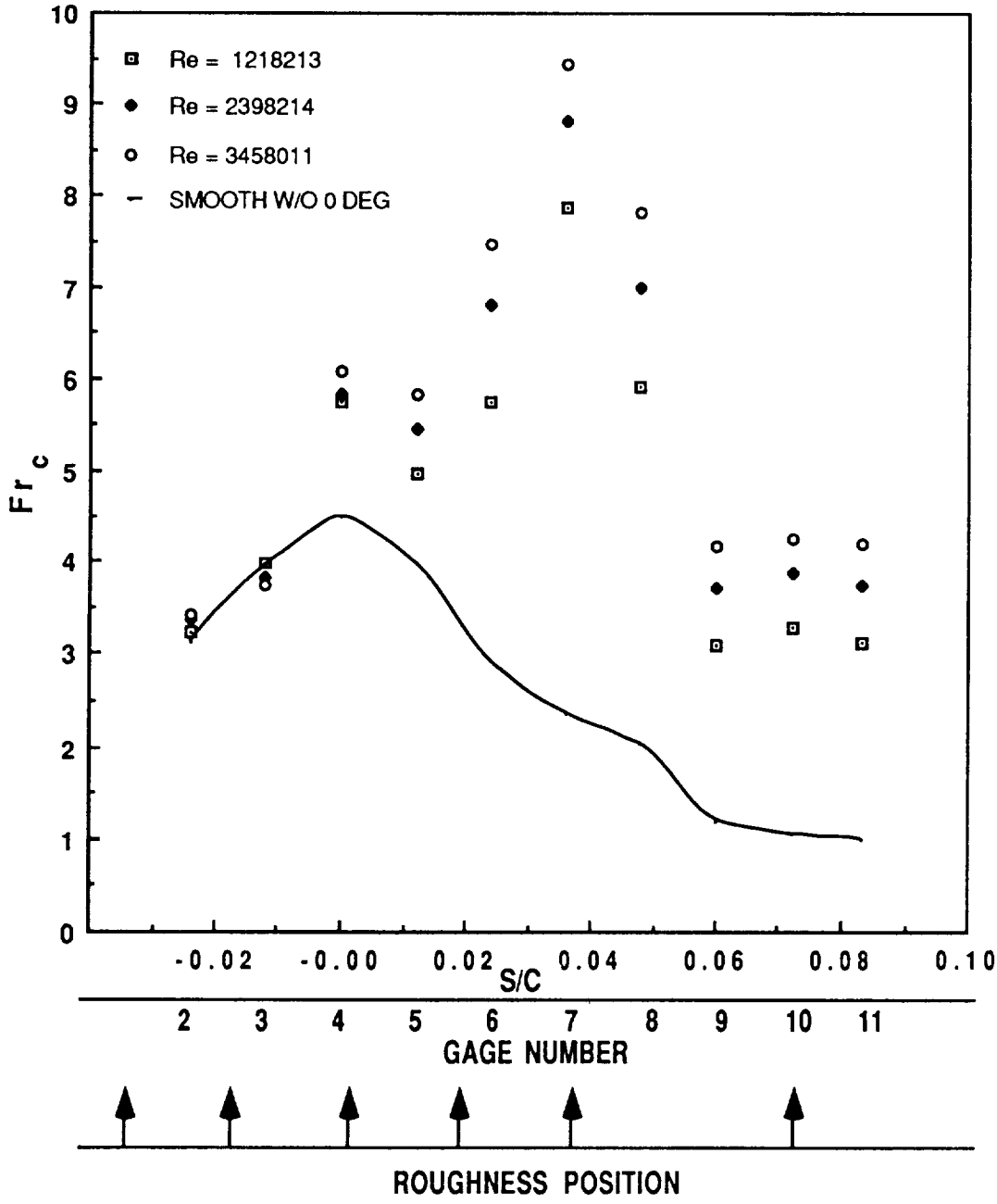

Figure 56. Frossling Nunber versus dimensionless surface distance: dense 1 roughness, 4 degree angle of attack, no spray air, IRT data.

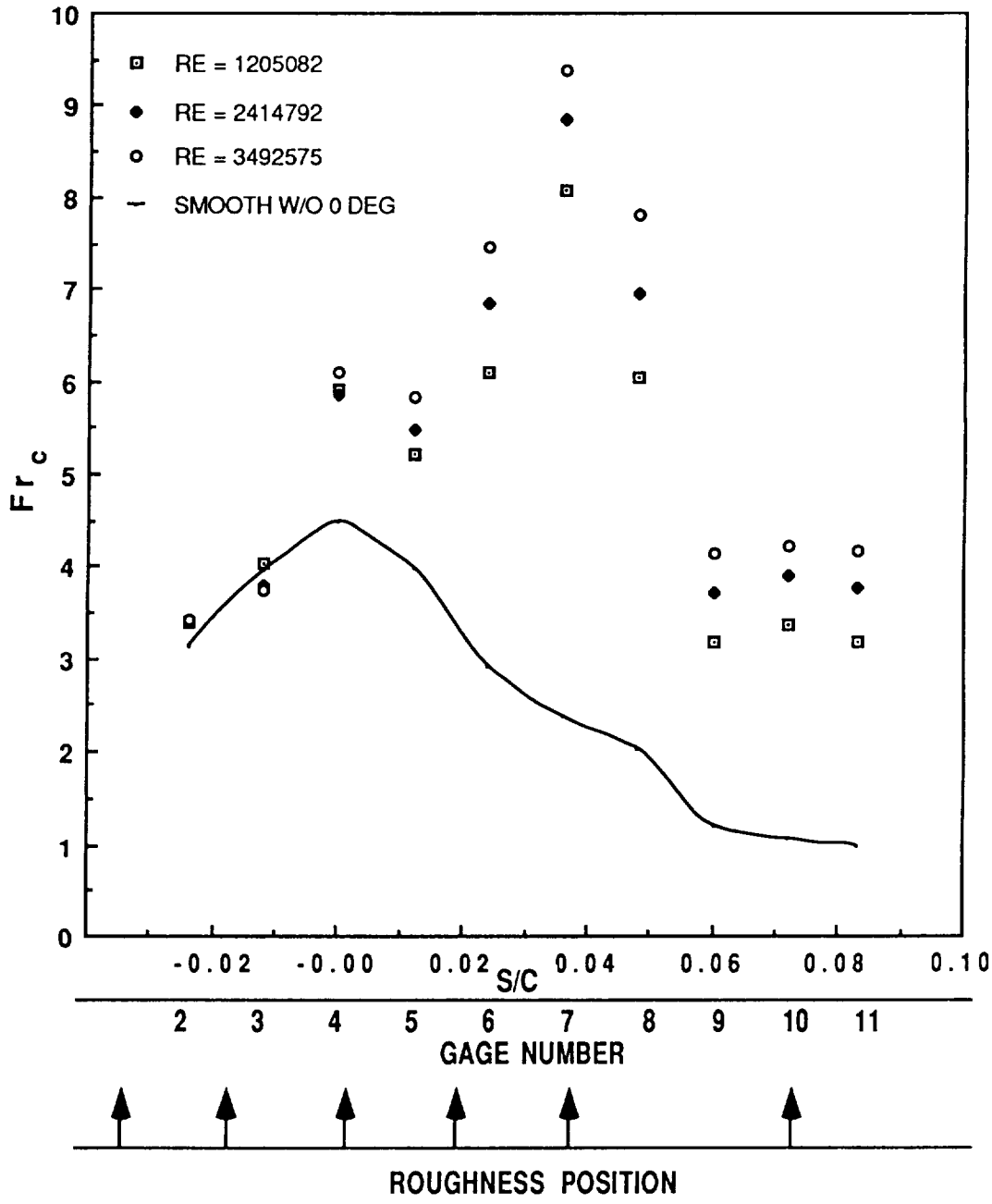

Figure 57. Frossling Number versus dimensionless surface distance: dense 1 roughness, 4 degree angle of attack, with spray air, IRT data.

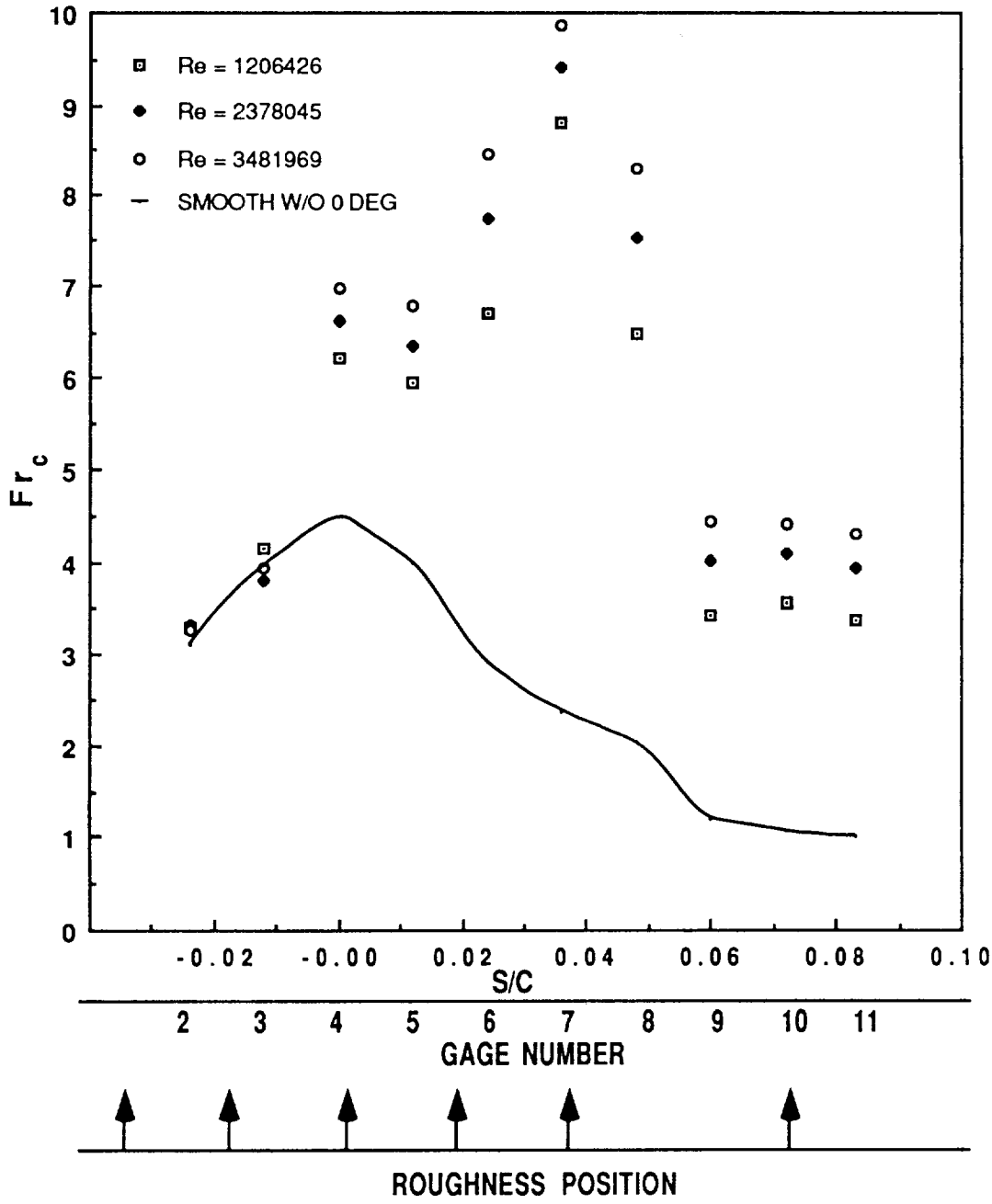

Figure 58. Frossling Number versus dimensionless surface distance: dense 1 roughness, 6 degree angle of attack, no spray air, IRT data.

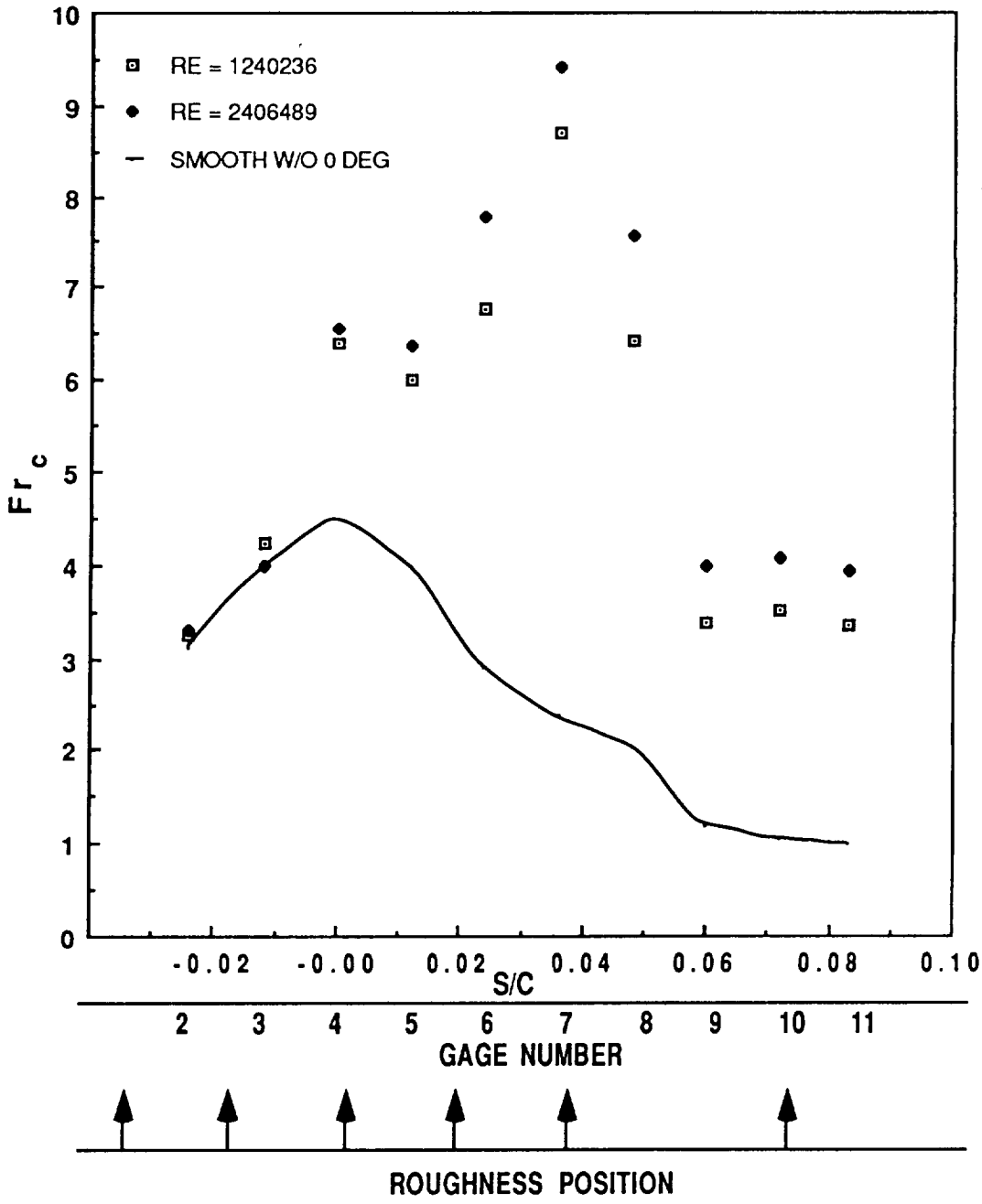

Figure 59. Frossling Number versus dimensionless surface distance: dense 1 roughness, 6 degree angle of attack, with spray air, IRT data.

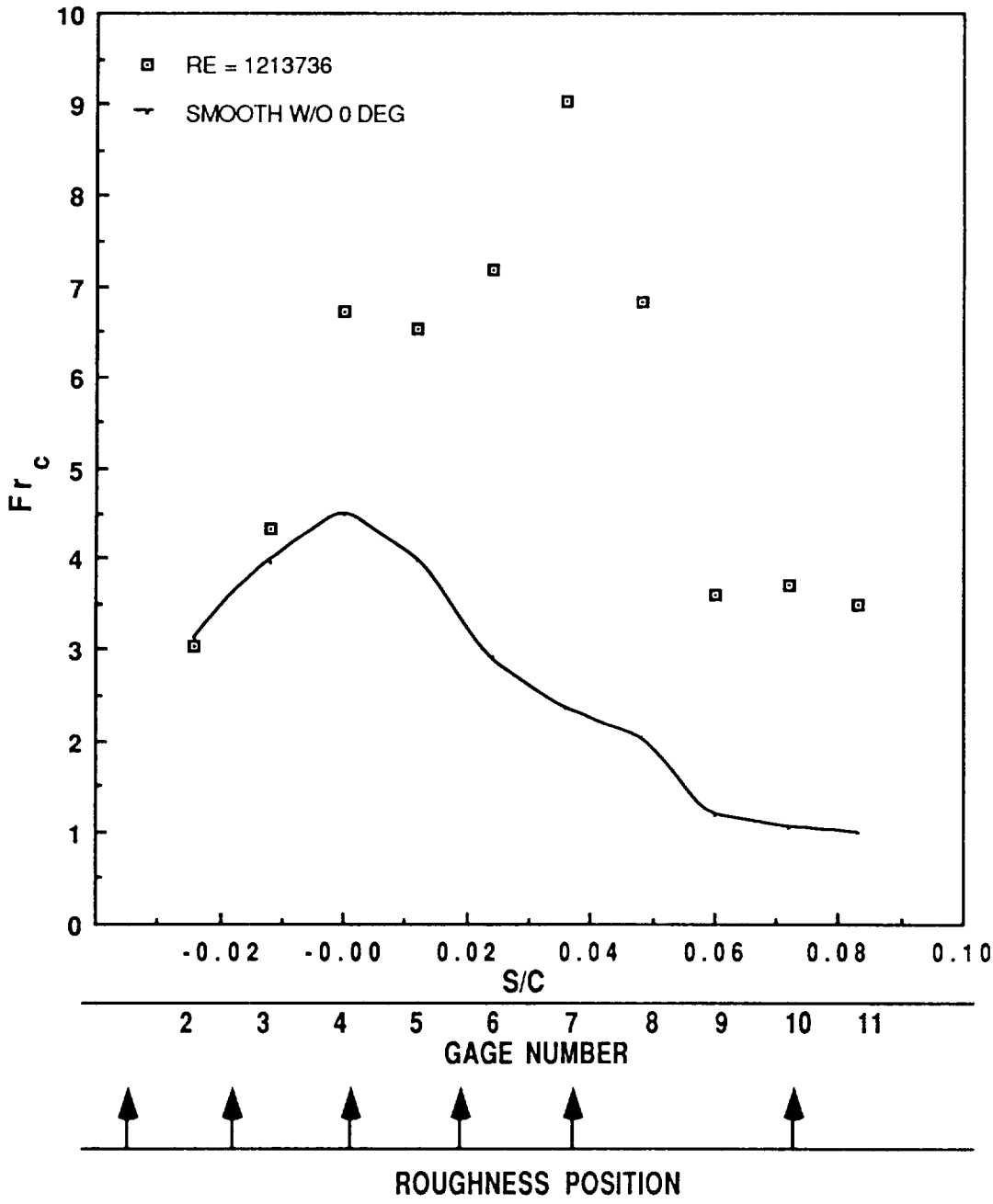

Figure 60. Frossling Number versus dimensionless surface distance: dense 1 roughness, 8 degree angle of attack, no spray air, IRT data.

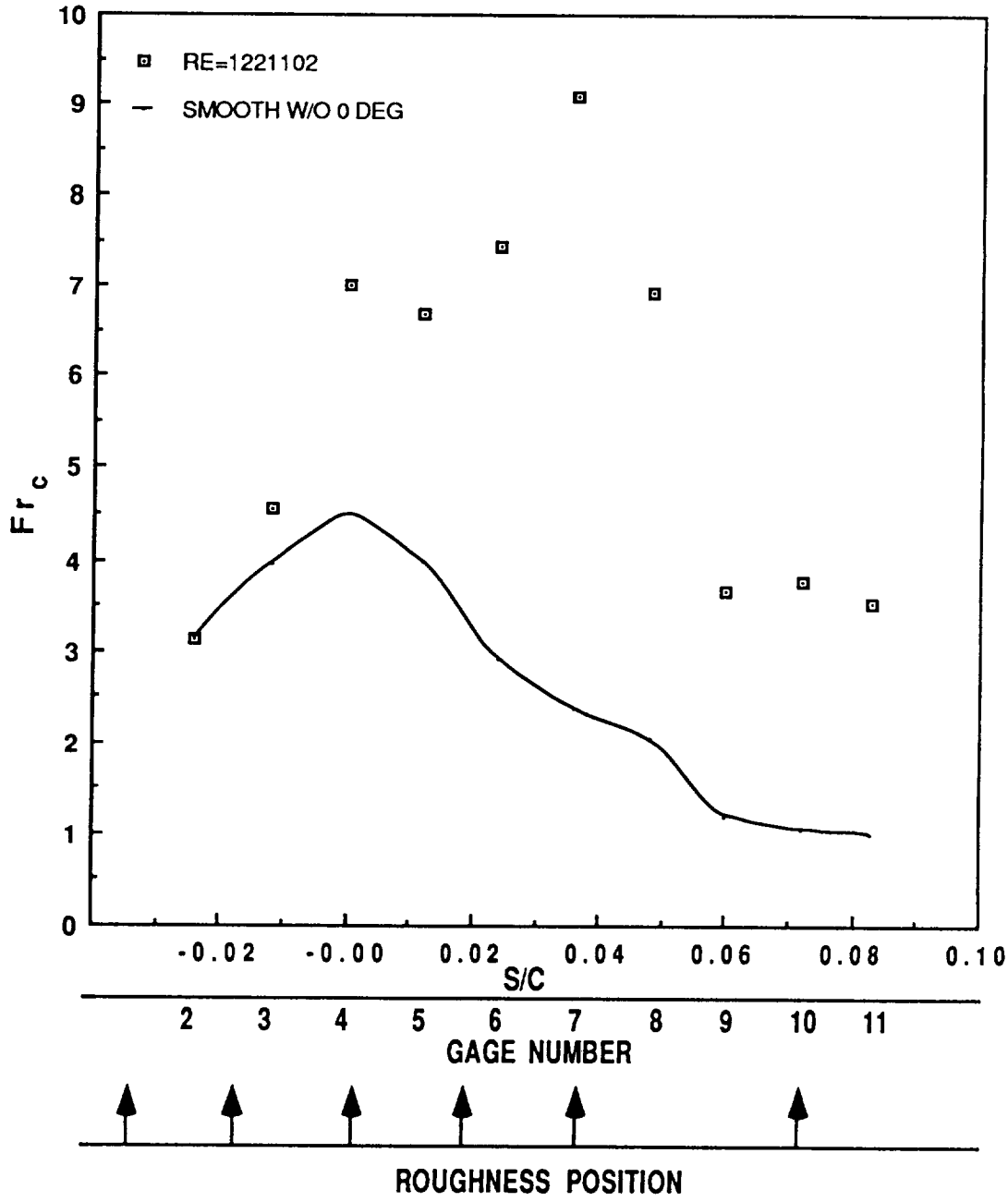

Figure 61. Frossling Number versus dimensionless surface distance: dense 1 roughness, 8 degree angle of attack, with spray air, IRT data.

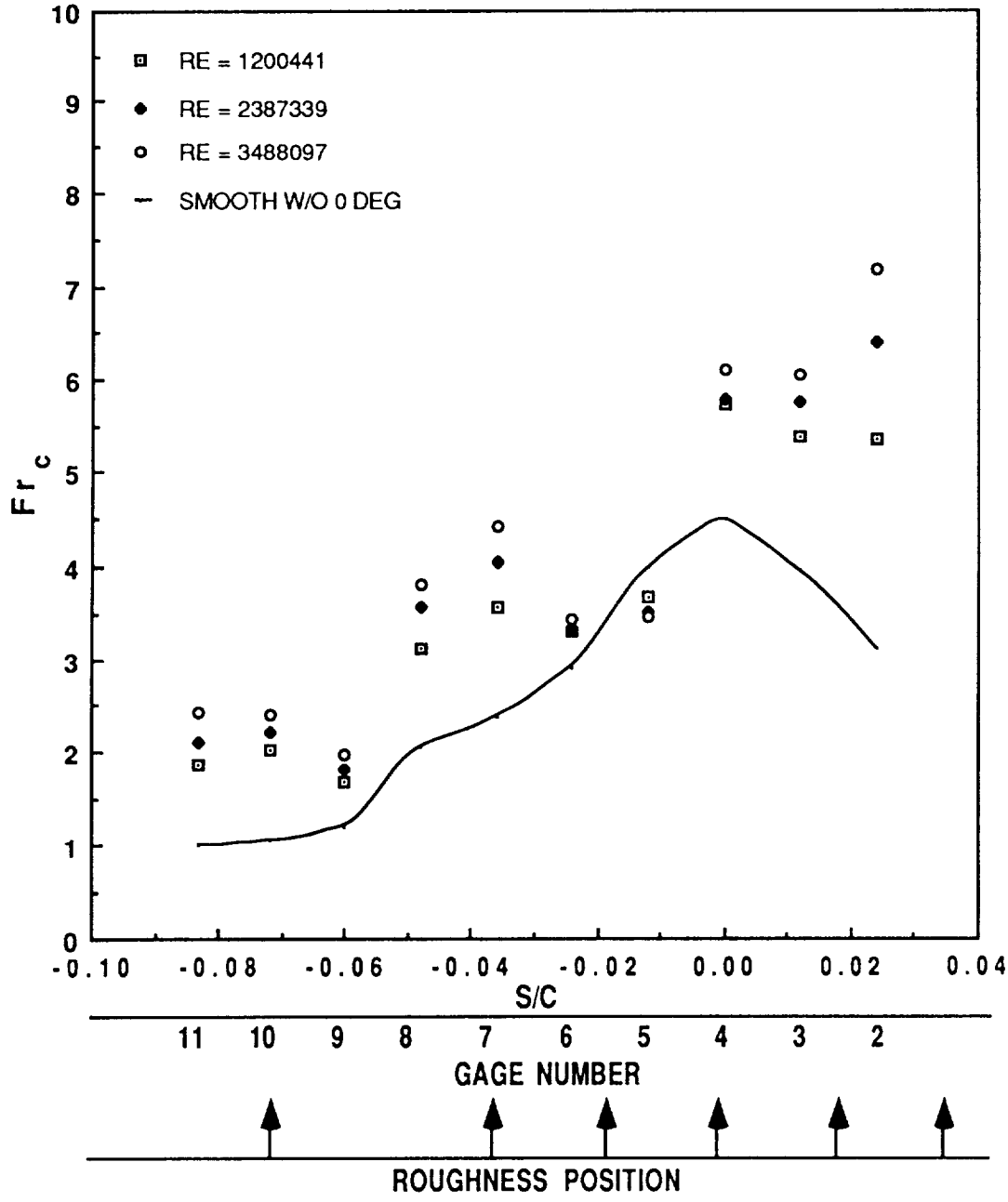

Figure 62. Frossling Number versus dimensionless surface distance: dense 1 roughness, -4 degree angle of attack, no spray air, IRT data.

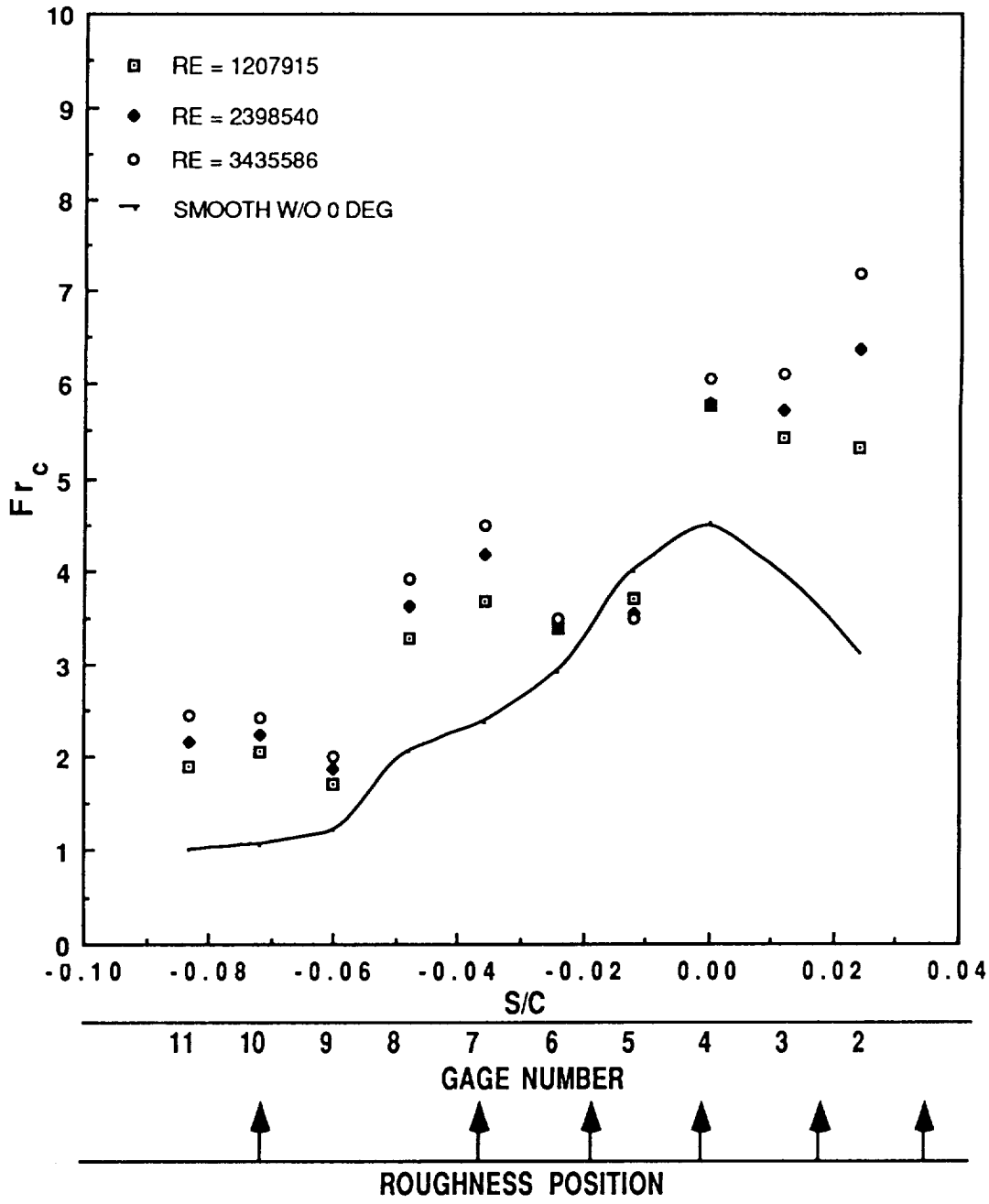

Figure 63. Frossling Number versus dimensionless surface distance: dense 1 roughness, -4 degree angle of attack, with spray air, IRT data.

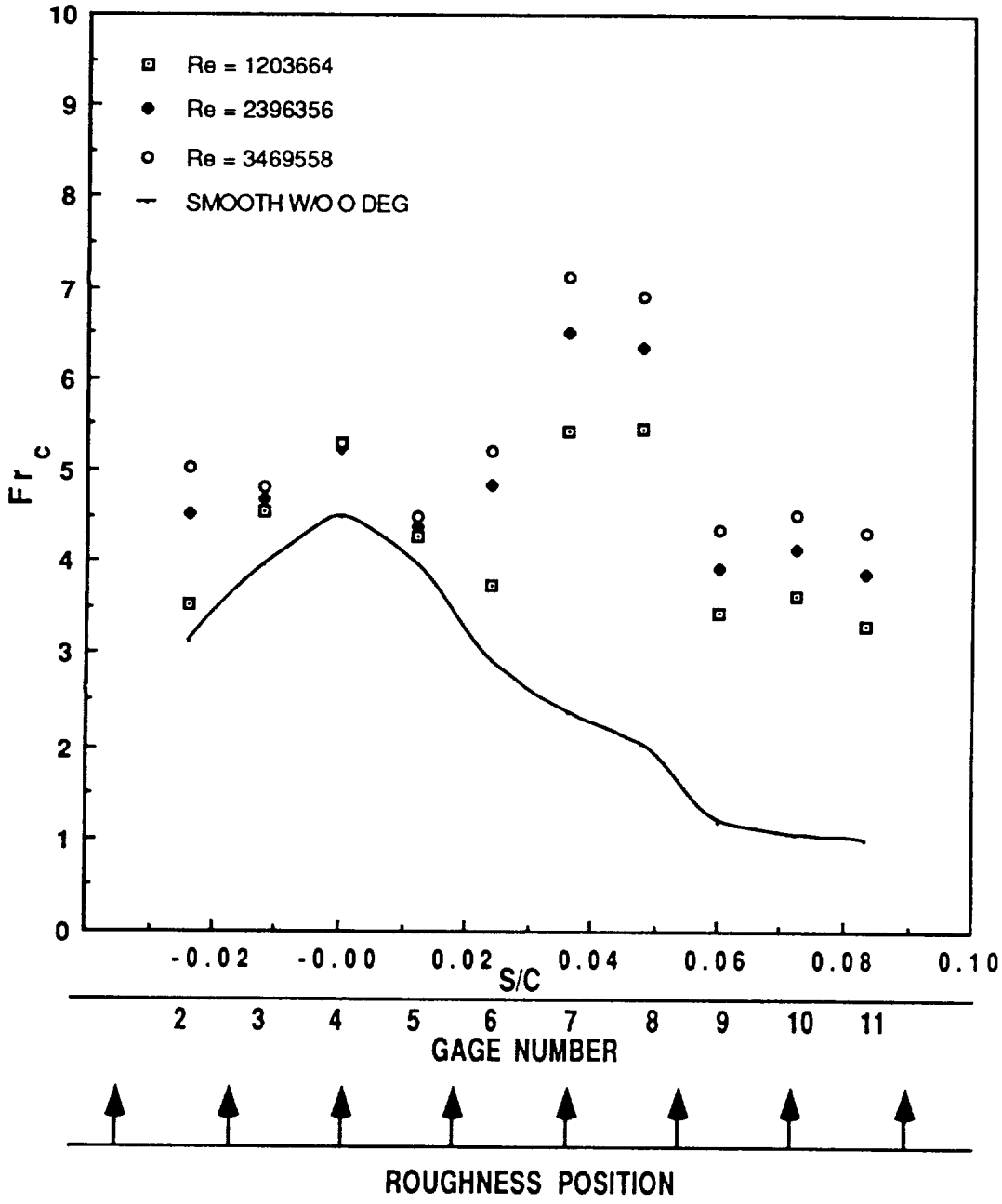

Figure 64. Frossling Number versus dimensionless surface distance: dense 2 roughness, 0 degree angle of attack, no spray air, IRT data.

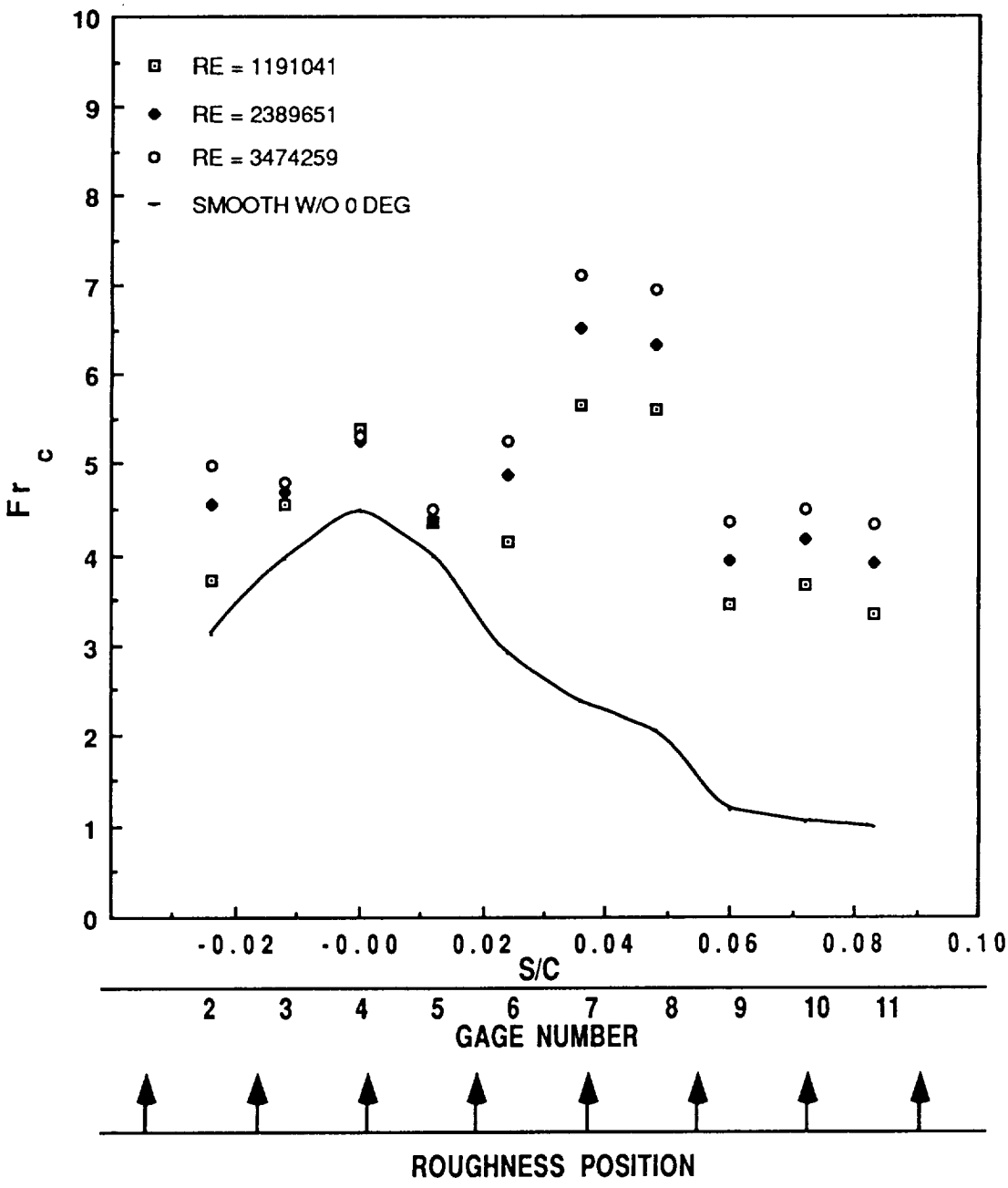

Figure 65. Frossling Number versus dimensionless surface distance: dense 2 roughness, 0 degree angle of attack, with spray air, IRT data.

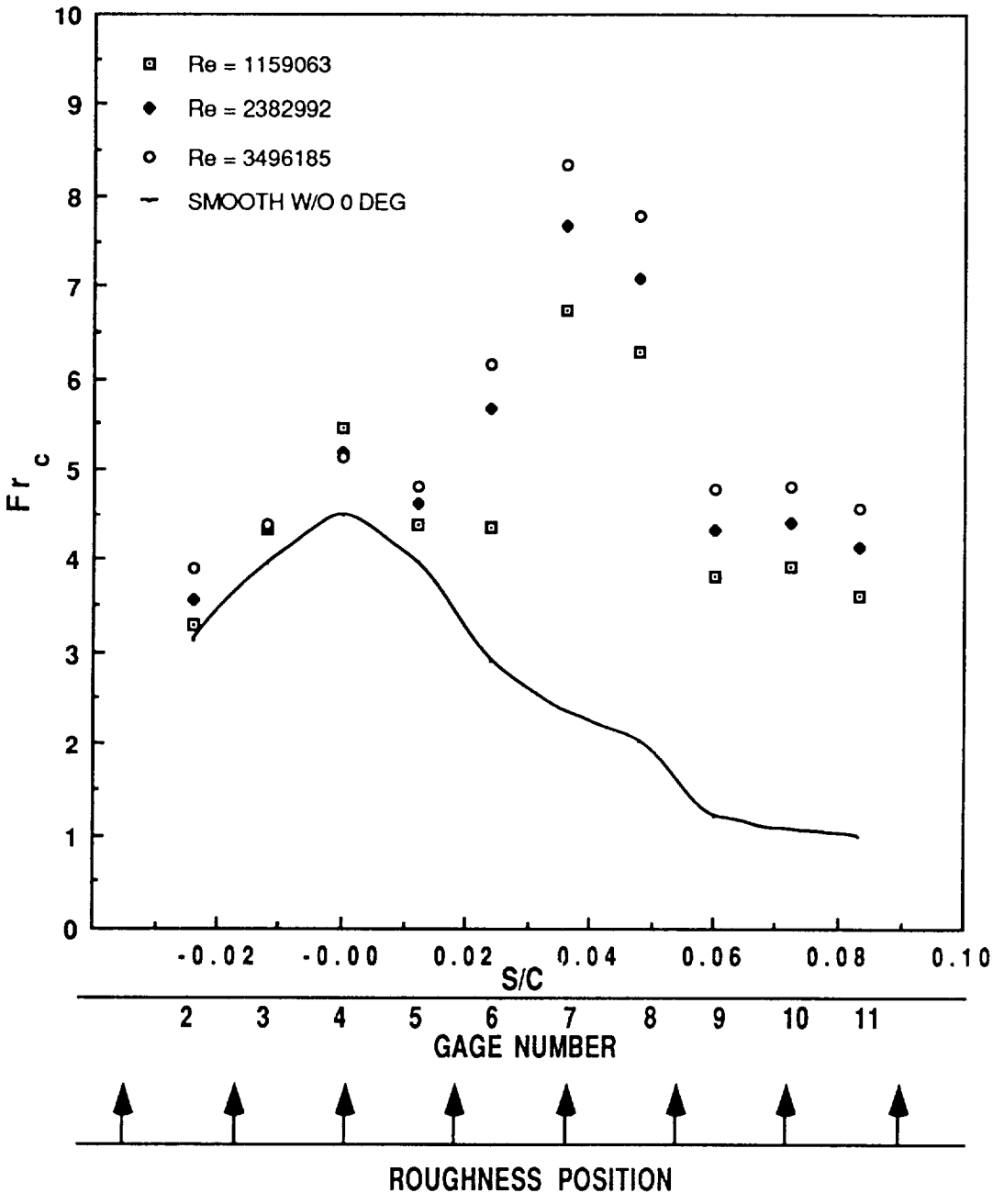

Figure 66. Frossling Number versus dimensionless surface distance: dense 2 roughness, 2 degree angle of attack, no spray air, IRT data.

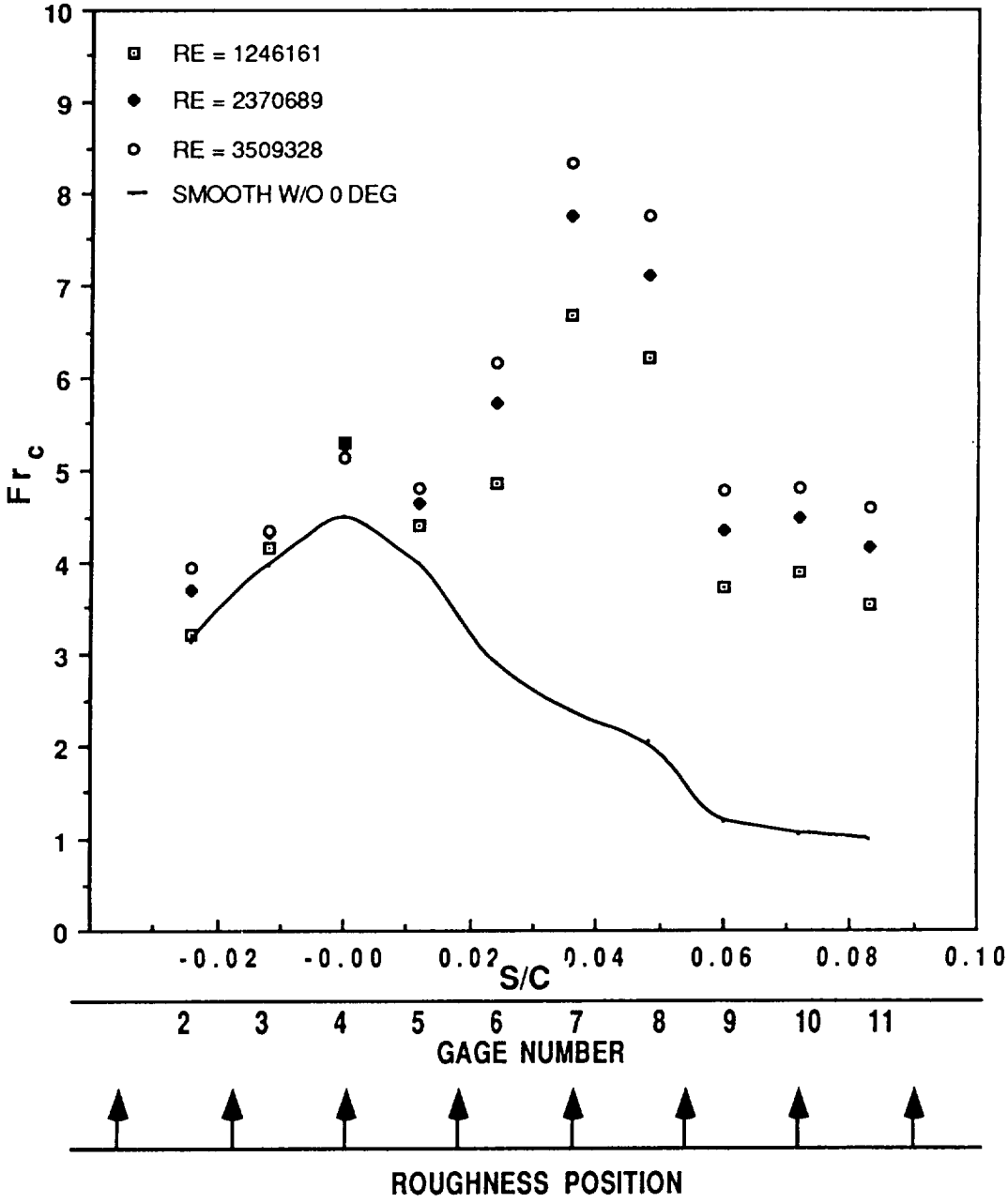

Figure 67. Frossling Number versus dimensionless surface distance: dense 2 roughness, 2 degree angle of attack, with spray air, IRT data.

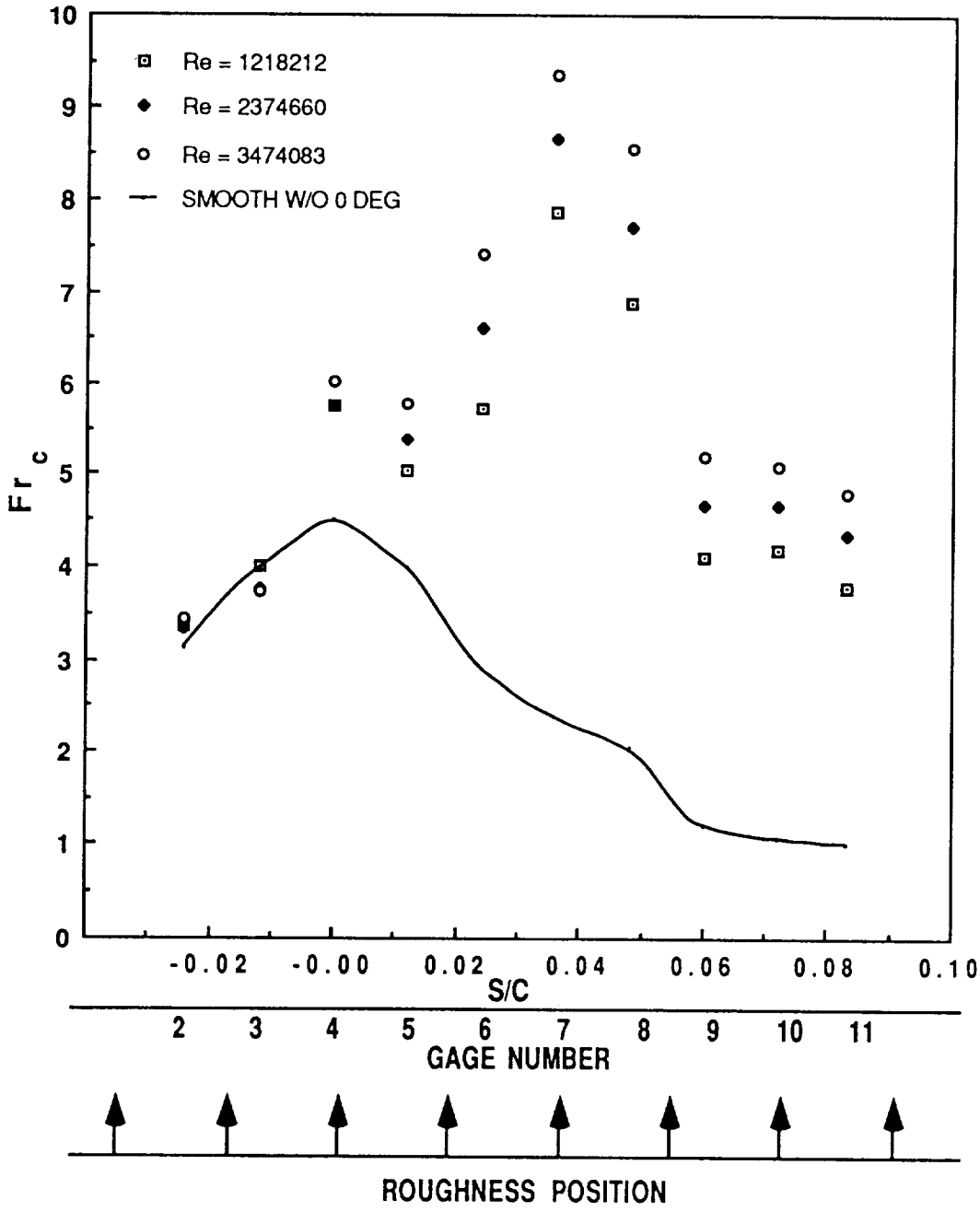

Figure 68. Froosling Number versus dimensionless surface distance: dense 2 roughness, 4 degree angle of attack, no spray air, IRT data.

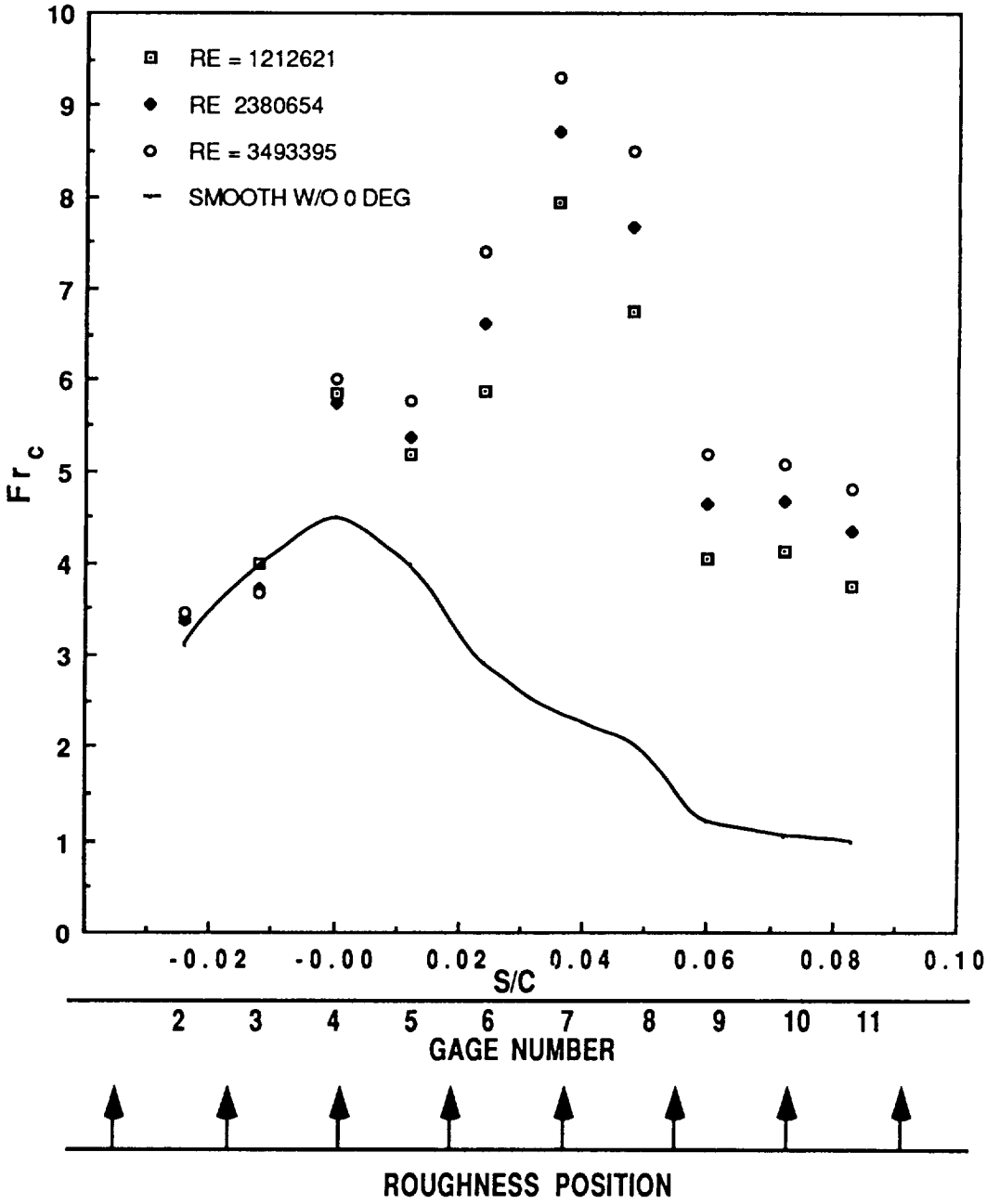

Figure 69. Frossling Number versus dimensionless surface distance: dense 2 roughness, 4 degree angle of attack, with spray air, IRT data.

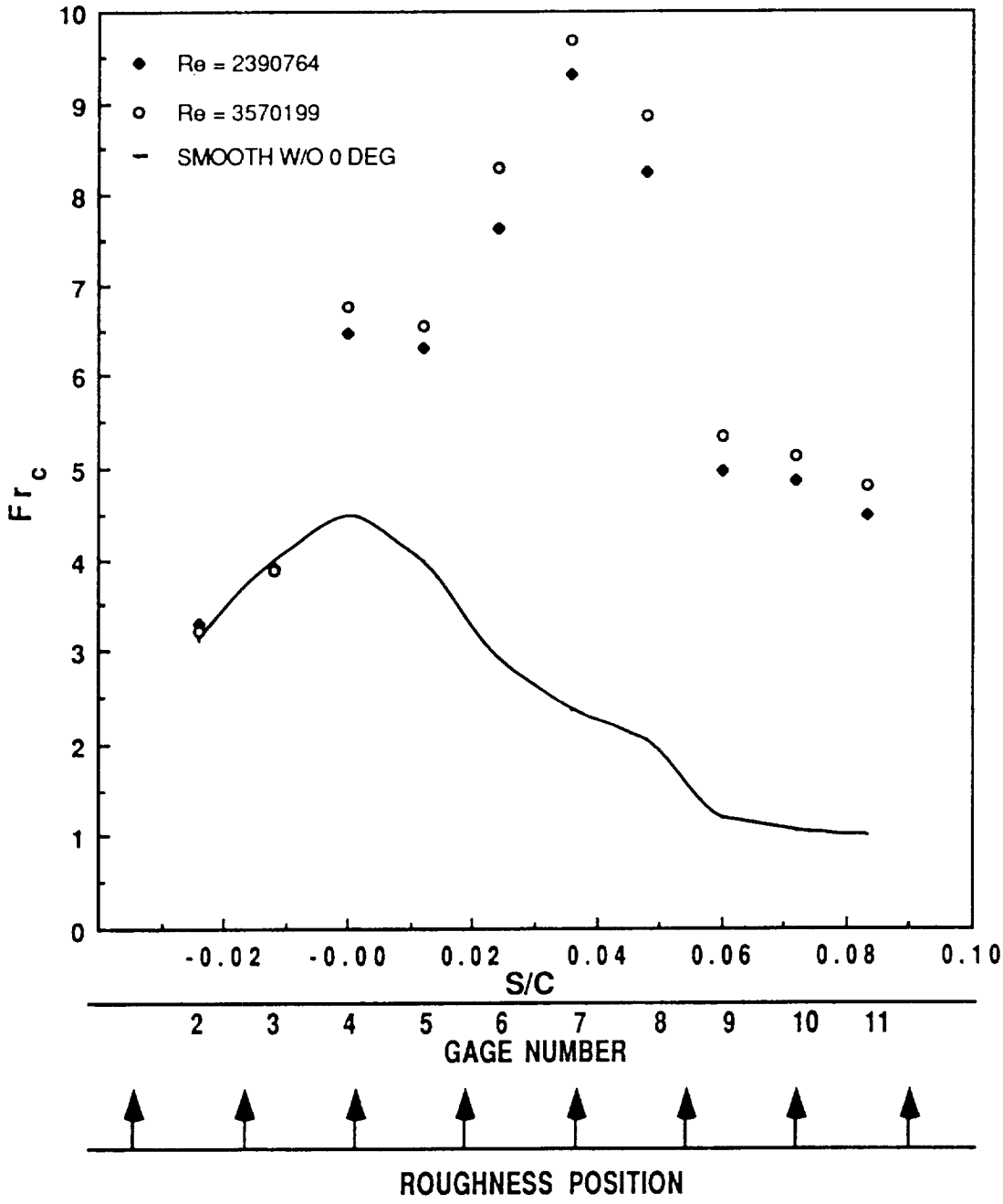

Figure 70. Frossling Number versus dimensionless surface distance: dense 2 roughness, 6 degree angle of attack, no spray air, IRT data.

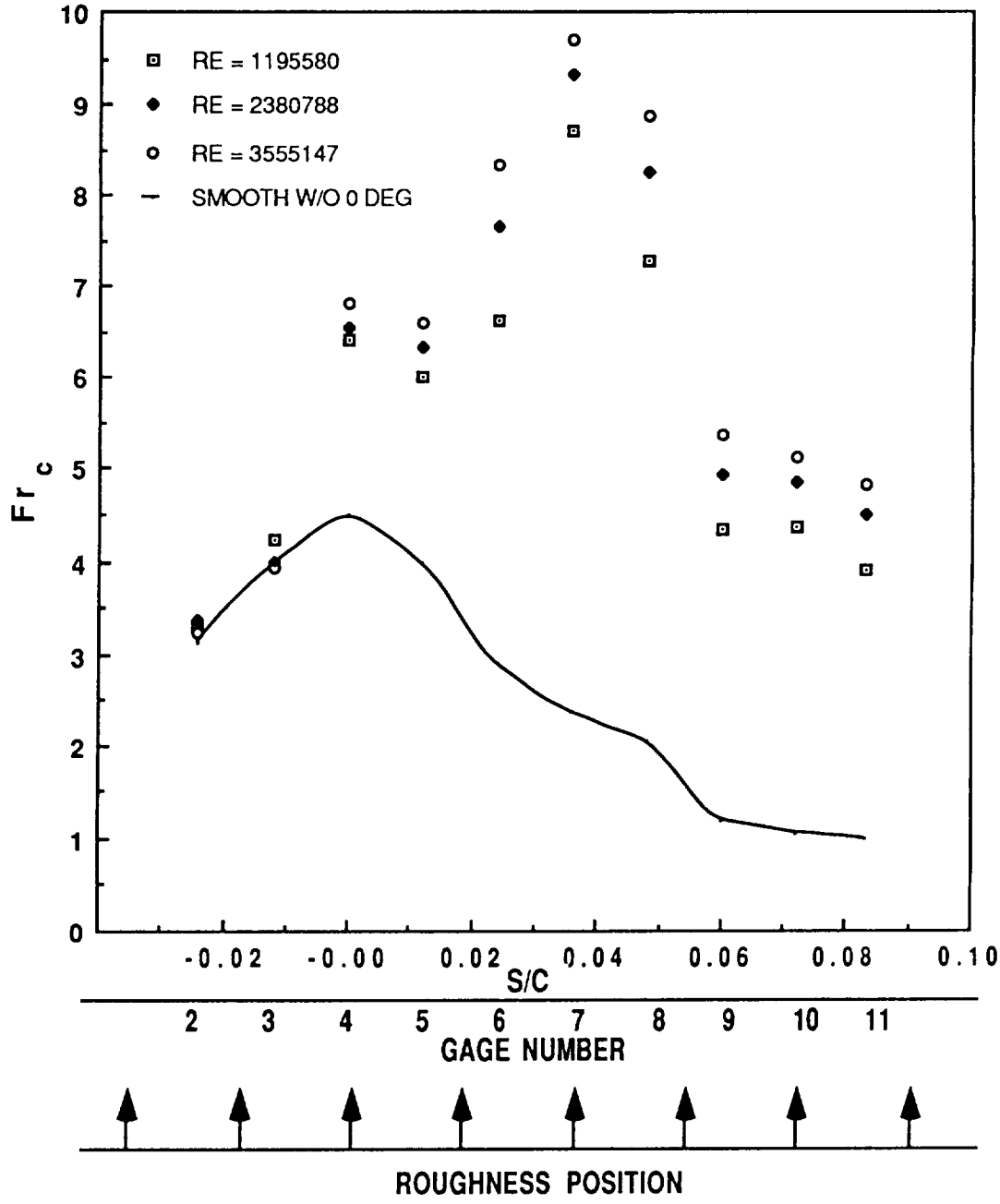

Figure 71. Frossling Number versus dimensionless surface distance: dense 2 *roughness*, 6 degree angle of attack, with spray air, IRT data.

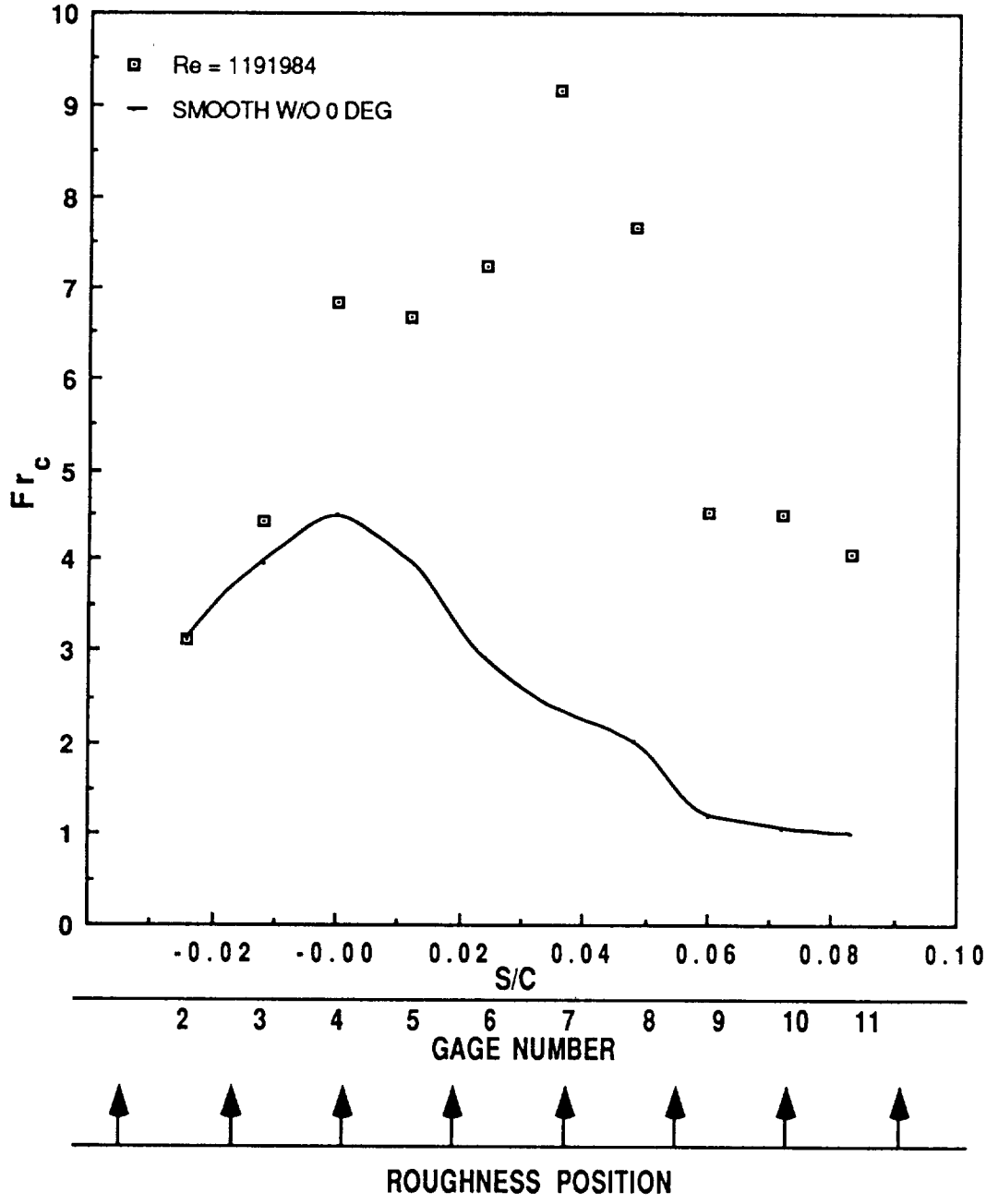

Figure 72. Frossling Number versus dimensionless surface distance: dense 2 roughness, 8 degree angle of attack, no spray air, IRT data.

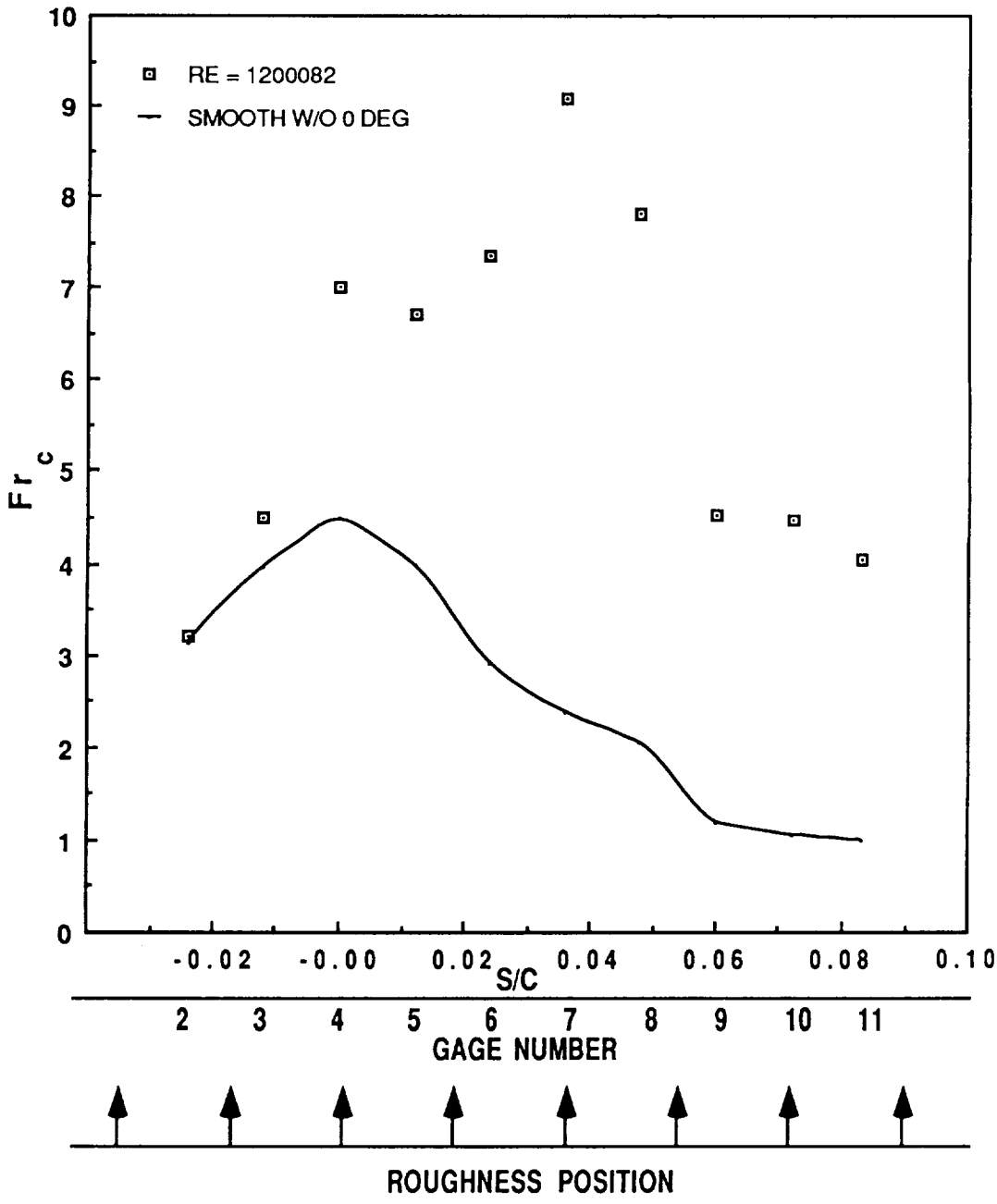

Figure 73. Frossling Number versus dimensionless surface distance: dense 2 roughness, 8 degree angle of attack, with spray air, IRT data.

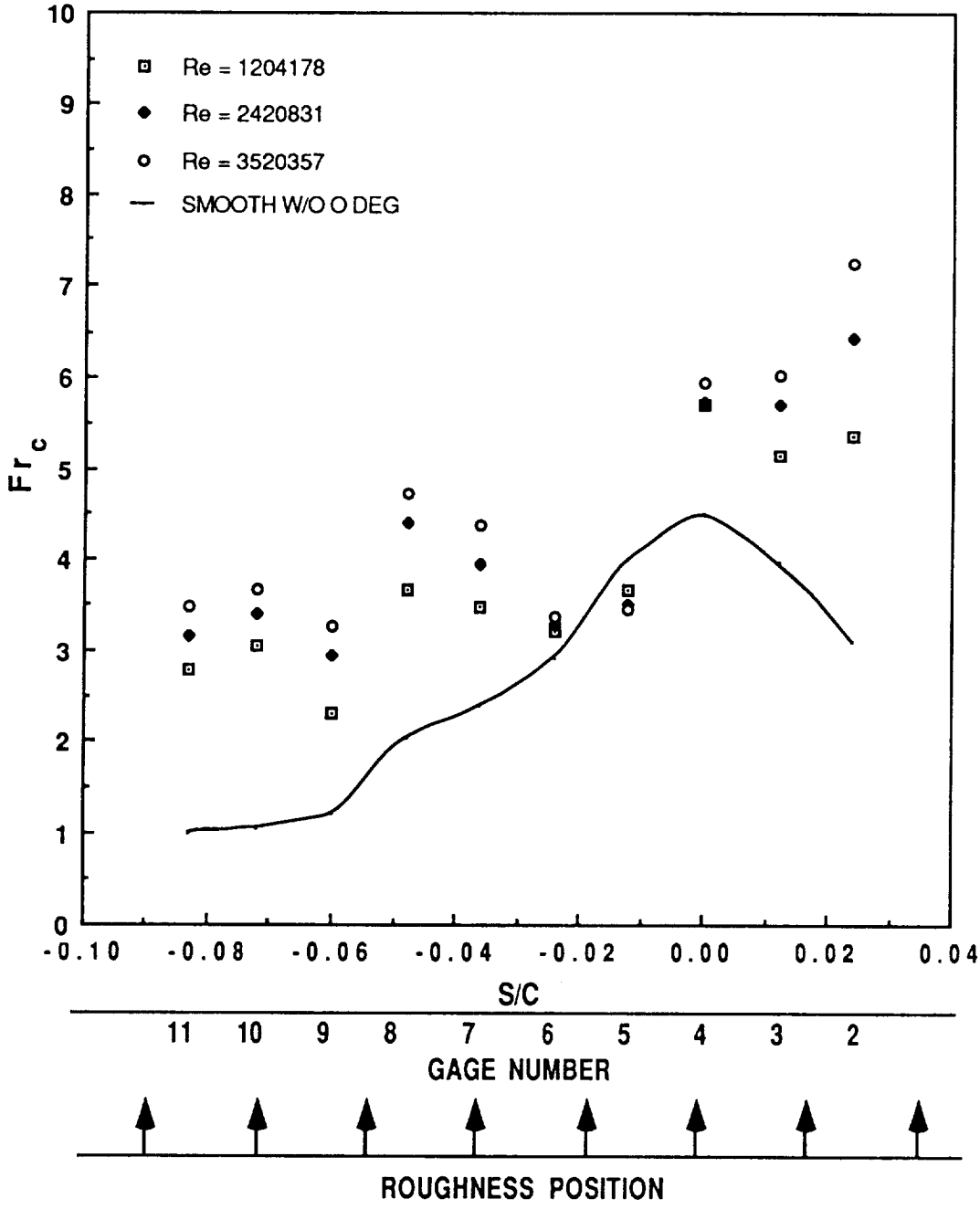

Figure 74. Frossling Number versus dimensionless surface distance: dense 2 roughness, -4 degree angle of attack, no spray air, IRT data.

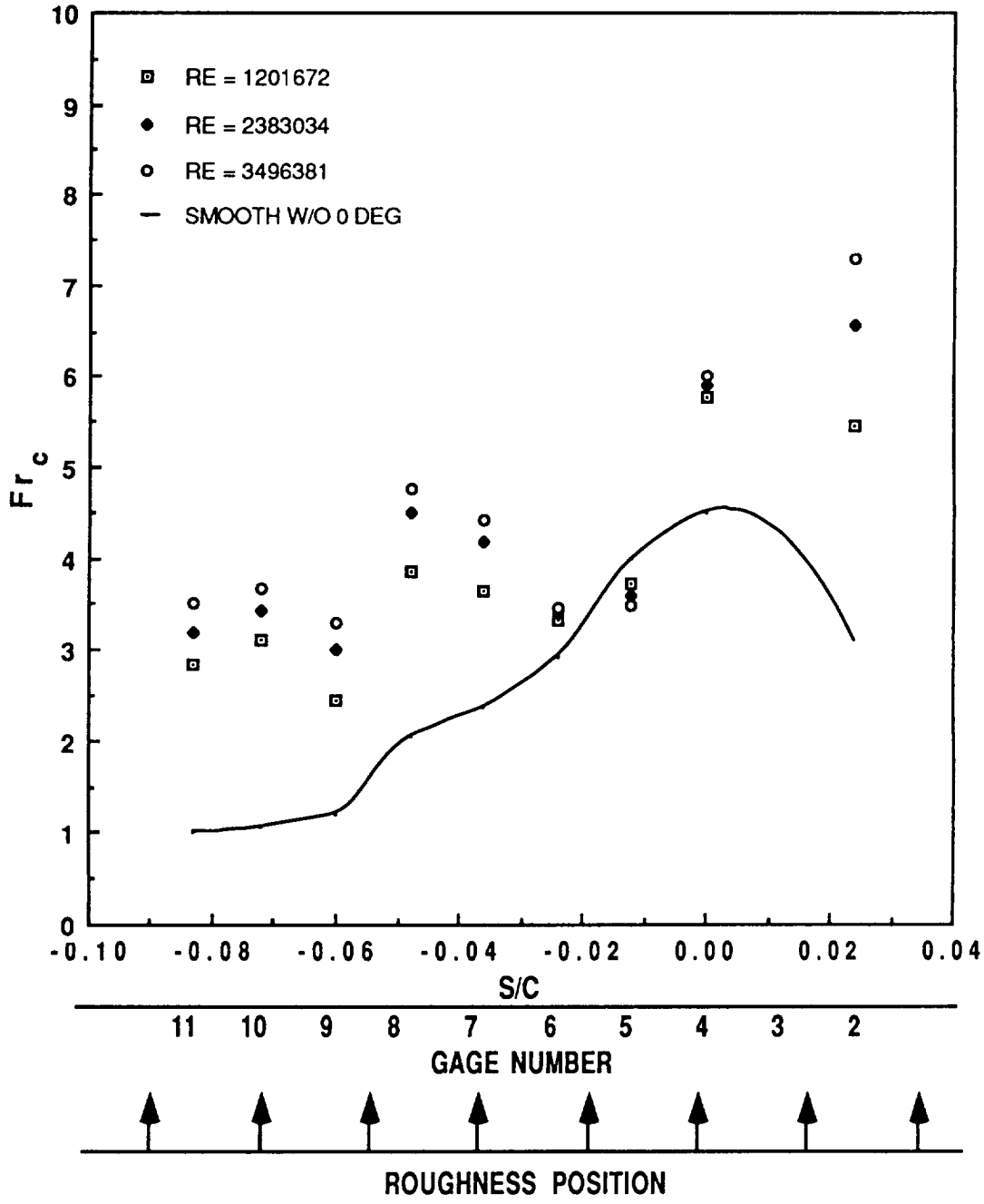

Figure 75. Frossling Number versus dimensionless surface distance: dense 2 roughness, -4 degree angle of attack, with spray air, IRT data.

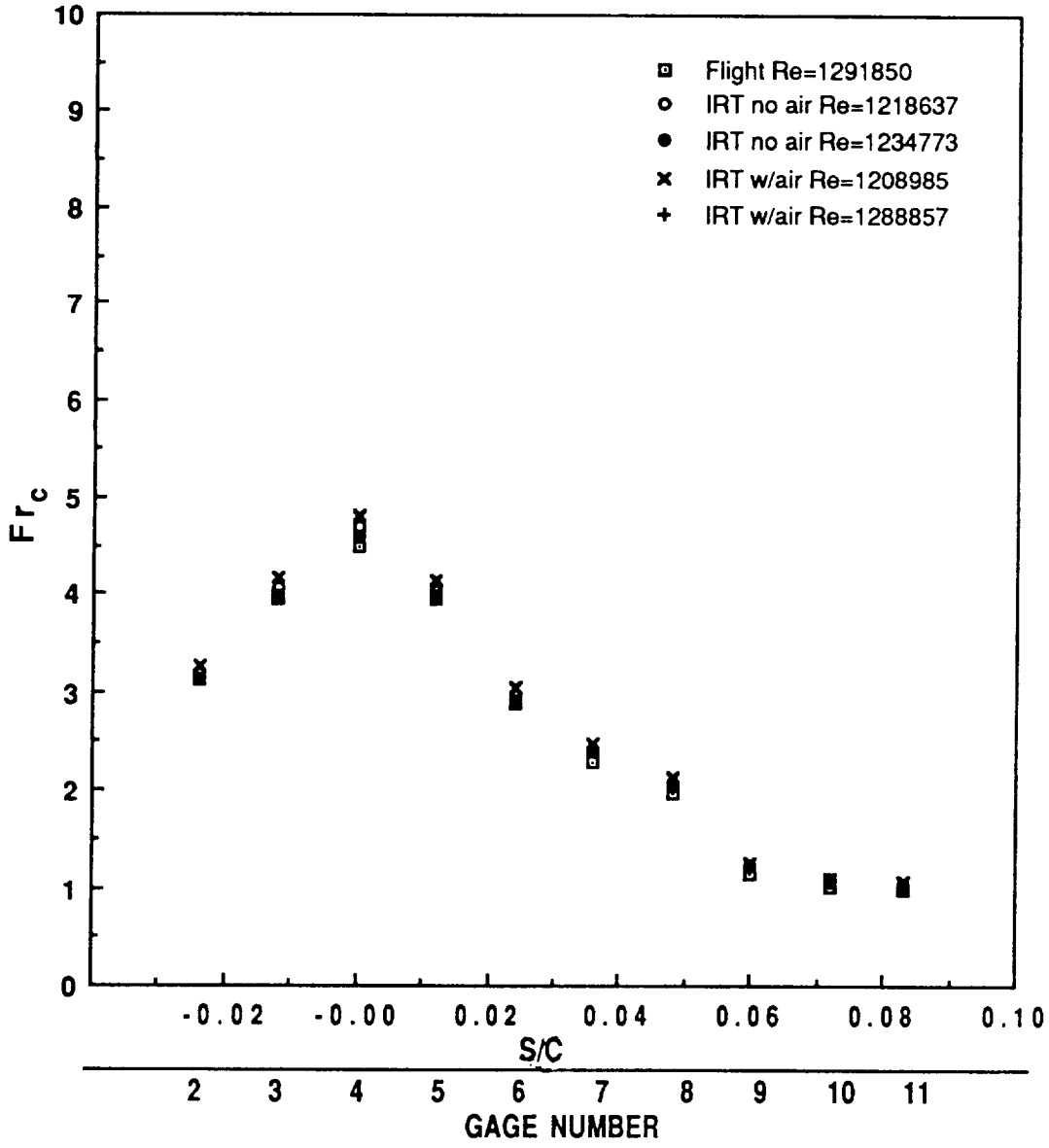

Figure 76. Frossling Number comparison for smooth airfoil, 0 degree angle of attack: flight data versus IRT data (with and without spray) for Re=1.2x10^6.

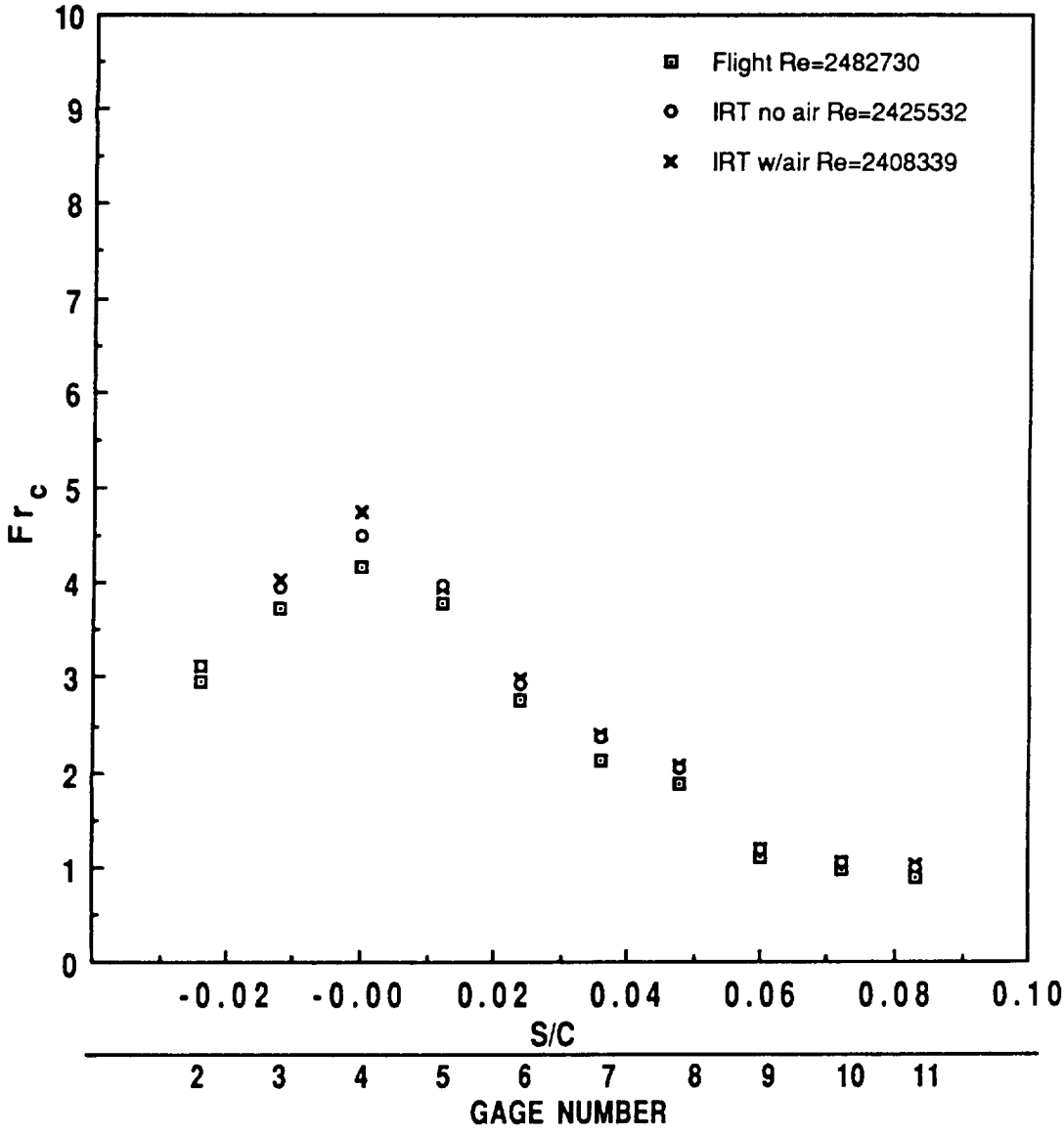

Figure 77. Frossling Number comparison for smooth airfoil, 0 degree angle of attack: flight data versus IRT data (with and without spray) for Re=2.4x10 6

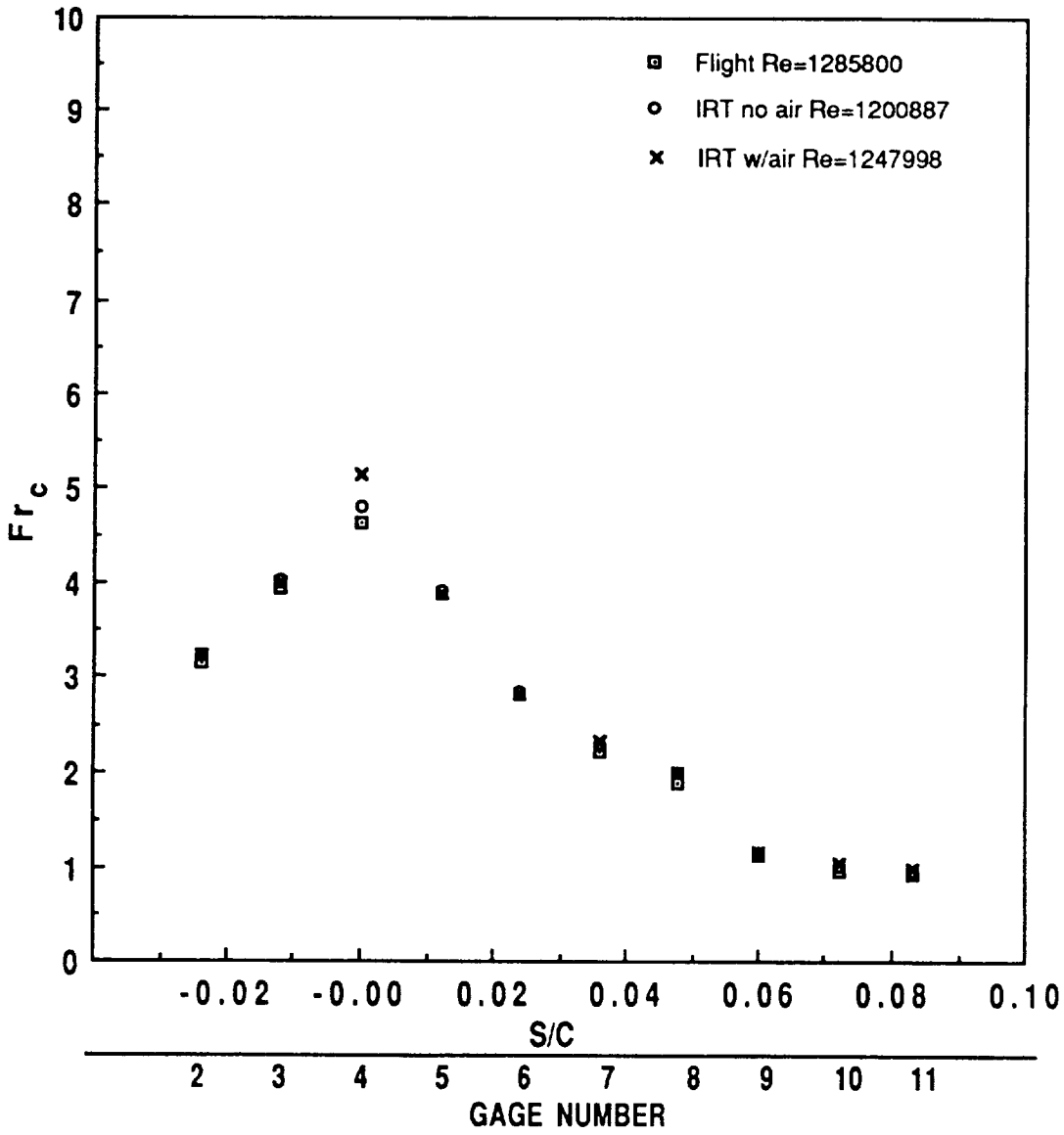

Figure 78. Frossling Number comparison for smooth airfoil, 2 degree angle of attack: flight data versus IRT data (with and without spray) for Re=1.2x10^6.

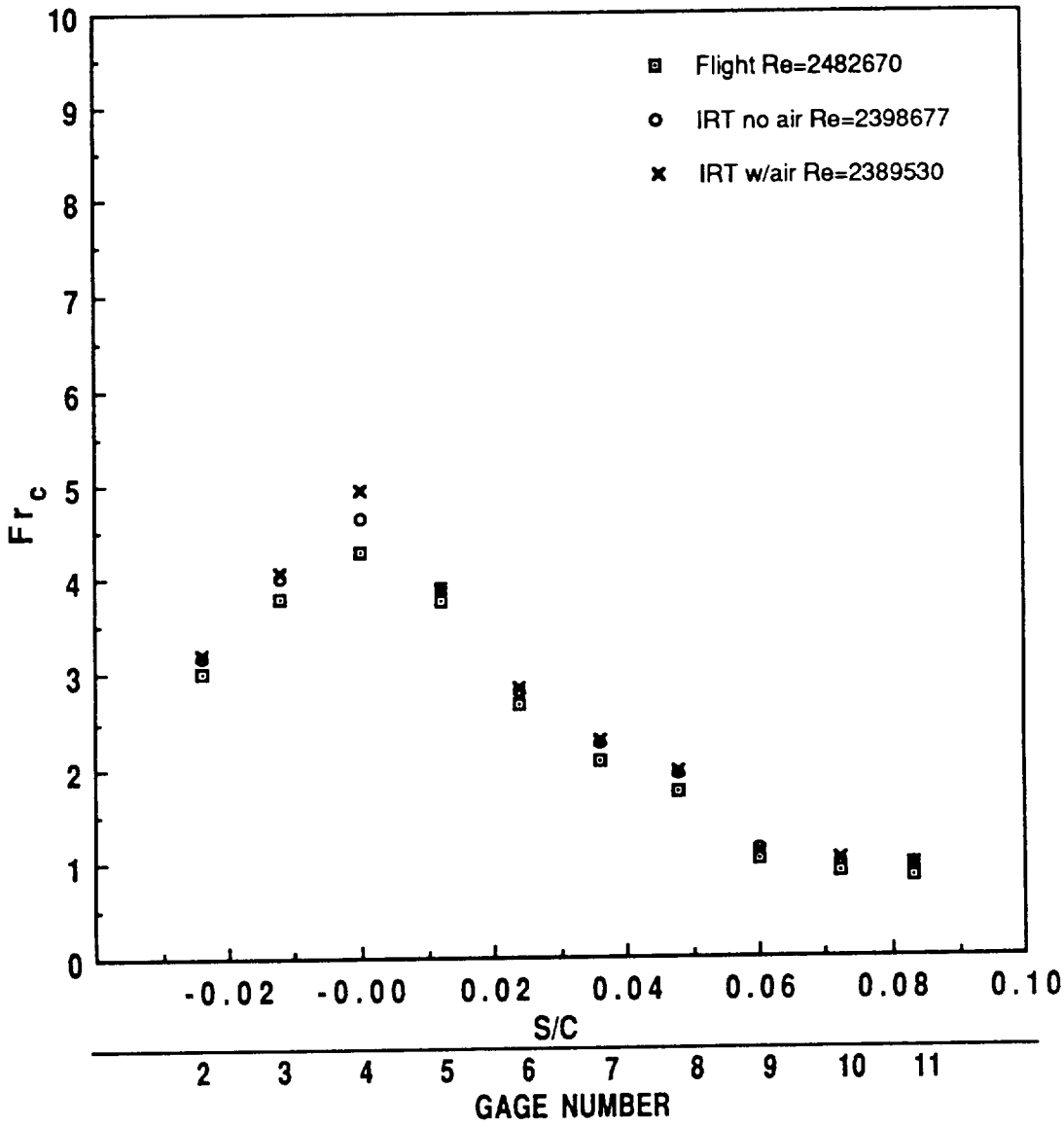

Figure 79. Frossling Number comparison for smooth airfoil, 2 degree angle of attack: flight data versus IRT data (with and without spray) for $Re=2.4x10^6$.

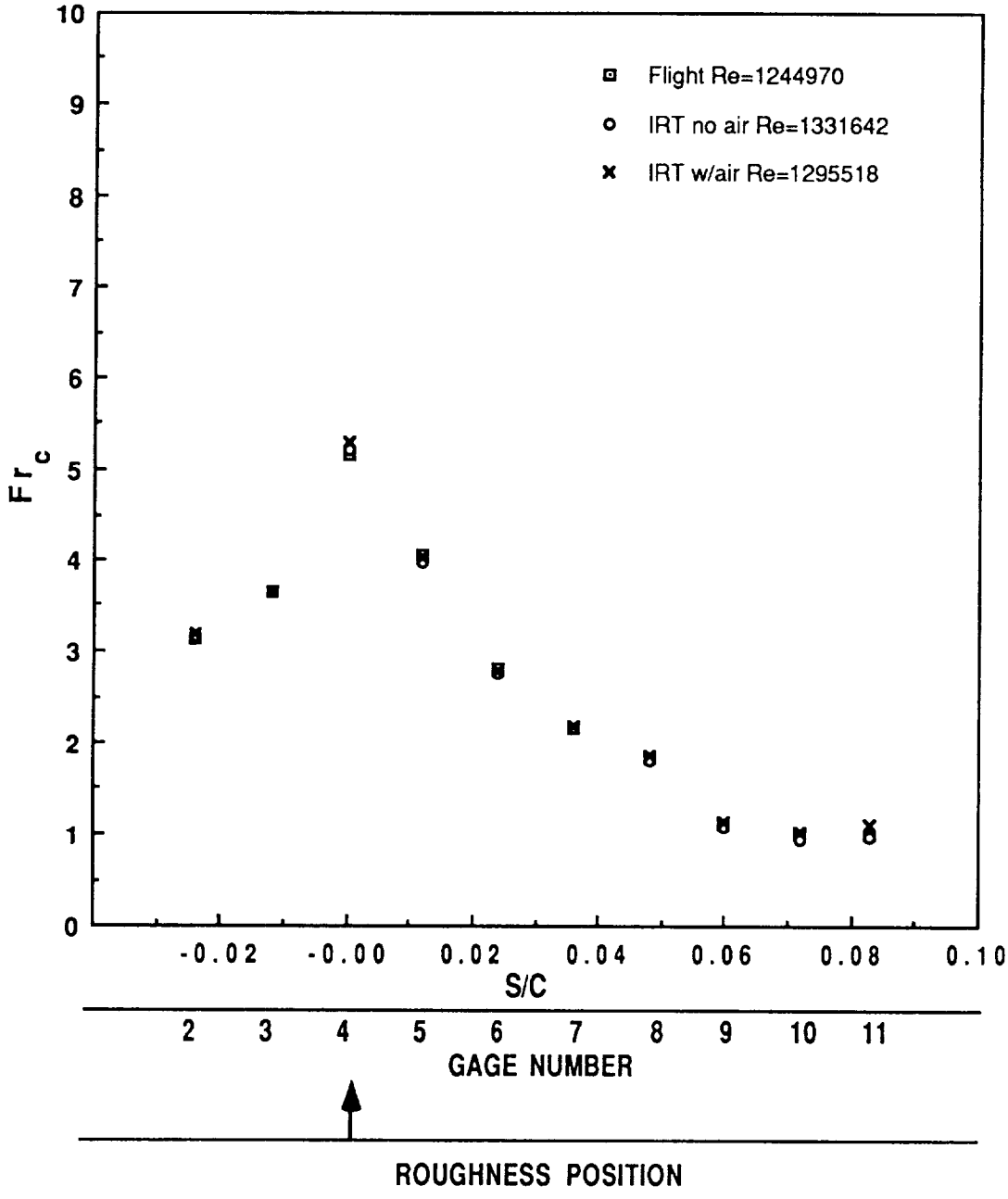

Figure 80. Frossling Number comparison for airfoil with leading edge roughness, 4 degree angle of attack: flight data versus IRT data (with and without spray) for Re=1.2x10 .[6]

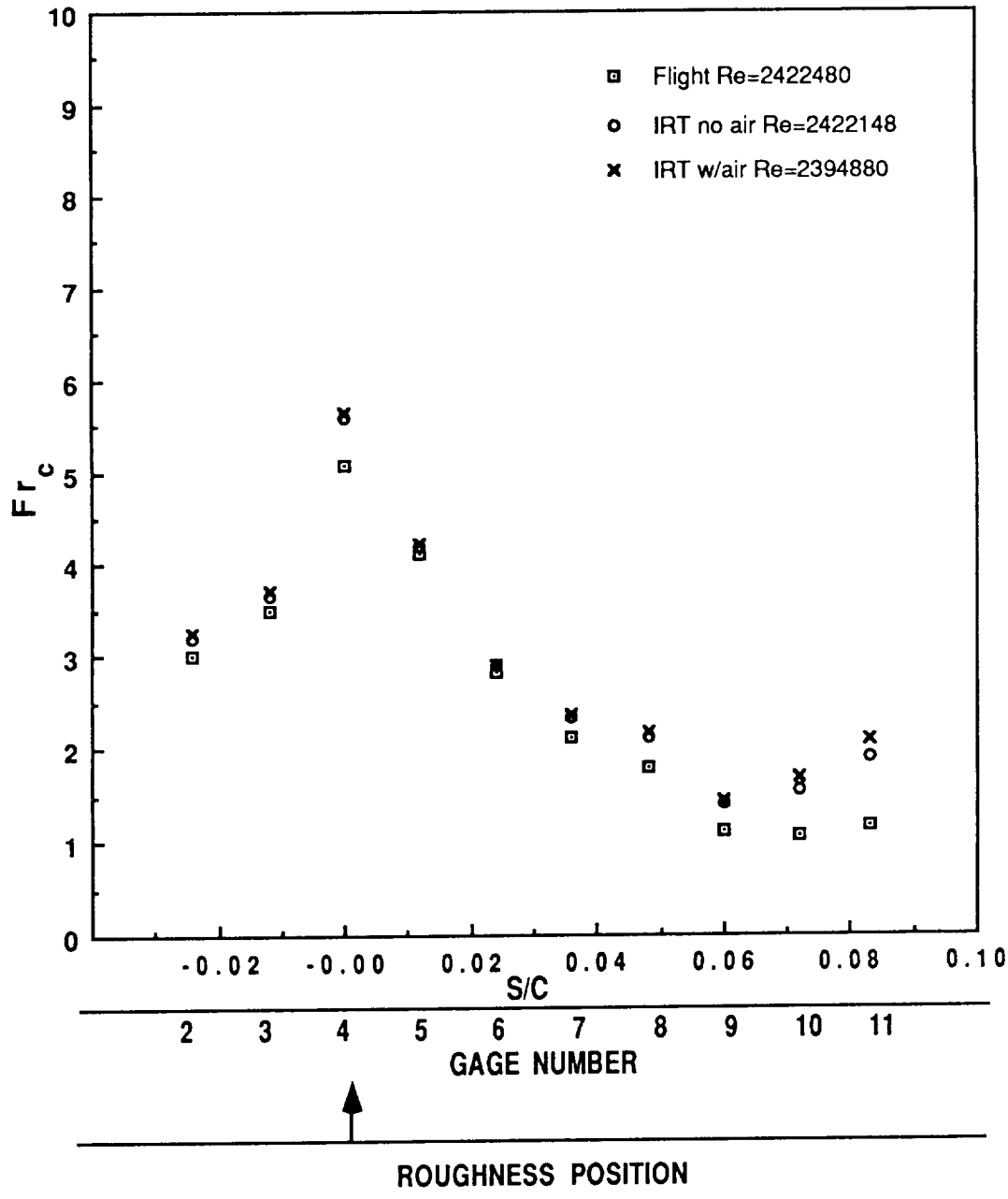

Figure 81. Frossling Number comparison for airfoil with leading edge roughness, 4 degree angle of attack: flight data versus IRT data (with and without spray) for $Re=2.4x10^6$.

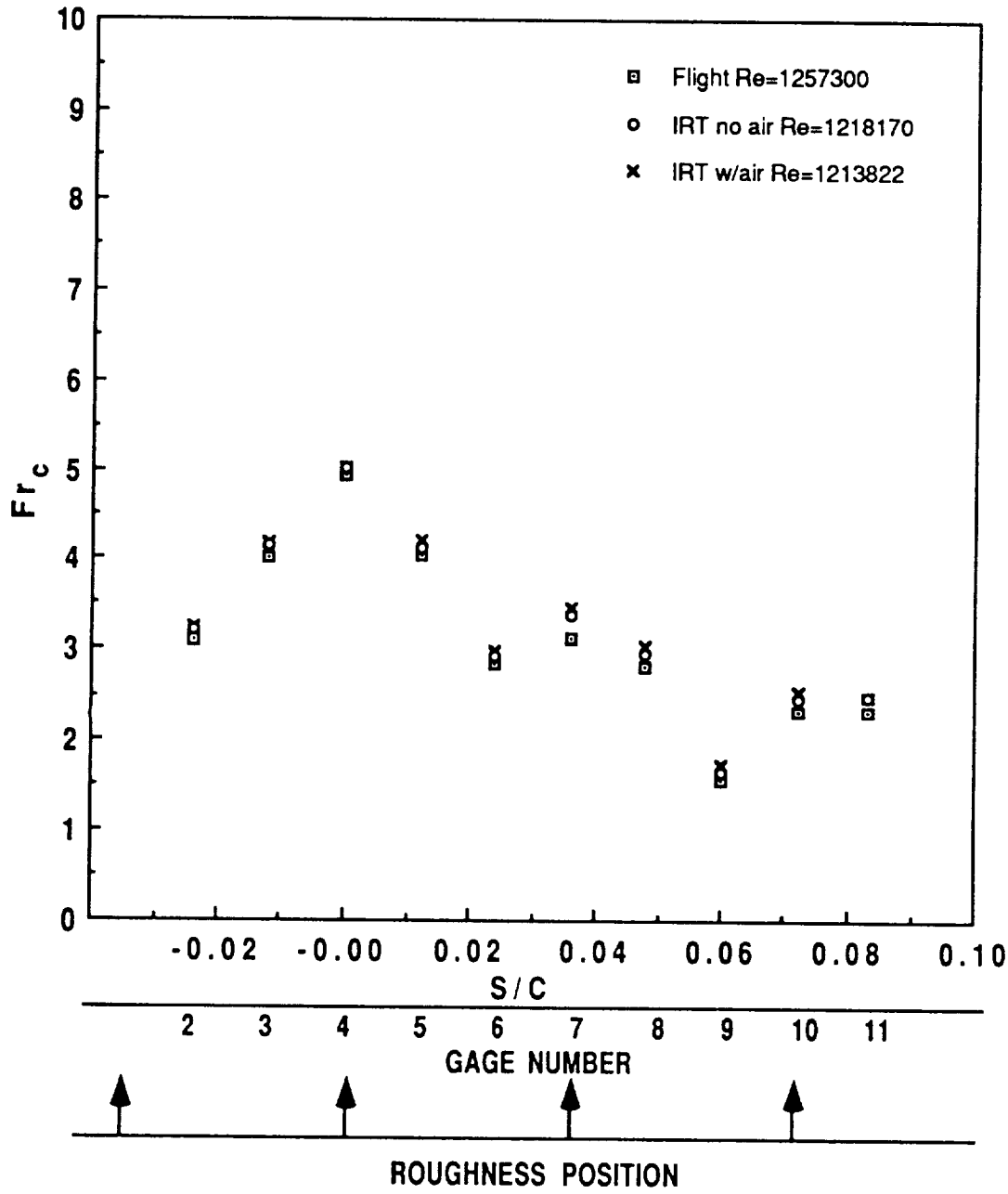

Figure 82. Frossling Number comparison for airfoil with sparse roughness, 0 degree angle of attack: flight data versus IRT data (with and without spray) for Re=1.2x10 ^{6}

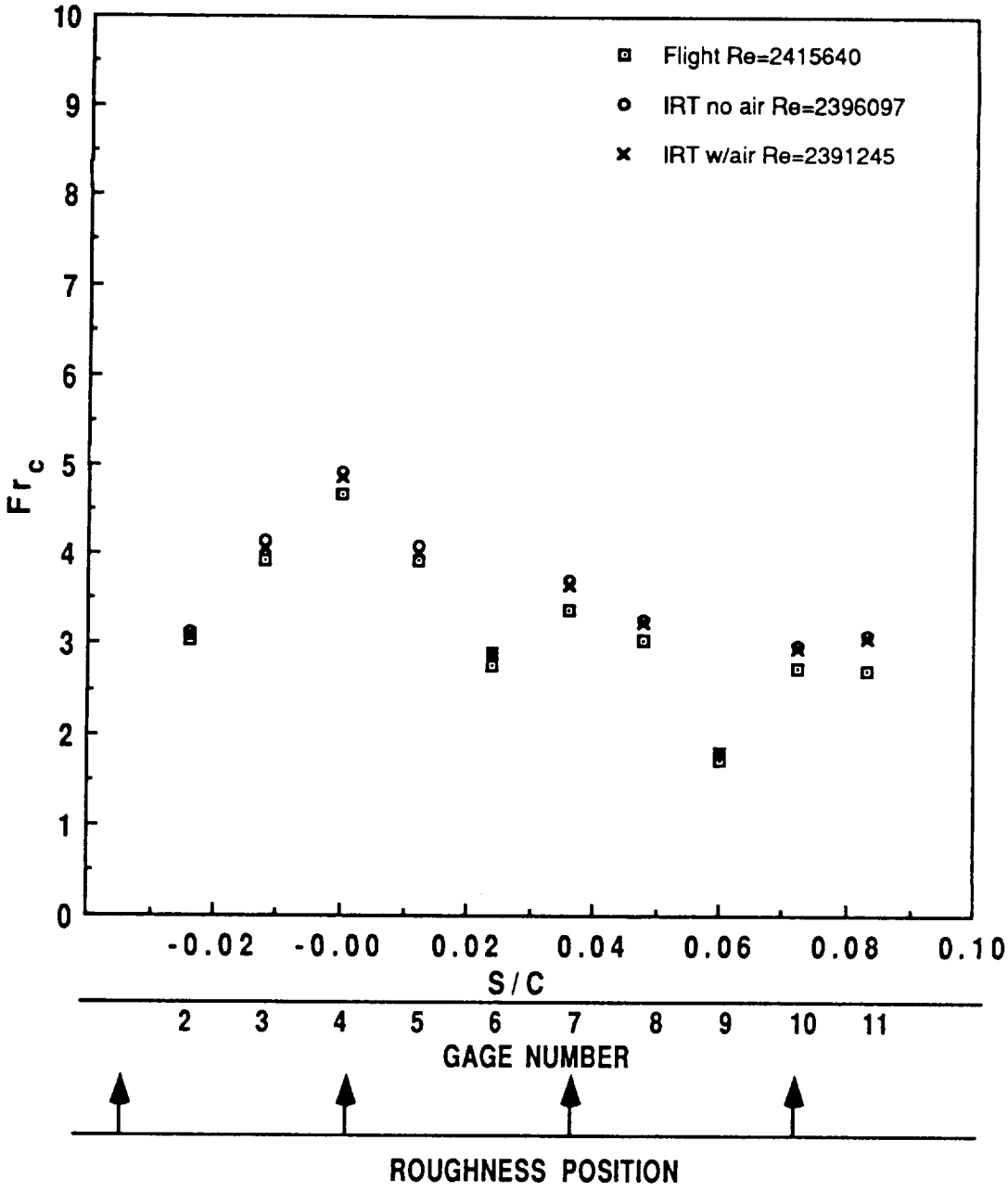

Figure 83. Frossling Number comparison for airfoil with sparse roughness, 0 degree angle of attack: flight data versus IRT data (with and without spray) for Re=2.4x10^6

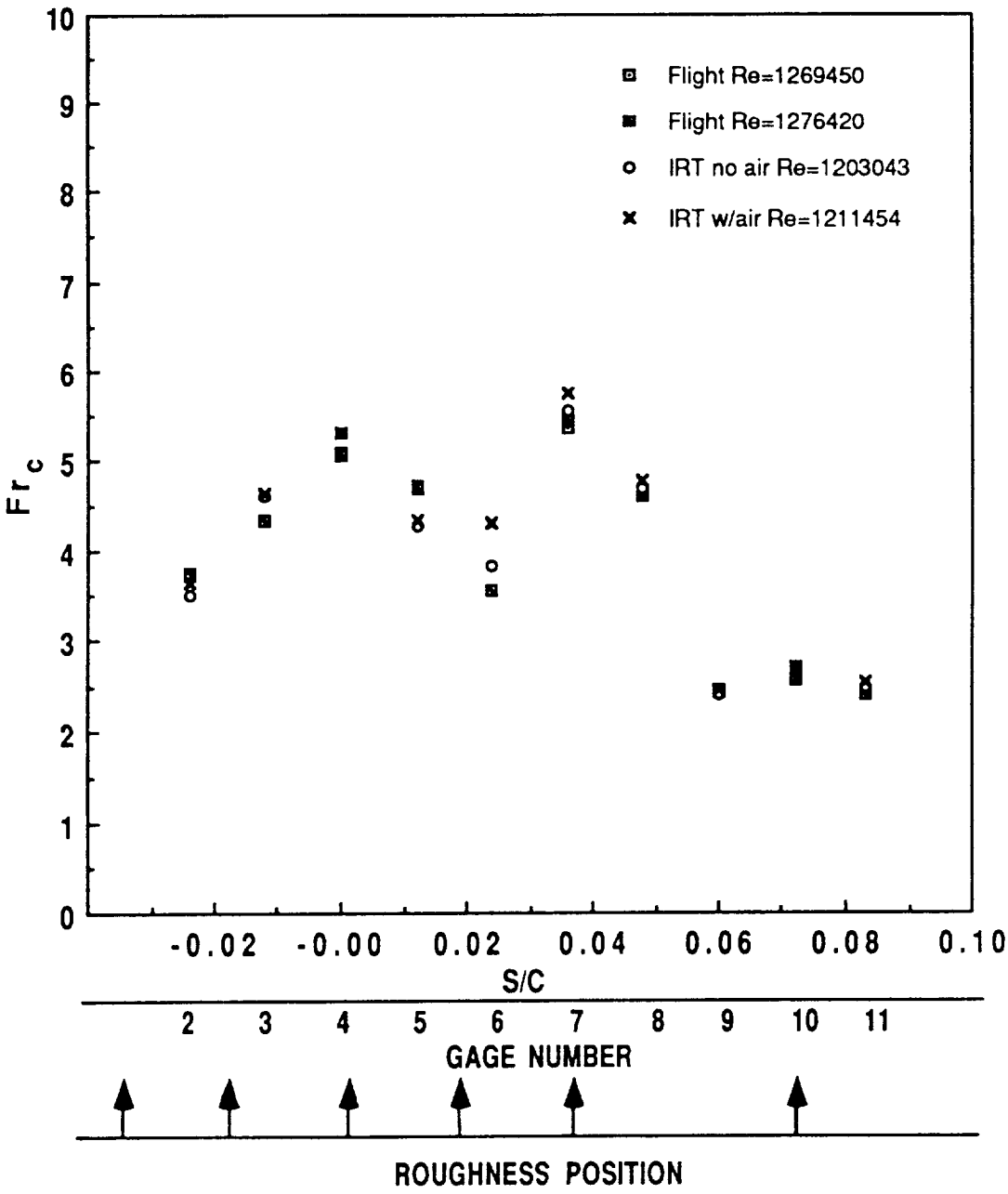

Figure 84. Frossling Number comparison for airfoil with dense 1 roughness, 0 degree angle of attack: flight data versus IRT data (with and without spray) for $Re=1.2x10^6$.

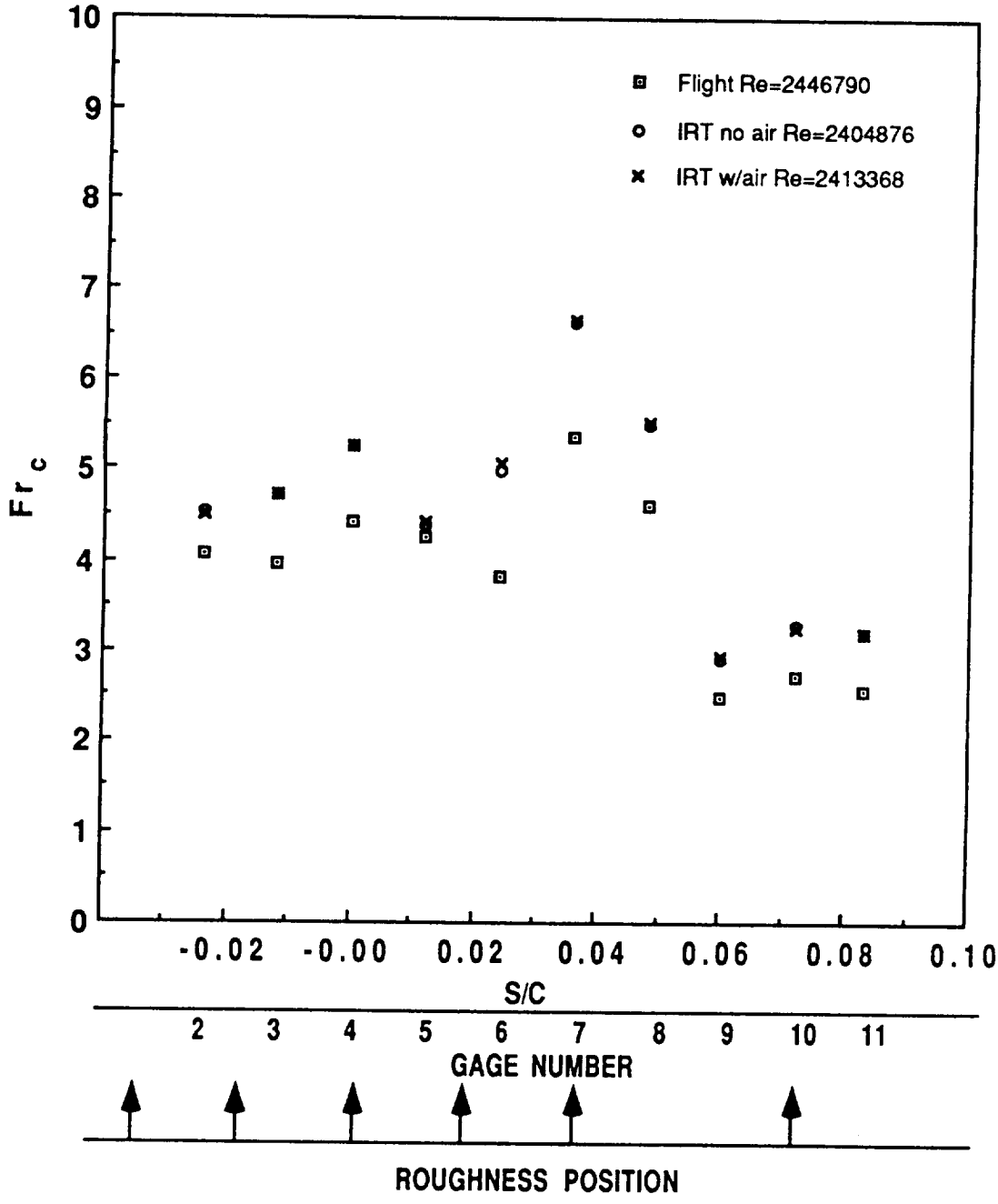

Figure 85. Frossling Number comparison for airfoil with dense 1 roughness, 0 degree angle of attack: flight data versus IRT data (with and without spray) for Re=2.4x10 ^{6}

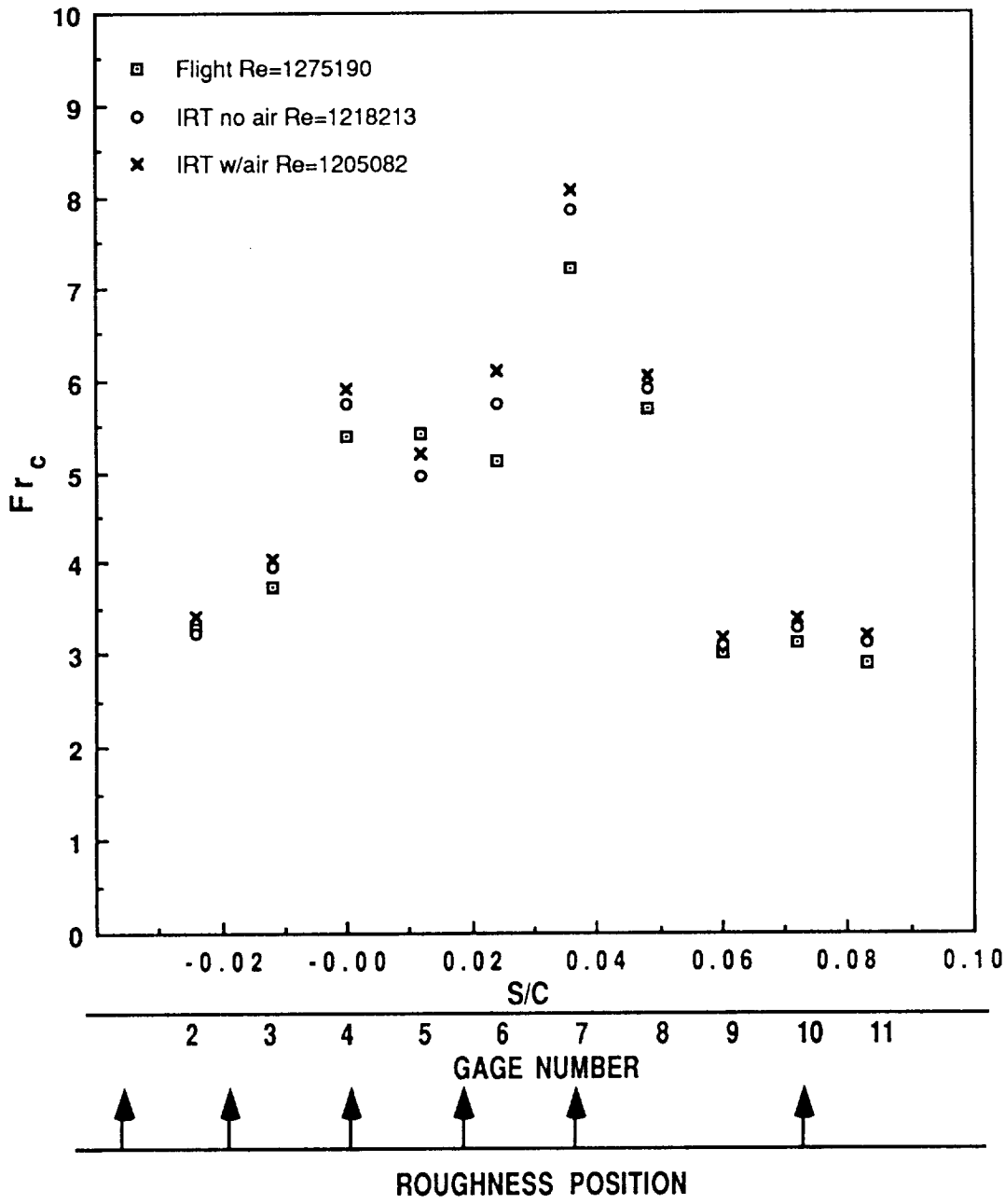

Figure 86. Frossling Number comparison for airfoil with dense 1 roughness, 4 degree angle of attack: flight data versus IRT data (with and without spray) for Re=1.2x10^6

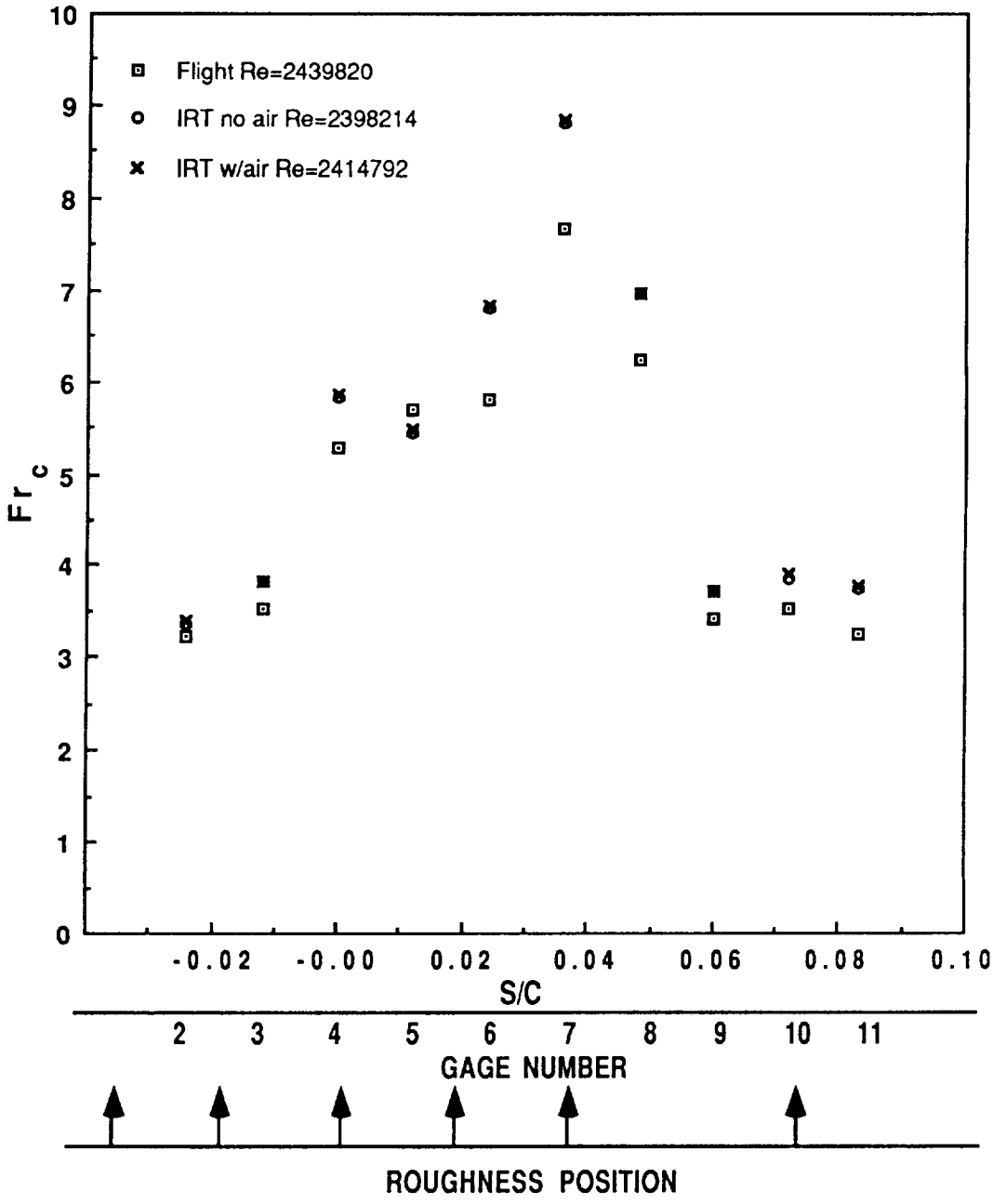

Figure 87. Frossling Number comparison for airfoil with dense 1 roughness, 4 degree angle of attack: flight data versus IRT data (with and without spray) for Re=2.4x10 ^{6}

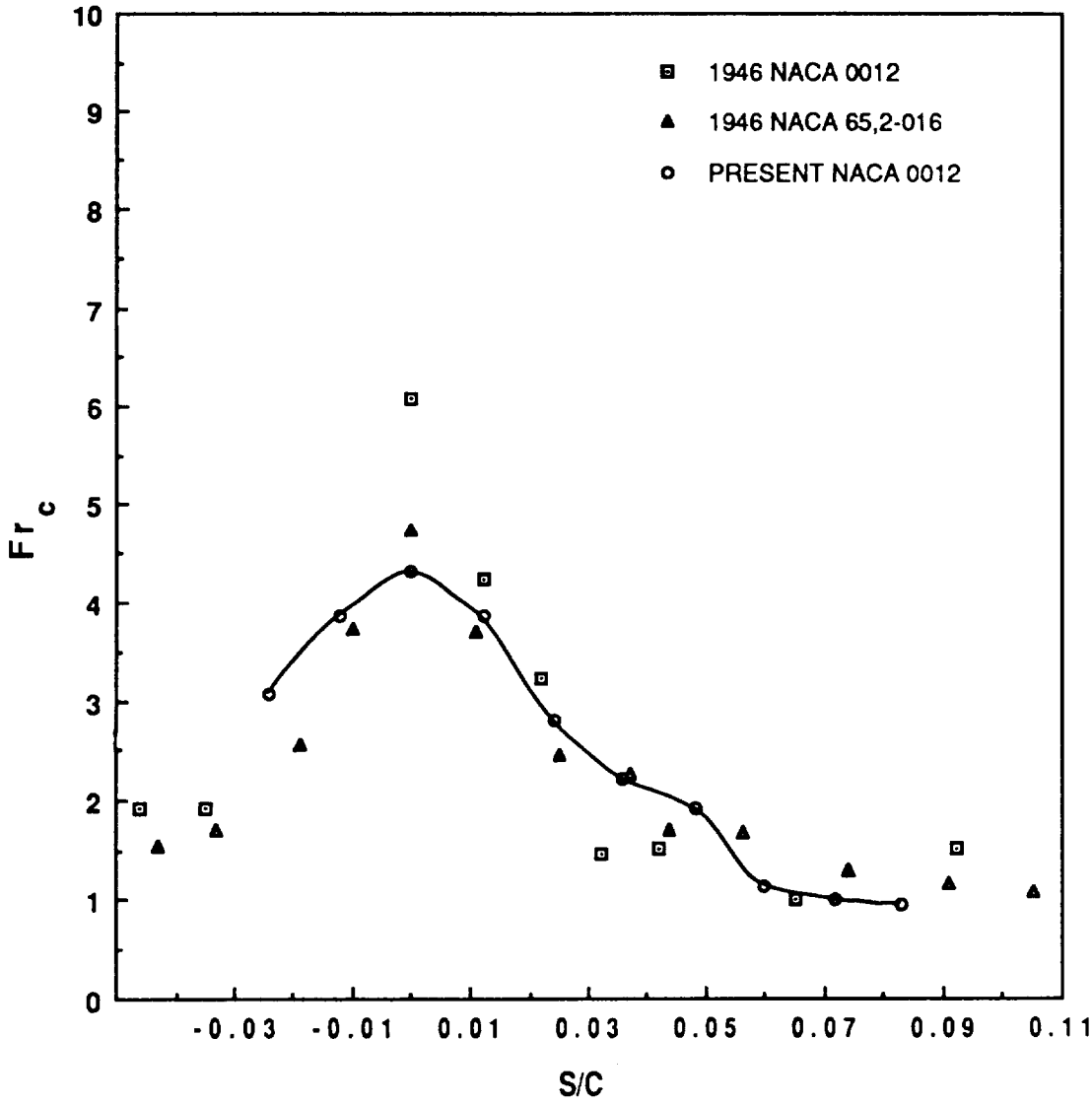

Figure 88. Frossling Number comparison for smooth airfoil, 0 degree angle of attack: present flight data versus previous NACA flight data [11].

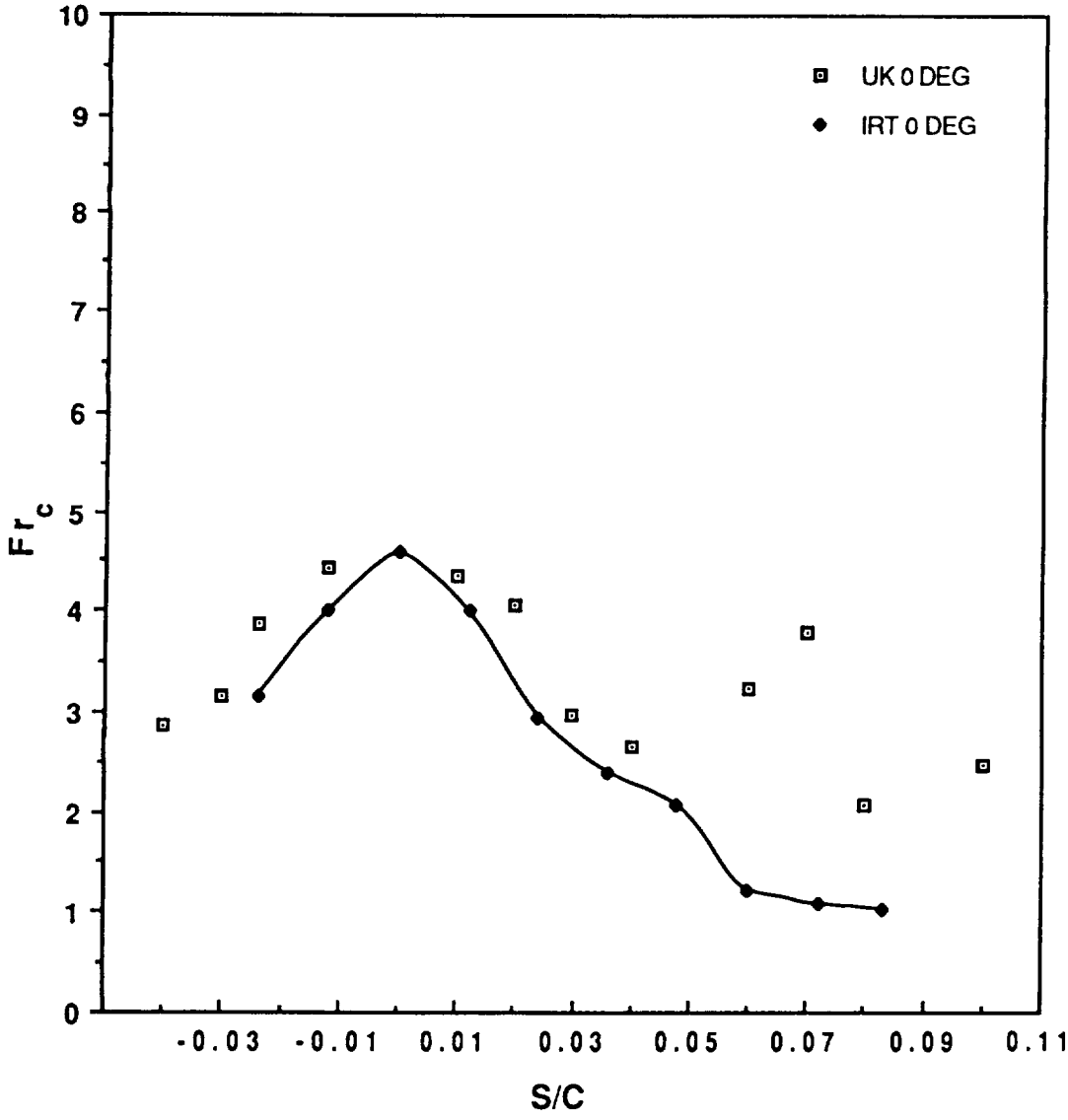

Figure 89. Frossling Number comparison for smooth airfoil, 0 degree angle of attack: present IRT data versus University of Kentucky tunnel data [14].

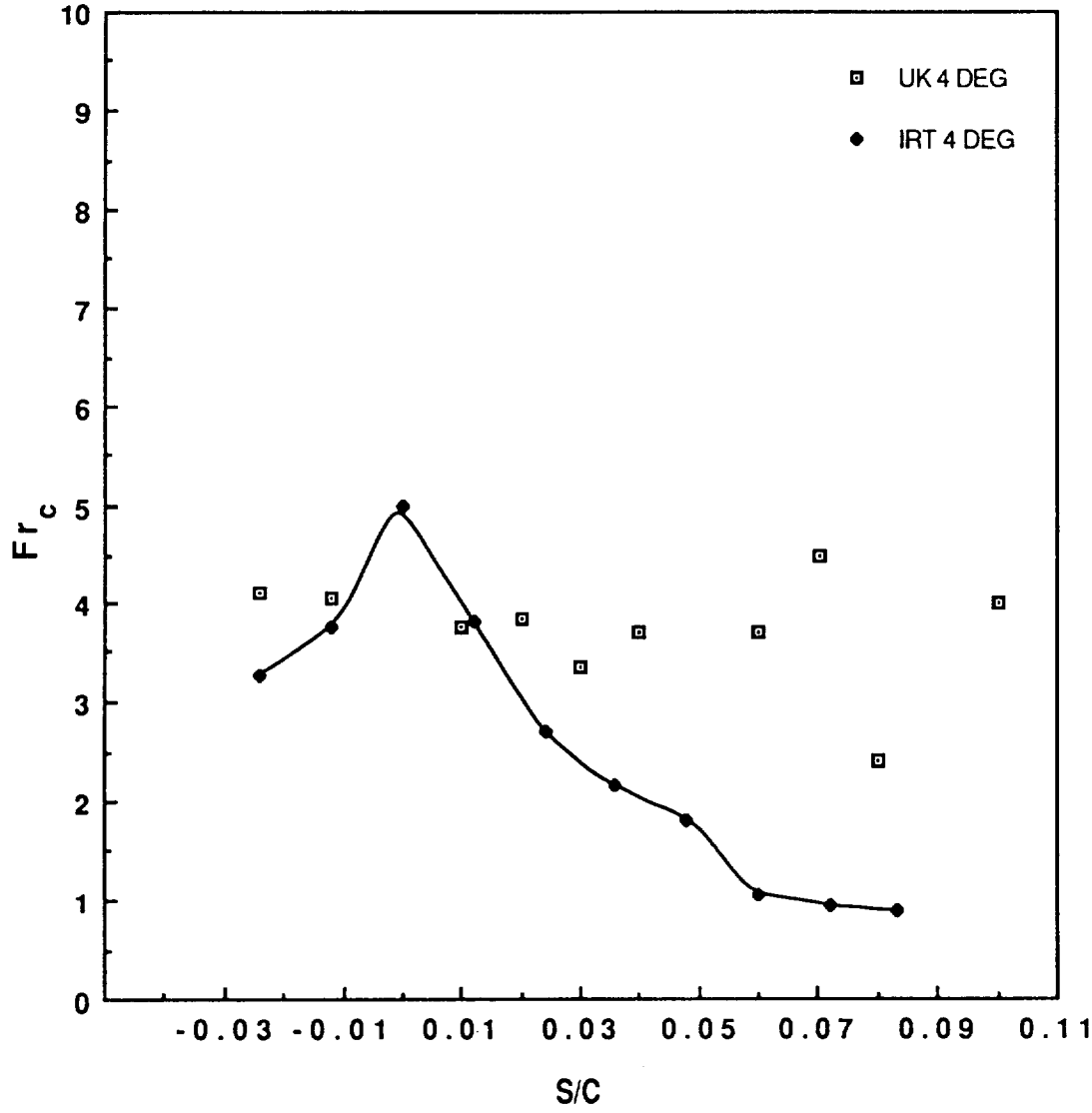

Figure 90. Frossling Number comparison for smooth airfoil, 4 degree angle of attack: present IRT data versus University of Kentucky tunnel data [14].

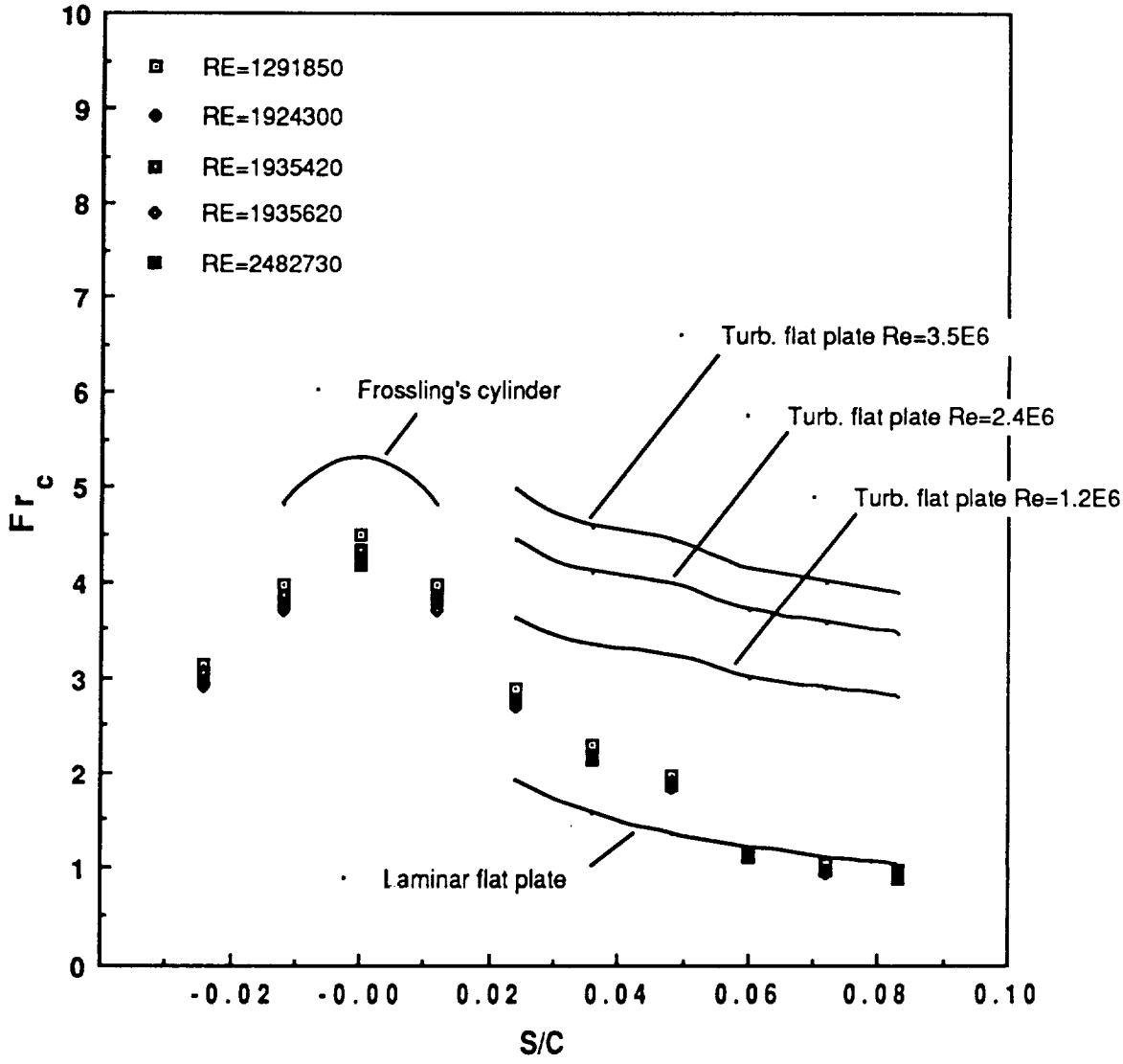

Figure 91. Frossling Number comparison for smooth airfoil, 0 degree angle of attack: flight data versus Dimensionless Correlations for Cylinder [16] and Flat Plate [17].

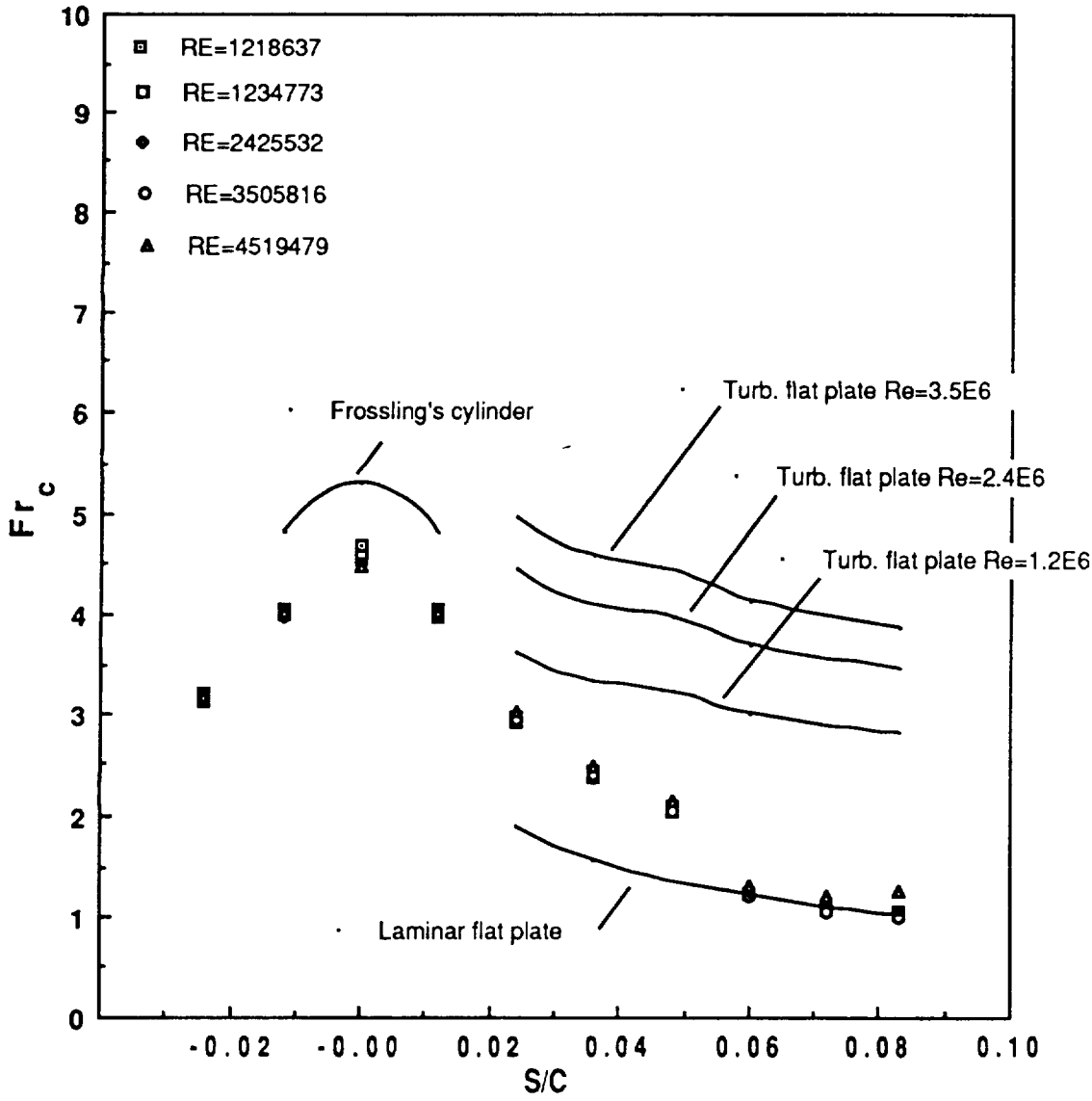

Figure 92. Frossling Number comparison for smooth airfoil, 0 degree angle of attack: IRT data (without spray) versus Dimensionless Correlations for Cylinder [16] and Flat Plate [17]

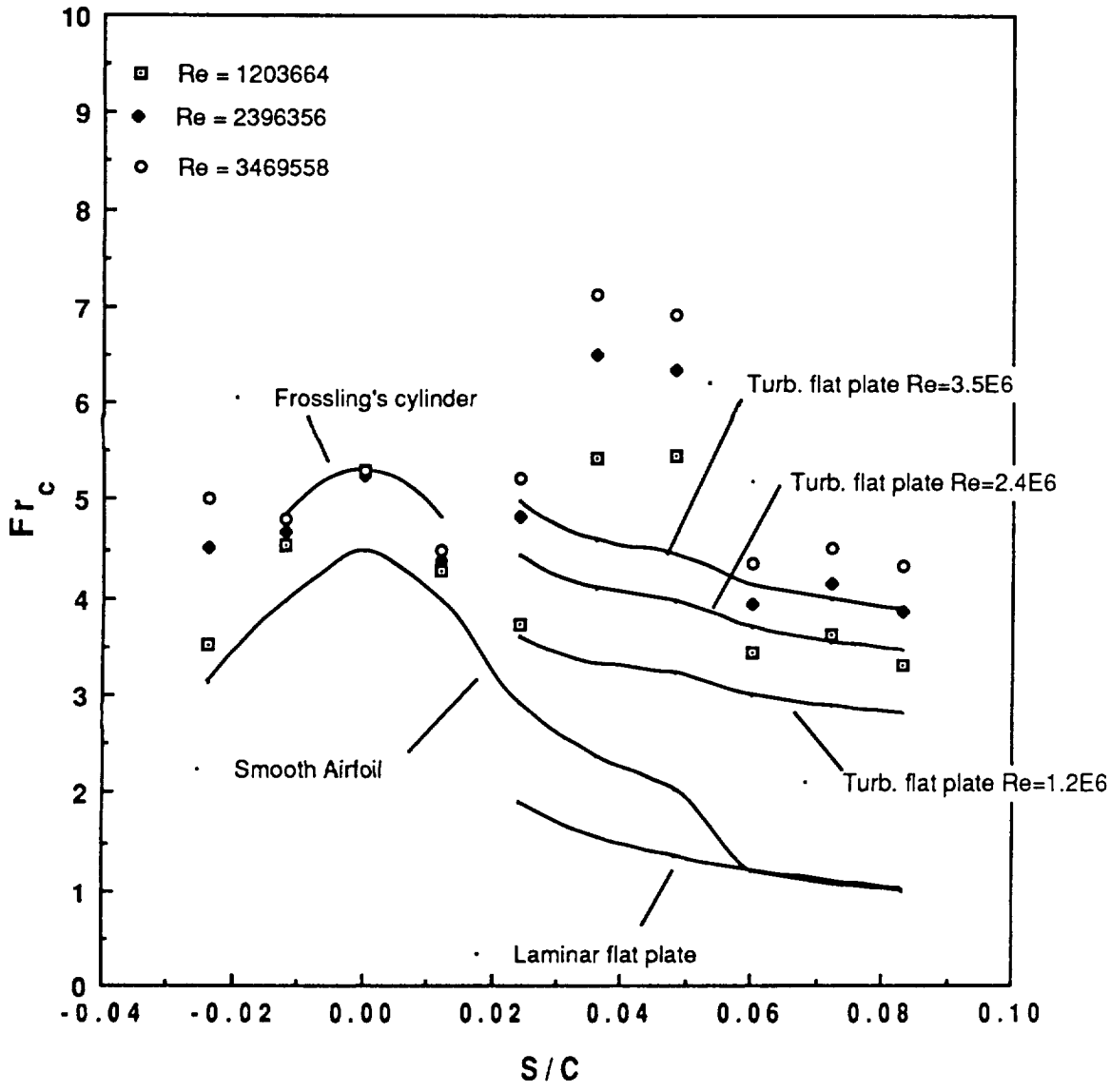

Figure 93. Frossling Number comparison for dense 2 roughness, 0 degree angle of attack: IRT data (without spray) versus Dimensionless Correlations for Cylinder [16] and Flat Plate [17].

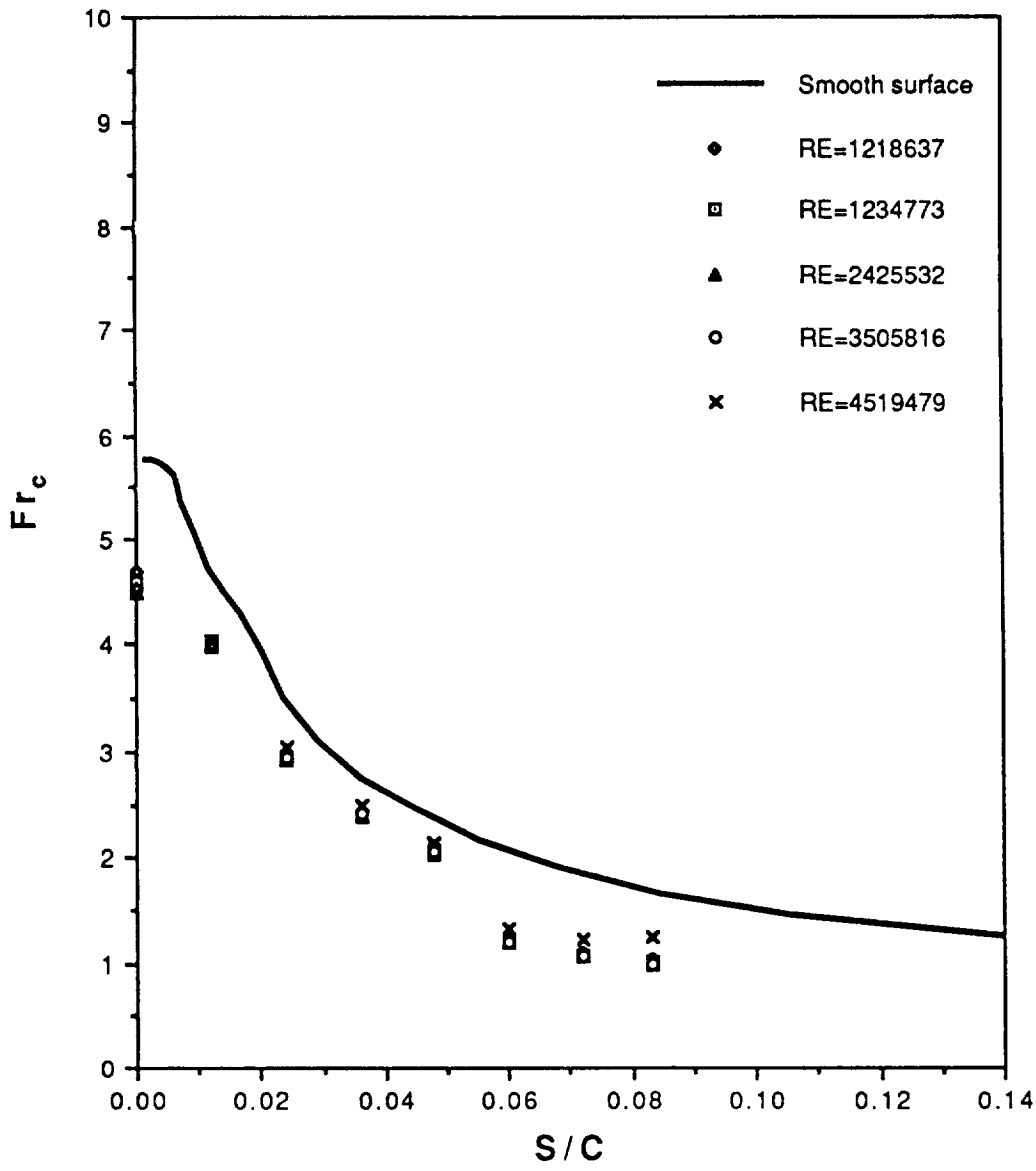

Figure 94. Frossling Number Comparison for smooth airfoil, 0 degree angle of attack: IRT data versus integral boundary layer solution.

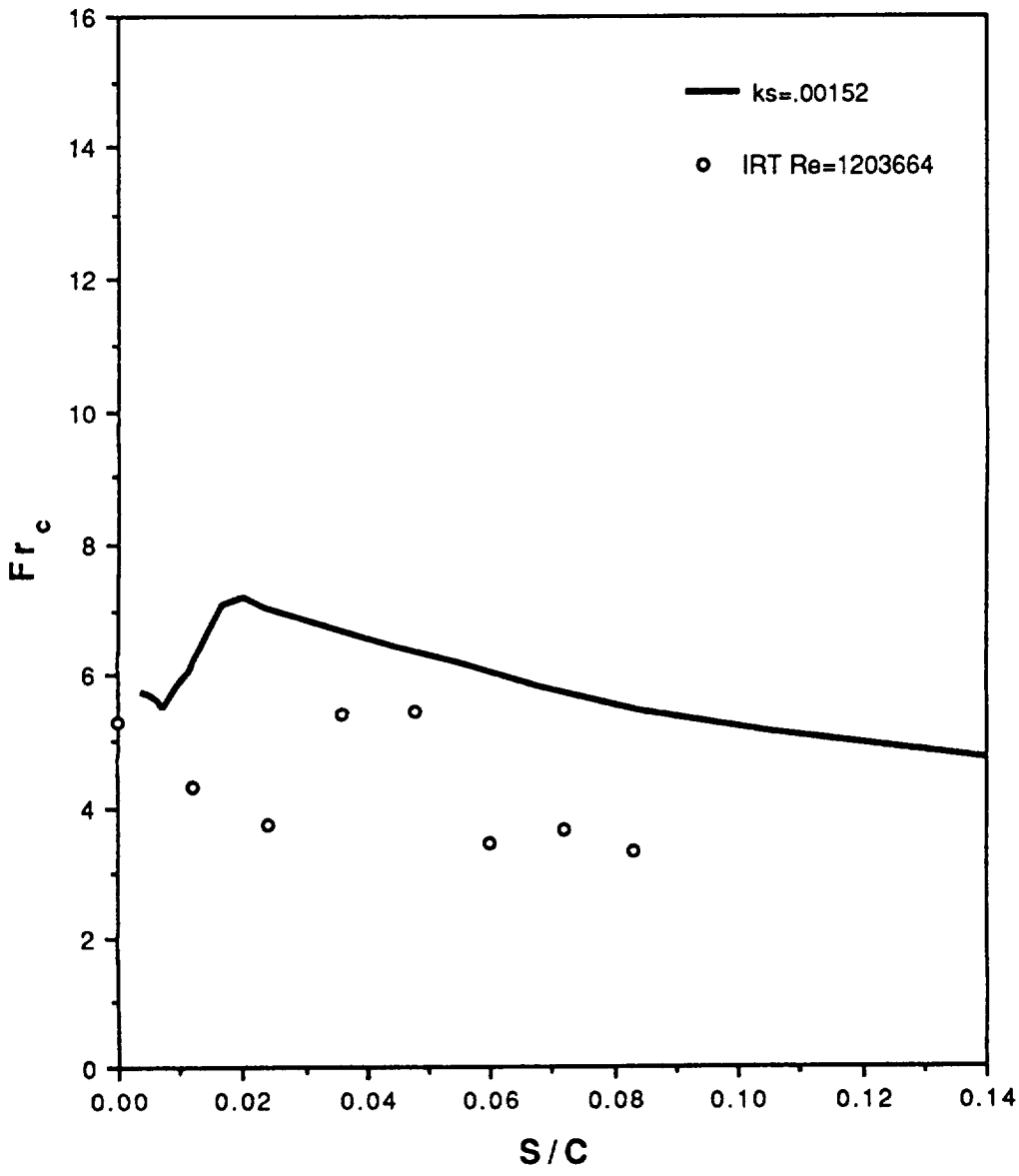

Figure 95. Frossling Number Comparison for dense 2 roughened airfoil, 105 ft/sec, 0 degree angle of attack: IRT data versus integral boundary layer solution.

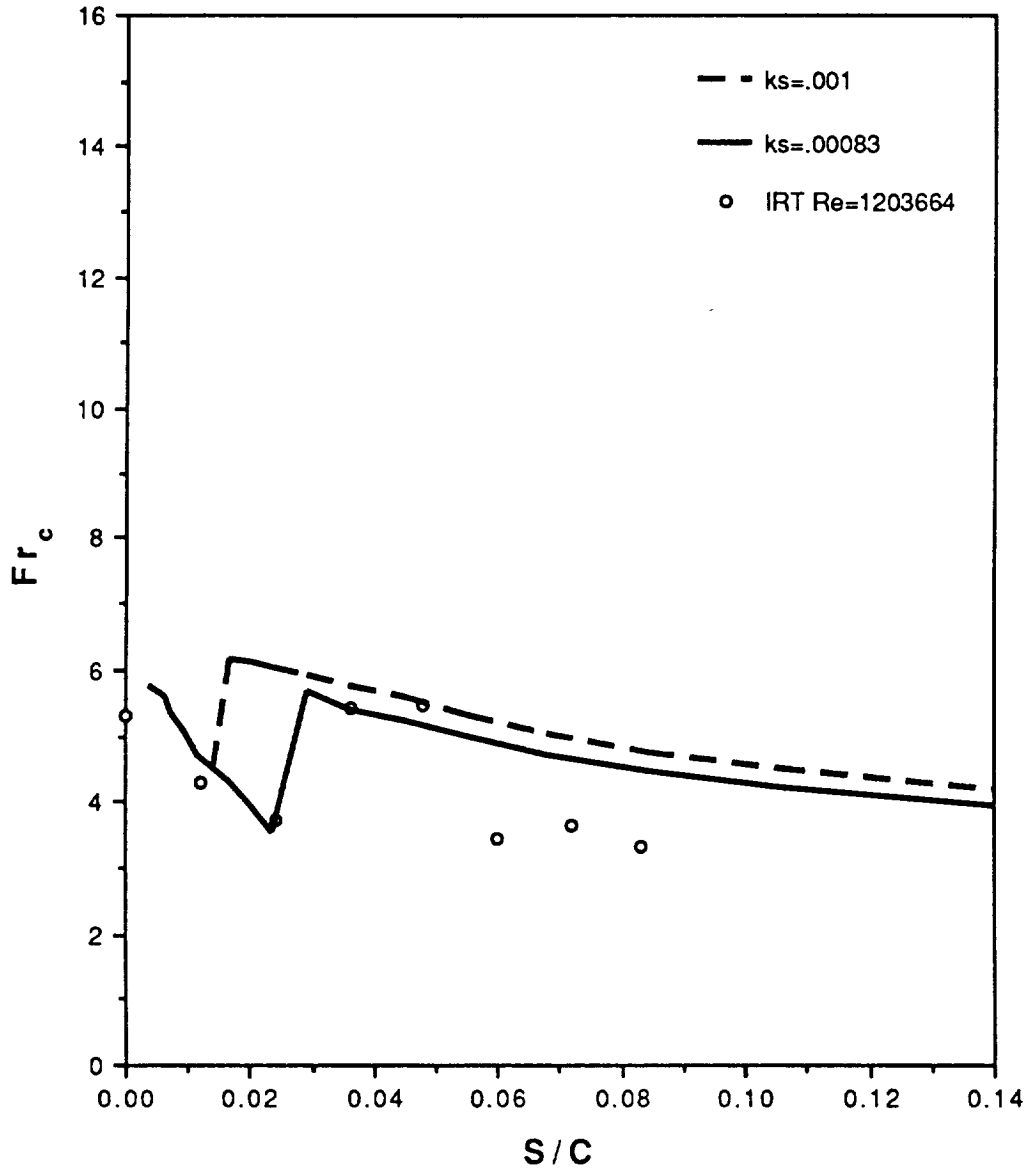

Figure 96. Frossling Number Comparison for dense 2 roughened airfoil, 105 ft/sec, 0 degree angle of attack: IRT data versus integral boundary layer solution.

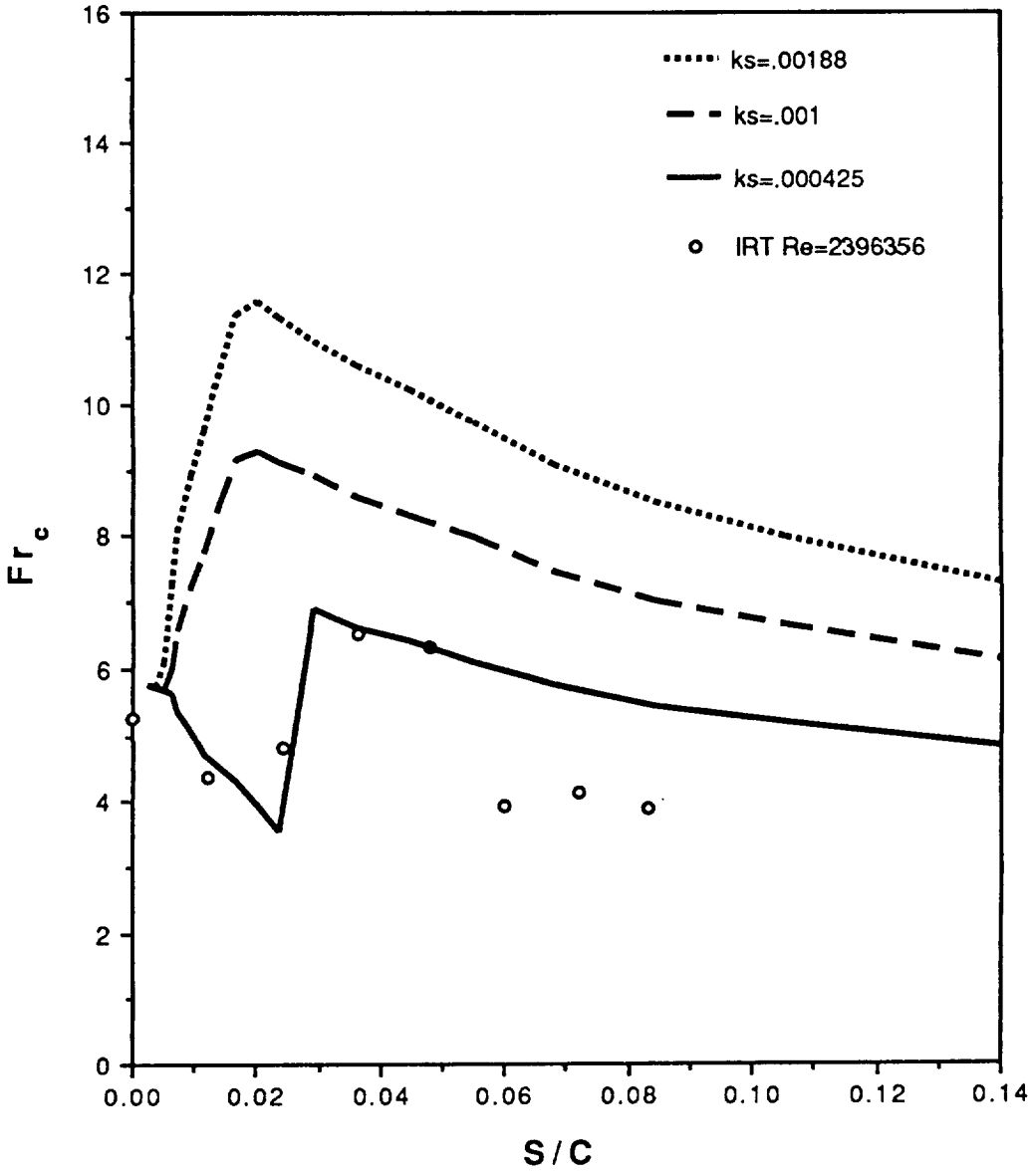

Figure 97. Frossling Number Comparison for dense 2 roughened airfoil, 205 ft/sec, 0 degree angle of attack: IRT data versus integral boundary layer solution.

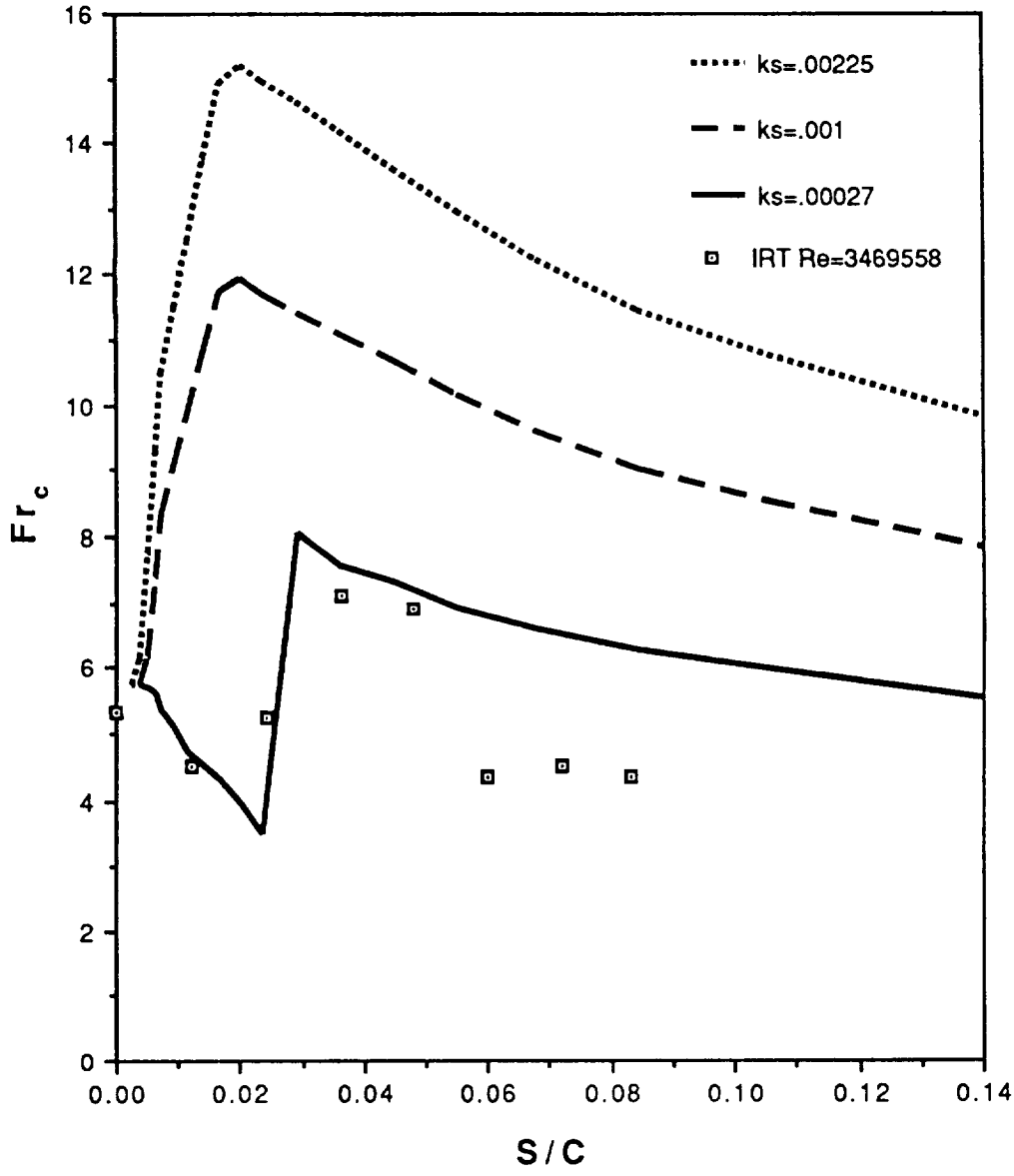

Figure 98. Frossling Number Comparison for dense 2 roughened airfoil, 310 ft/sec, 0 degree angle of attack: IRT data versus integral boundary layer solution.

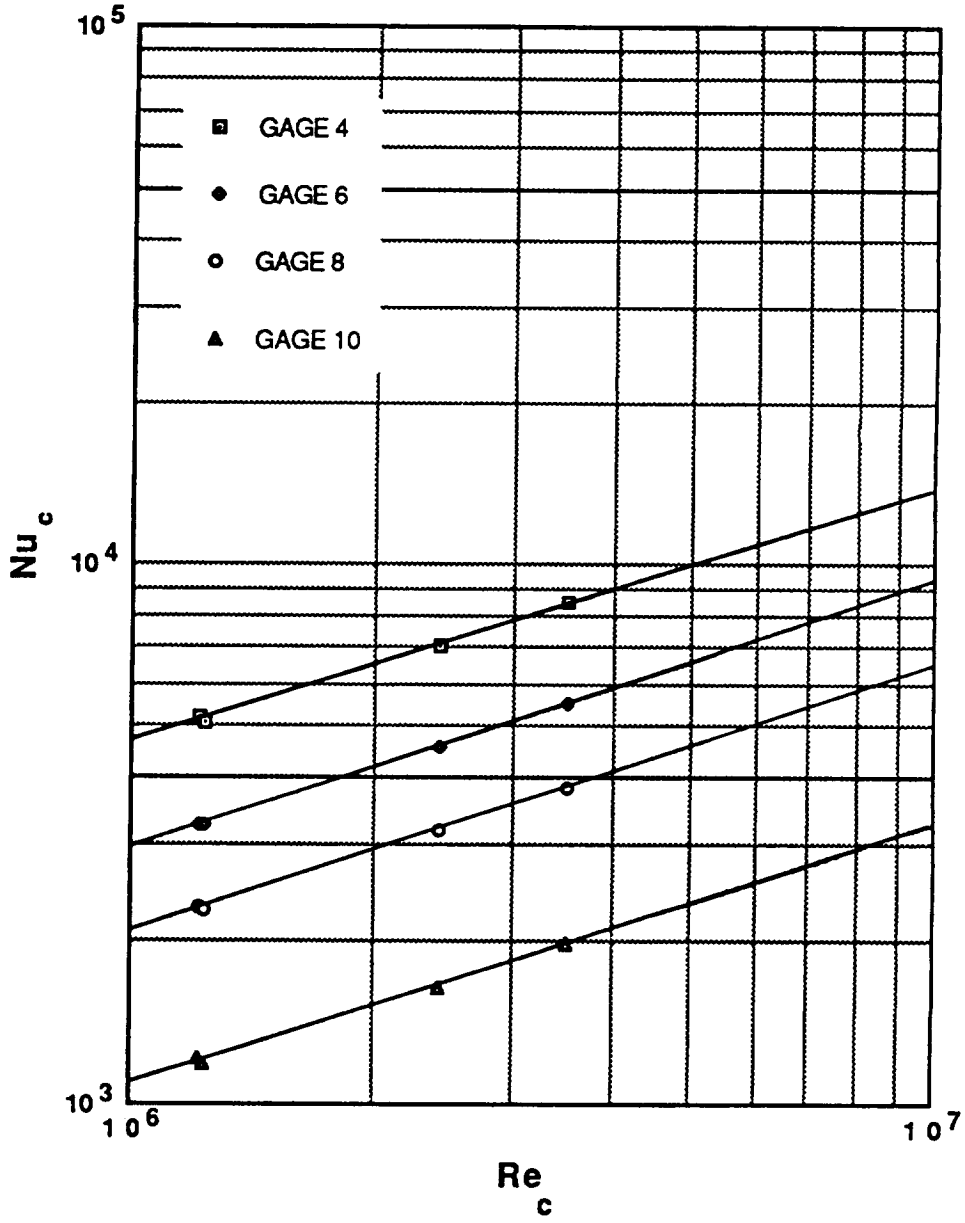

Figure 99. Nusselt Number versus Reynolds Number correlation for smooth airfoil, 0 degree angle of attack: IRT data (without spray).

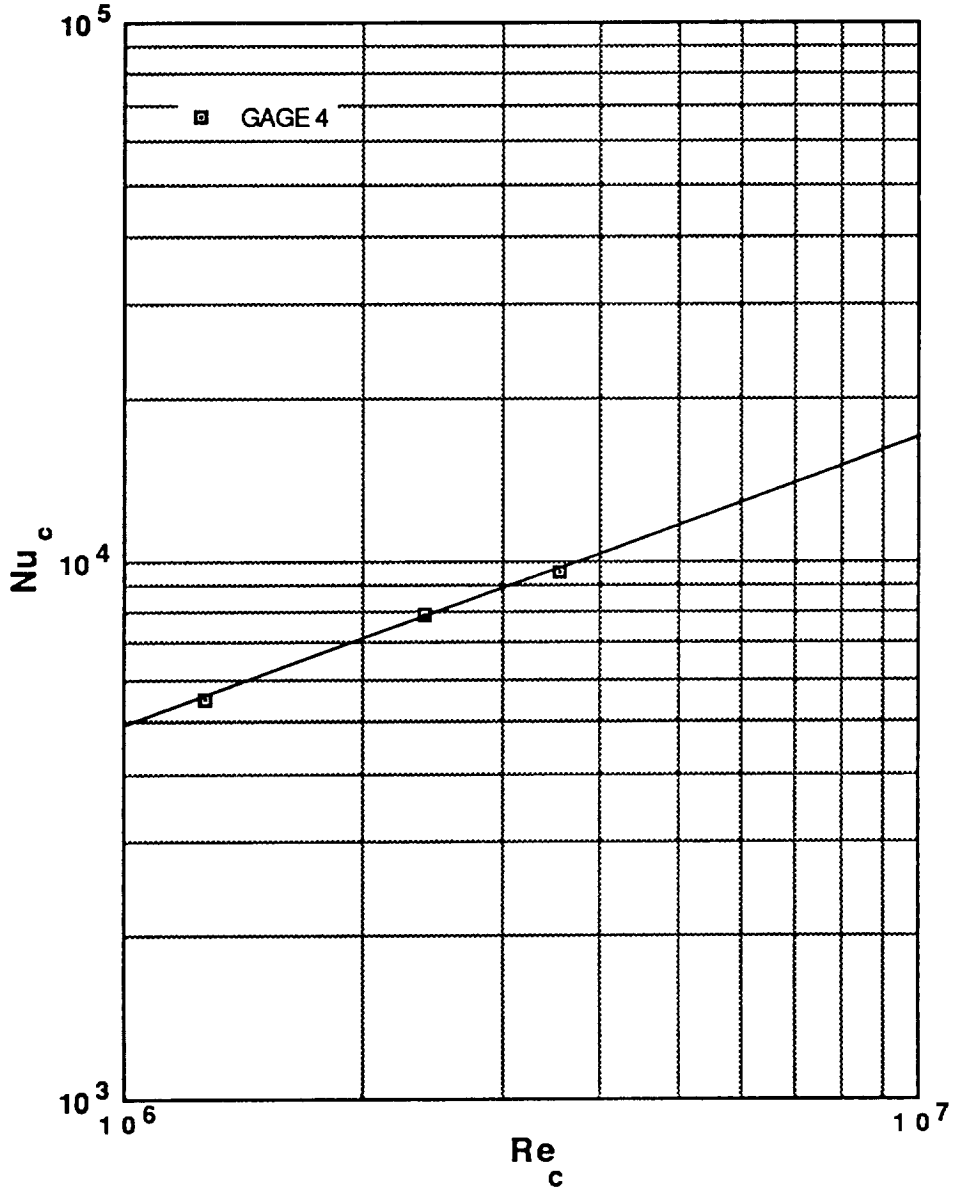

Figure 100. Nusselt versus Reynolds Number correlation for airfoil with leading edge roughness, 0 degree angle of attack: IRT data (without spray).

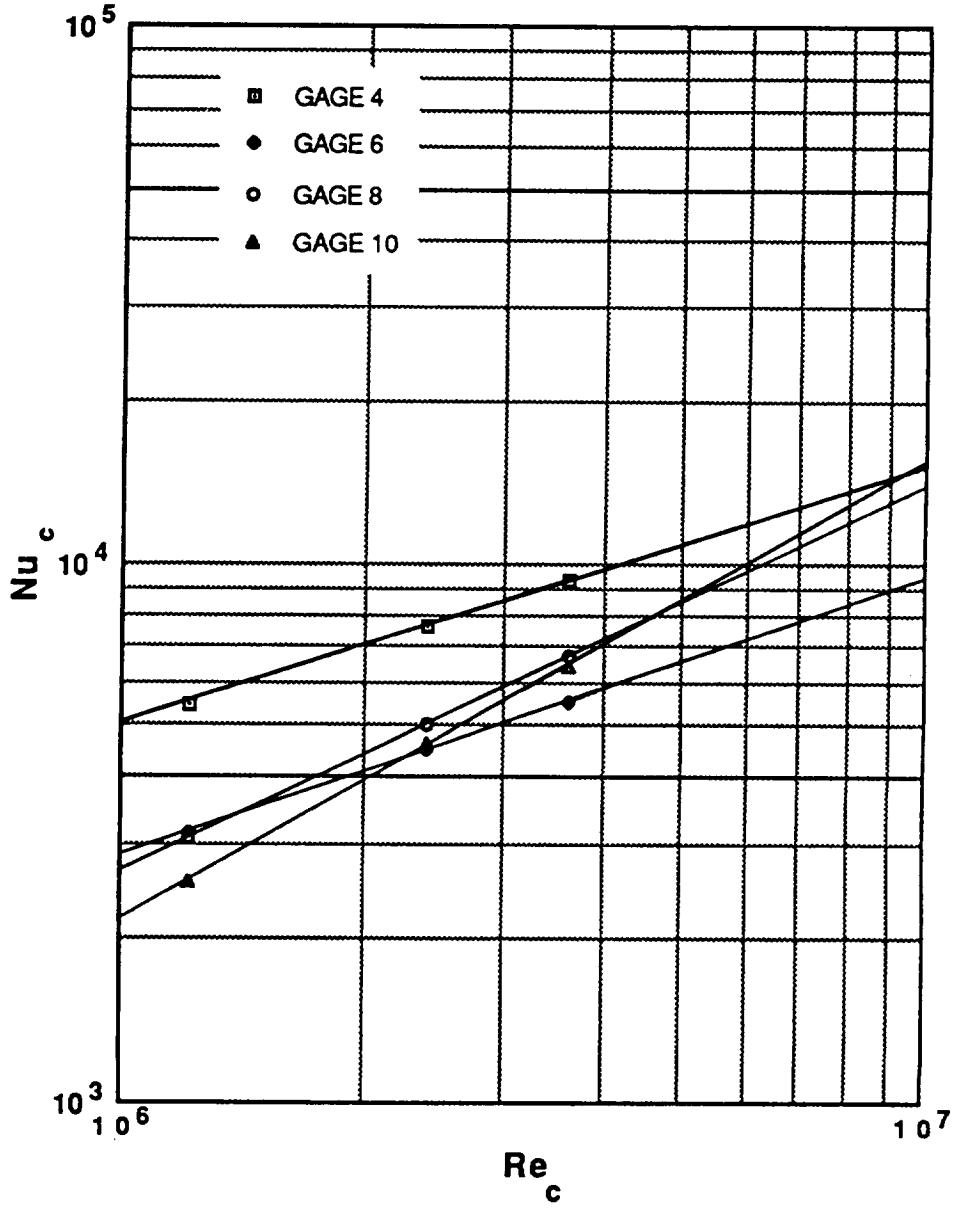

Figure 101. Nusselt Number versus Reynolds Number for airfoil with sparse roughness, 0 degree angle of attack: IRT data (without spray).

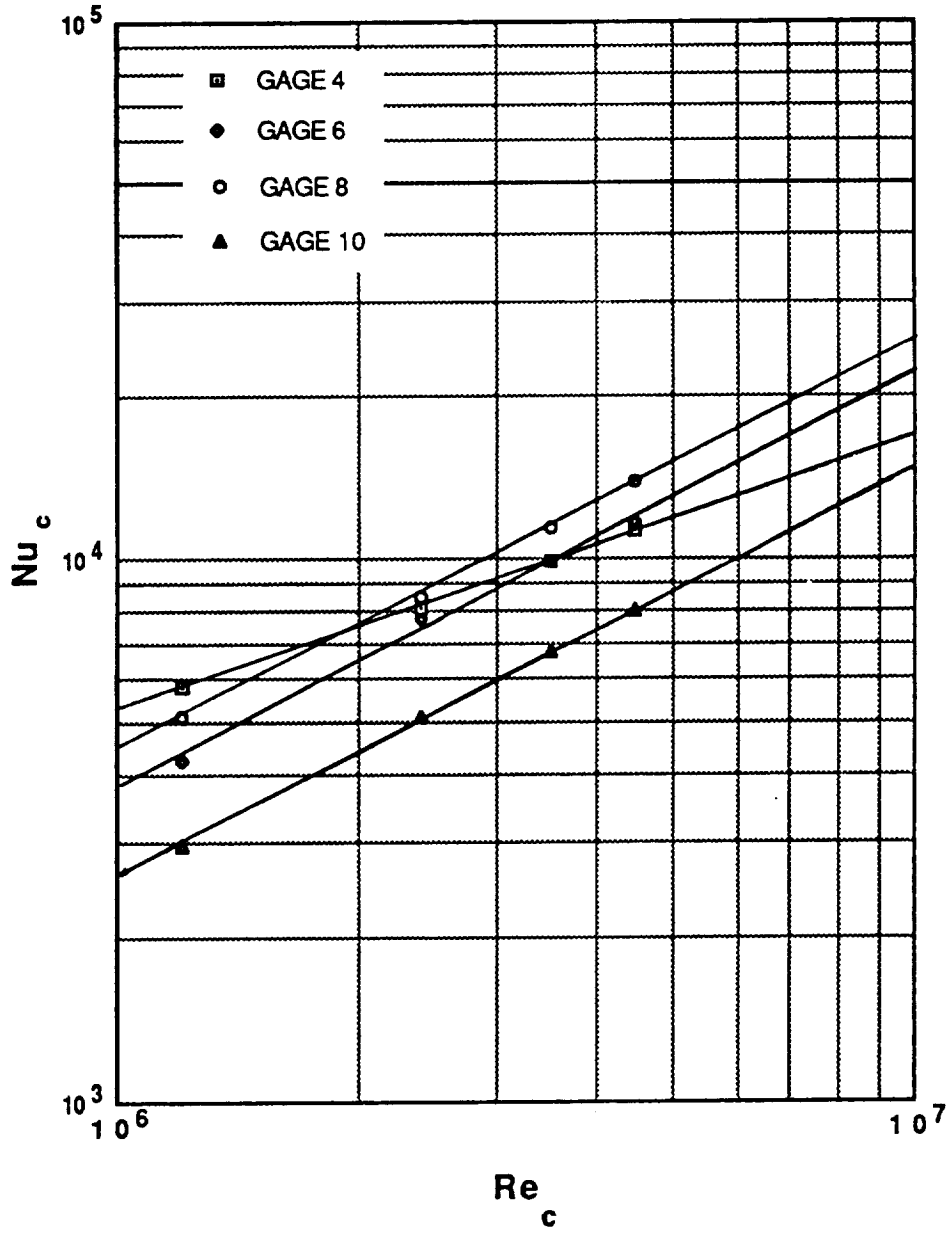

Figure 102. Nusselt Number versus Reynolds Number correlation for airfoil with dense 1 roughness, 0 degree angle of attack: IRT data (without spray).

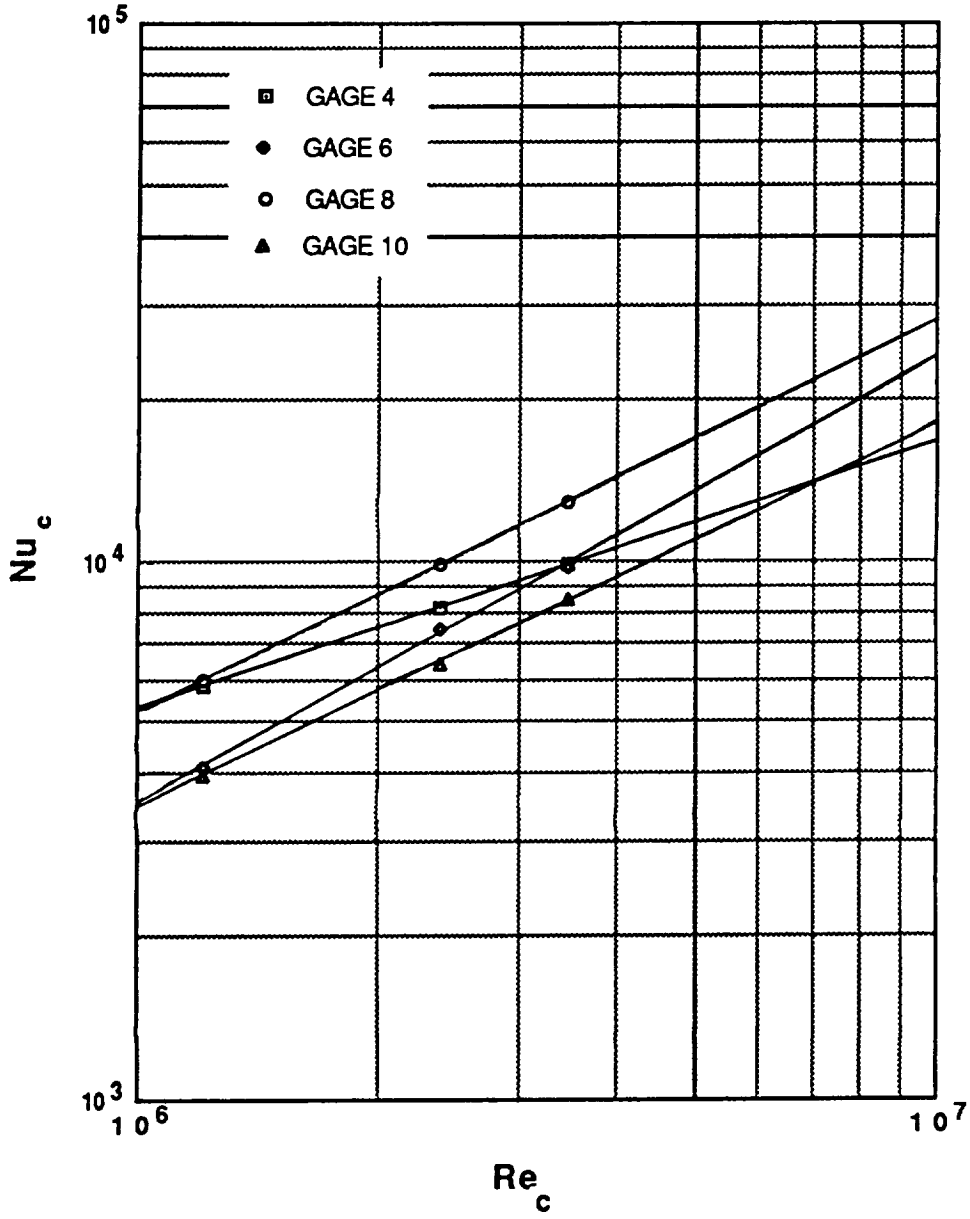

Figure 103. Nusselt Number versus Reynolds Number correlation for airfoil with dense 2 roughness, 0 degree angle of attack: IRT data (without spray).

APPENDIX A - Heat Loss Analysis

Some of the heat emitted from each heater was not directly convected from the aluminum strip surface, but rather was conducted through the epoxy on the sides and ends of the strips and then convected from the epoxy surface (see Figure A1). These heat losses to the epoxy gaps (see Figure A2) and ends (see Figure A3) were both determined from an exact solution [13,25] of a rectangle with two adjacent sides insulated (due to symmetry and a guard heater for the gap; limited heat penetration and a guard heater for the end), a third side at constant temperature (the gage temperature, T_w), and the fourth side convecting to the air.

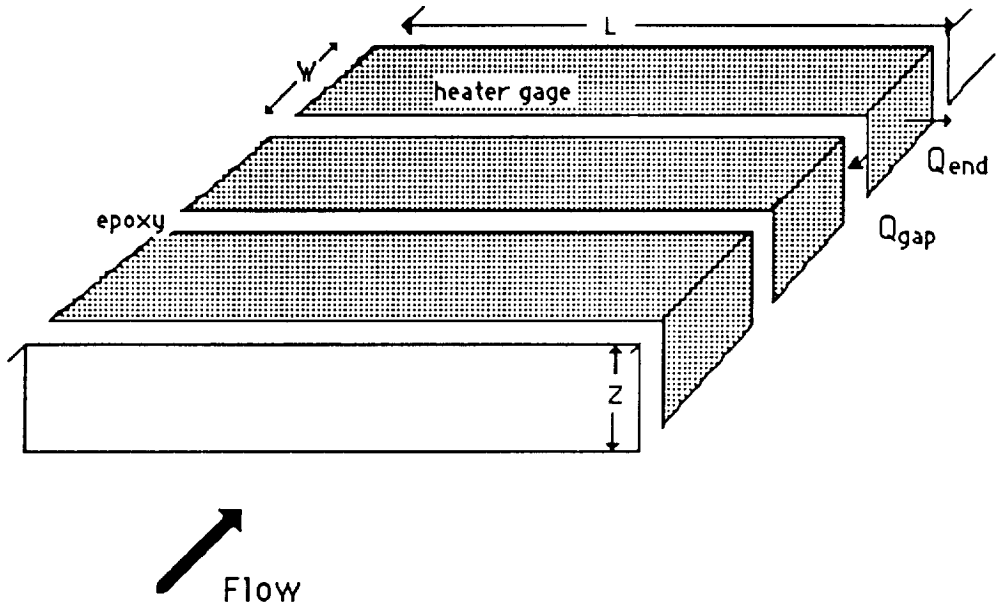

Figure A1. Heat losses from each gage through the epoxy gaps and ends.

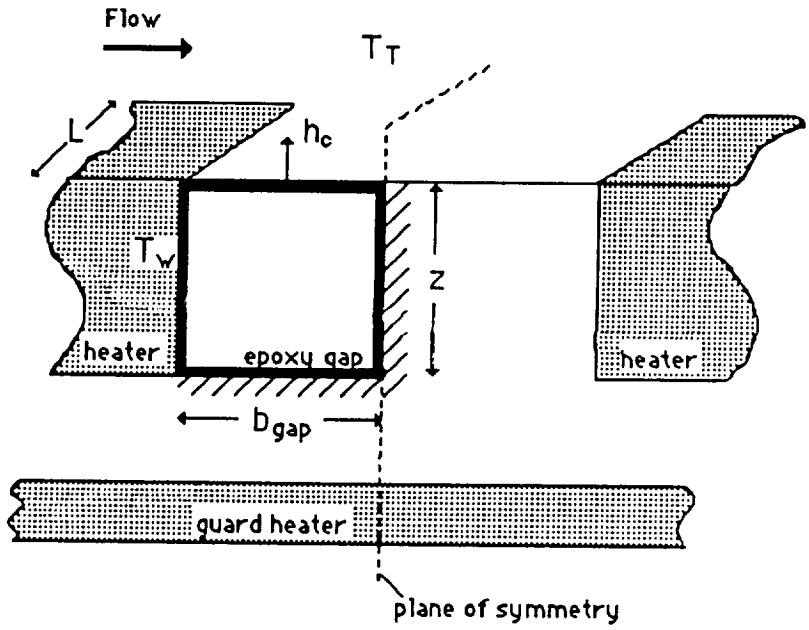

Figure A2. Gap loss model.

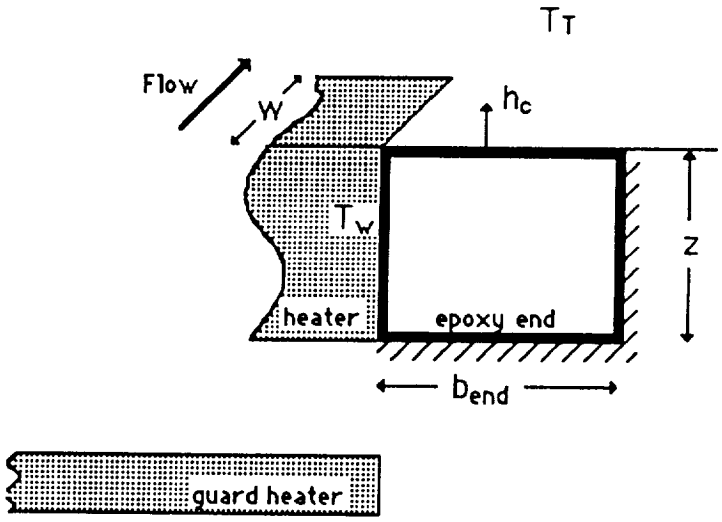

Figure A3. End loss model.

The solutions of these problems are:

$$Q_{gap} = 2h_c L(T_w - T_T) \sum_{n=1}^{\infty} \frac{\tan(\alpha_n z)\tanh(\alpha_n b_{gap})}{\alpha_n^2 z + \frac{h_c^2}{k_{ep}^2} z + \frac{h_c}{k_{ep}}} \qquad \text{(A-1)}$$

and

$$Q_{end} = 2h_c W(T_w - T_T) \sum_{n=1}^{\infty} \frac{\tan(\alpha_n z)\tanh(\alpha_n b_{end})}{\alpha_n^2 z + \frac{h_c^2}{k_{ep}^2} z + \frac{h_c}{k_{ep}}} \qquad \text{(A-2)}$$

where the α_n's are roots of:

$$z\alpha_n \tan(\alpha_n z) = \frac{h_c z}{k_{ep}} \qquad \text{(A-3)}$$

The quantity L is the length of each gage, W is the width and z is the gage depth. B_{gap} is the gap width divided by 2, and b_{end}, a fictional end length was estimated, through trial and error, at a sufficient length such that an insulated boundary condition could be assumed.

Gap losses for each gage generally ranged from 13 to 19%, while end losses were generally about 2 to 5%.

APPENDIX B - Error Analysis

An error analysis was conducted using the method outlined by Kline and McClintock [22] and is summarized as follows:

$$h_c = \frac{Q_{con}}{A\,\Delta T} = \frac{Q_{EI} - Q_{rad} - Q_{gap} - Q_{end}}{A\ (T_W - T_T)} \qquad \text{(B-1)}$$

where,

$Q_{EI} = E \times I =$ (heater voltage x heater current)

The uncertainty of h_C can be written, by definition, as:

$$dh_c = \left[\left(\frac{\partial h_c}{\partial Q_{EI}}\, dQ_{EI}\right)^2 + \left(\frac{\partial h_c}{\partial Q_{rad}}\, dQ_{rad}\right)^2 + \left(\frac{\partial h_c}{\partial Q_{gap}}\, dQ_{gap}\right)^2 + \left(\frac{\partial h_c}{\partial Q_{end}}\, dQ_{end}\right)^2 + \left(\frac{\partial h_c}{\partial A}\, dA\right)^2 + \left(\frac{\partial h_c}{\partial T_W}\, dT_W\right)^2 + \left(\frac{\partial h_c}{\partial T_T}\, dT_T\right)^2 \right]^{0.5} \qquad \text{(B-2)}$$

Substituting for the partial differential terms using (B-1) and dividing by h_C yields:

$$\frac{dh_c}{h_c} = \left[\left(\frac{dQ_{EI}}{Q_{con}}\right)^2 + \left(\frac{dQ_{rad}}{Q_{con}}\right)^2 + \left(\frac{dQ_{gap}}{Q_{con}}\right)^2 + \left(\frac{dQ_{end}}{Q_{con}}\right)^2 + \left(\frac{dA}{A}\right)^2 + \left(\frac{dT_W}{\Delta T}\right)^2 + \left(\frac{dT_T}{\Delta T}\right)^2 \right]^{0.5} \qquad \text{(B-3)}$$

The individual variable uncertainties were likewise determined from their respective defining equations:

$$\frac{dQ_{EI}}{Q_c} = \left[\left(\frac{I\,dE}{Q_c}\right)^2 + \left(\frac{E\,dI}{Q_c}\right)^2 \right]^{0.5} \qquad \text{(B-4a)}$$

•
•
•

and then the following estimates were employed:

$$dE = \left(E_{RMS}^2 + (.015E)^2\right)^{0.5}$$

$$dI = \left(I_{RMS}^2 + (.015I)^2\right)^{0.5}$$

gage: d(length)= .002 in. (length ± <0.1%)
d(width) = .001 in. (width ± 0.5%)
d(depth) = .0025 in. (depth ± 2.0%)

$$dT_W = \left(T_{W_{RMS}}^2 + (.005(T_W - T_{t.c.ref}))^2\right)^{0.5}$$

$$dT_T = \left(T_{T_{RMS}}^2 + (.001T_T)^2\right)^{0.5}$$

dk_{ep}=0.055 BTU/hr ft °F (k_{ep} ± 50.0%)

Using the above values in equation (B-3), the calculated errors in h_c for each gage for each experimental run were similar and averaged around 4.5%. A large part of the error was due to the Q_{gap} and Q_{end} terms in which the relatively large uncertainty in the k_{ep} value played a substantial role.

Finally the uncertainty of the Frossling Number is similarly calculated:

$$Fr_c = \frac{Nu}{Re^{0.5}} = \frac{\left(\frac{h_c c}{k}\right)}{\left(\frac{\rho V c}{\mu}\right)^{0.5}} \qquad \text{(B-5)}$$

$$\frac{dFr_c}{Fr_c} = \left[\left(\frac{dh_c}{h_c}\right)^2 + \left(\frac{dk}{k}\right)^2 + \frac{1}{4}\left(\left(\frac{dc}{c}\right)^2 + \left(\frac{d\mu}{\mu}\right)^2 + \left(\frac{d\rho}{\rho}\right)^2 + \left(\frac{dV}{V}\right)^2\right)\right]^{0.5} \qquad \text{(B-6)}$$

With the following estimates:

$d\mu$ =1.8x10^{-7} lb/ft sec ($\mu \pm 1.5\%$)
$d\rho$ =0.0014 lb/ft^3 ($\rho \pm 2.0\%$)
dV =4.0 ft/sec (V ±2.0%)
dc =0.1 in. (c ±0.5%)
dk =0.00022 BTU/hr ft °F (k ±1.5%)

the errors in Frossling Number were calculated to be around 5%.

NASA
National Aeronautics and Space Administration

Report Documentation Page

1. Report No.	2. Government Accession No.	3. Recipient's Catalog No.
NASA CR-4278		

4. Title and Subtitle
Heat Transfer Measurements From a NACA 0012 Airfoil in Flight and in the NASA Lewis Icing Research Tunnel

5. Report Date
March 1990

6. Performing Organization Code

7. Author(s)
Philip E. Poinsatte

8. Performing Organization Report No.
None (E-5228)

10. Work Unit No.
506-68-11

9. Performing Organization Name and Address
The University of Toledo
Department of Chemical Engineering
Toledo, Ohio 43606

11. Contract or Grant No.
NAG3-72

13. Type of Report and Period Covered
Contractor Report
Final

12. Sponsoring Agency Name and Address
National Aeronautics and Space Administration
Lewis Research Center
Cleveland, Ohio 44135-3191

14. Sponsoring Agency Code

15. Supplementary Notes
Project Manager, Mario Vargas, Propulsion Systems Division, NASA Lewis Research Center. This report was a thesis submitted in partial fulfillment of the requirements for the Master of Science Degree in Chemical Engineering to The University of Toledo in June 1989.

16. Abstract

Local heat transfer coefficients from a smooth and roughened NACA 0012 airfoil were measured using a steady state heat flux method. Heat transfer measurements on the specially constructed 0.533-m chord airfoil were made both in flight on NASA Lewis Twin Otter Research Aircraft and in the NASA Lewis Icing Research Tunnel (IRT). Roughness was obtained by the attachment of 2-mm diameter hemispheres to the airfoil surface in four distinct patterns. The flight data was taken for the smooth and roughened airfoil at various Reynolds numbers based on chord in the range 1.24×10^6 to 2.50×10^6 and at various angles of attack up to 4°. During these flight tests, the free stream velocity turbulence intensity was found to be very low (<0.1 percent). The wind tunnel data was taken in the Reynolds number range 1.20×10^6 to 4.52×10^6 and at angles of attack from −4° to 8°. The turbulence intensity in the IRT was 0.5 to 0.7 percent with the cloud making sprays off. Results for both the flight and tunnel tests are presented as Frossling number based on chord versus position on the airfoil surface for various roughnesses and angle of attack. A table of power law curve fits of Nusselt number as a function of Reynolds numbers is also provided. The higher level of turbulence in the IRT versus flight had little effect on heat transfer for the lower Reynolds numbers but caused a moderate increase in heat transfer at the higher Reynolds numbers. Turning on the cloud making spray air in the IRT did not alter the heat transfer. Roughness generally increased the heat transfer by locally disturbing the boundary layer flow. Finally, the present data was not only compared with previous airfoil data where applicable, but also with leading edge cylinder and flat plate heat transfer values which are often used to estimate airfoil heat transfer in computer codes.

17. Key Words (Suggested by Author(s))	18. Distribution Statement
Icing Heat transfer Airfoil	Unclassified − Unlimited Subject Category 02

19. Security Classif. (of this report)	20. Security Classif. (of this page)	21. No. of pages	22. Price*
Unclassified	Unclassified	194	A09

NASA FORM 1626 OCT 86

*For sale by the National Technical Information Service, Springfield, Virginia 22161

NASA-Langley, 1990

End Date; June 13, 1990